

AD-A272 998



2

ARMY RESEARCH LABORATORY



# Applicability and Performance Benefits of XD® Titanium Aluminides to Expendable Gas Turbine Engines

Pamela Sadler, K. Sharvan Kumar, and John A. S. Green

ARL-CR-61

August 1993

prepared by

Martin Marietta Laboratories  
1450 S. Rolling Road  
Baltimore, MD 21227-3898

under contract

DAAL04-91-C-0034



93-28452

Approved for public release; distribution unlimited.

93 11 19 09 4

The findings in this report are not to be construed as an official Department of the Army position unless so designated by other authorized documents.

Citation of manufacturer's or trade names does not constitute an official endorsement or approval of the use thereof.

Destroy this report when it is no longer needed. Do not return it to the originator.

REPORT DOCUMENTATION PAGE			Form Approved OMB No 0704-0188	
<small>Public reporting burden for this collection of information is estimated to average 1 hour per response, including the time for reviewing instructions, searching existing data sources, gathering and maintaining the data needed, and completing and reviewing the collection of information. Send comments regarding this burden estimate or any other aspect of this collection of information, including suggestions for reducing this burden, to Washington Headquarters Services, Directorate for Information Operations and Reports, 1215 Jefferson Davis Highway, Suite 1204, Arlington, VA 22202-4302, and to the Office of Management and Budget, Paperwork Reduction Project (0704-0188), Washington, DC 20503.</small>				
1. AGENCY USE ONLY (Leave blank)	2. REPORT DATE August 1993	3. REPORT TYPE AND DATES COVERED Final Rpt. 10/1/91 - 3/31/93		
4. TITLE AND SUBTITLE Applicability and Performance Benefits of XD® Titanium Aluminides to Expendable Gas Turbine Engines		5. FUNDING NUMBERS Contract # DAAL04-91-C-0034		
6. AUTHOR(S) Pamela Sadler, K. Sharvan Kumar, John A. S. Green				
7. PERFORMING ORGANIZATION NAME(S) AND ADDRESS(ES) Martin Marietta Laboratories 1450 S. Rolling Road Baltimore, MD 21227-3898		8. PERFORMING ORGANIZATION REPORT NUMBER MML TR 93-09		
9. SPONSORING/MONITORING AGENCY NAME(S) AND ADDRESS(ES) U. S. Army Research Laboratory Materials Directorate Watertown, MA 02172-0001 Attn: AMSRL-OP-PR-WT		10. SPONSORING/MONITORING AGENCY REPORT NUMBER ARL-CR-61		
11. SUPPLEMENTARY NOTES Wego Wang, COR				
12a. DISTRIBUTION / AVAILABILITY STATEMENT Approved for public release; distribution unlimited			12b. DISTRIBUTION CODE	
13. ABSTRACT (Maximum 200 words) <p>The purpose of this program was to produce XD® TiAl compressor rotors for the experimental P9005 gas turbine engine to be used in the Army's Integrated High Performance Turbine Engine Technology program. Specific tasks included the casting of XD® titanium aluminide, processing optimization, component design analysis modifications and final component machining to specifications. Specifically, an ingot of a Ti-45Al-2Mn-2V alloy containing 7 volume % TiB<sub>2</sub> was cast and then HIPed to eliminate residual porosity. Eight cylinders were machined from the HIPed material and isothermally forged. Microstructural analysis and mechanical property evaluation were performed on representative forgings. Several heat treatment schedules were examined, and the resulting microstructures were characterized using x-ray diffraction, optical and scanning electron microscopy. From these analyses, heat treatments were identified. Tensile behavior as a function of temperature, fracture toughness at room and elevated temperatures, creep resistance and fatigue response were evaluated. Fracture surfaces were characterized.</p> <p>Based on the observed mechanical properties, heat-treatment schedules were identified for the remaining forgings intended to be machined into final components. Williams International performed a detailed design analysis for the rotor. A local vendor was identified to machine the final component.</p>				
14. SUBJECT TERMS XD® process, Titanium aluminide, Titanium diboride, Composites, Microstructure, Processing, Properties.			15. NUMBER OF PAGES 164	
			16. PRICE CODE	
17. SECURITY CLASSIFICATION OF REPORT Unclassified	18. SECURITY CLASSIFICATION OF THIS PAGE Unclassified	19. SECURITY CLASSIFICATION OF ABSTRACT Unclassified	20. LIMITATION OF ABSTRACT UL	

NSN 7540-01-280-5500

Standard Form 298 (Rev. 2-89)  
Prescribed by ANSI Std. Z39-18  
298-102

## TABLE OF CONTENTS

LIST OF ILLUSTRATIONS .....	iv
LIST OF TABLES .....	vii
ABSTRACT .....	viii
I. INTRODUCTION .....	1
II. TECHNICAL BACKGROUND .....	4
A. Monolithic Titanium Aluminide Alloys .....	4
B. XD® Titanium Aluminide Composites .....	10
III. SCOPE OF PROGRAM AND STATEMENT OF WORK .....	16
A. Scope .....	16
B. Statement of Work .....	16
IV. TECHNICAL ACCOMPLISHMENTS .....	20
A. Design Analysis Performed at Williams International .....	20
1. Material selection .....	20
2. Heat transfer analysis .....	21
3. Elastic stress analysis .....	21
4. Critical flaw size prediction .....	21
5. Dynamic analysis .....	21
6. Rotor attachment and blade tip growth analyses .....	22
B. Alloy Production .....	23
C. Forging Characterization .....	25
D. Heat Treatment Optimization .....	28
E. Mechanical Property Testing .....	40
1. Tensile testing .....	40
2. Fracture toughness testing .....	48
3. High-cycle fatigue testing .....	51
4. Creep testing .....	53
F. Heat Treatment of Forgings .....	60
G. Final Rotor Machining .....	61
H. Summary .....	61
V. CONCLUSIONS AND RECOMMENDATIONS .....	62
VI. REFERENCES .....	64
APPENDIX A	
APPENDIX B	

## LIST OF ILLUSTRATIONS

Figure 1.	The titanium-aluminum binary phase diagram in the 36 to 56 atomic % aluminum range <sup>1</sup> .....	5
Figure 2.	Micrographs of three typical microstructures found in the titanium-aluminide binary system after heat treatment at 1350°C (2462°F) where (a) is a single-phase microstructure at 52 atomic % Al, (b) a duplex microstructure at 48 atomic % Al, and (c) a fully-transformed microstructure at 46 atomic % Al <sup>1</sup> .....	7
Figure 3.	Variation of phase morphology is shown for thermomechanically processed titanium aluminide alloys. Optical micrographs show (a) forged alloy and (b) extruded alloy. Bands of recrystallized TiAl grains are layered between Ti <sub>3</sub> Al and TiAl lamellae, which are noticeably different from the two-phase microstructures in Figure 2 <sup>14</sup> .....	11
Figure 4.	A typical forging from the eight forgings produced at Ladish Co. for this program .....	26
Figure 5.	A 10.2 cm (4 in) diameter cylinder electro-discharge machined from one of the forgings, which will serve as the "blank" or "preform" prior to final component machining.....	26
Figure 6.	The location of the seven metallographic specimens electro-discharge machined from a vertical slice of a forged cylinder .....	27
Figure 7.	Optical micrographs of samples A through G removed from the center portion of a forged cylinder .....	29-30
Figure 8.	Back-scattered electron micrographs from (a) sample A, (b) sample C, and (c) sample E, all removed from the center portion of a forged cylinder. Atomic number contrast differences reveal TiB <sub>2</sub> particulate as black, TiAl as grey, and Ti <sub>3</sub> Al as light grey in color .....	31
Figure 9.	Back-scattered electron micrographs after the second HIPing procedure. Depicted is (a) the as-HIPed microstructure, (b) heat treatment at 1300°C (2372°F) for 1 h, (c) heat treatment at 1330°C (2426°F) for 1 h, and (d) heat treatment at 1340°C (2444°F) for 1 h.....	32
Figure 10.	Optical micrographs of the alloy (a) in the as-HIPed condition, (b) after heat treatment at 1300°C (2372°F) for 1 h, and (c) after heat treatment at 1340°C (2444°F) for 1 h.....	33
Figure 11.	X-ray diffraction pattern of sample C in the as-forged condition. TiAl phase and TiB <sub>2</sub> particulate are the predominant phases with one peak of Ti <sub>3</sub> Al phase present .....	34
Figure 12.	Optical micrographs after heat treatment (a) at 1200°C (2192°F) for 1 h and (b) at 1340°C (2444°F) for 1 h. (a) shows bands of blocky, equiaxed phase and a coarsened lamellar-type microstructure, whereas (b) is fully lamellar.....	37

# LIST OF ILLUSTRATIONS (cont.)

Figure 13.	Micrographs after a duplex heat treatment of 1340°C (2444°F) for 1 h + 1200°C (2192°F) for 2 h where (a) shows an optical micrograph and (b) shows a back-scattered electron image. The angular black holes in (b) are from particulates pulled out of the matrix during specimen preparation.....	38
Figure 14.	Micrographs after a duplex heat treatment of 1340°C (2444°F) for 1 h + 1200°C (2192°F) for 10 h where (a) shows an optical micrograph and (b) shows a back-scattered electron image .....	39
Figure 15.	Secondary electron micrographs of the fracture surfaces of tensile specimens in (a) the as-HIPed condition that has an equiaxed microstructure and (b) after heat treatment at 1340°C (2444°F) for 1 h that has a lamellar microstructure .....	42
Figure 16.	Yield strength - temperature profiles for forged + HIPed, Ti-45Al-2Mn-2V + 7 volume % TiB <sub>2</sub> alloy .....	44
Figure 17.	Fracture strength versus temperature for forged + HIPed, Ti-45Al-2Mn-2V + 7 volume % TiB <sub>2</sub> alloy .....	45
Figure 18.	The effect of temperature on tensile ductility of the forged + HIPed, Ti-45Al-2Mn-2V + 7 volume % TiB <sub>2</sub> alloy .....	46
Figure 19.	Secondary electron micrographs of the fracture surfaces of tensile specimens tested at 20°C (68°F) for (a) lamellar and (b) lamellar + equiaxed microstructures and at 500°C (932°F) for (c) lamellar and (d) lamellar + equiaxed microstructures .....	47
Figure 20.	Fracture toughness variation with temperature for short-rod specimens tested at Metcut and notched-bend specimens tested at Martin Marietta .....	50
Figure 21.	Scanning electron micrographs depicting the fracture surface of two notched-bend specimens tested in 3-point bend at (a) 20°C (68°F) and (b) 400°C (752°F). While the mode of fracture is predominantly along the lamellar grains, a few areas of planar fracture are present in (b) .....	52
Figure 22.	Stress-cycles to failure (S-N curve) at room temperature for Ti-45Al-2Mn-2V + 7 volume % TiB <sub>2</sub> alloy showing its outstanding fatigue resistance .....	54
Figure 23.	High-cycle fatigue behavior at 200°C (392°F) expressed as maximum applied stress as a function of the number of cycles to failure. At the critical maximum stress of 172 MPa (25 ksi), cycles to failure exceeded 10 <sup>7</sup> cycles .....	55

# LIST OF ILLUSTRATIONS (cont.)

- Figure 24. Creep strain as a function of time to rupture at 800°C (1472°F) for 4 applied stress conditions: 138, 207, 276, and 345 MPa (20, 30, 40, and 50 ksi) ..... 56
- Figure 25. Back-scattered electron micrographs of the cross section of creep specimens tested at 800°C (1472°F): (a) the grip section, (b) the section adjacent to the fracture of the 138 MPa (20 ksi) specimen and (c) the section adjacent to the fracture of the 276 MPa (40 ksi) specimen (black-TiB<sub>2</sub>; grey-TiAl; light grey-Ti<sub>3</sub>Al) ..... 58
- Figure 26. The steady-state creep rate as a function of the initial applied stress for 3 forged alloys tested at 800°C (1472°F)<sup>18</sup> ..... 59

## LIST OF TABLES

Table I.	Proposed schedule depicting the work for the 19-month period, October 1991 through April 1993 .....	17
Table II.	Ingot chemistries for the doubly-melted, 20.3 cm (8") diameter x 50.8 cm (20") high ingot produced at TIMET. Ingot was processed by the vacuum arc remelting (VAR) method .....	24
Table III.	Matrix of mechanical testing performed in this program .....	41
Table IV.	Typical Mechanical Properties for XD® TiAl Alloys, Comparing the Alloy Used in this Study with Those Containing 0.8 Volume % TiB <sub>2</sub> .....	63

Accession For	
NTIS CRA&I	<input checked="" type="checkbox"/>
DTIC TAB	<input checked="" type="checkbox"/>
Unannounced	<input type="checkbox"/>
Justification .....	
By .....	
Distribution /	
Availability Codes	
Dist	Avail. Codes
A-1	

DTIC QUALITY INSPECTED 5



## ABSTRACT

The purpose of this program was to produce XD<sup>®</sup> TiAl compressor rotors for the experimental P9005 gas turbine engine to be used in the Army's Integrated High Performance Turbine Engine Technology (IHPTET) program. The 18-month program involved the casting of XD<sup>®</sup> titanium aluminide, processing optimization, component design analysis modifications and final component machining to specifications.

In this program, an ingot of a Ti-45Al-2Mn-2V alloy containing 7 volume % TiB<sub>2</sub> was produced at TIMET, Inc., and subsequently HIPed at Howmet's HIP Division. Eight cylinders were machined from the HIPed material and isothermally forged at Ladish Co. The microstructural analysis and mechanical property evaluation were performed on representative forgings.

Several heat treatment schedules were examined to obtain a range of microstructures varying from an essentially equiaxed structure to a fully lamellar morphology. The microstructures were characterized using x-ray diffraction, optical and scanning electron microscopy. From these analyses, heat treatments were identified that would yield desirable microstructures for obtaining the mechanical properties critical to the intended application. Tensile behavior as a function of temperature, fracture toughness at room and elevated temperatures, creep resistance and fatigue response were evaluated. Fracture surfaces were characterized.

Based on the observed mechanical properties, heat-treatment schedules were identified for the remaining forgings that were to be machined into final components. Williams International, on a subcontract from Martin Marietta Laboratories, performed a detailed design analysis for the rotor and their findings are included in Appendix A. A local vendor was identified to machine the final component, although this phase of the program was eliminated due to lack of funding.

## I. INTRODUCTION

Ordered intermetallic alloys are being considered for high-temperature structural applications such as engine components, which require strength, stiffness, damage tolerance, low density and creep rates and oxidation resistance. The high melting temperature and potentially good oxidation resistance make them good candidates for high-temperature usage. Nickel-based superalloys are presently used for high-temperature components, but their major drawback is their high density ( $\sim 8.0$  g/cc). The desire for enhanced performance has placed an unprecedented need for lightweight, high-temperature alloys. This has spawned the heightened research and development efforts of ordered intermetallic materials that have the potential to meet these requirements.

Ordered intermetallics are a class of materials where two metallic constituents coexist in a stoichiometric ratio with each species occupying specific lattice sites in the crystal structures. They have recently been the subject of extensive research, development, and application within the defense and aerospace industries. Much of the research on these unique materials has focused on overcoming the inherently low ductility and damage tolerance, and on learning the processing methodology required to successfully design, fabricate and structurally utilize components produced from these materials. Metallurgically, it is often convenient to refer to intermetallics as compounds that exhibit properties intermediate to those considered typical of conventional engineering metals, based upon their ability to be hot-worked and formed like metals, and those of ceramics because of their high resistance to deformation, high moduli, and sometimes excellent environmental resistance.

The two-phase, titanium aluminide class of ordered intermetallic alloys has been extensively studied as a replacement for nickel-based superalloys in certain applications. These alloys contain 45 to 48% aluminum are located within the  $\alpha_2$  ( $\text{Ti}_3\text{Al}$ ) +  $\gamma$  ( $\text{TiAl}$ ) phase regime. They possess high-temperature strength, a high melting point and about half the density of conventional nickel-based alloys. Drawbacks of titanium aluminides are low room-temperature fracture toughness and ductility, due to a limited number of operative slip systems available for dislocation motion in both the  $\alpha_2$  and the  $\gamma$  phases, low creep resistance, and formability limitations. In spite of these problems, the advantage of low density can be overwhelming in some applications. Ambient temperature properties can be improved by microstructural manipulation and chemistry

variation with addition of alloying elements. Oxidation resistance is dependent on the amount of  $\gamma$  phase present, which has greater oxidation resistance than  $\alpha_2$  phase. Investment casting and powder metallurgy processing have become relatively commonplace with the accomplishments of isothermal forging of ingot material and extrusion of alloyed powders. Progress is being made in foil and sheet production, which had been challenging due to the retention of the ordered crystal structure in the  $\gamma$  phase at typical processing temperatures.

Martin Marietta has a patented processing procedure called XD<sup>®</sup> Technology, resulting in the *in-situ* formation of ceramic particulates, short fibers, and whiskers in metal and intermetallic matrices. Synthesis of the reinforcement intrinsically within the matrix allows thermodynamic stability, at least in the solid state in the matrix under consideration, provides particle/matrix interface cleanliness, and produces a single-crystal reinforcement. The development of discontinuously-reinforced, titanium aluminide composite alloys using the XD<sup>®</sup> process was intended to improve materials properties such as ambient impact resistance and operational temperature creep resistance. Ceramic particulates refine the cast grain structure and enable property enhancement through thermomechanical processing and subsequent heat treatment.

It is the intention of this program to produce XD<sup>®</sup> titanium aluminide, 10.2 cm (4 in) diameter compressor rotors for the P9005 experimental gas turbine engine program, which will advance the development of the Army's IHPTET program. This disposable-engine program is being jointly pursued and developed by the Advanced Research Projects Agency (ARPA), the U.S. Army Missile Command (MICOM), and Williams. Potential ramifications are improved performance and reduced eventual system costs by providing a lightweight alternative to the stainless steel variant currently baselined and being designed for the experimental P9005 gas turbine engine. XD<sup>®</sup> titanium aluminides have half the density of steel and nickel-based alloys. In addition to the direct benefit of significant weight reduction, there is an associated performance benefit of reduced time for engine start and faster acceleration resulting from a lower polar moment of inertia. The successful implementation of XD<sup>®</sup> titanium aluminide into such a system will reduce the size and cost of the start cartridge.

The first phase of this program involved rotor material production. To accomplish this, previous experience in XD<sup>®</sup> titanium aluminide technology developed at Martin Marietta was utilized to select a suitable alloy composition and produce an ingot and forged pancakes. The extremely thin leading edges, approximately 0.039 cm

(0.016 in), were not suitable for investment casting as earlier proposed to the Army Research Laboratory (formerly known as the Army Materials Technology Laboratory). The details of ingot procurement and subsequent processing and the mechanical testing and heat treatment optimization tasks will be discussed along with the design analysis performed at Williams.

The original objective of this program included rotor production following final heat treatment of the forged pancakes, whereby final component dimensions would be achieved via electro-discharge machining. In preparation for this final machining, costing and preliminary studies were performed at an electro-discharge machining facility in Baltimore called E.D.M. Technologies, Inc. This task can be completed by E.D.M. Technologies if funding becomes available. Subsequent engine testing could then be performed at Williams under a separate program.

## II. TECHNICAL BACKGROUND

### A. Monolithic Titanium Aluminide Alloys

Research and development of ordered intermetallic alloys have increased to meet the high-temperature requirements in aerospace and energy-related applications. Materials that have similar thermal profiles as nickel-based superalloys but with lower densities are being sought. The renewed interest in near-gamma,  $\alpha_2$  and  $\gamma$ , titanium aluminide alloys, as lighter-weight, high-temperature capable materials, have made them potential replacements for such presently utilized materials as titanium-based alloys and nickel- and iron-based superalloys. Titanium aluminides have attractive properties of low density, high-melting temperature, good creep resistance, elevated-temperature modulus and strength, fatigue resistance, and relatively good oxidation resistance. Their major disadvantages are low ductility and fracture toughness properties at ambient temperature, which can be improved through microstructural modification via alloy and process development.

Interest in the  $\alpha_2 + \gamma$  intermetallic phase field of this binary system is not new. Development began during the 1950s with the search for high-temperature aircraft engine materials. However, progress was slow due to the complexity of the intermetallic system and lack of information in the  $\alpha_2 + \gamma$  phase regime of the binary phase diagram. Interstitial contamination and the strong effect of minor alloying elements on phase equilibria greatly hampered binary phase diagram computation. The vast body of information compiled over the past decade has greatly broadened our knowledge base of the ordered intermetallic phases of  $\alpha_2$  and  $\gamma$ . It was not until about 5 years ago that the high-temperature phase field of the binary phase diagram in the 40 to 55 atomic % aluminum region was established.<sup>1,2</sup> This phase diagram region as given by Huang and Hall<sup>1</sup> is reproduced in Figure 1. It is used extensively as a guide for heat treatment studies, more accurately depicts the effect of alloying element additions, and has improved our understanding of structure / property relationships in these alloys.

Three different microstructural morphologies are attainable in the 45 to 55 atomic % aluminum range. These morphologies are a two-phase duplex microstructure, containing equiaxed and lamellar morphologies, a two-phase lamellar morphology, and equiaxed single-phase  $\gamma$ . In the  $\alpha_2 + \gamma$ , two-phase regime, up to about 51 atomic % aluminum, two types of microstructural morphologies are produced--a duplex and a fully-transformed lamellar microstructure. Heat treatment in the  $\alpha + \gamma$  or  $\alpha_2 + \gamma$  phase

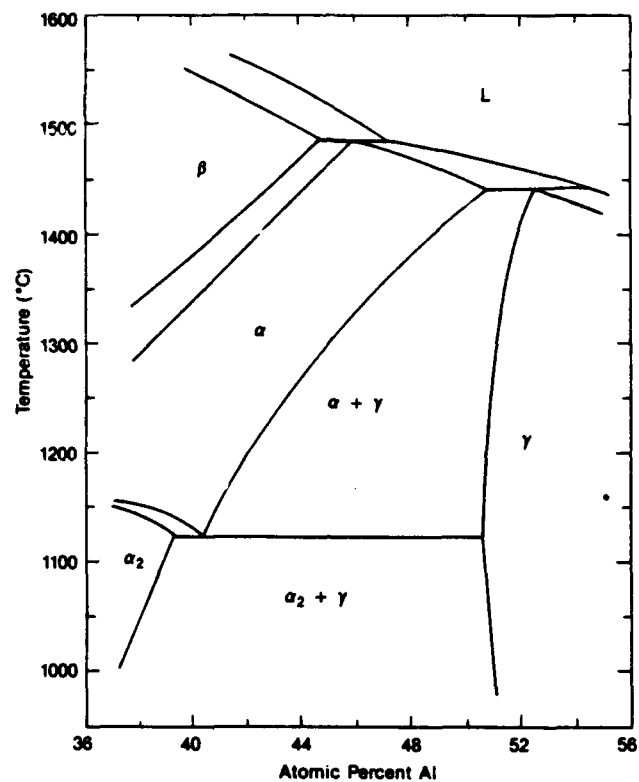


Figure 1. The titanium-aluminum binary phase diagram in the 36 to 56 atomic % aluminum range.<sup>1</sup>

fields, followed by slow cooling, yields a duplex microstructure of lamellar colonies, consisting of  $\alpha_2$  and  $\gamma$  laths, and an equiaxed single-phase  $\gamma$ . Heat treatment in the  $\alpha$  phase field, followed by slow cooling, fully transforms the microstructure to lamellar colonies. At aluminum contents greater than 51 atomic %, single-phase  $\gamma$  is present down to room temperature. Micrographs of different binary compositions after equivalent heat treatment within the  $\alpha + \gamma$  phase field show these three types of morphologies, depicted in Figure 2.<sup>1</sup> The variation in grain size for these alloys is correlated with phase stability and composition.

Mechanical property measurements at room temperature commonly have shown that the two phase microstructure of  $\alpha_2$  and  $\gamma$  is both more ductile and stronger (2% elongation and 600 MPa (87 ksi fracture stress) than single-phase  $\gamma$  (1% elongation and 400 MPa (58 ksi fracture stress)).<sup>1</sup> Both strength and ductility decrease with aluminum concentration greater than 48%. The fully transformed lamellar microstructure is comparably more brittle at room temperature. Deformation mechanisms are strongly influenced by processing conditions, constituent phase morphology, grain size, heat treatment, aluminum level and interstitial content.<sup>3</sup> All of these factors affect the percentages of  $\alpha_2$  and  $\gamma$  phases present. It has been shown that ductility of the alloy is influenced by both the aluminum content of the  $\alpha_2$  phase and the amount of  $\alpha_2$  phase present. High ductility measurements have been found at 10 volume %  $\alpha_2$  phase, while the alloy becomes more brittle at levels over 20 volume %.<sup>4</sup> A refined grain size improves the ductility of the two-phase alloys and a fine, lamellar microstructure has higher ductility compared to a coarse, lamellar microstructure for equivalent grain or colony sizes. Also, for equivalent grain size, the duplex microstructure has higher ductility than single-phase  $\gamma$ . Grain size also affects the creep properties of binary titanium aluminides. Typically, a coarse-grained alloy exhibits superior creep resistance relative to its fine-grained counterpart.

The resultant microstructure after heat treatment is also critical to fracture toughness and creep properties. Room temperature fracture toughness for two-phase alloys is approximately 25 MPa $\sqrt{m}$  (22.7 ksi $\sqrt{in}$ ) for fully lamellar microstructures and 15 MPa $\sqrt{m}$  (13.6 ksi $\sqrt{in}$ ) for the duplex. Single-phase  $\gamma$  has slightly higher fracture toughness than the duplex microstructure. Fracture in the lamellar microstructure is more difficult due to crack branching and bifurcation along and across the lamellae<sup>5</sup> while crack propagation is comparatively easier across the equiaxed microstructure. A drawback is that the high fracture toughness achieved in the fully lamellar

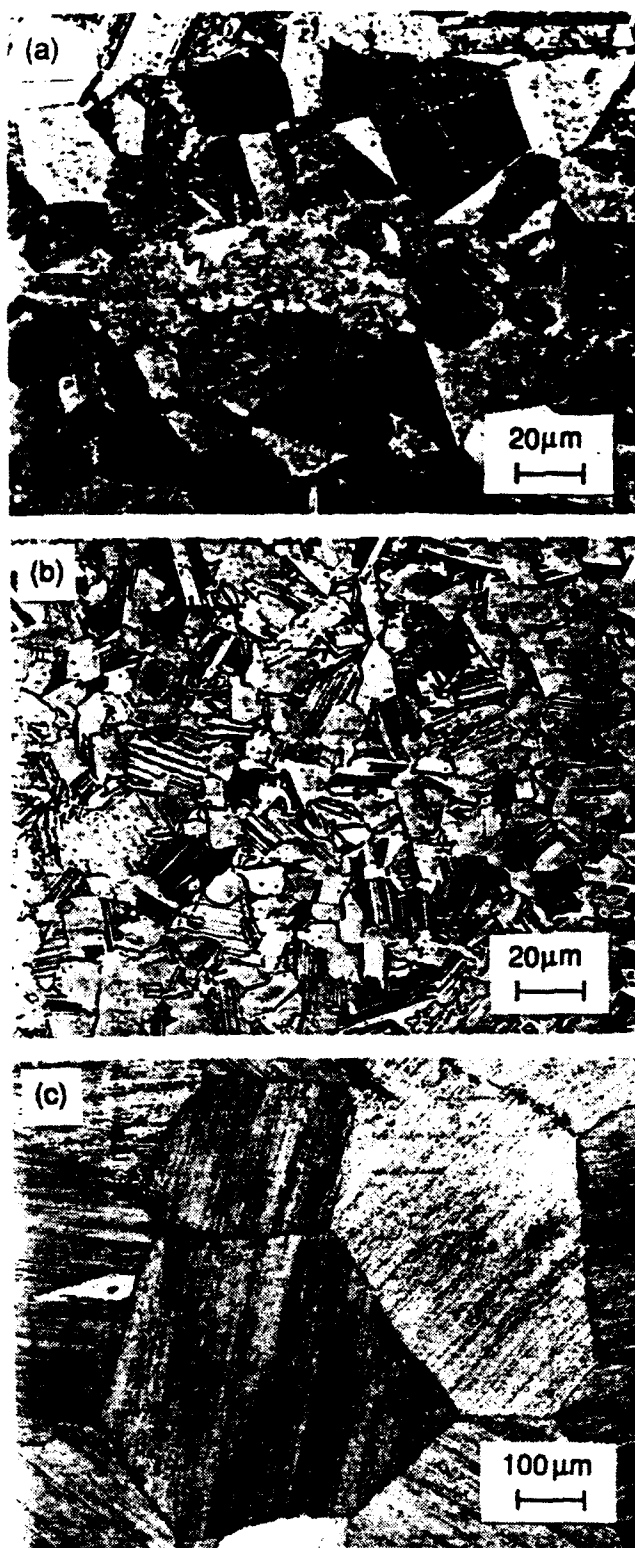


Figure 2. Micrographs of three typical microstructures found in the titanium-aluminide binary system after heat treatment at 1350°C (2462°F) where (a) is a single-phase microstructure at 52 atomic % Al, (b) a duplex microstructure at 48 atomic % Al, and (c) a fully-transformed microstructure at 46 atomic % Al.<sup>1</sup>



microstructure is accompanied by low ambient ductility. Creep resistance is highest for fully transformed lamellar microstructure (Ti-48Al), decreases for single-phase  $\gamma$  (Ti-52Al), and is the lowest for the duplex microstructure (Ti-48Al).<sup>6</sup>

Even though mechanical properties of the binary, two-phase alloy are more attractive, single-phase  $\gamma$  has higher oxidation resistance as compared to the two-phase alloy. Oxidation resistance dictates the maximum use temperature of near- $\gamma$  titanium aluminides. Various approaches have been examined to date to improve oxidation resistance. Unfortunately, as will be discussed, those factors that increase oxidation resistance lower room temperature ductility.

Ambient ductility and fracture toughness properties have been successfully improved through the systematic variation of aluminum content, addition of substitutional alloying elements, reduction of interstitial impurity, and enhancement of deformation processing. In general, ternary and quaternary alloys examined to date have utilized binary alloy compositions ranging from 45 to 52 atomic % aluminum with a maximum of five atomic % alloying element additions. Elemental addition of chromium, manganese and vanadium to the two-phase alloy, heat treated to the duplex microstructure, improves room temperature ductility but does not provide good oxidation resistance.

Many theories<sup>4,6,7,8</sup> have been developed to explain this ductilizing effect and include alloying effects on binary phase equilibria, site occupancy, and other intrinsic factors that increase dislocation mobility. Both the  $\alpha$ -transus and  $\gamma$ -solvus move downward and to higher aluminum contents with additions of chromium, manganese and vanadium, thereby increasing the volume fraction of the  $\alpha_2$  phase.<sup>7</sup> Grain size can be refined by alloying additions in a two-phase microstructure more effectively than in a single-phase. Reduced stacking fault energy, increased superdislocation mobility, and increased thermal twinning in  $\gamma$  phase have been reported in these alloys, and are factors contributing to higher ductility. For wrought Ti-46Al-2Cr alloy, the highest room temperature elongation was measured at 4.0% where isothermal forging, hot pressing and extrusion all showed between 2.6 and 4.0% elongation, depending on heat treatment conditions after processing.<sup>9</sup> Wrought two-phase alloy containing chromium and a duplex microstructure had greater ductility than chromium additions made to a Ti-52Al, single-phase  $\gamma$  alloy where no ductility improvements were observed.<sup>6</sup>

Niobium, tungsten and tantalum additions provide increased oxidation resistance, increased strength and reduced creep rates (via slowing diffusion rates) but lower ductility. Niobium, in particular, aids in the formation of an  $\text{Al}_2\text{O}_3$  protective layer. The addition of tungsten in the two-phase alloy results in  $\beta$ -phase precipitate formation, which promotes  $\alpha$  phase stability; both provide increased creep resistance. High-temperature oxidation of  $\gamma$  phase results in  $\text{TiO}_2$  and  $\text{Al}_2\text{O}_3$  formation with  $\text{TiO}_2$  having a higher rate of oxygen diffusion. Molybdenum and silicon in ternary alloys also increase oxidation resistance.<sup>10</sup> The molybdenum addition refines grain size, increases room temperature ductility and acts as a  $\beta$ -titanium stabilizer.

Much work has been performed to evaluate the effect of interstitial impurities on the structure and properties of titanium aluminides. Interstitial impurities are relevant since it is difficult in practice to produce high purity titanium aluminide alloys. For example, up to about 1,500 ppm oxygen, the binary phase boundaries are not changed significantly as oxygen is stabilized by  $\alpha$  (or  $\alpha_2$ ) phase presence. It was the presence of interstitial oxygen at higher levels that caused errors in binary phase diagram determinations. Oxygen, carbon and nitrogen typically range from 200 to 1,000 ppm; all have little solubility in  $\gamma$ . Oxygen is highly soluble in  $\alpha$ ,  $\alpha_2$  and  $\beta$  phases, stabilizing the supersaturated phase. The effect of oxygen on mechanical properties is dependent on the aluminum content. In the two-phase alloy,  $\alpha_2$  acts to "getter" oxygen away from  $\gamma$  phase. In  $\gamma$  phase, oxygen and nitrogen form precipitates of  $\text{Al}_2\text{O}_3$  and  $\text{Ti}_2\text{AlN}$ , respectively. This enhances oxidation resistance and reduces creep rates by precipitate-dislocation drag. In two-phase, duplex microstructures, oxygen and nitrogen removal from  $\gamma$  phase improves ductility.

Carbon, boron and hydrogen are also critical to mechanical properties. Carbon commonly forms  $\text{Ti}_2\text{AlC}$ , reducing creep rates. Carbon increases strength but lowers ductility. Boron increases crack resistance, maintains good strength and ductility levels, and enhances castability.<sup>11</sup> Additions of greater than 1.0 atomic % boron or 0.5 atomic % nitrogen change the solidification microstructure of cast alloy from columnar to fine, equiaxed grains, increasing strength.<sup>11</sup> Oxygen and carbon additions were found not to refine grain size. Hydrogen is more easily absorbed into the  $\alpha_2$  phase at elevated temperatures than into the  $\gamma$  phase. Hydrides are formed upon cooling with the most common type consisting of the  $\text{TiH}_2$  composition. The single effect of hydrogen on mechanical properties in these alloys is hard to conclude due to other microstructural effects.<sup>12</sup> The level of absorption is dependent on the amount of  $\alpha_2$  phase present in the two-phase alloy.

Material production is achieved by conventional ingot metallurgy and powder metallurgy. Ingot casting is performed by vacuum arc remelting and induction skull melting, both of which are widely used in present experimental production. Stringent processing controls must be achieved to prevent impurity contamination of the ingot and thermal stress cracking upon ingot cooling. HIPing is normally performed in the  $\alpha + \gamma$  phase field, at 138 to 172 MPa (20 to 25 ksi), to close casting porosity. Powder metallurgy practices can be utilized for alloy production achieving similar mechanical properties as those obtained in cast form.<sup>13</sup>

After alloy production, subsequent heat treating in the  $\alpha + \gamma$  or  $\alpha_2 + \gamma$  phase fields causes the formation (recrystallization) of  $\gamma$  grains within lamellar colonies yielding the duplex microstructure. When an ingot is heat treated in the  $\alpha$  phase field, then cooled to room temperature, a large grained lamellar microstructure is formed having low mechanical properties. Thermomechanical processing by isothermal, upset forging or extrusion using cast or powder metallurgy processed material refines the microstructure upon heat treatment through dynamic recrystallization and improves properties. The morphology variation after thermomechanical processing is shown in Figure 3 for both forged and extruded titanium aluminide alloys.<sup>14,15</sup> Bands of recrystallized  $\gamma$  grains are sandwiched between layers of  $\alpha_2$  and  $\gamma$  lamellae, which are noticeably different from the two-phase microstructures in Figure 2. It should be noted that thermomechanical processing of these alloys is non-trivial and formability and hot-workability improvements are needed for these alloys.

#### B. XD<sup>®</sup> Titanium Aluminide Composites

Titanium aluminides were considered originally as a replacement in certain nickel-based superalloy applications due to their good strength, high melting temperature and reduced density (half that of superalloys and iron-based alloys). However, the inherent low ambient ductility and fracture toughness limited their direct application, and inadequate fabricability hindered progress. Several approaches have been attempted to overcome these drawbacks. The utilization of XD<sup>®</sup> processing was viewed as a viable pathway to achieve the necessary properties to advance near- $\gamma$  titanium aluminides. Under DoD sponsorship, XD<sup>®</sup> titanium aluminides have been successfully applied to meet specific systems goals, outlined as follows.

The XD<sup>®</sup> process is a composite synthesis technique involving an exothermic reaction resulting in the *in-situ* formation of discontinuous particulates in a metallic or



Figure 3. Variation of phase morphology is shown for thermomechanically processed titanium aluminide alloys. Optical micrographs show (a) forged alloy and (b) extruded alloy. Bands of recrystallized TiAl grains are layered between  $\text{Ti}_3\text{Al}$  and TiAl lamellae, which are noticeably different from the two-phase microstructures in Figure 2.<sup>14</sup>

intermetallic matrix. Reinforcement shape, size, and volume fraction can be manipulated to vary mechanical properties. Additional features are the creation of thermodynamically stable, single-crystal reinforcements, high-melting temperature particulates, and clean particle/matrix interfaces. Such particles serve as an effective grain refiner and the process is compatible with conventional ingot and powder metallurgy processing, and can be generically applied to most metallic and intermetallic matrix systems. Ingot-based processing is advantageous over powder metallurgy techniques based on low cost production and the rapid transition to the established aerospace materials vendor base.

XD<sup>®</sup> titanium aluminide technology was extensively developed under fundamental research programs funded by the Advanced Research Projects Agency (ARPA), Naval Research Laboratory (NRL), and the NASP Joint Program Office (JPO). This effort involved 15 commercial companies, government laboratories, and universities, where the technology was successfully applied to the production and development of reinforced titanium aluminide alloys. An important accomplishment was that XD<sup>®</sup> titanium aluminide alloys could be produced by conventional ingot and powder metallurgy techniques. XD<sup>®</sup> ingot material can be produced by both induction melting and vacuum arc melting using titanium production facilities. Approximately 900 kg (2000 lbs) of XD<sup>®</sup> titanium aluminide material was produced and used to demonstrate powder atomization, forging, extrusion, rolling, welding, superplastic forming, and diffusion bonding. Through these programs, microstructure and mechanical properties were extensively characterized for a range of compositions subjected to several processing conditions. Subsequent developmental programs with the ARPA Initiative in Concurrent Engineering and commercial contracts with Howmet Corporation and Rolls Royce, Inc. have broadened the knowledge base of composite titanium aluminide alloys and vendor experience extensively. Demonstration components have been manufactured under Navy-funded programs through General Dynamics and an on-going Manufacturing Technology (Man Tech) program through Naval Air Warfare Center-Aircraft Division (NAWC-AD). The application of investment casting technology to XD<sup>®</sup> titanium aluminides has been further developed commercially by Howmet Corporation, who is licensed by Martin Marietta Corporation to manufacture XD<sup>®</sup> ingot material. Martin Marietta continues to produce XD<sup>®</sup> concentrate for various customers for the production of titanium aluminide composite alloys and for various experimental applications.

Many benefits have been realized with the incorporation of reinforcements into

titanium aluminide alloys. Various particulate stability and compatibility studies have been performed on matrix compositions within the  $\alpha_2 + \gamma$  phase region of the titanium-aluminum binary system. Equiaxed particulates are typically produced when binary refractory borides, nitrides or silicides are used; short-fibers or whiskers result with ternary borides or carbides.  $\text{TiB}_2$  particulates were found to be particularly suitable in the Ti-45 to 48 Al alloy and subsequently used for all composite titanium aluminide development. In comparison to the base alloy, it was observed that  $\text{TiB}_2$  particulate reinforcements increase strength and hardness values, especially as the volume fraction of borides is increased. In general, the addition of  $\text{TiB}_2$  to various alloys of  $\alpha_2 + \gamma$  titanium aluminides does not chemically degrade or alter either the matrix or particulate unless there is above 3 to 4 atomic % niobium in the matrix, where (Ti,Nb)B whiskers form. Niobium-containing whiskers have been shown to increase creep assistance of titanium aluminides.

The incorporation of  $\text{TiB}_2$  particulates in titanium aluminides not only improves strength properties, but the reinforcement stimulates microstructural modifications. Most notable is the refinement of the cast grain size from a typical columnar solidification structure to a uniform equiaxed one, thereby alleviating many of the associated processing difficulties. In addition to the direct mechanical property benefits created through introduction of the reinforcement in titanium aluminides, the presence of the dispersed phase in the two-phase matrix significantly impacts the material's response to thermomechanical processing. The lamellar morphology is influenced by wrought (thermomechanical) processing where dynamic recrystallization occurs, breaking down the lamellar microstructure into an equiaxed morphology. Particulates act as nucleation sites accelerating  $\gamma$  phase recrystallization. Heat treatment of the cast material can also cause lamellar to equiaxed morphology transformation, the kinetics being enhanced by the presence of these particulates. As discussed for monolithic titanium aluminides, ambient ductility is favored by an equiaxed microstructure while fracture toughness is enhanced by a lamellar morphology. The presence of particulates in these titanium aluminide alloys strongly influences phase transformation kinetics, which directly affects the mechanical property enhancement observed over monolithic variants.

In addition to matrix microstructure morphology, reinforcement shape can impact mechanical properties. Ductility, tensile strength, and creep properties have been compared for wrought XD<sup>®</sup> reinforced alloys containing either particulates or short-fibers.<sup>16</sup> It was discovered that short-fibers formed upon the addition of over 4 atomic % niobium. At ambient temperatures, particulate-reinforced alloys achieved up to 1.0%

elongation whereas short-fiber composites only had up to 0.4% elongation. At 800°C (1472°F), the short-fiber variant maintained a higher tensile yield strength and had a lower creep rate than the particulate-containing counterparts for the same matrix morphology. This study showed that while the high-temperature behavior of the short-fiber reinforced titanium aluminides was superior to the particulate-reinforced variant, it exhibited lower room temperature ductility. It should be noted that the short-fiber reinforced matrix contained niobium in solid solution. More work would be needed to realize the singular effect of the short-fiber reinforced titanium aluminide on mechanical properties from those effects due to niobium in solid solution.

Relative to unreinforced (monolithic) counterparts, XD<sup>®</sup> titanium aluminide alloys have demonstrated improved processability. At low-volume percentages, around 1 volume % TiB<sub>2</sub> loading, grain refinement occurs and increased subsequent fabricability is observed. Strength properties are also improved with the addition of TiB<sub>2</sub> reinforcements, with higher volume fraction loadings providing increased strength. Investment casting is effective up to approximately 10 volume % TiB<sub>2</sub> loading, and near net-shape powder metallurgy processing plus hot isostatic pressing (HIPing) can incorporate up to 60 volume % TiB<sub>2</sub> loading.

Mechanical properties have been previously obtained for reinforced variants of titanium aluminides for several processing and heat treating conditions. Strength comparisons for example, show an as-cast + heat-treated alloy with a nominal composition of Ti-48Al-2Mn-2V that is unreinforced, has an average ultimate strength of 505 MPa (73.2 ksi); this increases to 690 MPa (100 ksi) with 7 volume % TiB<sub>2</sub> loading and 725 MPa (105 ksi) with addition of up to 11 volume % TiB<sub>2</sub>. Room temperature ductilities for all these alloys, irrespective of TiB<sub>2</sub> content, were < 1%.

Room-temperature, short-rod fracture toughness measurements from XD<sup>®</sup> Ti-45 to 48Al-2Mn-2V alloys vary depending on processing and heat treatment condition. As-cast + HIPed alloy can have short-rod fracture toughness values ranging from 11<sup>18</sup> to 16 MPa√m<sup>19</sup> (10 to 14.5 ksi√in). In contrast, the Ti-47Al-2Nb-2Mn alloy, reinforced with TiB<sub>2</sub> particulates, in the forged and heat-treated condition, exhibited short-rod fracture toughness values that were higher ranging from 20 to 23 MPa√m<sup>20</sup> (18.1 to 23.3 ksi√in). It was shown<sup>5</sup> for a monolithic variant of Ti-47Al-2Mn-2V that room-temperature fracture toughness is influenced by the morphology of the matrix microstructure. This was similarly noted for a Ti-47Al-2V + 7 volume % TiB<sub>2</sub> alloy that had a fracture toughness averaging 16.5 MPa√m (15 ksi√in) for an as-cast, lamellar microstructure

while a forged alloy having an equiaxed microstructure, had an average toughness value of  $9 \text{ MPa}\sqrt{\text{m}}^{21}$  ( $8.2 \text{ ksi}\sqrt{\text{in}}$ ).

Creep properties of XD<sup>®</sup> titanium aluminides containing particulate and short-fiber reinforcements have been investigated as described earlier.<sup>16</sup> Creep resistance for several unreinforced and TiB<sub>2</sub>-reinforced binary alloys was also examined and mechanisms responsible for creep in such materials were proposed.<sup>17</sup> It was observed that the mechanism of creep deformation is independent of processing technique (ingot-vs-powder processing) and remains unchanged with the presence of TiB<sub>2</sub> particulate. Matrix grain size and phase morphology were found to strongly influence the rate of deformation. Particulate presence was shown to increase creep resistance.



### III. SCOPE OF PROGRAM AND STATEMENT OF WORK

#### A. Scope

The scope of this program is to adapt the compressor rotor design to XD® titanium aluminide materials, perform a design analysis for necessary structural modifications, and manufacture suitable material (including process optimization and property evaluation) to fulfill compressor rotor mechanical property requirements.

#### B. Statement of Work

Martin Marietta, in conjunction with Williams and its other subcontractors, has identified a mixed-flow compressor from a ARPA/MICOM experimental, expendable turbine engine that is to be manufactured from XD® titanium aluminide. This material represents a high-payoff alternative to the heavier 15-5 PH stainless steel currently being projected for this application. Alloy composition selection will be based on mutual agreement between Martin Marietta and design engineers at Williams through an XD® titanium aluminide property data base supplied by Martin Marietta. This assessment will be based on necessary physical and mechanical properties of the compressor rotor as well as the familiarity of our vendors with the alloy. The first year focuses on the production of material, mechanical property characterization and the design analysis at Williams. Following this work is a 6-month period during which three rotors will be produced. The proposed schedule depicting the work for this 19-month period (18 months technical performance + 1 month reporting) is shown in Table I. The work described above is divided into four tasks, which are detailed below; a fifth task comprises program management.

#### Task 1. Material production

Martin Marietta will produce an XD® titanium aluminide ingot of sufficient quantity to produce compressor rotors for engine testing. Ingot material will be hot isostatically pressed (HIPed) and machined into suitable forging billets. Isothermally forged pancakes will be produced having dimensions appropriate for subsequent rotor machining. Following forging, the materials characterization and mechanical testing studies described in Task 2 will be performed, after which heat treatment of four forged pancakes will be performed.

Table 1. Proposed schedule depicting the work for the 19-month period, October 1991 through April 1993.

Tasks	1991			1992												1993				
	Oct	Nov	Dec	Jan	Feb	Mar	Apr	May	Jun	Jul	Aug	Sept	Oct	Nov	Dec	Jan	Feb	Mar	Apr	May
<u>Task 1. Material</u>																				
Ingot Procurement																				
Hot Isostatic Pressing																				
Preform Machining																				
Forging																				
Heat Treatment Optimization / Mechanical Properties																				
Heat Treatment of 4 Forged Pancakes																				
<u>Task 2. Characterization</u>																				
Machining of Test Specimens																				
Metallographic Analysis																				
Mechanical Property Testing / Evaluation																				
<u>Task 3. Williams International Effort</u>																				
Design Analysis																				
Quarterly/Final Summary Report																				
<u>Task 4. Rotor Production</u>																				
Rotor Machining (3)																				
Delivery of Rotor to AMTL																				
<u>Task 5. Management</u>																				
Monthly Reports																				
Summary / Final Report																				
Kick-off Meeting																				
Annual Progress Review Meeting																				

## Task 2. Material characterization

Representative forged material will undergo material characterization. Heat treatment studies will be performed and optimal heat treatments selected for mechanical testing. Heat treatment parameters will be based on microstructural features that promise maximum property values for component performance optimization. Proposed mechanical testing includes tensile, creep, fracture toughness and high-cycle fatigue. The test conditions will be selected as warranted by the engine component requirements.

## Task 3. Williams International effort

Williams will perform a design analysis for an XD<sup>®</sup> titanium aluminide compressor rotor. The existing design of the rotor will be evaluated using XD<sup>®</sup> titanium aluminide material properties provided by Martin Marietta. To facilitate future engine testing, the XD<sup>®</sup> titanium aluminide compressor rotor capabilities will be determined to support spin testing and engine demonstration. A quarterly status report will be submitted after 3 months and a final summary report at the end of the investigation. A breakdown of technical tasks is shown below.

- 1.1 Material selection--selection of material composition based on existing material property data base.
- 1.2 Heat transfer analysis--evaluation of compressor rotor steady state operating temperature and transient state temperature caused by cartridge starting, including blade temperature.
- 1.3 Structural analysis--conduct elastic stress analysis for rotor steady state operation; determine overspeed burst limit and cartridge starting effect; blade thermal stresses; and ensure rotor structural capability for subsequent testing.
- 1.4 Dynamic analysis--determine blade resonance points; construct interference diagram; ensure adequate frequency margin for engine operation; and evaluate effect of cartridge starting on blade dynamic stresses.

1.5 Design review--analysis of rotor and shaft attachment design involving thermal expansion effects and rotor clearances and revision of drawings as required.

Task 4. Rotor production (subject to availability of government funds)\*

Three compressor rotors will be machined from the forged and heat-treated XD® titanium aluminide alloy.

Task 5. Reporting

Monthly progress reports will be issued to the Army Research Laboratory by Martin Marietta. An annual report will be submitted after the first year and a final report and three heat-treated and machined rotors will be delivered at the end of the program. An annual progress review meeting scheduled for August, 1992 did not occur.

\* Subsequently, the government indicated that funds were not available for the fabrication of the three compressor rotors. Therefore, the final report does not include Task 4.

#### IV. TECHNICAL ACCOMPLISHMENTS

##### A. Design Analysis Performed at Williams International

The objective of the subcontract with Williams was to perform a design analysis for an XD<sup>®</sup> titanium aluminide compressor rotor. The involvement of Williams in this program is essential due to their participation in the stainless steel expendable turbine engine program being simultaneously sponsored by the Army. The design analysis performed utilizes the design and database from the stainless steel compressor rotor program. Future work at Williams for this program would be to demonstrate the XD<sup>®</sup> titanium aluminide compressor rotor in the experimental P9005 gas turbine engine.

Presented below are the accomplishments for each task with details for each provided in Appendix A.

##### 1. Material selection

The XD<sup>®</sup> titanium aluminide material composition selected for the mixed flow compressor rotor was Ti-47Al-2Mn-2V + 7 volume % TiB<sub>2</sub>. The alloy composition suggested by Williams was based on a review of material property data provided by Martin Marietta for various TiB<sub>2</sub> containing titanium aluminide alloys shown below:

Ti-48Al-2V	Ti-48Al-2Mn-2V	Ti-47Al-2Mn-2V-2Cr
Ti-47Al-2Mn-Cr	Ti-47Al-2Mn-1Nb-1Cr	Ti-47Al-2Mn-1V-1Nb

The mechanical property data for Ti-47Al-2Mn-2V + 7 volume % TiB<sub>2</sub> are included in Appendix A.

The Ti-47Al-2Mn-2V alloy\* was selected because it displayed the best combination of strength and ductility at room temperature, with 697 to 731 MPa (101-106 ksi) ultimate tensile strength, 572 to 593 MPa (83 to 86 ksi) yield strength, and elongation consistently greater than 0.8%. With the low fracture toughness values observed 12.65 to 15.95 MPa√m (11.5 to 14.5 ksi√in), stringent nondestructive inspection of both the forgings (ultrasonic) and machined rotors (fluorescent penetrant) to very small critical flaw sizes was recommended.

\* Although data for Ti-48Al-2Mn-2V were used in the selection process, an alloy composition of Ti-47Al-2Mn-2V was selected for this study. This selection was based on the argument that above 48 atomic % aluminum level, properties deteriorated and hence conservatively, a 47 atomic % aluminum level was chosen.

## 2. Heat transfer analysis

The compressor rotor was analyzed with the existing heat transfer model (from the stainless steel rotor) using Martin Marietta's XD<sup>®</sup> titanium aluminide properties, including density, specific heat, thermal conductivity, and the thermal expansion coefficient. The analysis showed the rotor's maximum temperature during steady state operation was 216 °C (420°F). The cartridge starting process was analyzed and it was determined that the compressor rotor blades would achieve a maximum transient state temperature from 677°C to 927°C (1250°F to 1700°F), lasting approximately 8 s. The information from this analysis was used to perform the remaining program tasks. The material data used to conduct the analysis are listed in Appendix A.

## 3. Elastic stress analysis

An elastic stress analysis was conducted for steady state operation, for the thermal stresses on the compressor induced by cartridge starting, and to determine the overspeed burst limit. The steady state bore stresses were too high, 586 MPa at 177°C (84.9 ksi at 350°F), for operating the rotor at the maximum design speed of 115 krpm. To provide a minimum 10% burst margin, the engine speed upper limit will be 108.4 krpm.

The analysis for a start cartridge starting of the engine predicts a 671 MPa (97.3 ksi) elastic blade stress. The stress analysis predicts that the engine can be started with start cartridge impingement on the compressor rotor. However, in order to provide an additional margin of safety, low start temperatures will be provided by a hydrogen/depleted air start system for engine development testing. The elastic stress analysis can be found in Appendix A.

## 4. Critical flaw size prediction

The critical flaw size for the compressor rotor was calculated for XD<sup>®</sup> titanium aluminide. The critical crack size is 0.037 cm (0.0146 in) deep and 0.11 cm (0.0442 in) long. The calculation technique is defined in Appendix A.

## 5. Dynamic analysis

A dynamic analysis was conducted on the blades and splitters. The existing design for the compressor was used and XD<sup>®</sup> titanium aluminide property data

incorporated to construct interference diagrams and normalized tangential displacement contour curves for the blade and the splitter.

The sources of dynamic excitation are the diffuser vanes, the impingement nozzles, and the inlet struts. The disturbances caused by the 23 diffuser vanes and the eight impingement nozzles are minimal. However, the disturbances caused by the two-inlet struts are significant. A three-inlet strut design would reduce the risk by shifting the frequency of the interference outside of the run envelope. Using a three-inlet strut would require the fabrication of a new component within the engine, but would reduce the risk on the compressor rotor. Details of the dynamic analysis report are included in Appendix A.

#### 6. Rotor attachment and blade tip growth analyses

The rotor/shaft interference fits and blade tip growth were analyzed to determine if any drawing modifications would be required. The aft rotor pilot requires a minimum diametral interference of 0.0015 cm (0.0006 in); the forward pilot requires a 0.0015 cm (0.0002 in) diametral interference.

The blade growth data showed that no blade tip/flow path modifications would be required for the XD<sup>®</sup> titanium aluminide compressor rotor. The XD<sup>®</sup> titanium aluminide rotor has more running clearance than the baseline stainless steel rotor, therefore it is recommended that the XD<sup>®</sup> titanium aluminide rotor be shimmed forward by 0.015 cm (0.006 in) to reduce the tip clearances for the demonstrator rotor. For production applications beyond the demonstration phase, the rotor cover would need to be resized to achieve optimum performance. The rotor attachment analysis and the blade tip growth data are included in Appendix A.

In summary, the design analysis performed at Williams indicated no drawing modifications are required at this time in order for the XD<sup>®</sup> titanium aluminide compressor rotor to be run in the experimental P9005 gas turbine engine. Based on the design analyses, the following conclusions were reached:

- The material selected for the program was Ti-47Al-2Mn-2V + 7 volume % TiB<sub>2</sub>.
- The rotor speed will be limited to 108.4 krpm and will not be able to go to the 115-krpm design speed due to lack of burst margin.

- The dynamic analysis showed that an excitation occurs due to the two-inlet struts and that changing to a three-inlet strut would reduce the problem.
- The elastic thermal stresses due to hot gas cartridge starting are approximately 671 MPa (97.3 ksi) in the blades.

## B. Alloy Production

The nominal composition selected for this program was Ti-47Al-2Mn-2V + 7 volume % TiB<sub>2</sub>. The doubly-melted ingot was vacuum arc-remelted (VAR) at TIMET, Inc. (Henderson, Nevada). The ingot was 20.3 cm (8 in) in diameter by 50.8 cm (20 in) high. Visual examination of the ingot showed no cracking and no shrinkage cavity at the top. Chemistries were analyzed at the top and bottom portions of the ingot and are shown in Table II. The actual, averaged chemistry was on target with the exception of aluminum content, which varied from 1.2 to 1.9 % from the nominal composition of 47 atomic %. This is not too unusual since it is difficult to maintain aluminum content during the VAR process due to the volatile nature of the element. At 45.5 % aluminum, the alloy should be stronger, however, ductility may be slightly lower. The level of interstitial elements in the alloy is within specification.

Subsequent to ingot production, hot-isostatic pressing (HIPing) was performed at Howmet's HIP Division in Whitehall, MI. HIPing of titanium aluminide alloys is a common practice resulting in full densification of the ingot. Based on prior experience, the following HIPing parameters were used to achieve a homogeneous, lamellar microstructure throughout the ingot:

Temperature:	1260°C (2300°F ± 25°F)
Pressure:	172 MPa ± 3 MPa (25 ksi ± 500 psi)
Time at temperature:	4 h ± 15 m.

These typical HIPing conditions were optimized from research performed by Howmet's Applied Research Division, which has been working with titanium aluminide alloys for several years.

Following HIPing, ingots were electro-discharge machined at a local machining facility, E. D. M. Technologies, into cylinders for subsequent forging. These preforms were 7.6 cm (3.0 in) in diameter and approximately 21.1 cm (8.3 in) high and were based on recommended length/diameter ratios provided by Ladish Co. Reduction in height was planned to yield a forged pancake of 12.7 cm (5.0 in) in diameter by 7.6 cm



Table II. Ingot chemistries for the doubly-melted, 20.3 cm (8") diameter x 50.8 cm (20") high ingot produced at TIMET.  
Ingot was processed by the vacuum arc remelting (VAR) method.

CHEMISTRY DESIGNATION	COMPOSITION					MINOR CONSTITUENTS					TiB <sub>2</sub> * (vol %)
	Ti	Al	V	Mn	B	Fe	C	H	N	O	
Target (wt%): • Ti-47Al-2Mn-2V + 7 vol % TiB <sub>2</sub>	61.96	30.38	2.44	2.63	2.59	--	--	--	--	<0.1000	7
Measured (wt%):											
• Top of Ingot	62.78	29.70	2.42	2.80	2.30	0.068	0.011	0.0047	0.007	0.091	6.3
• Bottom of Ingot	63.86	29.20	2.22	2.47	2.25	0.056	0.012	0.0048	0.009	0.107	6.1
• Average Chemistry	63.31	29.45	2.32	2.64	2.28	0.062	0.012	0.0048	0.008	0.099	6.2

\* Assumes that all boron forms TiB<sub>2</sub>.

(3.0 in) high.

Upset forging was performed at Ladish Co. on eight preforms in a large, production scale press. The preforms were slowly heated in a vacuum furnace unit (pusher furnace) with simultaneous heating of the press dies. For each forging operation, the preform was transferred to the forging press and heating was resumed until a forging temperature of 1150°C (2100°F) was reached. Forging was performed at a strain rate of 10%/m until the desired height of 7.6 cm (3.0 in) was achieved. The piece was then cooled slowly in a ceramic medium of silocel.

There were some unexpected problems that arose during forging; unfortunately, Martin Marietta was not notified of them until after all eight forgings had been completed. Non-uniform deformation leading to folding on the sides of all the pancakes was evident (Figure 4). A few had actually undergone shear and tearing on the corners. Ladish Co. attributed the mishap to an inhomogeneous microstructure (grain size) across the preform diameter, but this was not consistent with the visual nature of the buckling. We believe the problem resulted from using an original length-to-diameter ratio, which may have been too large. In a conversation with Ladish Co. after receipt of the forgings, it was noted that they had not forged any titanium aluminide alloys having such length-to-diameter ratios. Fortunately, an examination of the forged pancakes indicated there was sufficient material available for rotor machining.

A 10.2 cm (4 in) diameter by 7.6 cm (3.0 in) high cylinder was electro-discharge machined from one of the forgings. A cylinder of this size is sufficient to serve as the "blank" or "preform" prior to final component machining. The final rotor dimensions are 9.6 cm (3.77 in) in diameter by 6.3 cm (2.48 in) high. This 10.2 cm (4 in) diameter cylinder is shown in Figure 5. It appeared free of any defects and was visually sound.

### C. Forging Characterization

Microstructural evaluation was performed on specimens removed from one of the forged pancakes. A 0.95 cm (3/8 in) thick slice of material, representative of the entire vertical section of the forging, was cut and five metallographic specimens were removed, one from each of the corners and the middle section to verify microstructural homogeneity. These samples were labelled A through E. Edge pieces also were removed for evaluation and labelled F and G. The location of these specimens is indicated in a drawing of the vertical slice removed from a forging shown in Figure 6.

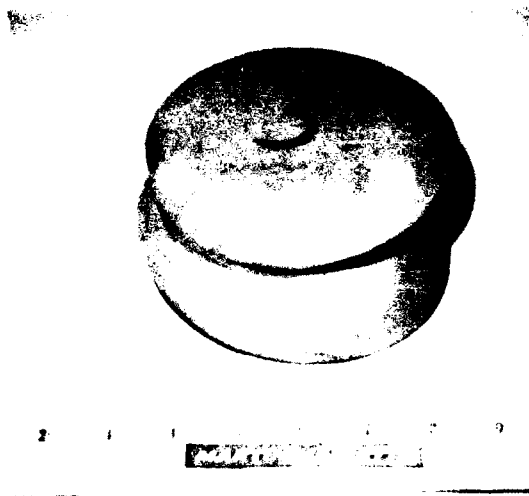


Figure 4. A typical forging from the eight forgings produced at Ladish Co. for this program.

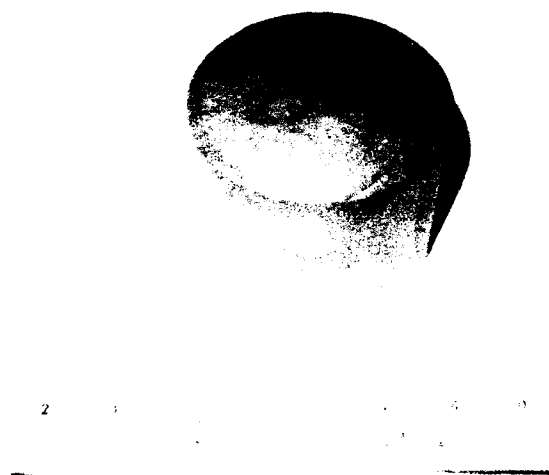


Figure 5. A 10.2 cm (4 in) diameter cylinder electro-discharge machined from one of the forgings, which will serve as the "blank" or "preform" prior to final component machining.

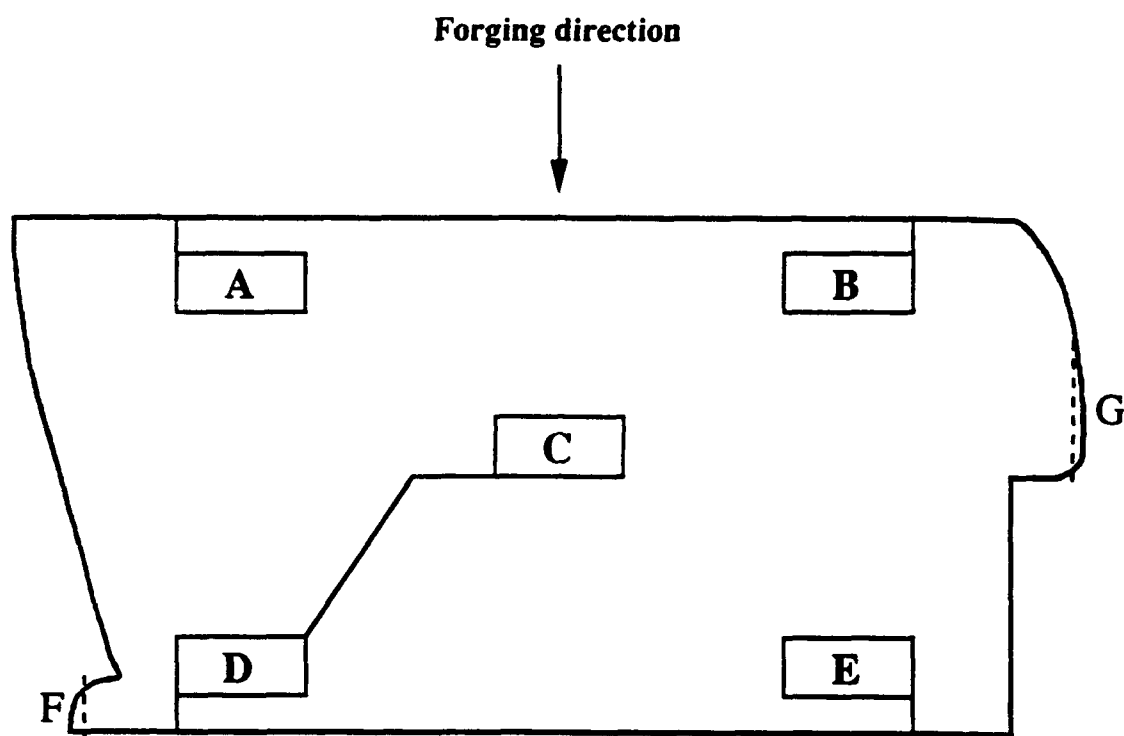


Figure 6. The location of the seven metallographic specimens electro-discharge machined from a vertical slice of a forged cylinder.

Microstructural integrity was examined using optical microscopy and SEM techniques. Optical micrographs of the samples are shown in Figure 7. The surface evaluated for each sample was along the forging or longitudinal direction. Evidence of forging shear, through the bent lamellar grains, is apparent in all micrographs, but to varying degrees. Sample A appeared less worked relative to the other specimens. The microstructure of sample E appeared coarser than the rest. The microstructures of F and G specimens were similar. Back-scattered electron imaging was performed on samples A, C, and E. These micrographs are shown in Figure 8. The black areas are  $\text{TiB}_2$ ; the matrix consists of a light grey phase,  $\text{Ti}_3\text{Al}$ , and a grey phase,  $\text{TiAl}$ . No detectable differences were observed in the relative amounts of  $\alpha_2$  and  $\gamma$  phases present.

Close examination of low magnification optical micrographs from all specimen locations indicated a minor amount of residual porosity was still present in the material. This was somewhat surprising since the ingot had first been HIPed and then forged. It was decided that the 8 forgings would undergo another HIPing cycle identical to that performed previously on ingot material to ensure closure of this porosity. The 8 forgings were sent to Howmet's HIP Division for the 4 h HIPing procedure as described previously. Microscopy performed after this second HIPing cycle showed no porosity like that observed earlier. The microstructure consisted of equiaxed phases of  $\text{TiAl}$  and  $\text{Ti}_3\text{Al}$  as shown in Figures 9 and 10.

X-ray diffraction was performed using a computer-controlled, Scintag diffractometer. A 1-cm<sup>2</sup> piece of forged material from sample C was used for the x-ray analysis, and the face exposed was along the forging direction. The scan generated is shown in Figure 11. All peaks were identified;  $\gamma$  phase and  $\text{TiB}_2$  accounted for most of the peaks, while only the 100% intensity peak of  $\alpha_2$  phase could be precisely characterized. The partitioning of the quaternary alloying elements between the two phases  $\text{TiAl}$  and  $\text{Ti}_3\text{Al}$  is unknown as is their specific site occupancy in the two lattice structures; this virtually precludes the possibility of using the x-ray data to generate useful information regarding the relative contents of the constituent phases. Also deviations from stoichiometry of the coexisting phases leave unanswered questions regarding site occupancy. Superimposed on this problem is the possible presence of texture from forging that could erroneously influence such calculations.

#### D. Heat Treatment Optimization

It was indicated by Williams that for steady state operation of the compressor

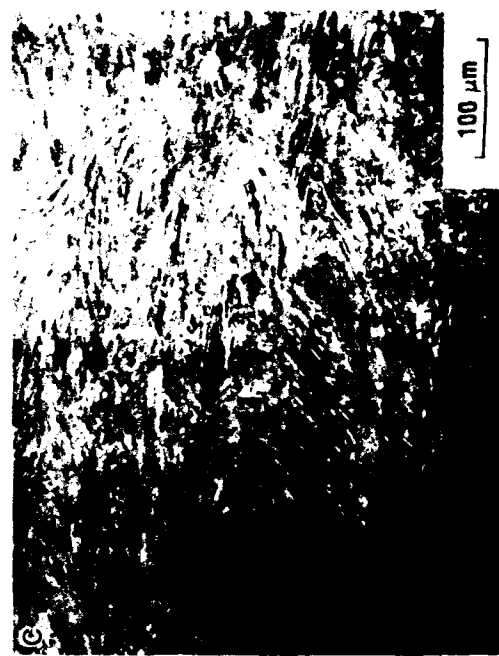
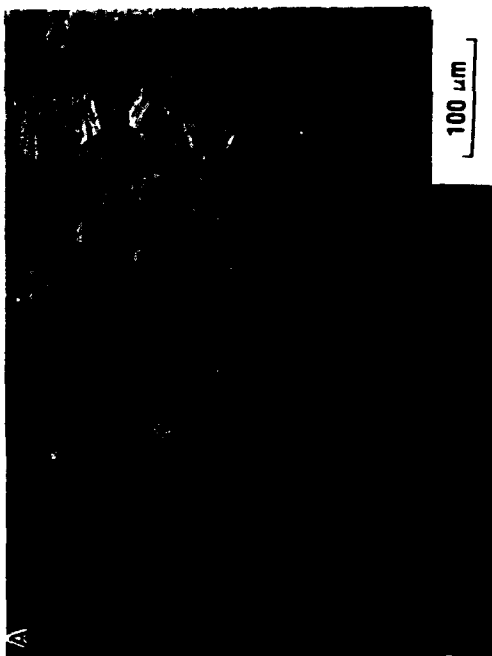
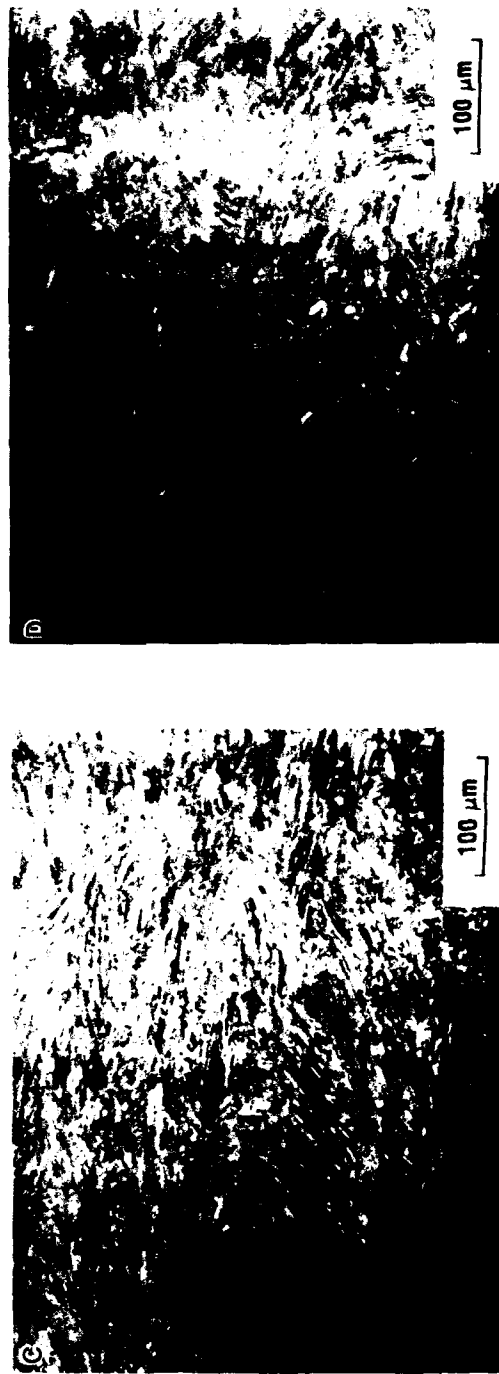
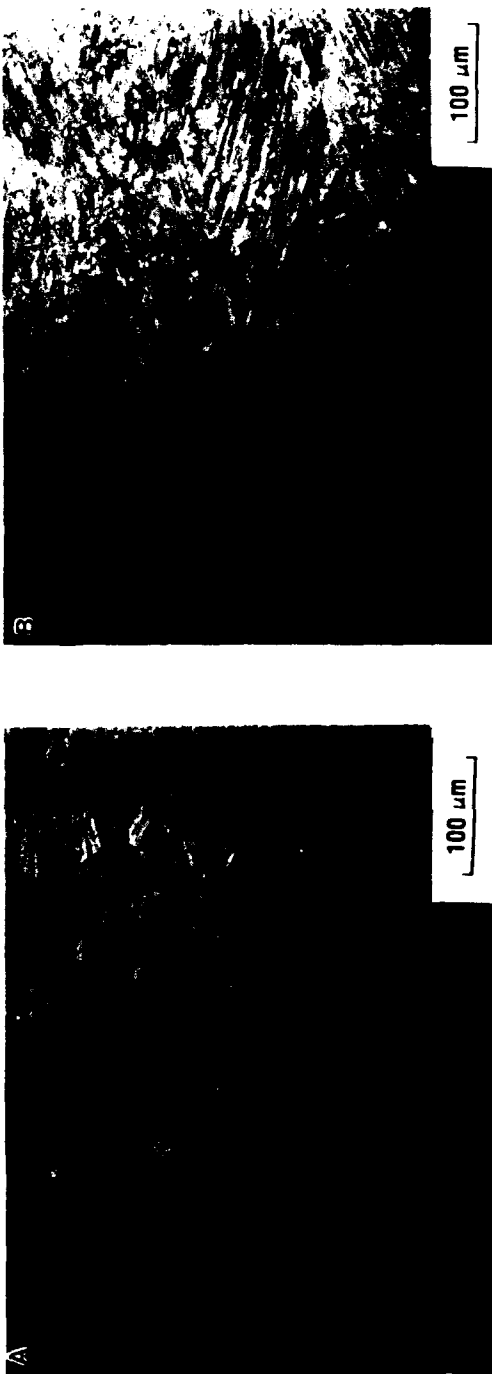


Figure 7. Optical micrographs of samples A through D removed from the center portion of a forged cylinder.

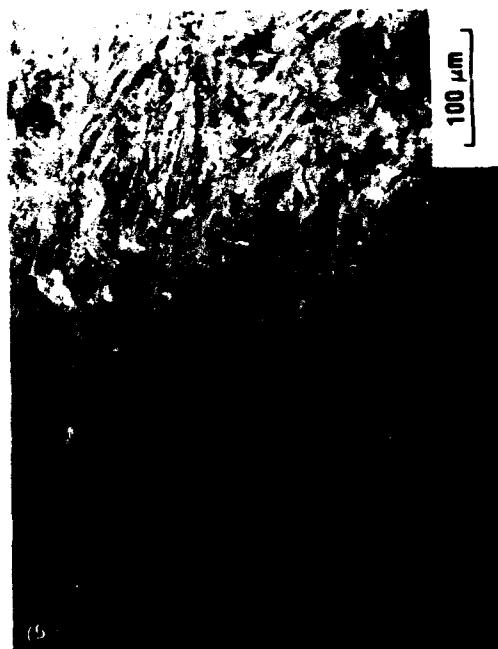
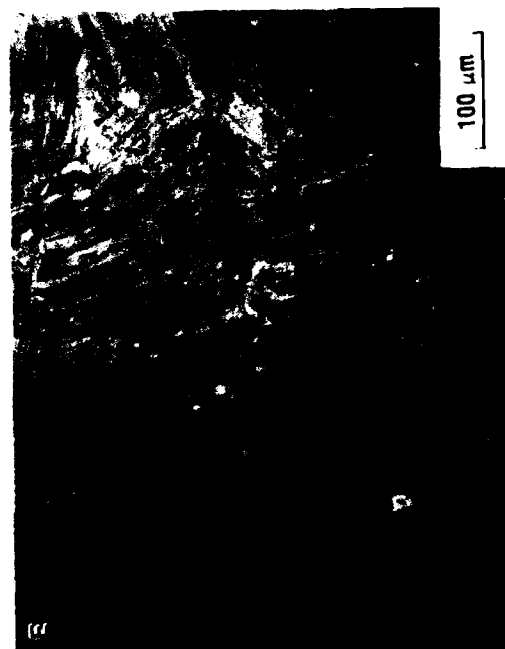
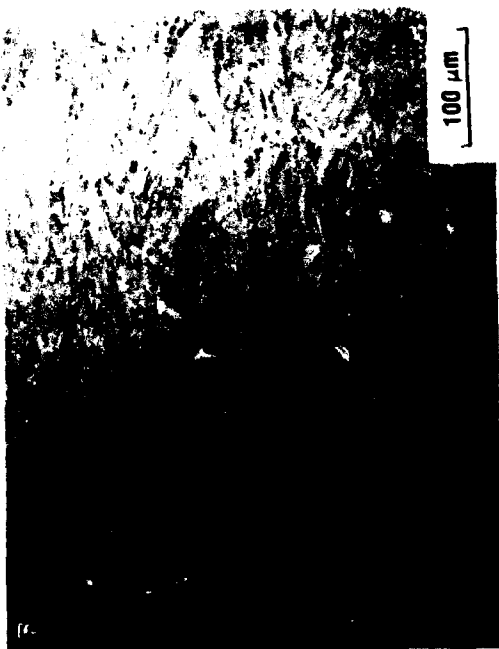


Figure 7. (cont.) Optical micrographs of samples E through G removed from the center portion of a forged cylinder.

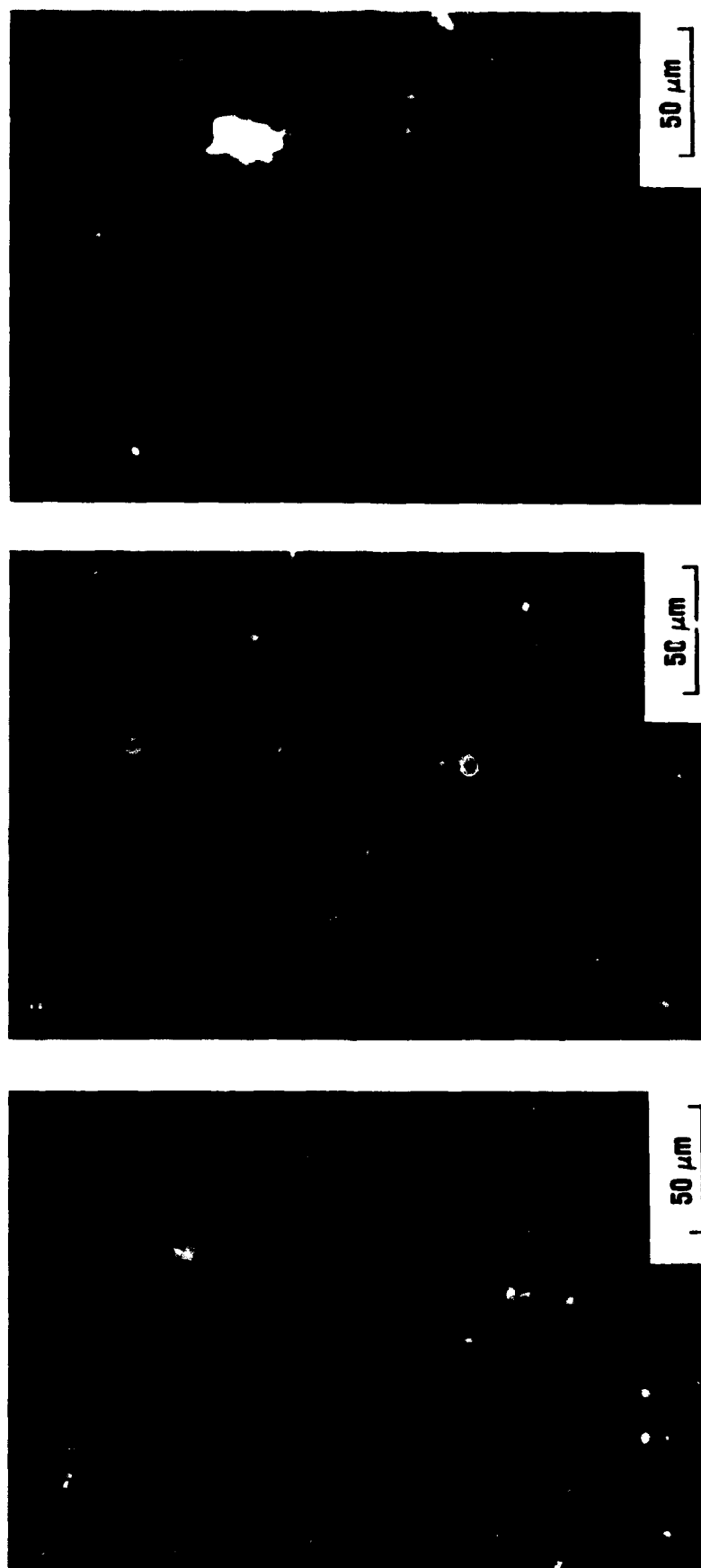


Figure 8. Back-scattered electron micrographs from (a) sample A, (b) sample C, and (c) sample E, all removed from the center portion of a forged cylinder. Atomic number contrast differences reveal TiB<sub>2</sub> particulate as black, TiAl as grey, and Ti<sub>3</sub>Al as light grey in color.



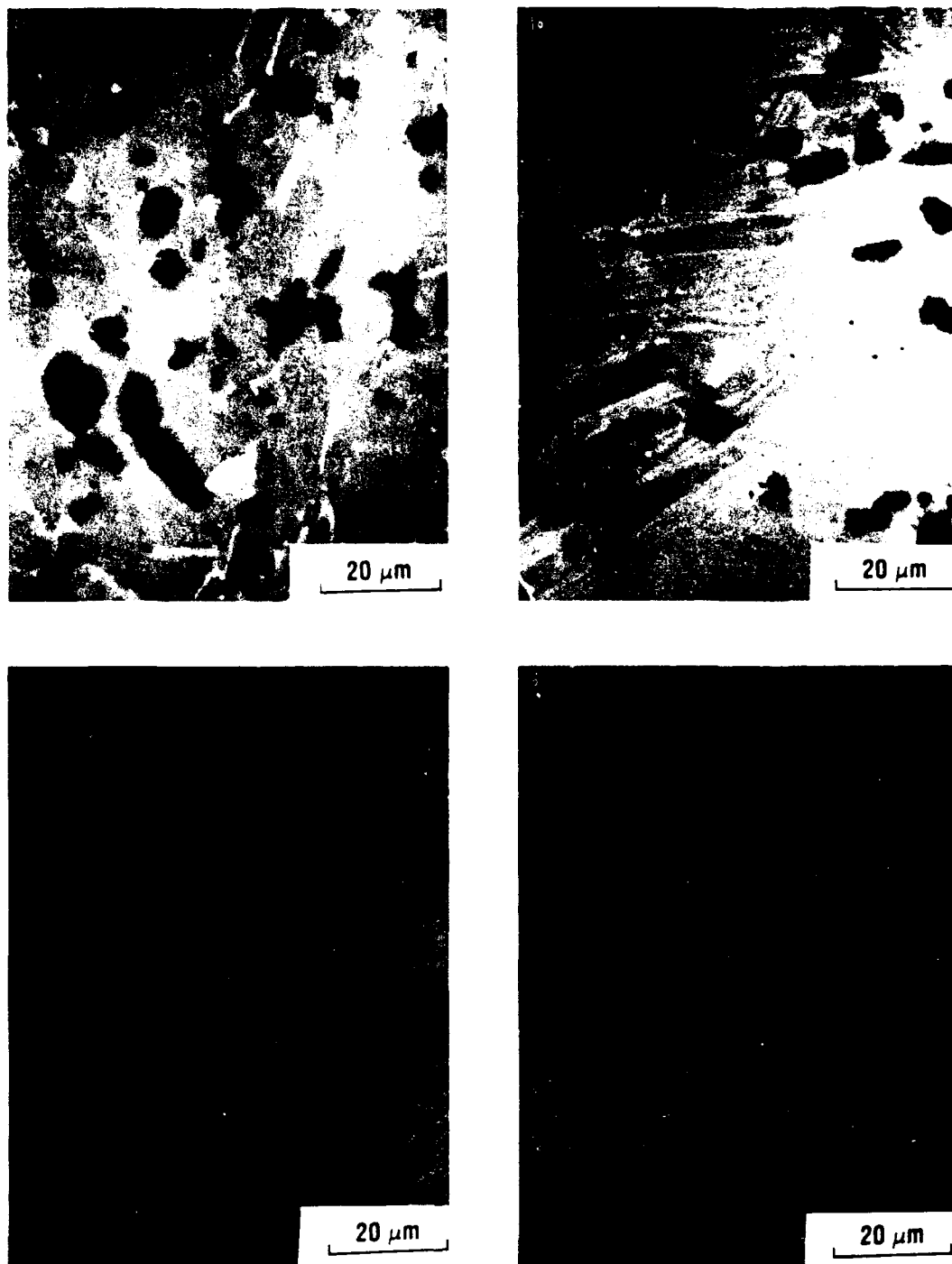


Figure 9. Back-scattered electron micrographs after the second HIPing procedure. Depicted is (a) the as-HIPed microstructure, (b) heat treatment at 1300°C (2372°F) for 1 h, (c) heat treatment at 1330°C (2426°F) for 1 h, and (d) heat treatment at 1340°C (2444°F) for 1 h.

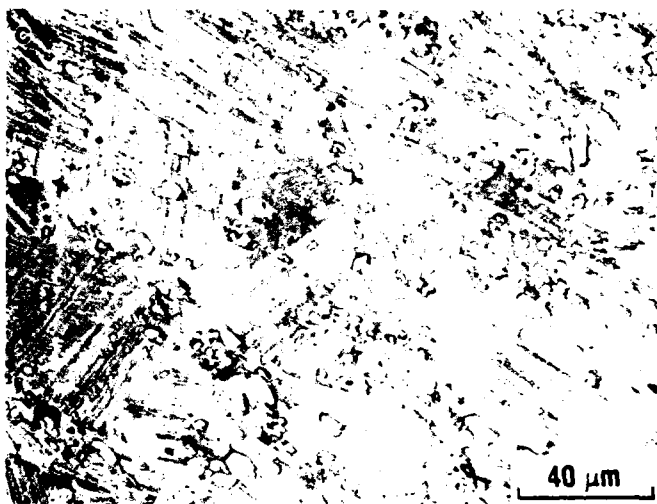
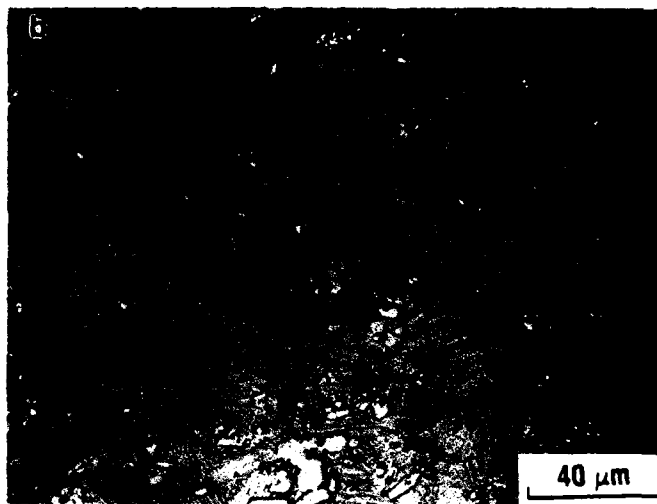
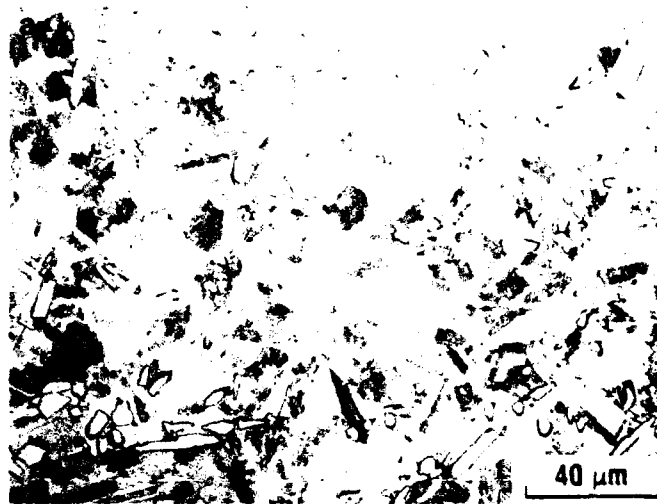


Figure 10. Optical micrographs of the alloy (a) in the as-HIPed condition, (b) after heat treatment at 1300°C (2372°F) for 1 h, and (c) after heat treatment at 1340°C (2444°F) for 1 h.

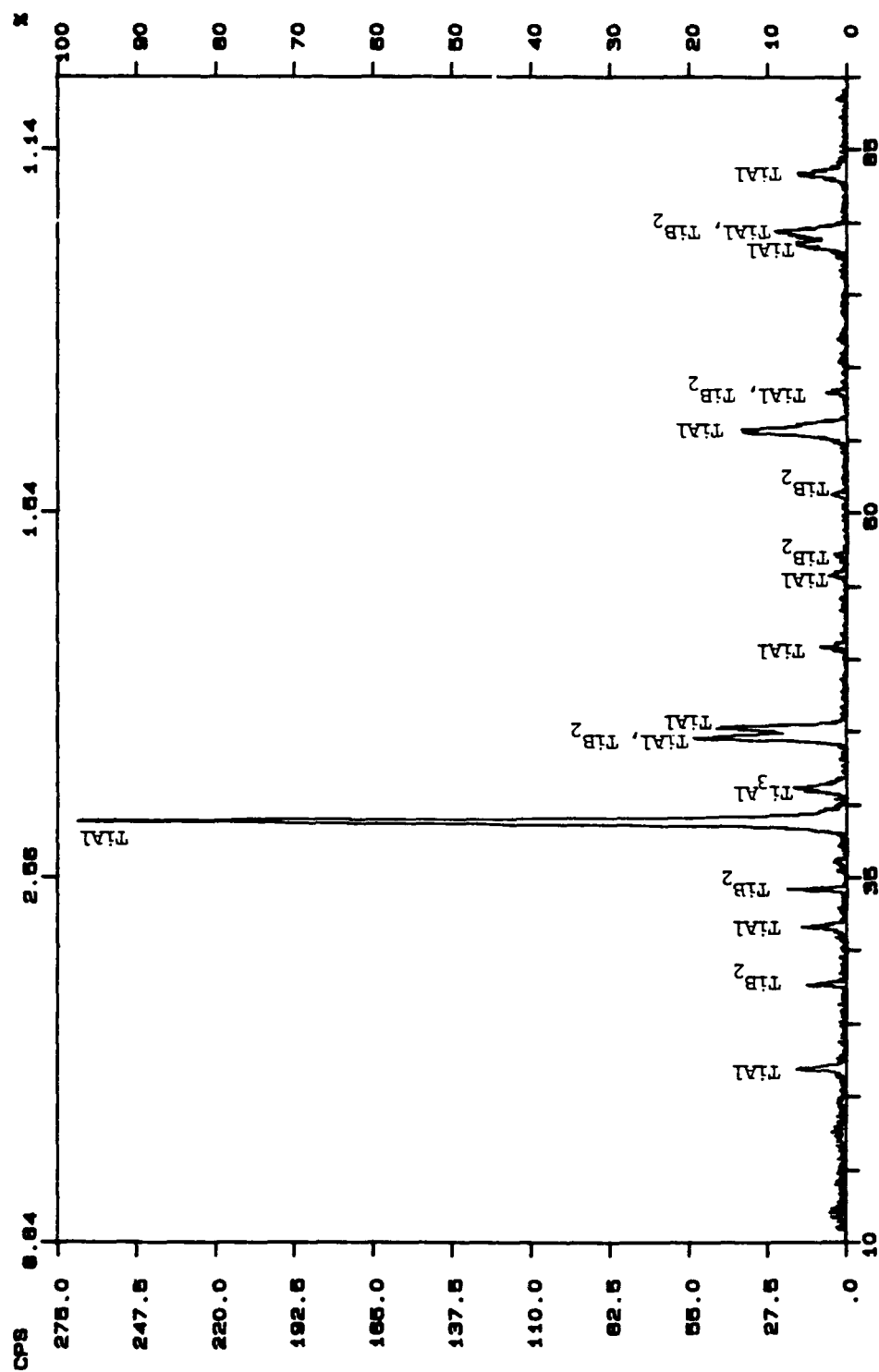


Figure 11. X-ray diffraction pattern of sample C in the as-forged condition. TiAl phase and TiB<sub>2</sub> particulate are the predominant phases with one peak of Ti<sub>3</sub>Al phase present.

rotor at about 216°C (420°F), strength, fracture toughness and ductility should be optimized which, in turn, implies microstructural control via appropriate heat treatments.

Fracture toughness and ductility can be optimized with a microstructure containing a duplex microstructure of lamellar + equiaxed; higher fracture toughness is obtained for a lamellar microstructure whereas higher ductility is retained with an equiaxed microstructure.

Previous work had shown that ductility varied less upon transitioning from a fully equiaxed to a fully lamellar microstructure whereas fracture toughness was significantly more sensitive to morphology. Therefore, the types of heat treatments that were planned involved the generation of both a fully lamellar microstructure (to optimize fracture toughness) and a duplex microstructure that contains both lamellar and equiaxed grains (to obtain some ductility and sufficient fracture toughness). Heat treatments performed on wrought material in previous studies were at 900°C (1652°F), in the  $\alpha_2 + \gamma$  phase field, and 1200°C (2192°F), in the  $\alpha + \gamma$  phase field, holding at temperature for 5 to 50 h, and slow cooling to room temperature.

Prior to recognizing the need for a second HIPing cycle, heat treatments were performed on the as-forged material. Specimens from forged stock were cleaned in acetone, wrapped in tantalum foil and encapsulated in a quartz tube under a partial pressure of argon to prevent specimen oxidation during heat treatment. Heat treatment was performed at 900°C (1652°F), 1100°C (2012°F), and 1200°C (2192°F), with a holding time of 8 h. The quartz tube was pulled from the furnace and allowed to cool in air to room temperature. The metallography on these specimens showed a continuous increase in equiaxed morphology. However, after the additional HIPing step was performed on the forgings, this information was disregarded, since the microstructure after the second HIPing (fully equiaxed) differed from that after forging (duplex microstructure of lamellar + equiaxed).

It is important to recognize that the second HIPing cycle used in this study, after forging, is atypical. The micrographs of the forging after HIPing in Figures 9a and 10a show the elimination of porosity but a difference in the microstructure from that observed prior to HIPing (Figure 7). The wavy lamellar morphology observed in the as-forged condition underwent a transformation to a fully equiaxed morphology during the HIPing process. This mandated the identification of an unusual heat treatment cycle to go from the equiaxed structure to a mixed morphology microstructure rather than the

normal situation where the transition is from a near-fully lamellar morphology to a mixed (lamellar + equiaxed) morphology.

To achieve the lamellar microstructure, heat treatments were performed in the  $\alpha$  phase field. Since it was not clear exactly where the  $\alpha$ -transus temperature was for this particular composition, two trial heat treatments were performed at 1300°C (2370°F) and 1330°C (2425°F). Specimens were wrapped in tantalum foil and encapsulated in a quartz tube under a partial pressure of argon before heat treatment for 1 h, followed by a slow air cool. Back-scattered electron images and optical micrographs of these samples are shown in Figures 9b and 10b for the 1300°C (2370°F) heat treatment and Figure 9c for the 1330°C (2425°F) heat treatment. A small amount of blocky  $\gamma$  phase was observed at 1330°C (2425°F), so heat treatment was performed at 1340°C (2445°F) to ensure a fully lamellar microstructure, as depicted in Figure 9d and 10c.

The fully lamellar microstructure could be attained upon heat treatment at 1340°C (2445°F) for 1 h followed by slow air cooling. Achieving a mixed morphology of equiaxed and lamellar microstructure was not as straightforward. Heat treatments were performed on forged + HIPed material at 1000°C (1832°F), 1200°C (2192°F), and 1250°C (2282°F) for various lengths of time and slowly air cooled. The morphology consisted of bands of blocky equiaxed phases and a coarsened lamellar-type of microstructure that was distinctly different from those lamellae produced on cooling from 1340°C (2445°F). Figure 12 compares optical micrographs from heat treatment at 1200°C (2192°F) for 1 h (Figure 12a) to that heat treated at 1340°C (2445°F) for 1 h (Figure 10c or Figure 12b which are obtained from the same specimen).

Alternate heat treatments were identified that produced the familiar mixed-morphology microstructure. Samples were heat treated at 1340°C (2445°F) for 1 h then held at 1200°C (2192°F) for 2, 5, or 10 h. The first step of this heat treatment transformed the previously equiaxed morphology into the lamellar morphology. Aging in the  $\alpha + \gamma$  phase field, at 1200°C (2192°F) resulted in the gradual formation of equiaxed  $\gamma$  phase. Micrographs of the duplex heat treatments at 1340°C (2445°F) for 1 h + 1200°C (2192°F) for 2 h and 1340°C (2445°F) for 1 h + 1200°C (2192°F) for 10 h are shown in Figures 13(a,b) and 14(a,b), respectively. It is estimated the quantity of equiaxed microstructure in the 1340°C for 1 h + 1200°C (2192°F) for 10 h heat specimen is about 15 - 20%.

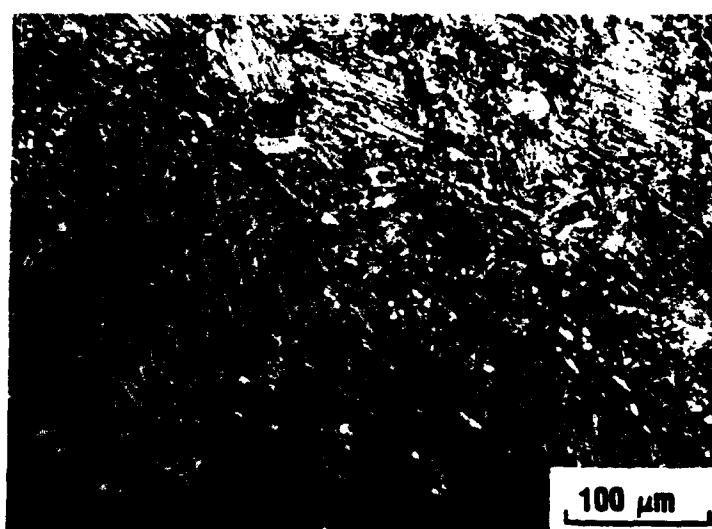
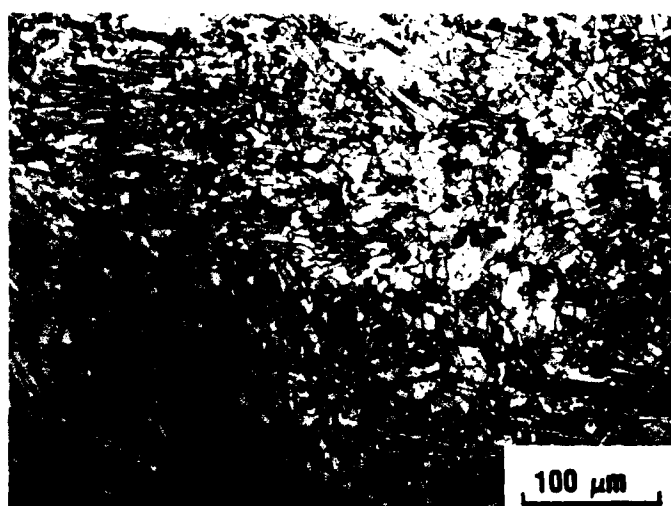


Figure 12. Optical micrographs after heat treatment (a) at 1200°C (2192°F) for 1 h and (b) at 1340°C (2444°F) for 1 h. (a) shows bands of blocky, equiaxed phase and a coarsened lamellar-type microstructure, whereas (b) is fully lamellar.

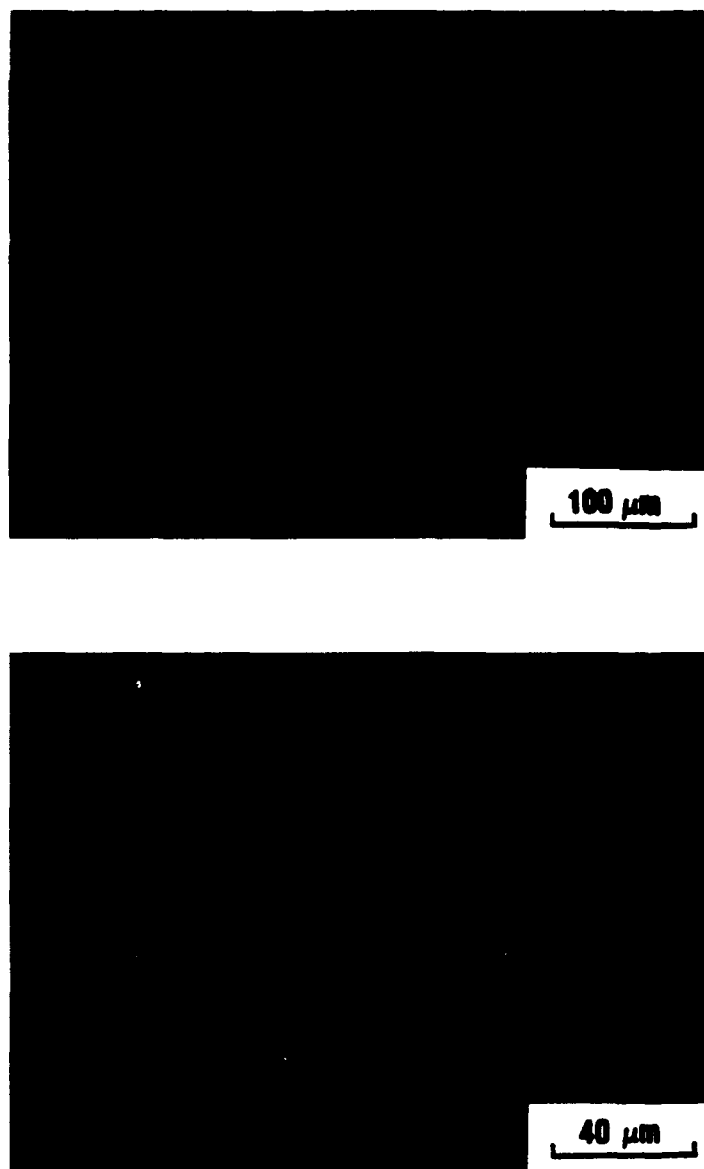


Figure 13. Micrographs after a duplex heat treatment of 1340°C (2444°F) for 1 h + 1200°C (2192°F) for 2 h where (a) shows an optical micrograph and (b) shows a back-scattered electron image. The angular black holes in (b) are from particulates pulled out of the matrix during specimen preparation.

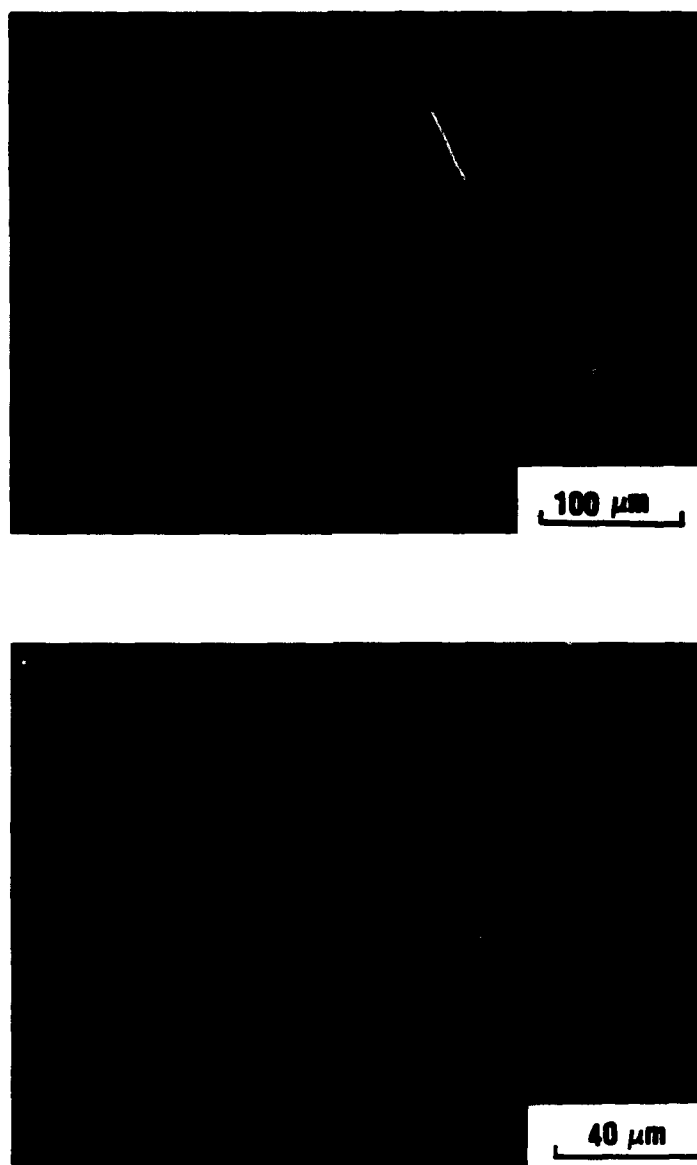


Figure 14. Micrographs after a duplex heat treatment of 1340°C (2444°F) for 1 h + 1200°C (2192°F) for 10 h where (a) shows an optical micrograph and (b) shows a back-scattered electron image.



## E. Mechanical Property Testing

Mechanical properties were measured on forged + HIPed + heat-treated specimens. Mechanical properties evaluated and the testing conditions relevant to the compressor rotor were established through recommendations made by the design engineers at Williams.

Following their recommendations, forged + HIPed material was electro-discharge machined for mechanical testing. The blanks were cleaned and wrapped in tantalum foil and encapsulated in quartz under a partial pressure of argon before heat treatment. Heat treatments were performed on the specimen test blanks to produce either a lamellar or a lamellar + equiaxed microstructure, according to the following schedule:

**Heat Treatment #1** (lamellar microstructure): 1340°C (2444°F) for 1 h in a quartz tube and subsequently air cooled to room temperature.

**Heat Treatment #2** (lamellar + equiaxed microstructure): 1340°C (2444°F) for 1 h in a quartz tube and then air cooled to room temperature; this was followed by a second heat treatment at 1200°C (2192°F) for 10 h and air cooling to room temperature.

Tensile and short-rod fracture toughness specimen blanks were subjected to either of the two heat treatment schedules to produce a fully lamellar microstructure or a lamellar + equiaxed microstructure. Notched-bend fracture toughness, creep and the high-cycle fatigue specimen blanks underwent Heat Treatment #2 to produce the fully lamellar microstructure. The matrix of mechanical tests performed is shown in Table III. Each type of mechanical test is described separately.

### 1. Tensile testing

The strength and ductility of the titanium aluminide compressor are important factors in the viability of this component for missile engine applications. Tensile testing was performed at various temperatures at Martin Marietta and yield strength, fracture strength, and ductility were obtained. The titanium aluminide alloy used in this program appears stronger than expected perhaps due to the lower aluminum content resulting from ingot production. Ductility at room temperature was less than 1%.

Room-temperature, tensile tests were initially performed on 5 tensile specimens that were 5.72 cm (2.25 in) long, containing 0.89 cm (0.350 in) diameter button heads, and a gauge length of 4.32 cm (1.70 in) with a gauge diameter of 0.37 cm (0.145 in).

Table III. Matrix of mechanical testing performed in this program.

MECHANICAL TEST	PROPERTY DATA	TESTING CONDITIONS	TEST # PER CONDITION
Tensile	YS, UTS, %el	20, 200, 500, 700, 900°C (68, 392, 932, 1292, 1652°F)	2
Fracture Toughness-- (Short Rod, Notched-Bend)	K <sub>Q</sub>	20, 200°C (68°F, 392°F) (SR) 20, 200, 300, 400°C (68, 392, 572, 752, °F) (NB)	2 (SR); 2 (NB)
High-cycle Fatigue	N <sub>c</sub>	20°C (68°F), $\sigma_{crit} = 483$ MPa (70 ksi)(+6 other stresses) R = -1; 200°C (392°F), $\sigma_{crit} = 172$ MPa (25 ksi) (+7 other stresses) R = -1	2
Creep	$t_R, \epsilon = f(t), \epsilon_{ss}$	800°C (1472°F) at 138, 207, 276, & 345 MPa (20, 30, 40, & 50 ksi)	2

Three tensile blanks were heat treated to induce the lamellar microstructure and 2 tensile blanks were tested in the as-HIPed condition, which had an equiaxed microstructure. The tensile test results are compiled in Table B-I in Appendix B. As expected, the lamellar microstructure was stronger than its equiaxed counterpart. It should be noted that the strength of the lamellar microstructure was fairly high and 4 of the 5 specimens tested failed outside of the gauge section.

The fracture surfaces for each of the two material conditions tested were examined and representative micrographs are shown in Figure 15. Figure 15a shows a typical micrograph of the as-HIPed (equiaxed) microstructure where failure is predominantly by transgranular cleavage whereas in the lamellar microstructure, shown in Figure 15b, failure occurs along the interfaces of the lamellae.

To ensure that failure occurred in the gauge section, the tensile specimen geometry was modified by reducing the total length to 3.96 cm (1.56 in), increasing the gauge length to 2.54 cm (1 in), and incorporating an incomplete 0.24 cm (3/32 in) radius

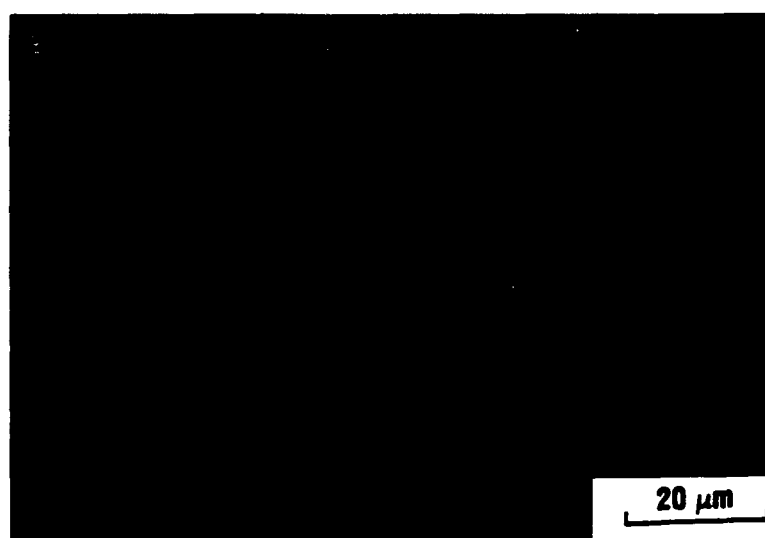
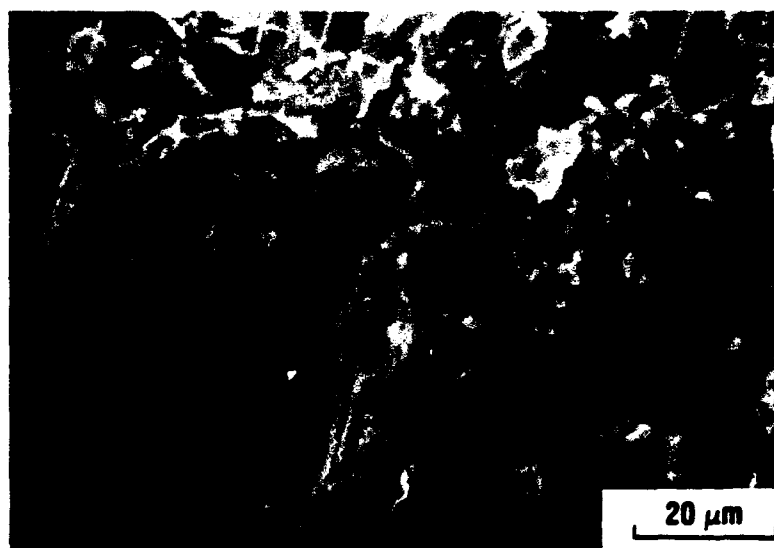


Figure 15. Secondary electron micrographs of the fracture surfaces of tensile specimens in (a) the as-HIPed condition that has an equiaxed microstructure and (b) after heat treatment at 1340°C (2444°F) for 1 h that has a lamellar microstructure.

into the button head end. Four specimens were tested, 2 at room temperature and 2 at 500°C (932°F); failure continued to occur outside the gauge at the gauge radius. The remaining 16 specimens were re-machined to incorporate a more shallow neck region having a different radius of 0.25 cm (0.10 in), a gauge length of 1.78 cm (0.7 in) and a decreased gauge diameter of 0.30 cm (0.120 in). Plots of the yield strength, fracture strength and ductility as a function of temperature are presented in Figures 16, 17, and 18, respectively. A tabulation of the tensile data is shown in Table B-II in Appendix B.

For both the lamellar and the duplex microstructures, yield strength is fairly temperature insensitive in the temperature range 20°C to 600°C (68°F to 1112°F), remaining above about 550 MPa (80 ksi). In the range 600°C - 900°C (1112°C - 1652°F), the yield strength decreases from 550 MPa (80 ksi) to about 200 MPa (29 ksi), Figure 16. There is not a significant difference in the yield strength-temperature profiles between the lamellar and the duplex microstructures. The ambient-temperature yield strength of the fully equiaxed microstructure is somewhat lower than the lamellar and duplex microstructure counterparts.

Fracture strength variation with temperature for the HIPed, forged and heat-treated alloy reveals a mild positive temperature dependence of strength, the effect being more pronounced for the duplex structure (Figure 17). This behavior is noted in the temperature range 20°C to 600°C (68°F to 1112°F) beyond which fracture strength decreases with increasing temperature. This positive temperature dependence of strength is likely due to a higher work hardening rate at intermediate temperatures, caused by the interaction of slip and twinning. In addition, the slightly higher ductility in the mixed morphology microstructure at 500°C (932°F) and higher permits the specimen to support a larger stress prior to failure (Figures 18 and 19). Ductility remains below 1% for both the lamellar and the duplex microstructures at temperatures below ~ 500°C (932°F); further increases in temperature lead to improvements in ductility reaching ~ 5% at 900°C (1652°F), Figure 18. The fully equiaxed microstructure reveals the highest ductility at ambient temperature.

The fracture surfaces of the tensile specimens tested at 20°C (68°F) and 500°C (932°F) for both the lamellar and the duplex microstructures were examined in an SEM (Figures 19 a-d). For both microstructures, the 20°C (68°F) specimens exhibited features characteristic of crack propagation along the interphase interface (i.e., interlamellar interface). The fracture morphology of the specimens tested at 500°C (932°F) was

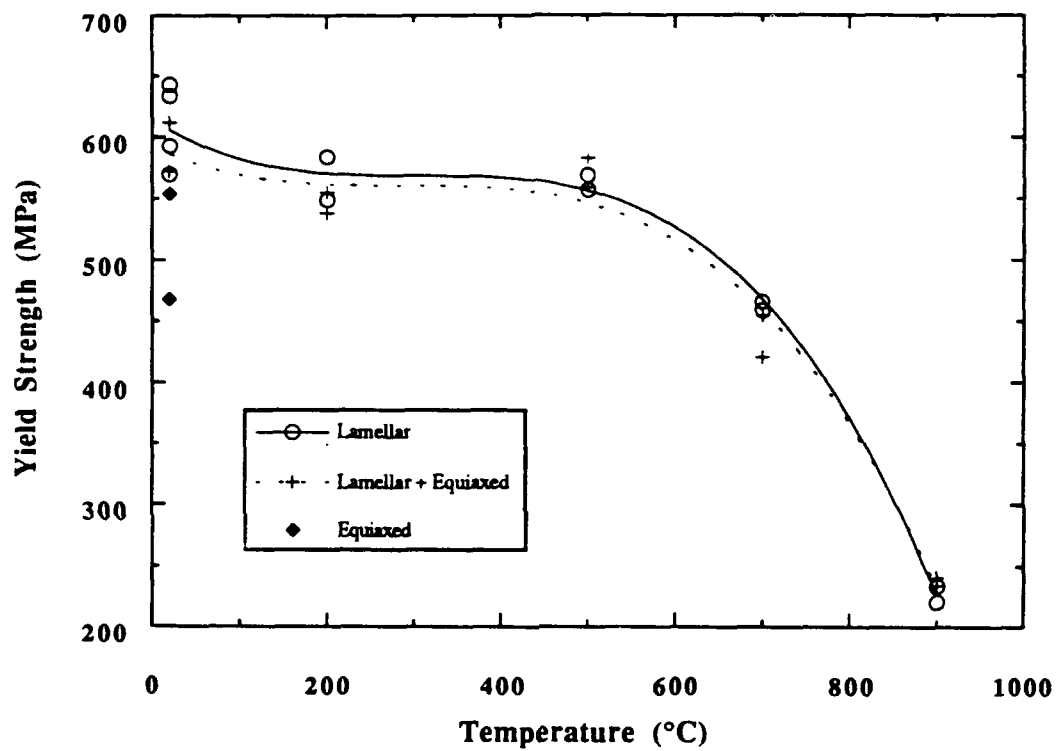


Figure 16. Yield strength - temperature profiles for forged + HIPed, Ti-45Al-2Mn-2V + 7 volume % TiB<sub>2</sub> alloy.

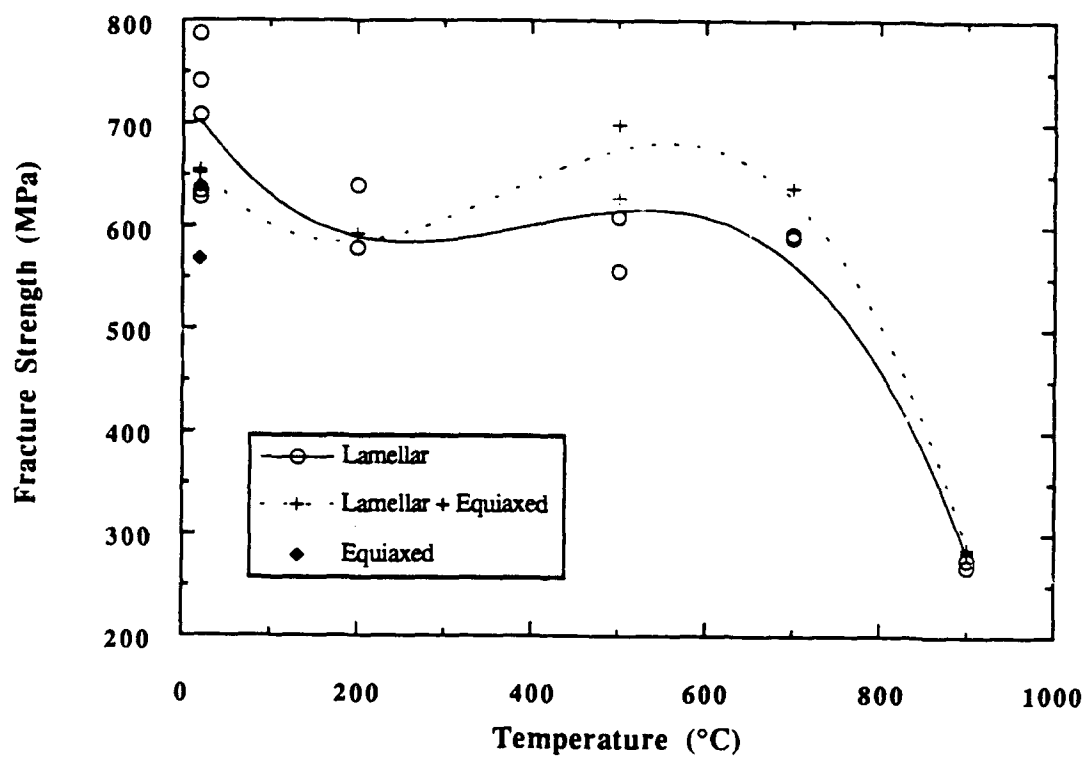


Figure 17. Fracture strength versus temperature for forged + HIPed, Ti-45Al-2Mn-2V + 7 volume % TiB<sub>2</sub> alloy.

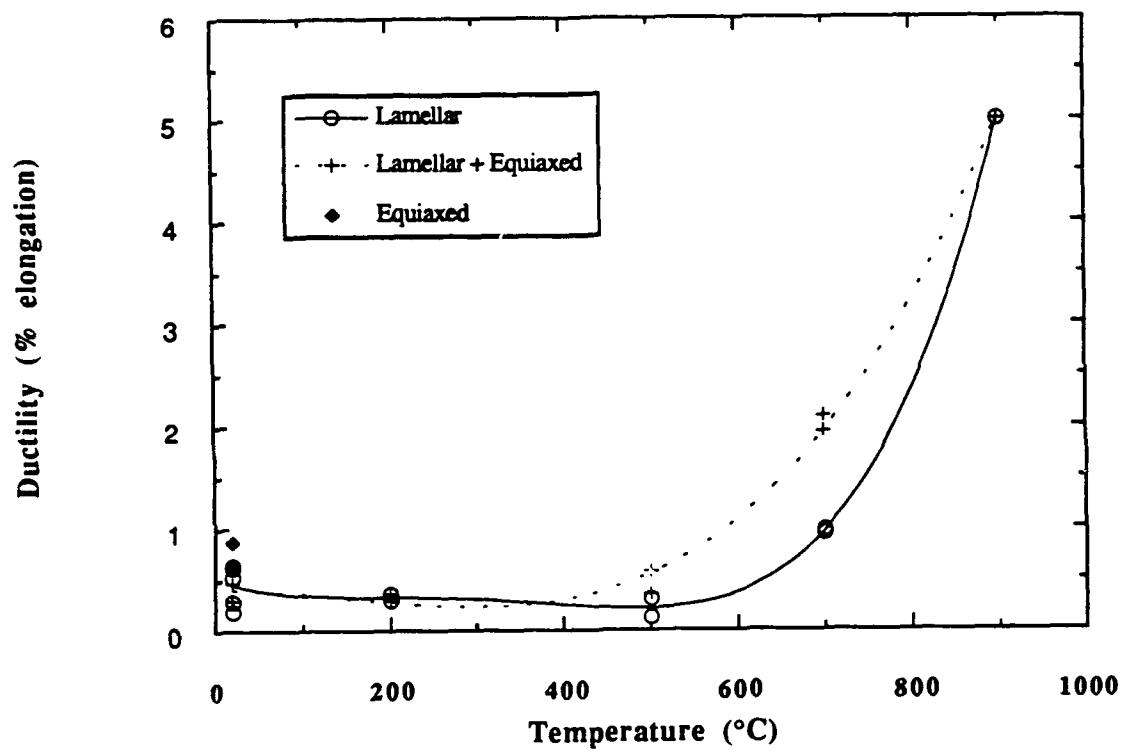


Figure 18. The effect of temperature on tensile ductility of the forged + HIPed, Ti-45Al-2Mn-2V + 7 volume % TiB<sub>2</sub> alloy.

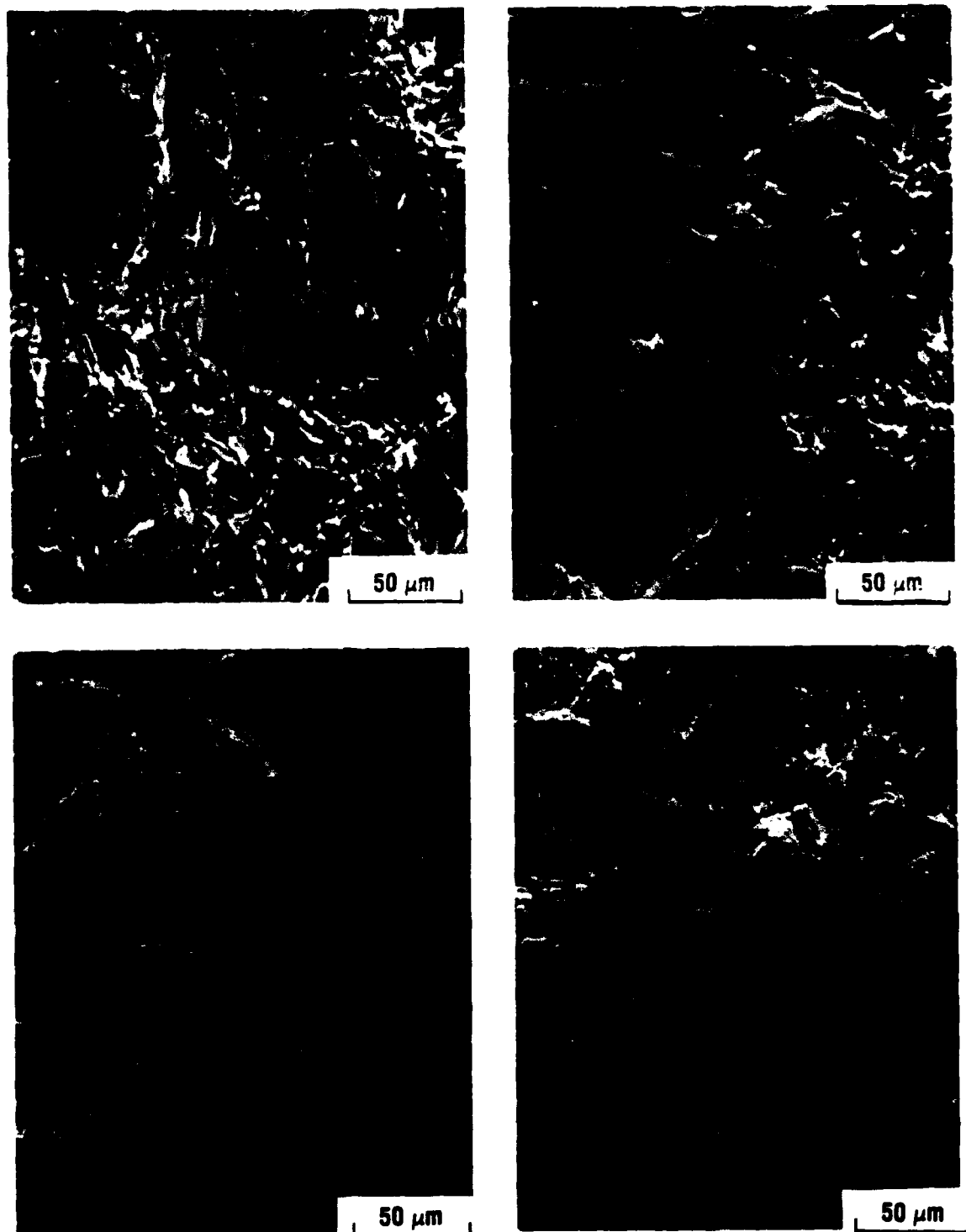


Figure 19. Secondary electron micrographs of the fracture surfaces of tensile specimens tested at 20°C (68°F) for (a) lamellar and (b) lamellar + equiaxed microstructures and at 500°C (932°F) for (c) lamellar and (d) lamellar + equiaxed microstructures.



similar to that observed at ambient temperature. Fracture surfaces of specimens tested at higher temperatures were oxidized and did not yield useful information.

## 2. Fracture toughness testing

Strength, ductility, and fracture toughness are important properties to be emphasized in the successful application of titanium aluminide alloys to the compressor rotor component. In the initial alloy selection, it was indicated that fracture toughness should be maximized to exceed  $15.8 \text{ MPa}\sqrt{\text{m}}$  ( $14.4 \text{ ksi}\sqrt{\text{in}}$ ), that value achieved on as-cast Ti-45Al-2Mn-2V + TiB<sub>2</sub> alloys. In this program, fracture toughness testing was performed for both short-rod and notched-bend specimens following ASTM standards. Short-rod fracture toughness tests were performed at Metcut Research Associates, Inc. (Metcut) whereas the notched-bend specimens were tested at Martin Marietta.

Eight short-rod fracture toughness specimens were heat treated, 4 having a lamellar microstructure and 4 having a lamellar + equiaxed microstructure. Testing was performed at Metcut Research Associates, Inc. (Metcut) following ASTM E1304-89<sup>22</sup> using a closed loop servo controlled hydraulic system with a 89,000 N (20,000 lb) capacity. The specimen geometry was 1.9 cm (0.775 in) in length by 1.23 cm (0.500 in) in diameter. Four bars were tested at room temperature and 4 at 200°C (392°F), the latter of which is based on the anticipated operating temperature of the compressor rotor. At each temperature, 2 specimens were heat treated to produce the lamellar microstructure and the other 2 to produce a lamellar + equiaxed microstructure.

The short-rod fracture toughness results are shown in Figure 20 and the actual data are compiled in Table B-III in Appendix B. The room temperature toughness values are much higher than those previously measured for other XD<sup>®</sup> alloys having a similar alloy composition (15 - 20  $\text{MPa}\sqrt{\text{m}}$ ). It was decided to have these tests performed at Metcut due to their ability to also conduct higher-temperature tests (e.g., 200°C).

The fracture toughness values represented in Figure 20 are  $K_{QVM}$ . Normally,  $K_{IVM}$  values would be reported using this ASTM standard, where the "M" denotes calculation using the maximum load criteria; however, none of the specimens failed within the range of valid criterion designated for the ASTM standard. The relevant sections of the ASTM standard that were not complied with by the individual specimens are listed in Table B-III in Appendix B.  $K_{QV}$  values were reported for those tests that

allowed two unload points to be generated before failure. Each specimen exhibited smooth crack-growth behavior and failure occurred through the thickness of the test bar; however, unexpectedly, in all tests, failure occurred at a 45°-90° angle from the notch plane. Exact reasons for this behavior remain unclear at present.

The room-temperature, fracture toughness values for both microstructures were higher than expected, but the difference in fracture toughness with morphology variation is smaller at room temperature than that at 200°C (392°F) (Figure 20). The mixed-microstructure contains a lower quantity of the lamellar component that provides the high toughness by crack branching and bifurcation. In order to clearly distinguish between the fracture toughness of the two microstructures in this study, a higher ratio of equiaxed-to-lamellar morphology or an all equiaxed microstructure would perhaps be needed, exceeding the 15 to 20% equiaxed morphology estimated for those specimens subjected to Heat Treatment #2.

Fracture toughness testing was also performed at Martin Marietta using notched-bend specimens following the ASTM Standard E 399. Ten specimens were electro-discharge machined from forged + HIPed stock material and cut into 6.35 cm (2.5 in) long and 0.64 cm (0.25 in) by 1.27 cm (0.5 in) blanks. Heat treatment was performed to produce a lamellar microstructure. The 2 large faces were ground to remove the electro-discharge machined layer, notches were placed in the specimens, and then precracked in lab air at room temperature. Two of the specimens fractured during the pre-cracking procedure and could not be used. Three-point bend testing was performed using an Instron machine and monitored using load-displacement curves at 20°C (68°F), 200°C (392°F), 300°C (572 °F), and 400°C (752°F). From the load-displacement curves, fracture toughness was evaluated and the results are summarized in Table B-IV in Appendix B.

Notched-bend fracture toughness results are shown in Figure 20. Toughness values obtained were  $K_Q$ , not  $K_{IC}$ , for reasons similar to those observed in short-rod fracture testing. A fracture toughness of  $\sim 19.5 \text{ MPa}\sqrt{\text{m}}$  ( $17.6 \text{ ksi}\sqrt{\text{in}}$ ) was obtained at room temperature that gradually increased to  $\sim 26.7 \text{ MPa}\sqrt{\text{m}}$  ( $24.0 \text{ ksi}\sqrt{\text{in}}$ ) at 300°C (572°F). Further increase in temperature to 400°C (752°F) did not provide any further appreciable increase in toughness. These values are much lower than those obtained for the lamellar specimens tested using the short-rod geometry.

Regarding this difference, it is of interest to note that previous short-rod fracture

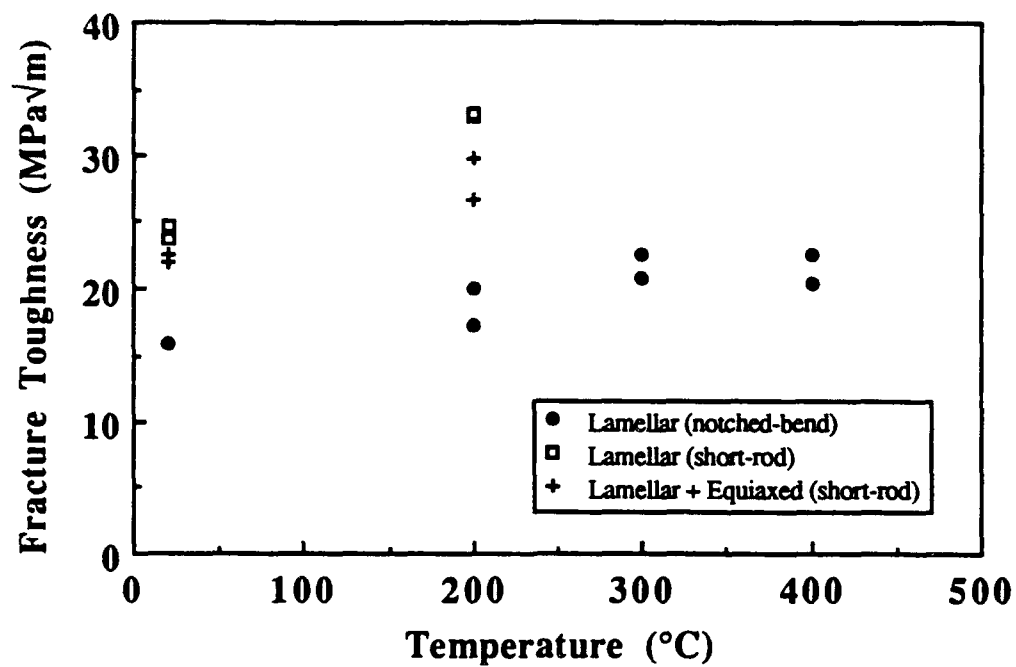


Figure 20. Fracture toughness variation with temperature for short-rod specimens tested at Metcut and notched-bend specimens tested at Martin Marietta.

toughness testing of XD<sup>®</sup> alloys at room temperature has been performed at Ceramtec and had not shown such high fracture toughness values as those measured in the present study at Metcut. Ceramtec performs fracture toughness tests in a Fractometer I, built at Terra Tek, according to ASTM Standard E 1304-89. In this test, a bellow is placed into the Chevron notch that expands when liquid mercury is injected into the bellow, propagating the crack to failure. This procedure differs from that used at Metcut. In a recent study on an internal program, Ti-47Al-2V + 7 volume % TiB<sub>2</sub> alloy was tested at room temperature using both the short-rod configuration at Ceramtec and the notched-bend configuration at Martin Marietta. For a lamellar + equiaxed microstructure, the short-rod specimens could not be broken as the specimen plasticity during testing exceeded the capabilities of the equipment; a fracture toughness of at least 19.8 MPa√m (18 ksi√in) was indicated, whereas the notched-bend specimens exhibited an average fracture toughness of 16.9 MPa√m (15.4 ksi√in). It is felt that the values reported by Metcut (and Ceramtec from other studies) could be inflated due to errors associated with the testing method. On the other hand, the values obtained from notched-bend testing give a minimum value; the true value could lie in between these two. In the present study, the notched-bend fracture toughness at room temperature is 16 MPa√m (17.8 ksi√in), which is above the acceptable limit for the compressor rotor design.

Fracture surfaces of notched-bend specimens were examined in the SEM for a specimen tested at 20°C (68°F) and 400°C (752°F) in the 3-point bend configuration and representative micrographs are shown in Figure 21. In both cases, fracture propagation along the interlamellar interface.

### 3. High-cycle fatigue testing

High-cycle fatigue tests were performed at Howmet's Mechanical Testing Division at 20°C (68°F) and at 200°C (392°F). Initial stress levels were chosen according to the maximum design stresses predicted at these two temperatures by Williams--483 MPa (70 ksi) at room temperature and 172 MPa (25 ksi) at 200°C (392°F). Other stresses levels were selected based on the results of the initial and each subsequent test. The recommended R ratio was  $R = -1$ ; test frequency was 60 Hz.

Eight specimens were tested at each temperature. The 16 specimens were heat treated to produce a fully lamellar microstructure before machining to the final specimen geometry of a 7.35 cm (3 in) long bar, having a 1.225 cm (0.500 in) gauge length and cylindrical grips. Testing was discontinued if failure did not occur after  $10^7$  cycles.

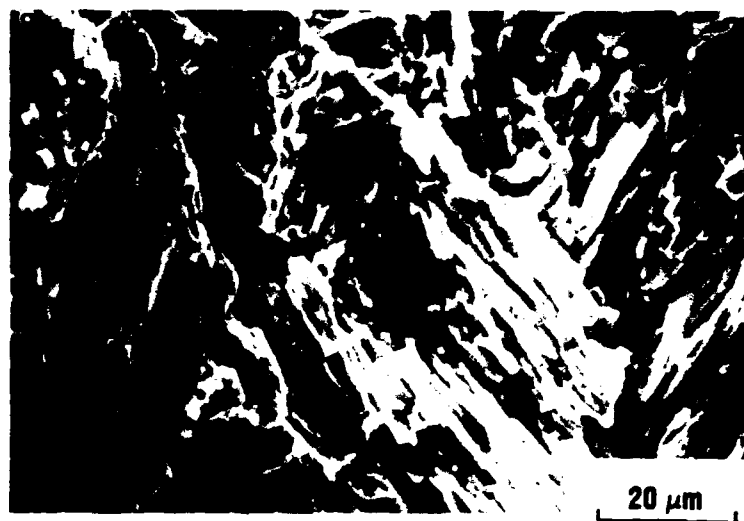


Figure 21. Scanning electron micrographs depicting the fracture surface of two notched-bend specimens tested in 3-point bend at (a) 20°C (68°F) and (b) 400°C (752°F). While the mode of fracture is predominantly along the lamellar grains, a few areas of planar fracture are present in (b).

The high-cycle fatigue results are shown in Figures 22 and 23, for testing at room temperature and 200°C (392°F) respectively, and the data summarized in Table B-V in Appendix B. The high-cycle fatigue life at the maximum design stress for both temperatures was good. At the critical stress level predicted by Williams, 483 MPa (70 ksi), at room temperature, the average failure occurred after over  $10^6$  cycles, or after over 7.5 h of operation. In contrast, the component life is expected to be no longer than 20 m. At 200°C (392°F), for the maximum stress of 172 MPa (25 ksi), the specimen withstood  $10^7$  cycles. A linear regression analysis was performed on each set of data and a good-fit correlation could be made for the data at each temperature with the exception of the test at 552 MPa (80 ksi) at 200°C (392°F), which appeared to break prematurely. The linear regression analysis indicated the predicted runout to  $10^7$  cycles at 20°C (68°F) was 460 MPa (66.7 ksi) and at 200°C (392°F) was 441 MPa (64.0 ksi).

#### 4. Creep testing

The creep properties of this alloy are not specifically critical for the application of the compressor rotor in the P9005 gas turbine engine since the rotor will only see temperatures above its ductile-to-brittle transition temperature for less than 10 s. However, upon recommendations from Williams, testing was performed at several constant stress conditions at 800°C (1472°F). Specimens were subjected to heat treatments to allow transformation to a lamellar microstructure. Creep measurements were performed at Howmet's Mechanical Testing Division under constant stress conditions of 138, 207, 276 and 345 MPa (20, 30, 40 and 50 ksi).

Eight specimen blanks were heat treated to produce a lamellar microstructure and machined into 5.08 cm (2 in) long test specimens having a threaded grip section. During testing, the amount of creep strain was measured at 15 min intervals and a representative curve from each stress condition is shown in Figure 24. The set of complete data tables and figures for each test performed can be found in Table B-VI and Figures B-1 through B-4, respectively, in Appendix B. While the secondary (steady-state) and tertiary creep regimes are easily distinguished, primary creep behavior is not prominent in these alloys. Comparison of the rupture time at the different stress levels indicates the creep behavior of this alloy is load sensitive. For an increase of only 69 MPa (10 ksi), the time to failure at a constant stress load of 138 and 207 MPa (20 and 30 ksi) differs by a factor of 5.

Post-testing metallography was performed on two creep specimens, T8-1 and

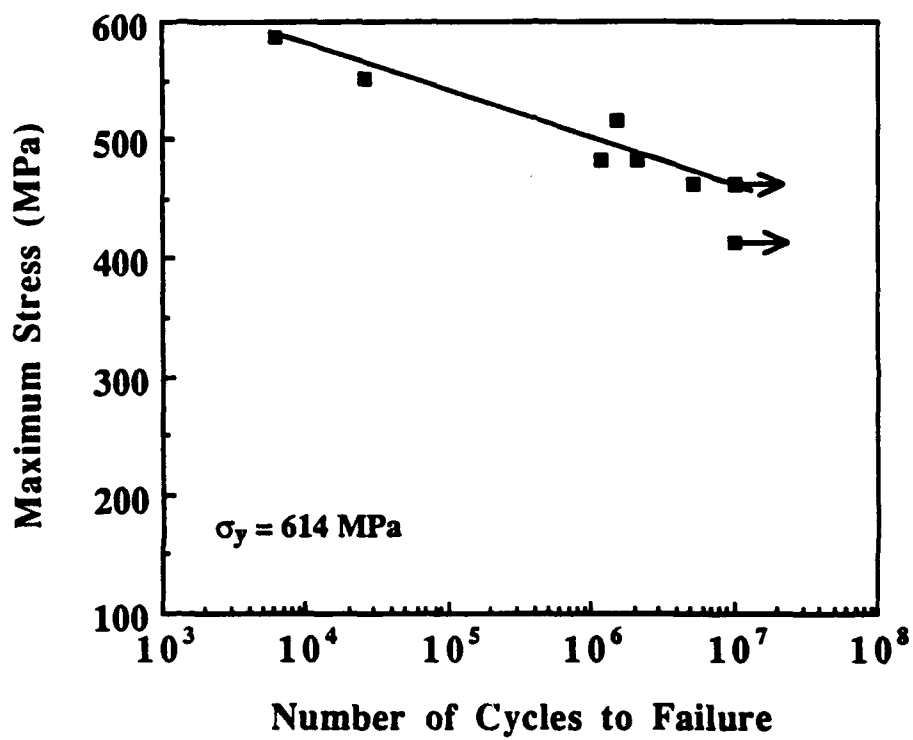


Figure 22. Stress-cycles to failure (S-N curve) at room temperature for Ti-45Al-2Mn-2V + 7 volume % TiB<sub>2</sub> alloy showing its outstanding fatigue resistance.

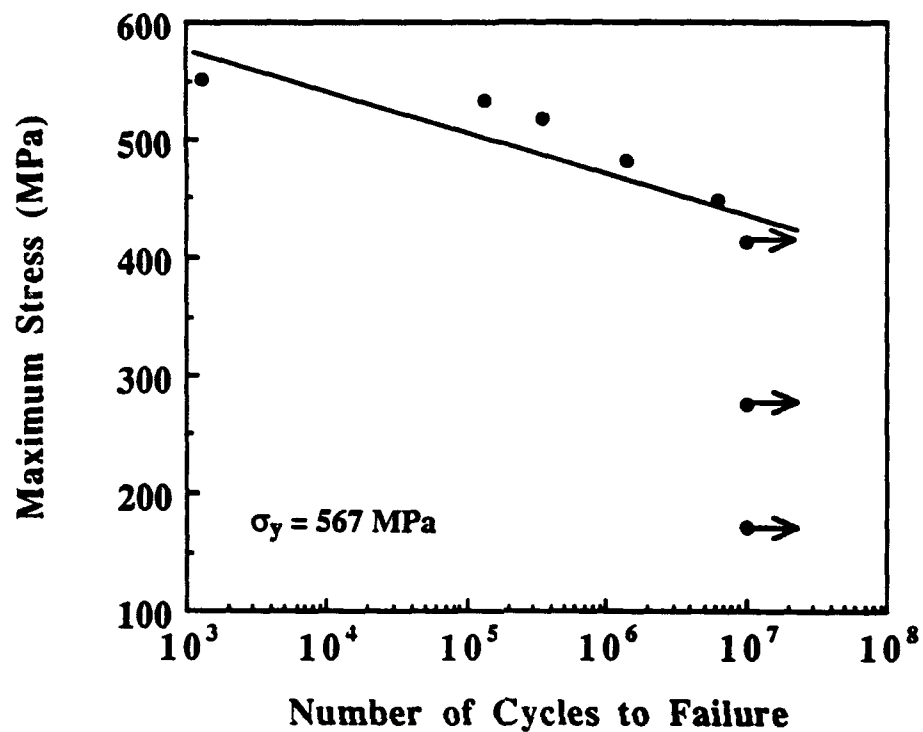


Figure 23. High-cycle fatigue behavior at 200°C (392°F) expressed as maximum applied stress as a function of the number of cycles to failure. At the critical maximum stress of 172 MPa (25 ksi), cycles to failure exceeded  $10^7$  cycles.



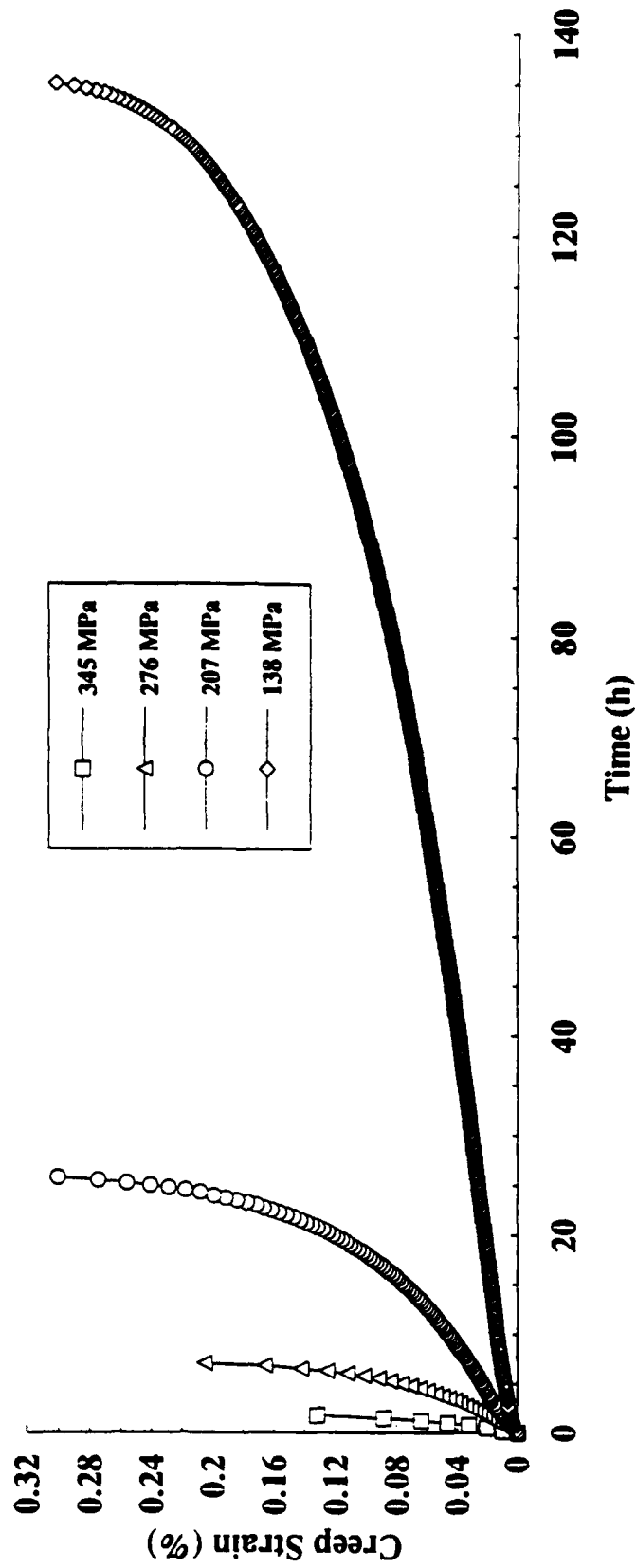


Figure 24. Creep strain as a function of time to rupture at 800°C (1472°F) for 4 applied stress conditions: 138, 207, 276, and 345 MPa (20, 30, 40, and 50 ksi).

T8-5, tested at 138 and 276 MPa (20 and 40 ksi), respectively. The specimens were sliced along their length and examined in the SEM. A lamellar microstructure was present in the specimen grip sections (at the threaded end). Adjacent to the fracture region of each creep specimen, there was evidence of thickening of the  $\alpha_2$  phase observed in addition to bending of the lamellar grains. Figure 25 shows representative micrographs of the structure at the grip section and adjacent to the fracture region for the two stress states mentioned above. It appears that the  $\alpha_2$  phase present in the specimen tested at 138 MPa (20 ksi) is more blocky or equiaxed in nature, while that tested at 276 MPa (40 ksi) is only partly equiaxed, possibly resultant from the longer exposure time at temperature for the 138 MPa (20 ksi) test. The formation of these small equiaxed grains from the morphologically unstable lamellar is viewed as a possible mechanism by which creep occurs and can lead to a degradation in creep response due to the grain boundary regions generated by the transformation.

These creep data can be compared with those data previously compiled for a cast + heat-treated, reinforced Ti-45Al-2Mn-2V alloy, tested at a constant stress of 138 MPa (20 ksi) at 816°C (1500°F). The respective rupture times for the 7 volume % and 11 volume % TiB<sub>2</sub> reinforced alloys were 102 and 130 h.<sup>19</sup> It is apparent that the creep mechanisms for these TiB<sub>2</sub>-reinforced alloys are comparable, indicating the particulate loading and processing differences have only minor effects on the creep resistance of these materials. It should be noted that microstructural evaluation of the cast + heat-treated alloy revealed the retention of a lamellar morphology following 16 h at 900°C (1652°F).

An important creep parameter used in the theoretical analysis of creep behavior of a metal is the steady-state creep rate,  $\epsilon_{ss}$ , quantitatively described by the power law creep relationship.  $\epsilon_{ss}$  is directly proportional to  $\sigma^n$ , where  $\sigma$  is the imposed stress and  $n$  is the stress exponent for creep. Figure 26 compares the steady-state creep rate with the applied stress for the XD<sup>®</sup> forged + heat-treated alloy used in this study and a binary XD<sup>®</sup> TiAl alloy having comparable processing history. The steady-state creep rate for the XD<sup>®</sup> Ti-45Al-2Mn 2V alloy is higher than that for the binary XD<sup>®</sup> TiAl alloys, although the stress exponent, 'n' for these alloys are comparable; this implies different activation energies in the two cases. A possible implication is that two different creep mechanisms are operative. Alternately, it is possible that the quaternary additions significantly influence the diffusion coefficient thereby affecting  $Q$  even for similar operative mechanisms.

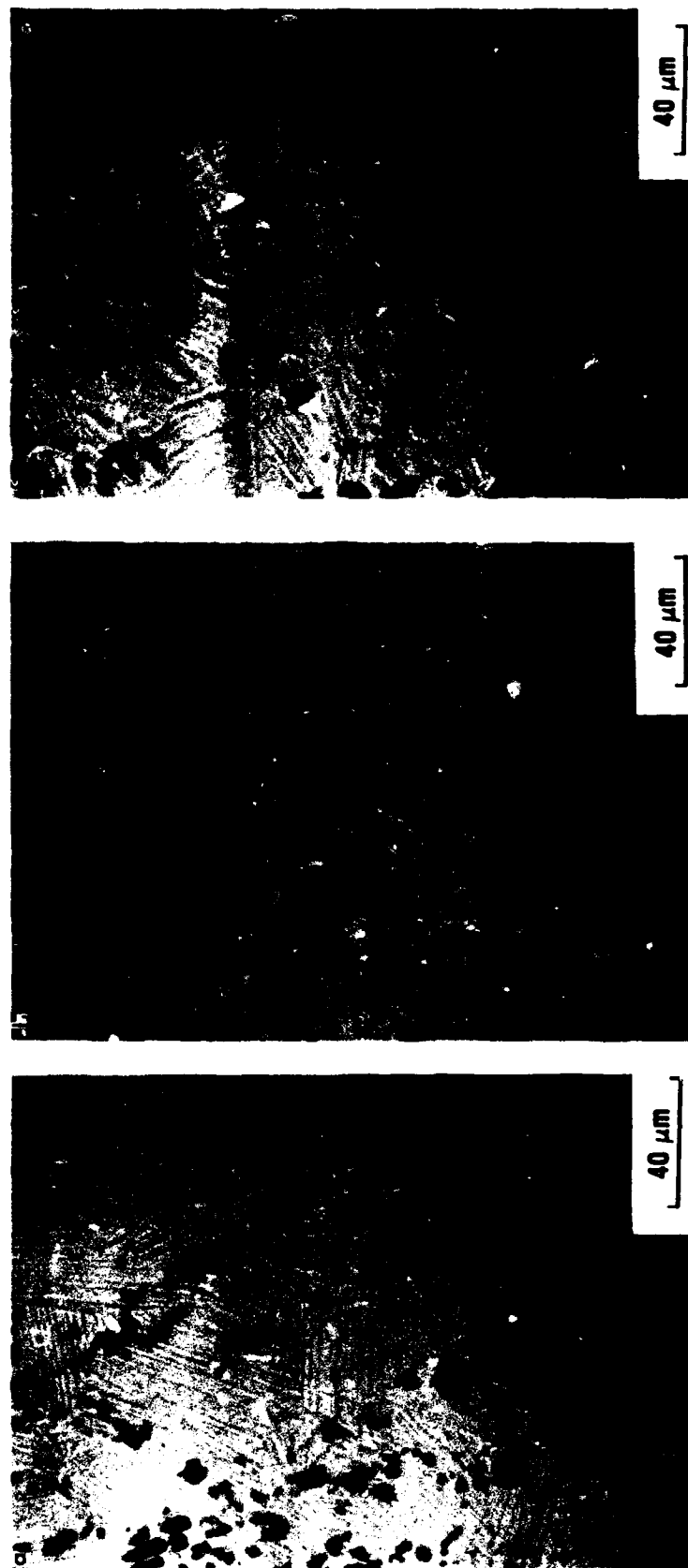


Figure 25. Back-scattered electron micrographs of the cross section of creep specimens tested at 800°C (1472°F): (a) the grip section, (b) the section adjacent to the fracture of the 138 MPa (20 ksi) specimen and (c) the section adjacent to the fracture of the 276 MPa (40 ksi) specimen (black-TiB<sub>2</sub>; grey-TiAl; light grey-Ti<sub>3</sub>Al).

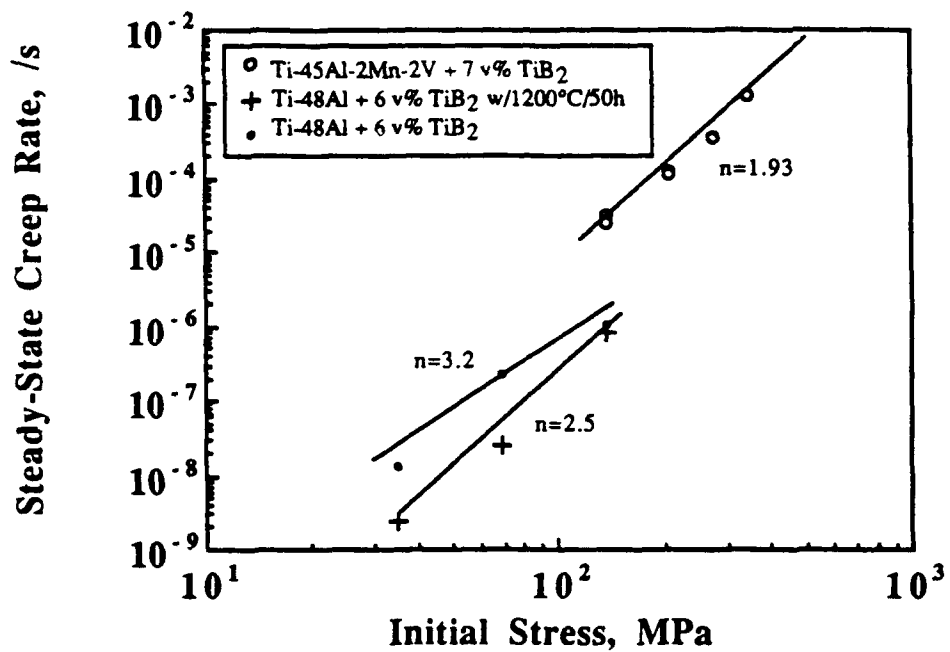


Figure 26. The steady-state creep rate as a function of the initial applied stress for 3 forged alloys tested at 800°C (1472°F).<sup>18</sup>

Previous studies<sup>6,23</sup> on the creep response of monolithic TiAl alloys have discussed the role of various microstructural features in influencing creep resistance. Specifically, it was shown that fully lamellar structures show significant improvements in creep properties over duplex microstructures. The increased creep resistance for a lamellar structure was explained in terms of the  $\alpha_2$  laths acting as reinforcements. The large grain size of the lamellar structure may also play an important role for improvement creep properties. Alternate explanations provided include the role of grain boundary morphology in influencing creep. The presence of serrated grain boundaries in a Ti-48Al alloy was argued as being responsible for the superior creep response observed in that alloy. Additionally, it was also indicated that, as the aluminum content in the alloy was decreased, the extent of grain boundary serration decreased; this was associated with a loss in creep resistance. In light of these observations, the superior creep resistance of the Ti-48Al XD<sup>®</sup> alloys from a previous study (Figure 26), relative to the alloy used in the present study, may be attributed to the aluminum content differences. Other factors, such as differences in grain size between the two alloys, would also be responsible for the observed trend in the creep data.

#### F. Heat Treatment of Forgings

The goal of this program was to produce sufficient XD<sup>®</sup> TiAl material from which compressor rotors could ultimately be machined; as a subset, an optimal thermal-mechanical processing route was to be defined. As previously discussed, the results of mechanical testing indicated the Ti-45Al-2Mn-2V + 7 volume % TiB<sub>2</sub> alloy performed best when it contained a lamellar microstructure.

In preparation for final heat treatment, 4 forged + HIPed pancakes were sand-blasted and wrapped in tantalum foil for heat treatment at Solar Atmospheres, Inc. The tantalum foil was used to protect the molybdenum fixtures in their furnace. Heat treatment was performed in a reduced pressure, argon-rich atmosphere. The pancakes were placed in the furnace at room temperature and ramped up to 1340°C (2444°F) and held for 1.5 h. Cooling was achieved at a rate of 66°C (150°F) per minute down to room temperature. These pancakes are being sent to the Army Research Laboratory along with the remaining 2 pancakes not used in the mechanical testing task as the final deliverables in this program in addition to this final report.

### G. Final Rotor Machining

A local machining facility, E. D. M. Technologies, was found that has the necessary equipment to perform the final rotor machining. The rotor design from Williams was successfully downloaded to their CAD/CAM system and they would be able to complete production of the compressor rotors if funds becomes available in the future.

### H. Summary

In this program, a Ti-45Al-2Mn-2V + 7 volume % TiB<sub>2</sub> alloy was produced, microstructurally characterized as a function of heat treatment and evaluated in terms of strength, ductility, fracture toughness, fatigue and creep resistance. The compressor rotor design analysis was simultaneously performed at Williams International. A variety of heat treatments were examined to obtain a correlation between heat treatment and microstructural change. Appropriate heat treatments were identified to produce a fully lamellar microstructure as well as a duplex structure consisting of approximately 15-20 percent by volume of the equiaxed structure. At room temperature (for a fully lamellar microstructure), yield strength was in the range 570 - 650 MPa (83 - 94 ksi), which was higher than anticipated, ductility was under 1% and fracture toughness appeared greater than 19.6 MPa√m (17.8 ksi√in) (measurements ranged from 19.6 to 29.4 MPa√m (17.8 to 26.7 ksi√in). An excellent response was noted in high-cycle fatigue at room temperature, with failure occurring at 10<sup>6</sup> - 10<sup>7</sup> cycles for a stress level of 480 MPa (70 ksi). At 200°C (392°F), which is exactly the steady-state operational temperature for the component, fatigue resistance remains essentially the same as at 20°C (68°F). The strength, ductility and toughness were also measured at elevated temperatures, and strength and ductility remained insensitive to temperatures up to 500°C (932°F). At higher temperatures, strength decreased with increasing temperature and ductility increased to over 5% at 900°C (1652°F).

Based on these observations, 4 forgings were appropriately heat treated to obtain a fully lamellar microstructure. A vendor was chosen to perform the final compressor rotor machining; this task, however, was not funded.

## V. CONCLUSIONS AND RECOMMENDATIONS

The overall goal of this program was to evaluate the potential to use XD<sup>®</sup> TiAl alloys for compressor rotors in missile engines. To this end, the technical objectives involved design analysis by Williams International; material production and processing by TIMET, Howmet and Ladish Co.; and thermal-mechanical processing and material characterization by Martin Marietta. The final component machining was scheduled at E.D.M. Technologies. From this program, the following conclusions have emerged:

- Detailed design analysis revealed that an existing design for the rotor could be utilized with no modifications and would permit significant gains due to the reduction in density relative to the existing stainless steel component.
- Sufficient quantities of XD<sup>®</sup> TiAl materials were cast, HIPed, forged and HIPed again.
- A heat-treatment route was identified to produce a fully lamellar microstructure; this microstructure was shown to exhibit a desirable combination of mechanical properties.
- Strength, toughness and fatigue resistance goals were exceeded at ambient and steady-state operating temperatures by a material exhibiting a fully lamellar microstructure; ductility, however, was consistently less than 1% below 500°C (932°F).

This program has illustrated that mechanical property goals can be met by XD<sup>®</sup> TiAl for the compressor rotor application. The next logical step would be to machine the component and engine test their performance.

If the component is ductility limited, then there are alternate alloy compositions that have recently become available that do meet the goals. Specifically, when this program was initiated, a much smaller alloy selection was available than is today. Currently, XD<sup>®</sup> TiAl alloys containing 0.8 volume % TiB<sub>2</sub> particles are becoming available that yield better ductility relative to those measured in this program. These

new alloys constitute the most recent development in this continuously evolving field, and typical properties are shown for two such alloys in Table IV below against properties obtained in this program. We recommend these alloys for future efforts for such components.

Table IV. Typical Mechanical Properties for XD® TiAl Alloys, Comparing the Alloy Used in this Study with Those Containing 0.8 Volume % TiB<sub>2</sub>

Alloy	YS (MPa)		Ductility (%)		K <sub>Ic</sub> (MPa√M)	HCF (20°C)	
	20°C	650°C	20°C	650°C		Stress (MPa)	Cycles
Ti-45Al-2Mn-2V + 7 TiB <sub>2</sub>	~620	~500	0.25	0.8	~19	483	>10 <sup>6</sup>
Ti-45Al-2Mn-2Nb + 0.8 TiB <sub>2</sub>	~590	~470	1.5	3.0	~15.2	N/A*	
Ti-47Al-2Mn-2Nb + 0.8 TiB <sub>2</sub>	~410	~350	1.25	3.5	~14.0	N/A**	

\* HCF at 650°C (R=0.1): ~ 520 MPa, > 10<sup>6</sup> cycles

\*\* HCF at 650°C (R=0.1): ~ 350 MPa, > 10<sup>7</sup> cycles

#### ACKNOWLEDGMENTS

We would like to acknowledge Mike DiPietro for his assistance with some of the mechanical testing and Candi Krug for her assistance with the preparation of the final report. One of the authors (Pamela Sadler) acknowledges the support and guidance provided by Steve Kampe in the early stages of the program.



## VI. REFERENCES

1. S.-C. Huang and E. L. Hall, *Met Trans A*, **22A**, No. 2, 1991, 427-39.
2. C. McCullough, J. J. Valencia, C. G. Levi and R. Mehrabian, *Acta Met.*, **37**, 1989, 1321-36.
3. E. L. Hall and S.-C. Huang, Microstructure/Property Relationships in Titanium Aluminides and Alloys, 1990 TMS Conf. Proceedings, Detroit, MI, ed. Y.-W. Kim and R. R. Boyer, Warrendale, PA, The Materials Society, 1991, 47-64.
4. Y.-W. Kim, *JOM*, July, 1989, 24-30.
5. S. L. Kampe, P. Sadler, D. E. Larsen and L. Christodoulou, Microstructure/Property Relationships in Titanium Aluminides and Alloys, 1990 TMS Conf. Proceedings, Detroit, MI, ed. Y.-W. Kim and R. R. Boyer, Warrendale, PA, The Materials Society, 1991, 313-22.
6. S.-C. Huang and D. S. Shih, Microstructure/Property Relationships in Titanium Aluminides and Alloys, 1990 TMS Conf. Proceedings, Detroit, MI, ed. Y.-W. Kim and R. R. Boyer, Warrendale, PA, The Materials Society, 1991, 105-22.
7. S.-C. Huang, E. L. Hall and D. S. Shih, *ISIJ*, **31**, No. 10, 1991, 1100-5.
8. S.-C. Huang and E. L. Hall, *Acta Met.*, **39**, 1991, 1053-60.
9. S.-C. Huang, D. W. McKee, D. S. Shih and J. C. Chesnutt, Intermetallic Compounds, Structure and Mechanical Properties (JIMIS-6), Proc. of International Symposium, ed. O. Izumi, The Japan Institute of Metals, Sendai, Japan, 1991, 363-70.
10. H. Anada and Y. Shida, Intermetallic Compounds, Structure and Mechanical Properties (JIMIS-6), Proc. of International Symposium, ed. O. Izumi, The Japan Institute of Metals, Sendai, Japan, 1991, 731-5.
11. S.-C. Huang and E. L. Hall, High-Temperature Ordered Intermetallic Alloys IV, Vol. 213, ed. L. A. Johnson, D. P. Pope, and J. O. Stiegler, Pittsburgh, PA, Materials Research Society, 1991, 827-32.
12. A. W. Thompson and W.-Y. Chu, Microstructure/Property Relationships in Titanium Aluminides and Alloys, 1990 TMS Conf. Proceedings, Detroit, MI, ed. Y.-W. Kim and R. R. Boyer, Warrendale, PA, The Materials Society, 1991, 165-177.
13. F. H. Froes, C. Suryanarayana and D. Eliezer, *ISIJ International*, **31**, No. 10, 1991, 1235-48.
14. Y.-W. Kim, High-Temperature Ordered Intermetallic Alloys IV, Vol. 213, ed. L. A. Johnson, D. P. Pope, and J. O. Stiegler, Pittsburgh, PA, Materials Research Society, 1991, 777-94.

15. S. Krishnamurthy and Y.-W. Kim, Microstructure/Property Relationships in Titanium Aluminides and Alloys, 1990 TMS Conf. Proceedings, Detroit, MI, ed. Y.-W. Kim and R. R. Boyer, Warrendale, PA, The Materials Society, 1991, 149-63.
16. S. L. Kampe, J. A. Clarke and L. Christodoulou, Materials Research Society Symposium Proceedings, Vol. 194, Materials Research Society, 1990, 225-32.
17. S. L. Kampe, J. D. Bryant, and L. Christodoulou, *Met Trans*, **22A**, p. 447-54.
18. S. L. Kampe, M. A. VanMeter, A. H. Barrett, and L. Christodoulou, "XD® Titanium-Aluminide Composite Aero-Control Surfaces for Tactical Missile Applications," Final Report to General Dynamics, MML TR # 91-48C.
19. S. L. Kampe, P. Sadler, and L. Christodoulou, Martin Marietta/Howmet Joint Research Program, MML TR # 90-31(c).
20. P. Sadler, A. R. H. Barrett, and S. L. Kampe, Final Report to Rolls Royce, Inc., MML TR # 91-53C.
21. D. E. Larsen, M. L. Adams, S. L. Kampe, L. Christodoulou, and J. D. Bryant, "Influence of Matrix Phase Morphology on Fracture Toughness in a Discontinuously Reinforced XD® Titanium Aluminide Composite," *Scripta Metall.*, **24** (1990), 851-6.
22. ASTM Designation E 1304-89, "Standard Test Method for Plane-Strain (Chevron-Notch) Fracture Toughness of Metallic Materials", 1992 Annual Book of ASTM Standards, Vol. 03.01.
23. D. M. Dimiduk, D. B. Miracle, Y.-W. Kim, and M. G. Mendiratta, *ISIJ International*, **31**, No. 10, 1991, p. 1223-34.

APPENDIX A--WILLIAMS INTERNATIONAL DESIGN ANALYSIS

This appendix incorporates the details of the design analysis performed at Williams. A general overview was given in Chapter IV. TECHNICAL ACCOMPLISHMENTS, of this report. Topics were separated according to the designated work tasks as shown:

- Material selection
- Heat transfer analysis
- Elastic stress analysis
- Critical flaw size prediction
- Dynamic analysis
- Rotor attachment and blade tip growth analyses

Further questions on the analyses and attached figures should be directed to either Pam Sadler at Martin Marietta or Tim Nielsen at Williams.

#### 1. Material selection

Williams was sent material property data provided by Martin Marietta for the various XD<sup>®</sup> titanium aluminide matrix compositions listed below. All alloys contained 7 volume % TiB<sub>2</sub>:

Ti-48Al-2V	Ti-48Al-2Mn-2V	Ti-47Al-2Mn-2V-2Cr
Ti-47Al-2Mn-2Cr	Ti-47Al-2Mn-1Nb-1Cr	Ti-47Al-2Mn-1V-1Nb

The mechanical property data for the above compositions used in the materials evaluation process are shown in Table 1-1. A thorough review was made based on the structural requirements necessary for the component. The alloy chosen by the design engineers at Williams was Ti-47Al-2Mn-2V + 7 volume % TiB<sub>2</sub>. Processing experience of this alloy composition in other programs at Martin Marietta made it an excellent candidate for this application.

The Ti-47Al-2Mn-2V + 7 volume % TiB<sub>2</sub> alloy displayed the best combination of strength and ductility at room temperature, with 697 to 731 MPa (101 to 106 ksi) ultimate tensile strength, 572 to 593 MPa (83 to 86 ksi) yield strength, and elongation consistently greater than 0.8%. The low fracture toughness values, 12.65 to 15.95 MPa√m (11.5 to 14.5 ksi√in), will probably necessitate nondestructive inspection of the forgings (ultrasonic) and machined rotors (florescent penetrant) to very small critical flaw sizes.

Table 1-1. Room-temperature mechanical properties for Ti-48Al-2Mn-2V + 7 volume % TiB<sub>2</sub> alloys in the cast, HIPed, and forged condition.

Conditions	Yield Strength (MPa)	Fracture Strength (MPa)	Elongation (% strain)	Fracture Toughness (MPa√m)
As - forged	587	697	0.95	--
Forged + H.T.*:				
900°C / 16 h	566	704	0.85	16.1
900°C / 50 h	576	731	1.10	--
1100°C / 16 h	600	725	0.82	12.8

\* H.T. = heat treated

## 2. Heat transfer analysis

The heat transfer analysis was performed to determine the maximum metal temperature that a mixed flow compressor rotor made from XD<sup>®</sup> titanium aluminide will experience during a hot gas start cycle (cartridge start) and the steady state operating temperature for the sea level, 0.8-mach number, standard day operating condition. These two analyses were performed using the previously developed 2D/3D model from the stainless steel analysis. However, it was necessary to modify the fluid network contained in the stainless steel design in order to more accurately simulate the fluid flow characteristics along the compressor backface. This section comprises a discussion on the thermal analysis performed from engine start through steady state operation, followed by the conclusions from the analysis.

The experimental P9005 gas turbine engine is started by impinging hot gases on the blades of the mixed flow compressor at the exducer. The start sequence extends over a period of 8 s, the characteristics of which are as follows:

- Start sequence is initiated and the engine accelerates from 0 - 70,000 rpm in 2 s. The start gas mass flow rate and the start nozzle upstream pressure are held constant at 90.72 g/s and 10.34 MPa (0.2 lb<sub>m</sub>/s and 1.500 ksia), respectively.
- The mixed flow compressor continues to be impinged upon by the start jets for an additional 6 s, maintaining an engine speed of 70,000 rpm. The start gas mass flow is reduced to 64.41 g/s (0.142 lb<sub>m</sub>/s) at a nozzle upstream pressure of 7.34 MPa (1.065 ksia) and is held constant for this portion of the start sequence. This portion of the start sequence is necessary to allow the hot start gases to heat the catalytic combustor to the required operating temperature.

There are eight hot gas start nozzles, which are equally spaced and positioned at a radius of 1.80 in. Figure 2-30 shows the start nozzle geometry used in this analysis. The start gas temperature is 1093°C (2000°F) throughout the start sequence.

Calculations revealed that the start nozzle design is incapable of permitting full expansion of the start gases, which results in a series of oblique downstream shocks along with a corresponding series of expansion and contractions of the start jet (see Figure 2-30). The implication of this is that the blade surface area contacted by the start jet will not be equivalent to the area of the start nozzle exit, but rather some larger area. The

procedure for calculating the diameter of a jet, which is experiencing expansion and contractions due to oblique shocks, is extremely complex and beyond the scope of this analysis. However, the literature does indicate that a very rough approximation of the jet diameter is twice the nozzle exit diameter. For this analysis, the jet diameter impinging on the blade is estimated to be 0.35 cm (0.138 in).

Since the start gases are under-expanded throughout the start sequence, the start jet velocity remains constant. The start jet velocity was calculated to be 1,172 m/s (3,845 ft/s).

Two things occur during the start sequence that have a major impact on the resulting compressor temperature. First, as the engine accelerates to 70,000 rpm during the first two s, the heat transfer coefficient decreases due to a drop in the relative velocity between the start jet and the compressor blade. Secondly, there is a decrease in the start jet relative temperature, again due to the decrease in relative velocity of the start jet. Table 2-1 specifies the relative temperature and heat transfer coefficients at times equal to 0, 2, and 8 s of the start cycle.

Simulation of the start jet impinging on the compressor blade using the ANSYS finite element code necessitated modifying the heat transfer coefficients given in Table 2-1. The reason is that during the engine start sequence, the start jet initially comes in contact with a given blade approximately 1.17 cm (0.46 in) upstream of the exducer, measured along the blade surface. The impingement point of the jet then traverses the surface of the blade, traveling from the initial point of contact toward the exducer as the blade rotates away from the start nozzle. Once the impingement point of the start jet reaches the exducer, the compressor rotor has rotated far enough that the jet now comes in contact with the next blade. Because there are eight start nozzles in the engine, this occurs eight times per revolution per blade. The impact this has on blade temperature is that the blade experiences a series of heating and cooling cycles. Figure 2-31 represents the "saw tooth" temperature curve, which results at any given point on a blade due to the heating and cooling that the blade experiences during an engine start cycle.

Difficulty is encountered when attempting to simulate the start cycle exactly since one load step is required for each occurrence of a start jet coming in contact with a given blade (i.e., 65,333 load steps would be required to model the complete 8 s start cycle). To overcome this, the heat transfer coefficient was systematically reduced, thereby allowing the start cycle to be simulated using only three load steps. The procedure for

determining the "modified" heat transfer coefficient begins by recognizing that the total heat flux into the compressor rotor over the 8 s start cycle must remain consistent regardless of the modeling technique used. This would seem to imply that the start cycle could also be simulated by reducing the time of the start cycle rather than reducing the heat transfer coefficient, but since the amount of heat that can be conducted to cooler areas of the blade and rotor is time dependent, decreasing the total start time would result in a maximum blade temperature, which is unrealistically high. This necessitates that the heat transfer coefficient be modified in two ways:

1. Adjusting the heat transfer coefficient to account for any given blade being in contact with a start jet only a portion of the time:

number of total blades = 20

number of start jets = 8

Assuming one start jet, a given blade is in contact with the one start jet:

$(100\%)/(20 \text{ blades}) = 5\% \text{ of the time.}$

With 8 start nozzles, the total time a given blade is in contact with any start jet increases to  $(8 \text{ start nozzles}) \times (5\%) = 40\% \text{ of the time.}$

2. When the start jet comes in contact with a given blade, the area of contact is only a portion of the total blade area that is contacted by the jet as it sweeps across the blade. The ANSYS model requires that the heat transfer coefficient be applied over the entire area of blade that comes into contact with the start jet, rather than an area equivalent to the start jet cross sectional area. The heat transfer coefficient was adjusted to account for the increased contact area in the ANSYS model relative to the actual contact area. The jet cross sectional area was calculated to be approximately one-third of the total blade area contacted. The heat transfer coefficient was therefore reduced to 33%.

Combining the above two factors results in ANSYS heat transfer coefficient of:

$$H(\text{ansys}) = H(\text{actual}) \times (40/100) \times (33/100) = H(\text{actual})(0.132)$$

Simulating the start cycle as described above has an averaging effect on the compressor metal temperature, thus eliminating the "saw tooth" characteristic of the curve shown in Figure 2-31. This "averaged" ANSYS-calculated temperature is compared to the actual temperature in Figure 2-31.

The results and conclusions from the above analysis are depicted in the tables and figures indicated as follows. Physical property data used for the calculation of these



analyses was supplied by Martin Marietta. Plots of temperature vs. specific heat, thermal diffusivity and thermal conductivity are shown in various forms in Figures 2-32 through 2-35.

Steady state temperature plots for the XD<sup>®</sup> titanium aluminide compressor are shown in Figures 2-1 through 2-3, and can be compared to the steady state temperature plots for the steel compressor shown in Figures 2-4 through 2-6. Table 2-2 lists the performance parameters of the engine and the XD<sup>®</sup> titanium aluminide compressor rotor for the sea level, 0.8 mach number, standard day operating condition.

The transient temperature plots for the hot gas start are shown in Figures 2-7 through 2-10. The transient temperature plots represent the metal "averaged" temperature. The locations of the nodes for which temperatures were plotted in Figures 2-7 through 2-10 are shown in Figure 2-11. The maximum compressor metal temperature occurs at a time of 0.916 s. The compressor temperature distribution in the blade, splitter and disk for time equal to 0.916 s is shown in Figures 2-12 through 2-14. The isotherm plots in Figures 2-15 through 2-17 show the compressor temperature distribution in the blade, splitter and disk at the end of the start cycle (time equal to 8 s).

The model was also run without adjusting the heat transfer coefficient to account for the difference in areas between the start jet cross sectional area and the total contacted blade area. The transient temperature plots shown in Figures 2-18 through 2-21 represent an estimate of the maximum metal temperature the compressor will experience during the hot gas start cycle. The maximum metal temperature occurs at a time of 0.524 s. Figures 2-22 through 2-24 show the temperature distribution in the blade, splitter and disk at the time the maximum metal temperature is achieved. The locations of the nodes for which temperatures were plotted in Figures 2-18 through 2-24 are shown in Figure 2-11. The isotherm plots in Figures 2-25 through 2-27 show the compressor temperature distribution in the blade, splitter and disk at the end of the start cycle (time = 8 s).

The modified compressor backface fluid network is shown in Figures 2-28 and 2-29.

Steady state temperature distributions of both compressor materials were similar, with a maximum exducer temperature of approximately 216°C (420°F). The start transient results indicate a potential temperature range near the tip, for a short period, of 677°C to 927°C (1250°F to 1700°F), due to assumptions made in the analysis.

```

ANSYS      4.4A
APR 14 1992
15:16:15
PLOT NO 1
POST1 STRESS
STEP=1
ITER=30
TEMP
SMX -699.298

```

ZV	= 1
*DIST	= 1.40/
*XF	= 0.73/834
*YF	= -1.08
*ZF	= 0.080084
ANC2	= 0
PRECISE HIDEIN	
A	= 150
B	= 170
C	= 190
D	= 210
E	= 230
F	= 250
G	= 270
H	= 290
I	= 310
J	= 330
K	= 350
L	= 370
M	= 390
N	= 410
O	= 430
P	= 450
Q	= 470
R	= 490
S	= 510
T	= 530

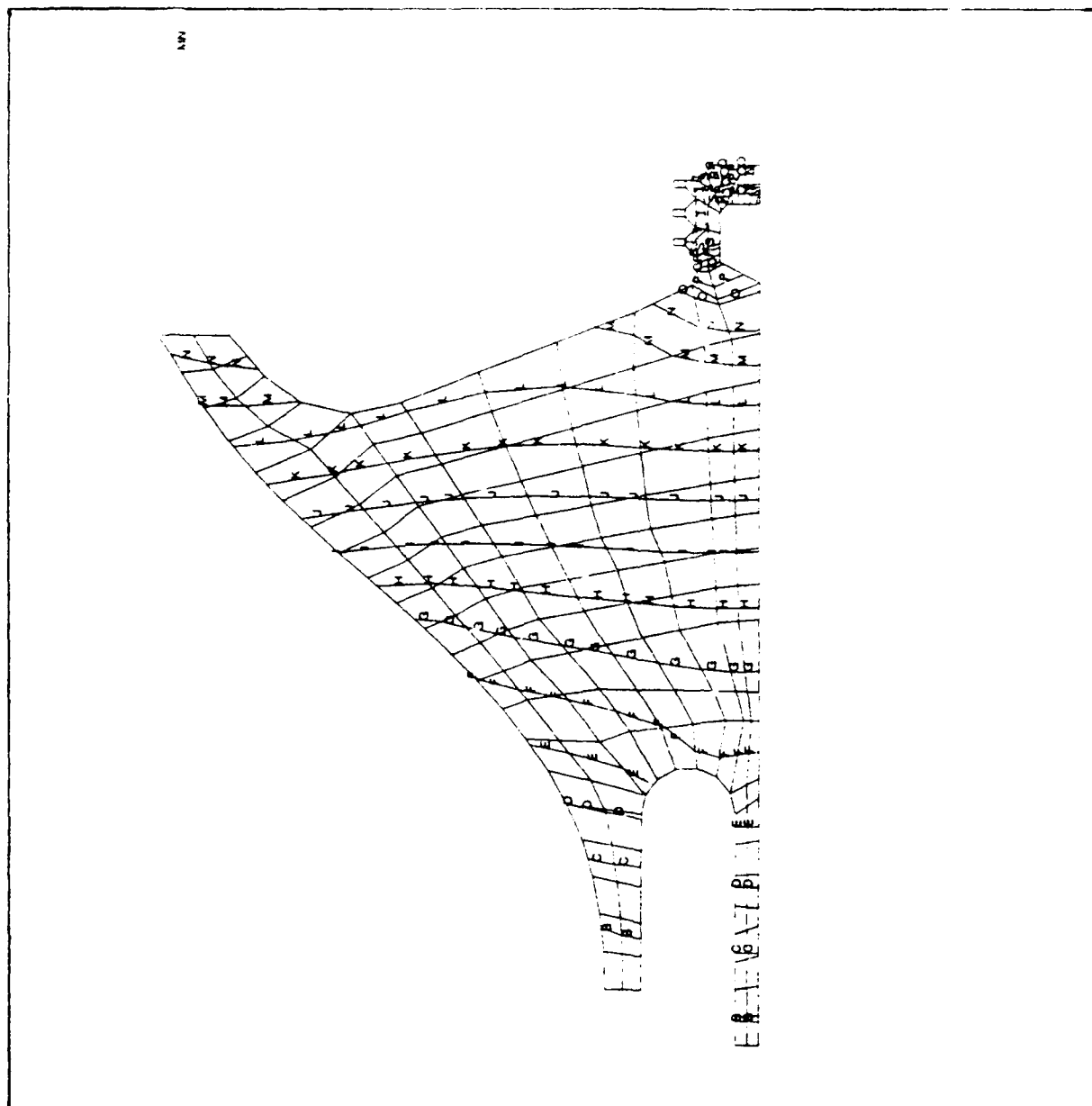


Figure 2-1. Steady state temperatures (in °F) for the compressor disk for SL40.8/Sld day operating condition for  $\lambda D^{0.6}$  titanium aluminides.

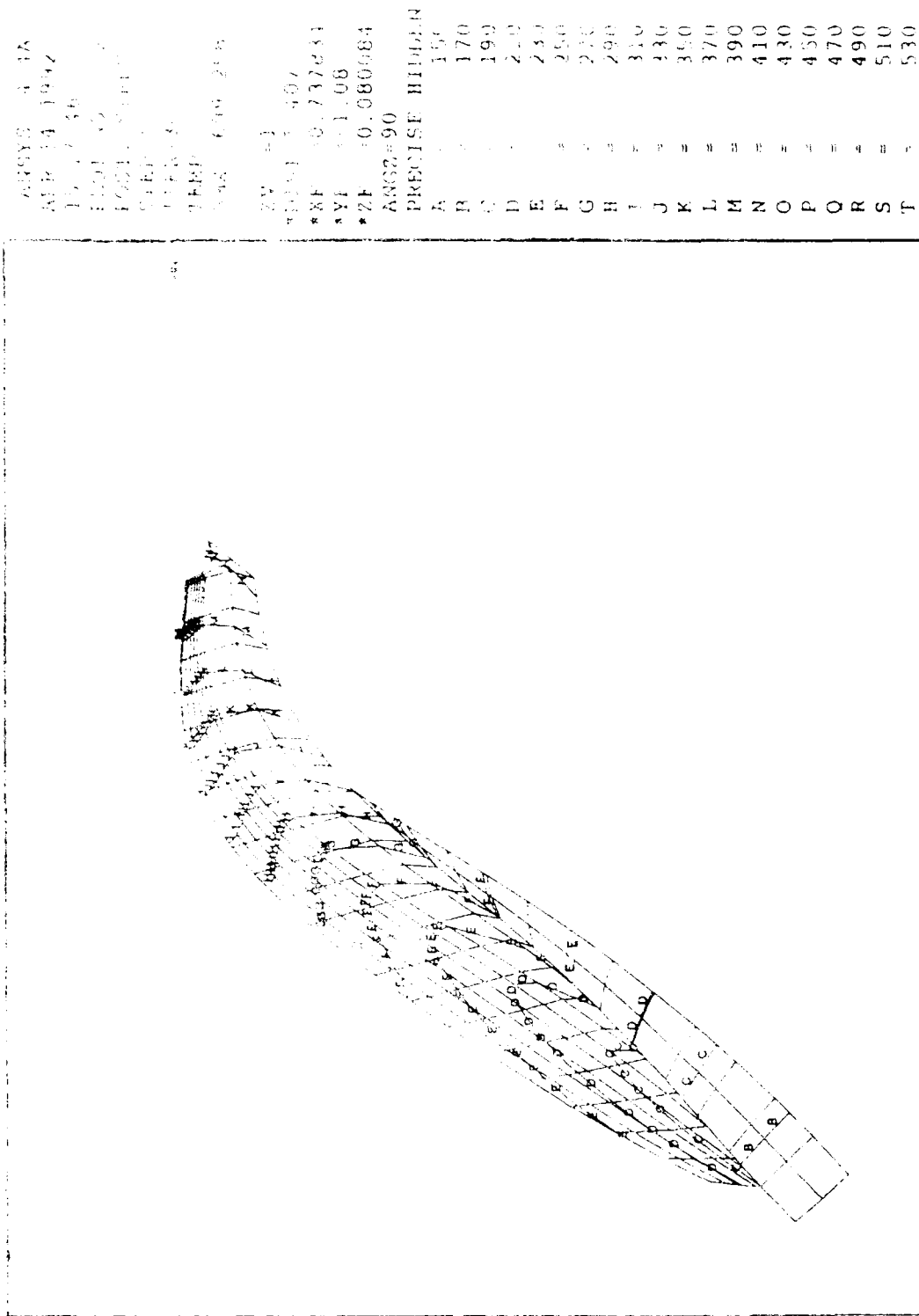


Figure 2-2. Steady state temperatures (in °F) for the compressor blade for SL/0.8/Std day operating condition for XD% titanium aluminides.

ANSYS 4.4A  
 APR 14 1992  
 15:18:49  
 PLOT NO. 3  
 POST1 STRESS  
 STEP=1  
 ITER=30  
 TEMP  
 SMX =699.298

ZV =1  
 \*DIST=0.614399  
 \*XF =1.335  
 \*YF =-1.166  
 \*ZF =0.080084  
 ANGZ=90  
 PRECISE HIDDEN  
 A = 150  
 B = 170  
 C = 190  
 D = 210  
 E = 230  
 F = 250  
 G = 270  
 H = 290  
 I = 310  
 J = 330  
 K = 350  
 L = 370  
 M = 390  
 N = 410  
 O = 430  
 P = 450  
 Q = 470  
 R = 490  
 S = 510  
 T = 530

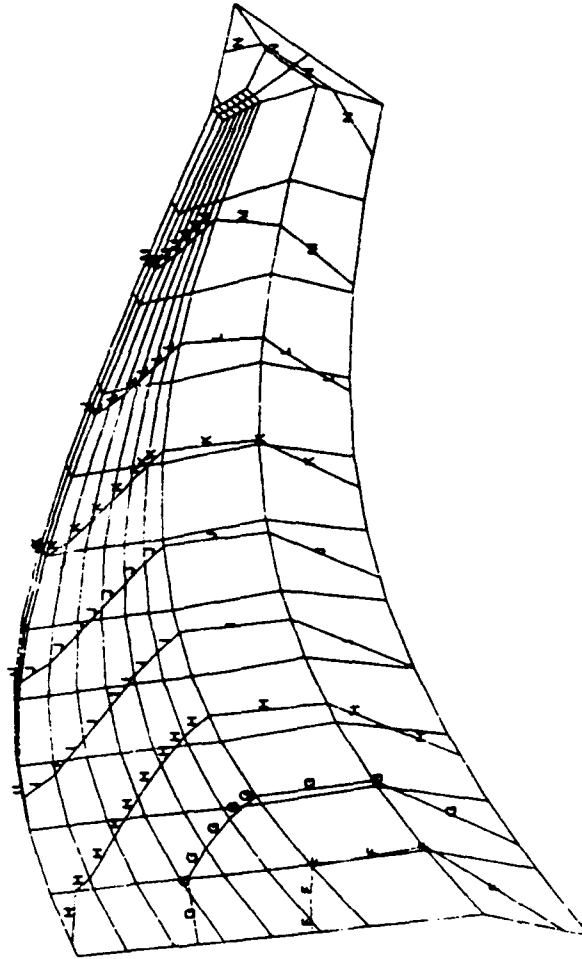


Figure 2-3. Steady state temperatures (in °F) for the compressor splitter for SL/0.8/Sid day operating condition for XD® titanium aluminides.

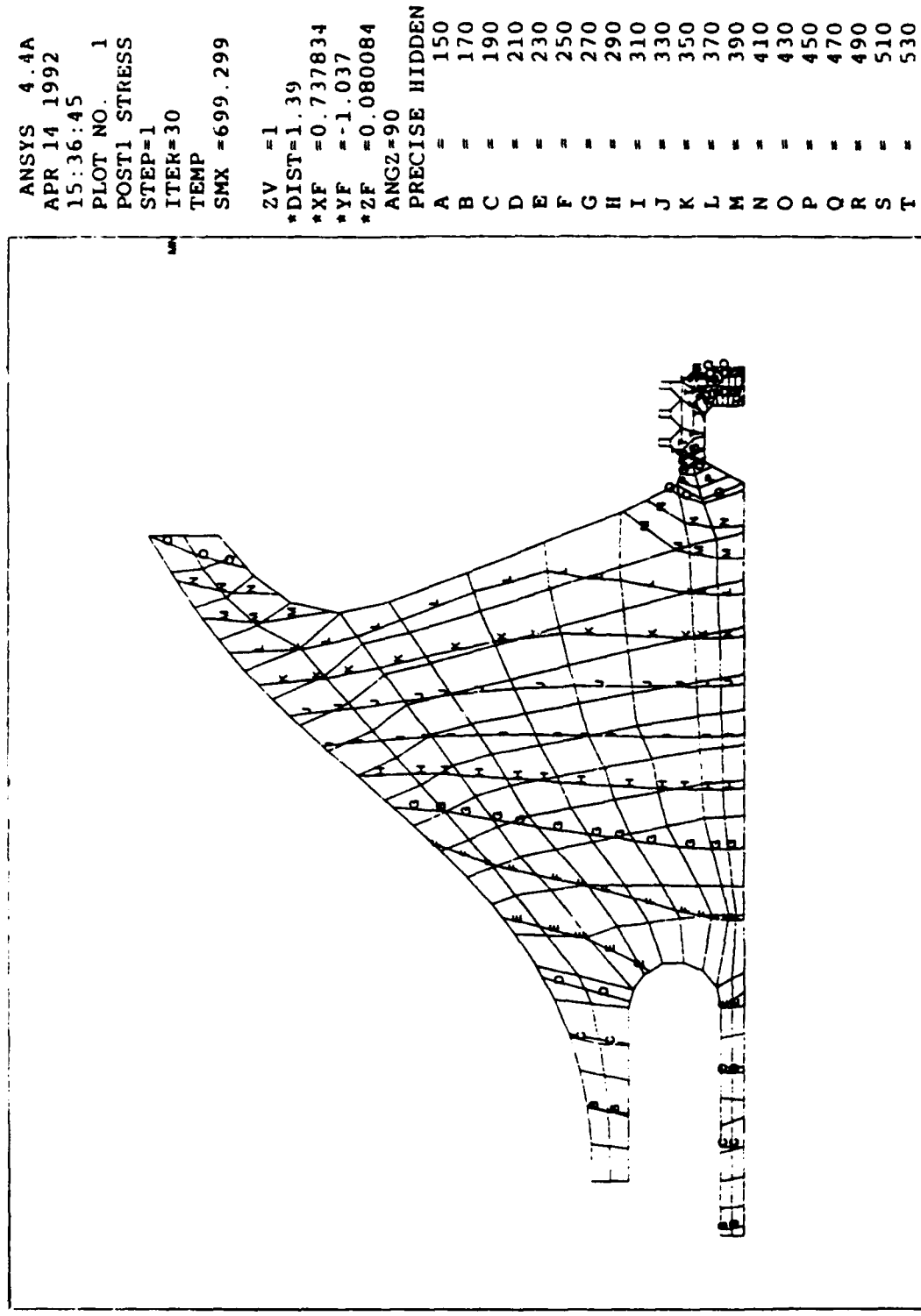


Figure 2-4. Steady state temperatures (in °F) for the compressor disk for SL0.8/Sld day operating condition for stainless steel.

```

ANSYS  4.4A
APR 14 1992
15:37:40
PLOT NO.  2
POST1  STRESS
STEP=1
ITER=30
TEMP
SMX  -699.299

ZV  =1
*DIST=1.259
*XF  -0.935679
*YF  =-0.670721
*ZF  =0.080084
ANGZ=90
PRECISE HIDDEN
A  = 150
B  = 170
C  = 190
D  = 210
E  = 230
F  = 250
G  = 270
H  = 290
I  = 310
J  = 330
K  = 350
L  = 370
M  = 390
N  = 410
O  = 430
P  = 450
Q  = 470
R  = 490
S  = 510
T  = 530

```

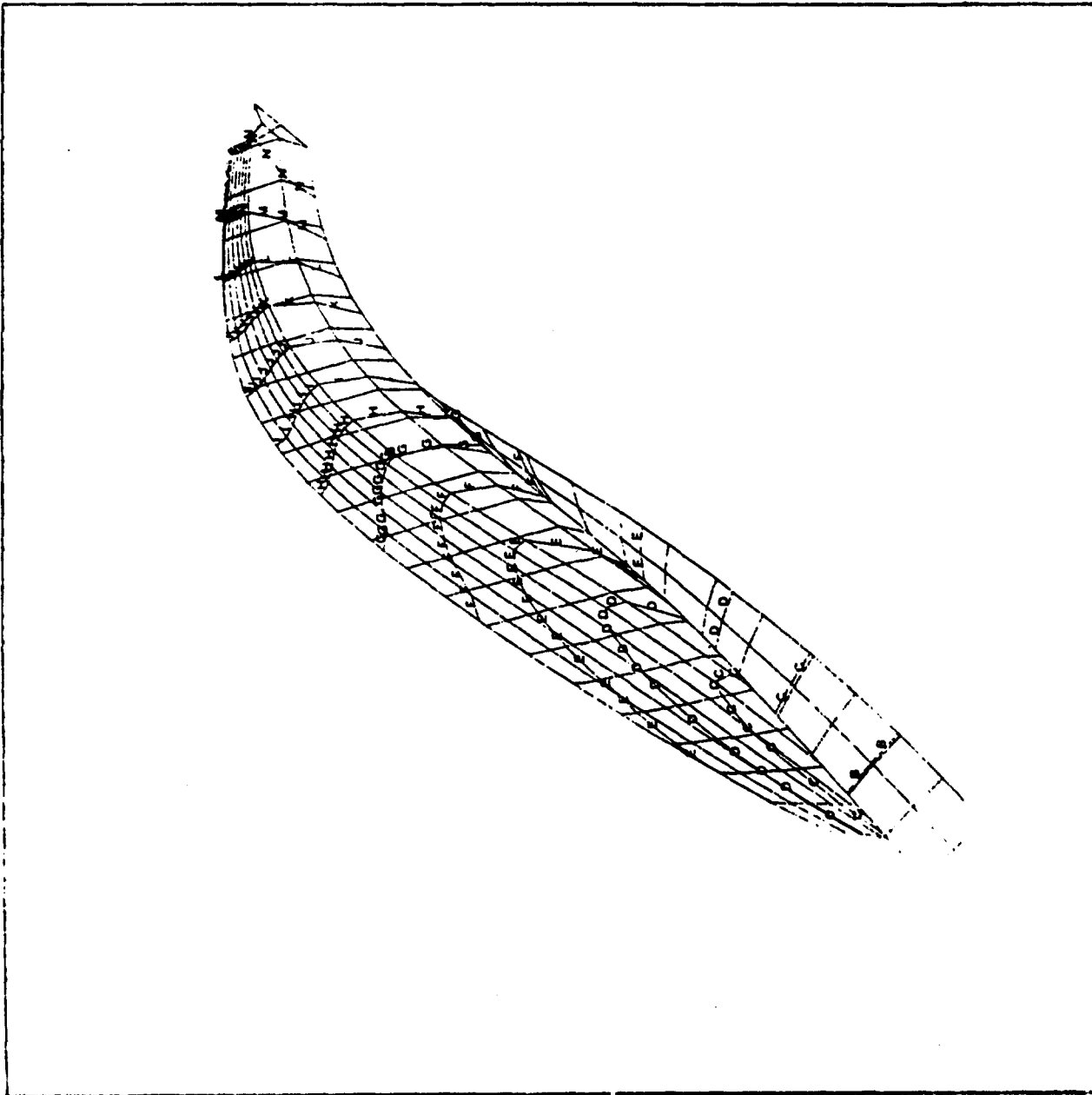


Figure 2-5. Steady state temperatures (in °F) for the compressor blade for SL/0.8/Sld day operating condition for stainless steel.

ANSYS 4.4A  
 APR 14 1992  
 15:48:51  
 PLOT NO. 4  
 POST1 SIRESS  
 STEP=1  
 ITER=30  
 TEMP  
 SMX -699.299

ZV = 1  
 \*DIST=0.609747  
 \*XF = 1.321  
 \*YF = -1.18  
 \*ZF = 0.080084  
 ANGZ=90  
 PRECISE HIDDEN  
 A = 150  
 B = 170  
 C = 190  
 D = 210  
 E = 230  
 F = 250  
 G = 270  
 H = 290  
 I = 310  
 J = 330  
 K = 350  
 L = 370  
 M = 390  
 N = 410  
 O = 430  
 P = 450  
 Q = 470  
 R = 490  
 S = 510  
 T = 530

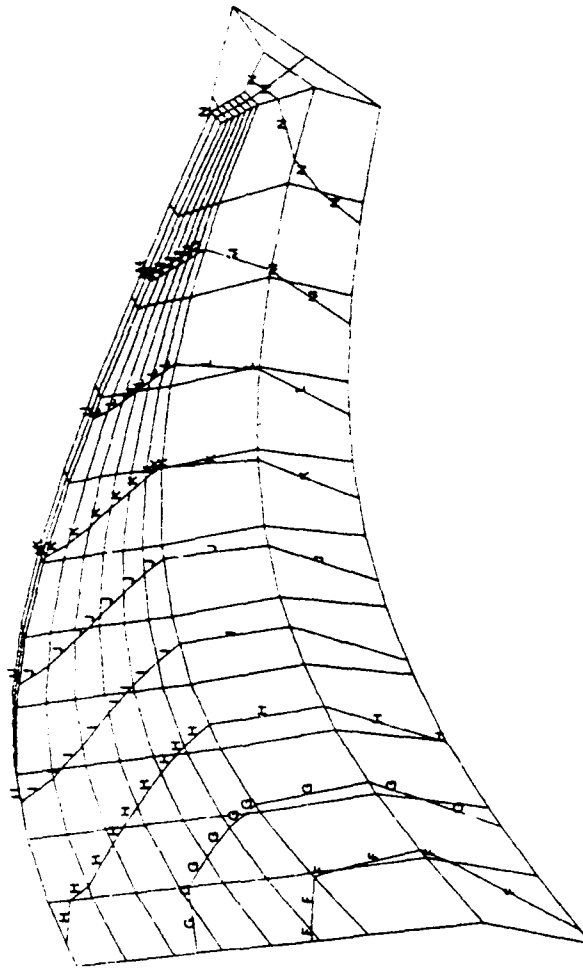


Figure 2-6. Steady state temperatures (in °F) for the compressor splitter for SL/0.8/Std day operating condition for stainless steel.

ANSYS 4.4A  
 APR 14 1992  
 16:13:57  
 PLOT NO. 1  
 POST26

2V = 1  
 DIST = 0.6666  
 XF = 0.5  
 YF = 0.5  
 ZF = 0.5

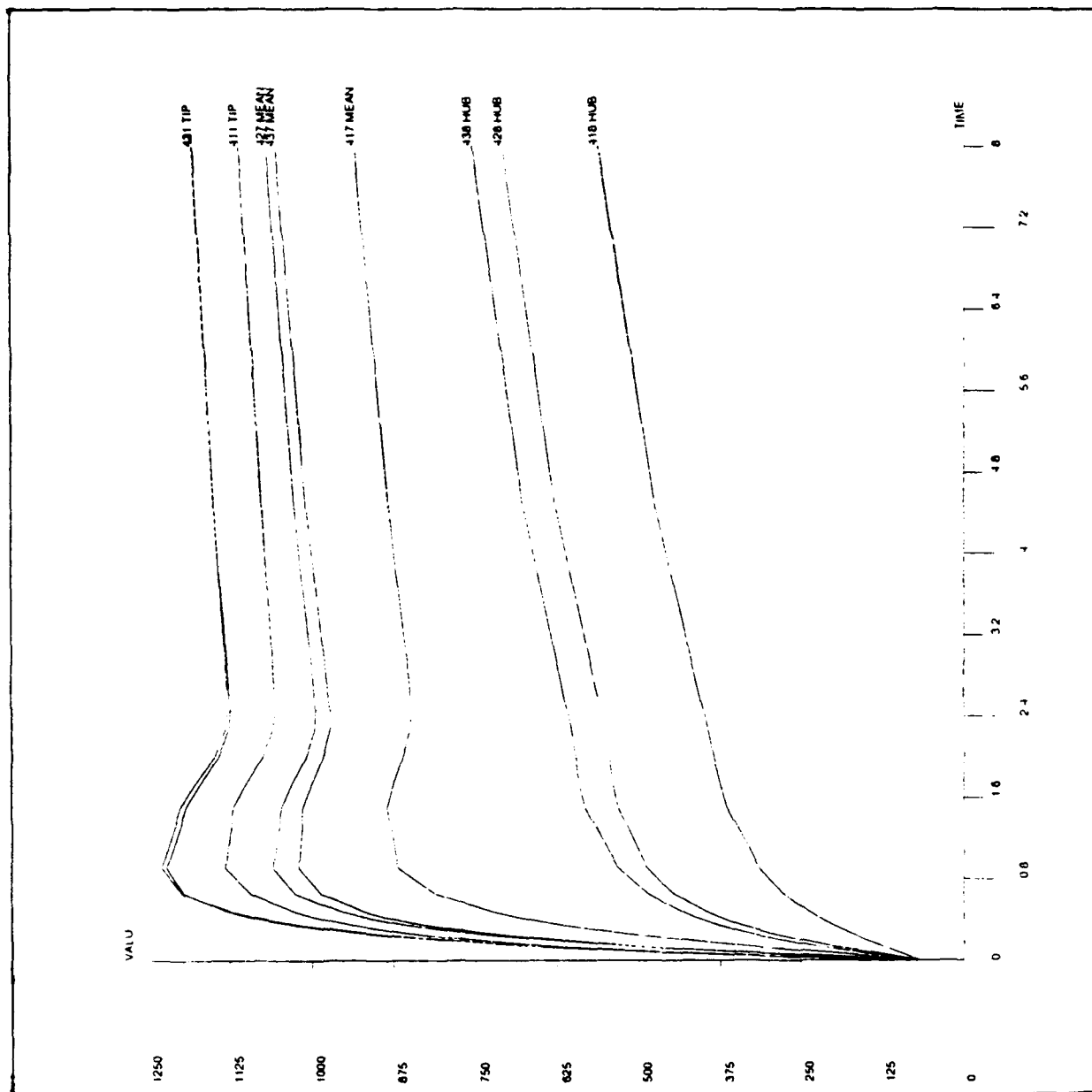


Figure 2-7. Blade temperatures (in °F) during hot gas start cycle for XD titanium aluminides.



ANSYS 4.4A  
APR 14 1992  
16:21  
PLOT NO. 2  
POST26

ZV = 1  
DIST=0.6666  
XF = 0.5  
YF = 0.5  
ZF = 0.5

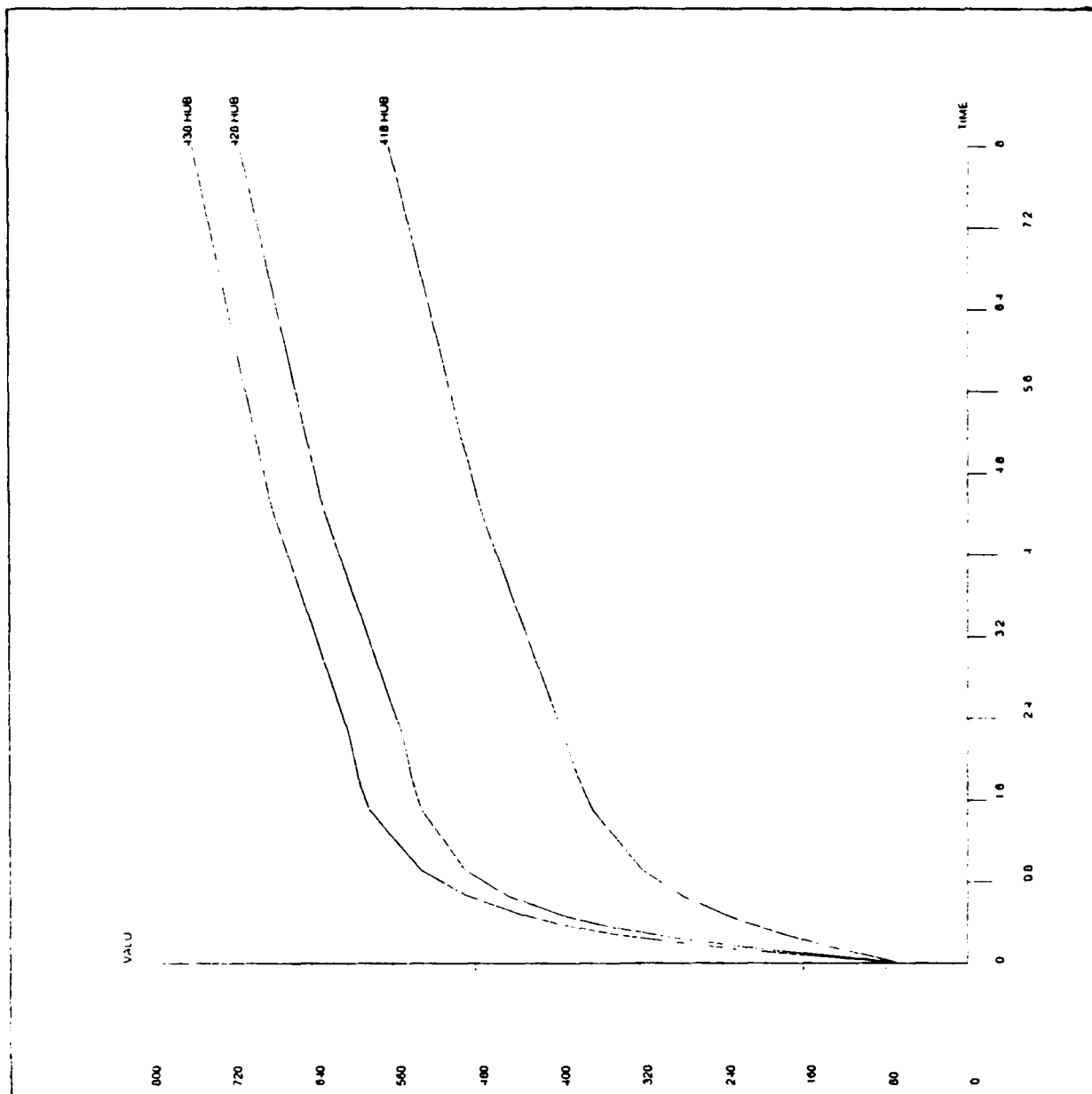


Figure 2-8. Blade hub temperatures (in °F) during hot gas start cycle for XD® titanium aluminides.

ANSYS 4.4A  
APR 14 1992  
16:21:38  
PLOT NO. 3  
POST26

ZV = 1  
DIST=0.6666  
XF = 0.5  
YF = 0.5  
ZF = 0.5

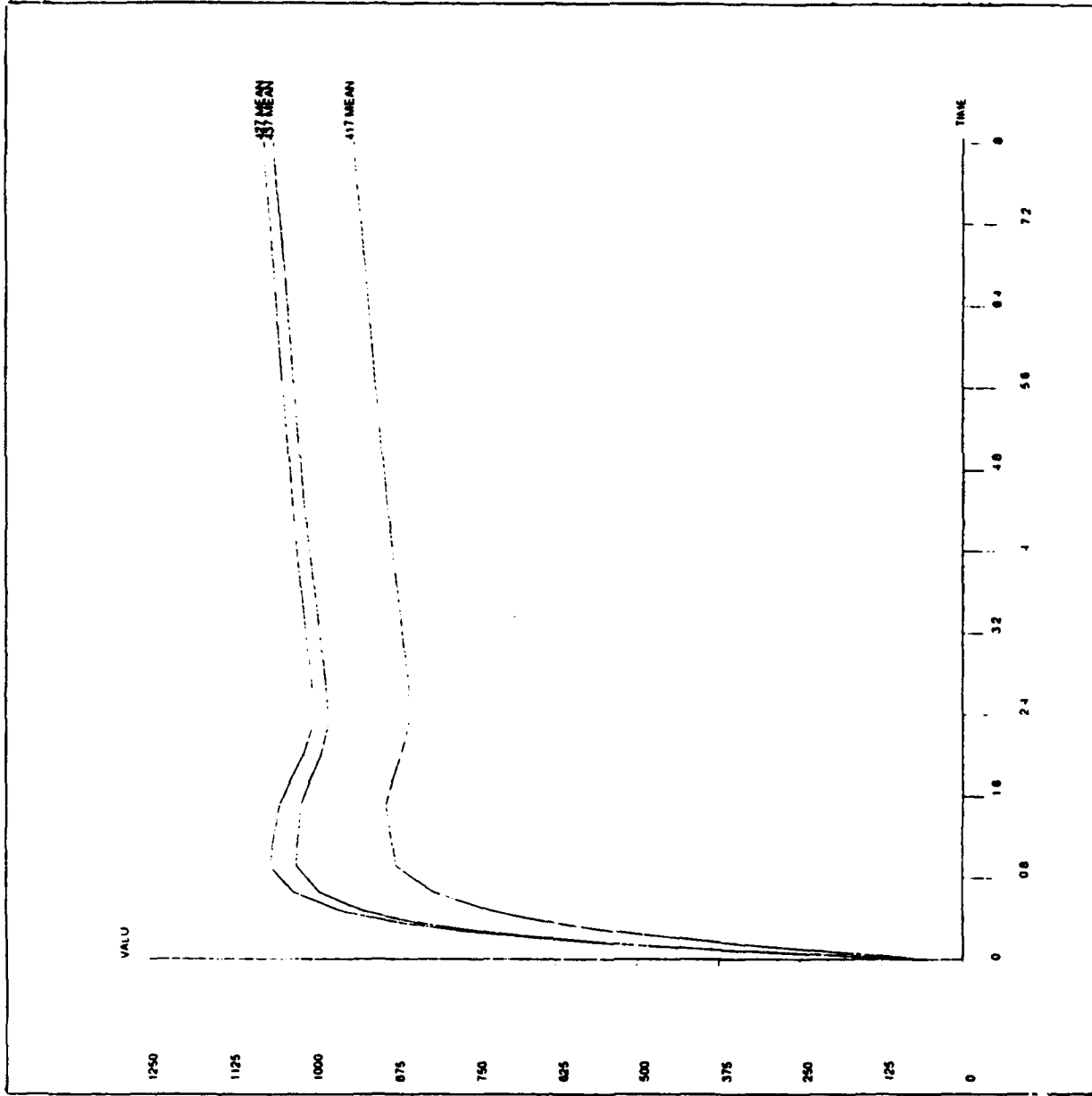


Figure 2-9. Blade mean temperatures (in °F) during hot gas start cycle for XD titanium aluminides.

ANSYS 4.4A  
APR 14 1992  
16:21:47  
PLOT NO. 4  
POST26

ZV = 1  
DIST=0.6666  
XF = 0.5  
YF = 0.5  
ZF = 0.5

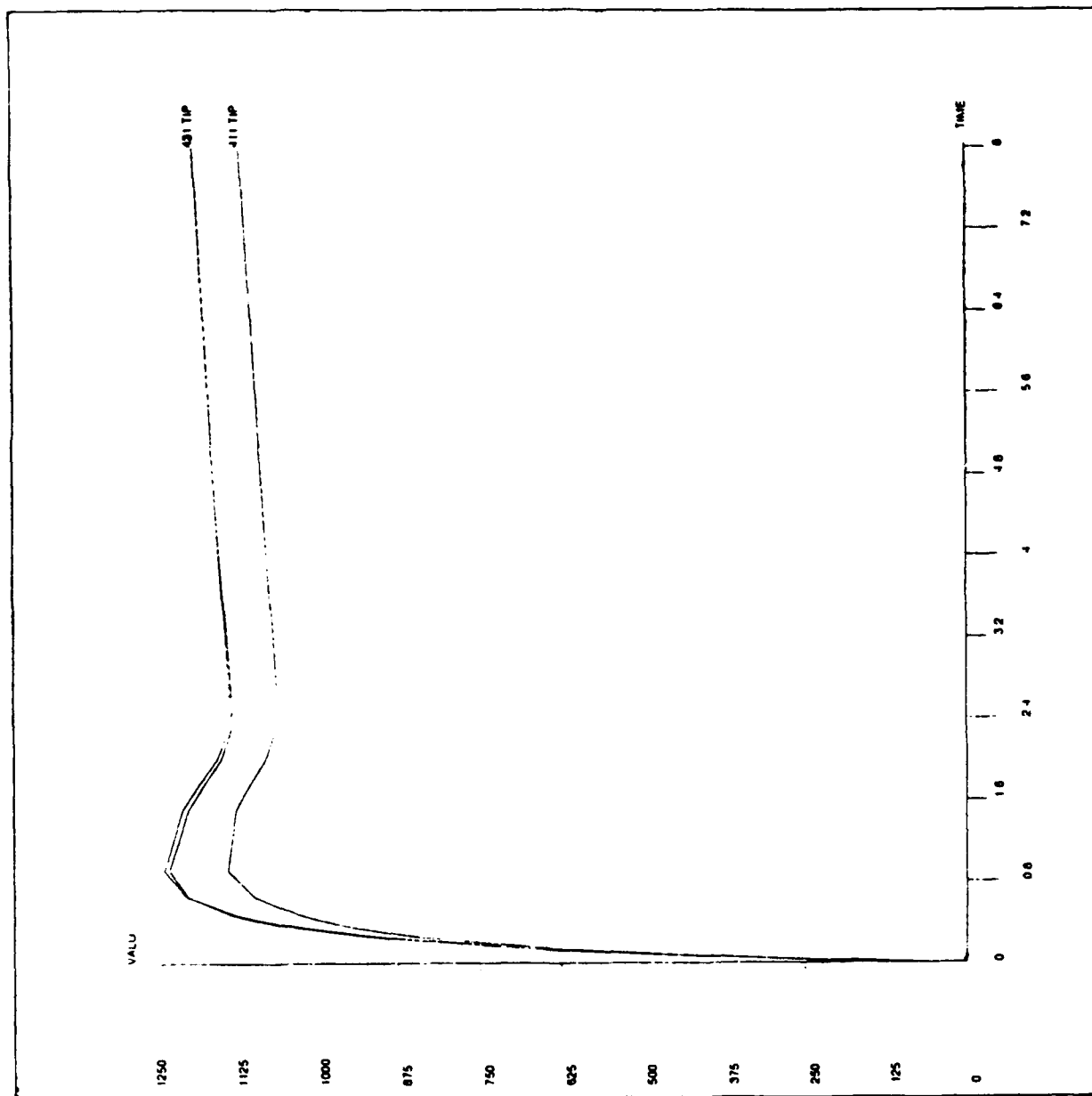


Figure 2-10. Blade tip temperatures (in °F) during hot gas start cycle for XD® titanium aluminides.

ANSYS 4.4A  
 APR 16 1992  
 9:51:05  
 PLOT NO. 1  
 PREP7 ELEMENTS  
 TYPE NUM

ZV =1  
 \*DIST=0.459799  
 \*XF =1.671  
 \*YF =-1.357  
 \*ZF =0.080084  
 ANGZ=90  
 PRECISE HIDDEN

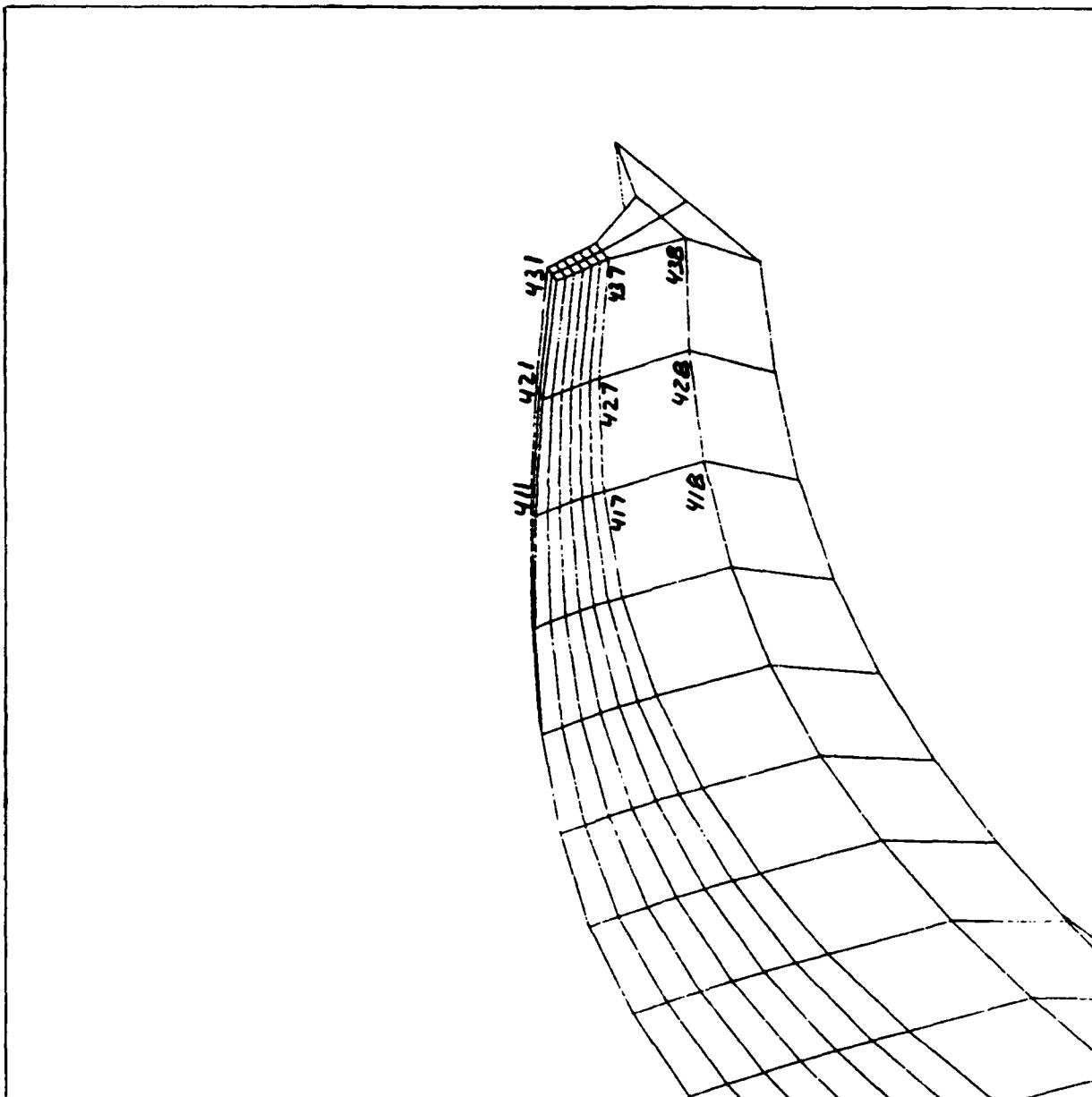


Figure 2-11. Locations of nodes for which temperatures (in °F) are plotted in Figures 7 through 10 and Figures 18 through 24.

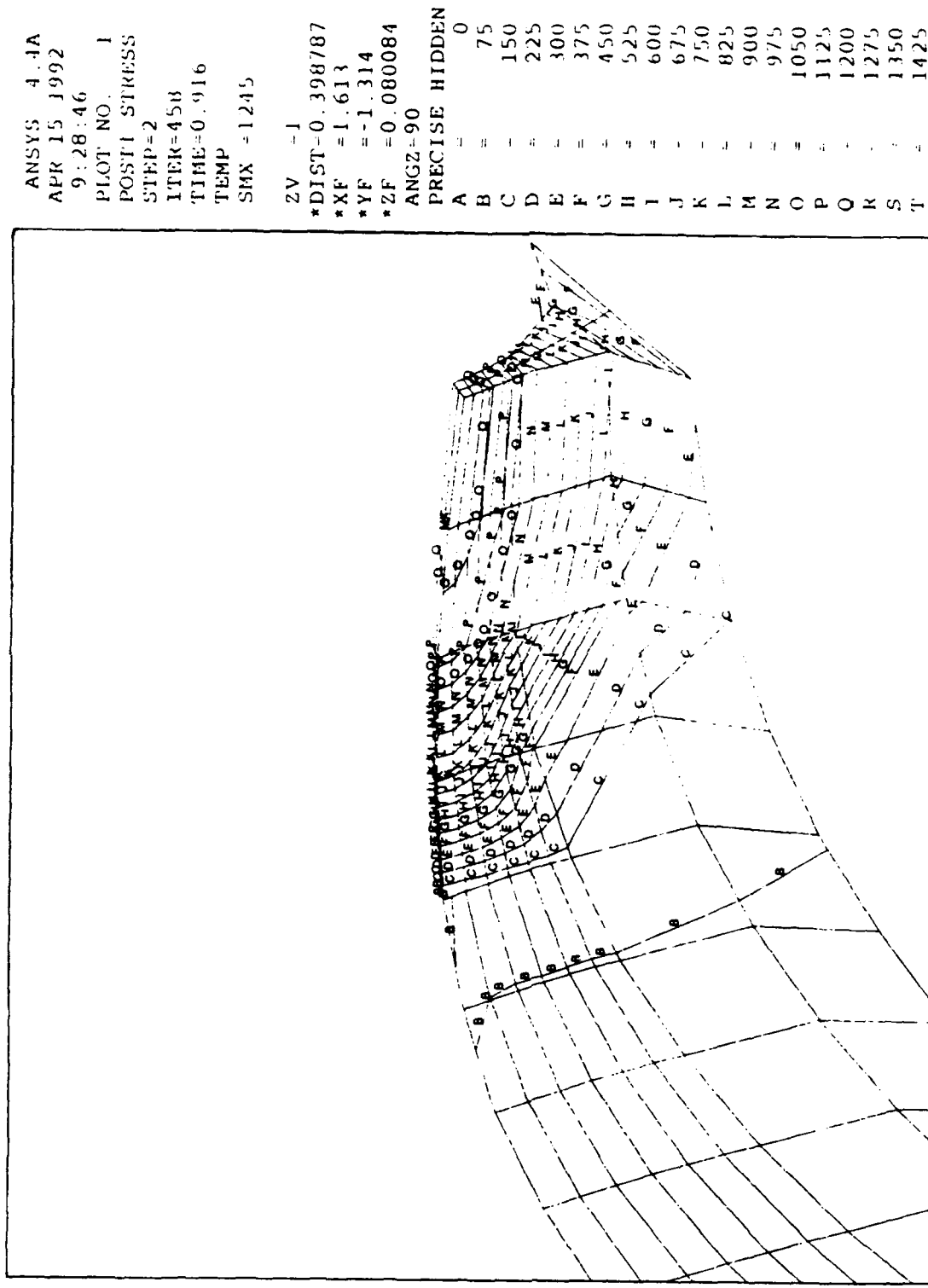


Figure 2-12. Blade temperature distribution (in °F) at time = 0.916 second of start cycle for XD® titanium aluminides.

ANSYS 4.4A  
 APR 15 1992  
 9:29:51  
 PLOT NO. 2  
 POST1 STRESS  
 STEP=2  
 ITER 458  
 TIME=0.916  
 TEMP  
 SHX -1215

SV 1  
 \*DIST 0.4718  
 \*XF 1.32/  
 \*YF -1.29/  
 \*ZF 0.080084  
 ANGLE=90  
 PRECISE HIDDEN  
 A - 0  
 B - 75  
 C - 150  
 D - 225  
 E - 300  
 F - 375  
 G - 450  
 H - 525  
 I - 600  
 J - 675  
 K - 750  
 L - 825  
 M - 900  
 N - 975  
 O - 1050  
 P - 1125  
 Q - 1200  
 R - 1275  
 S - 1350  
 T - 1425

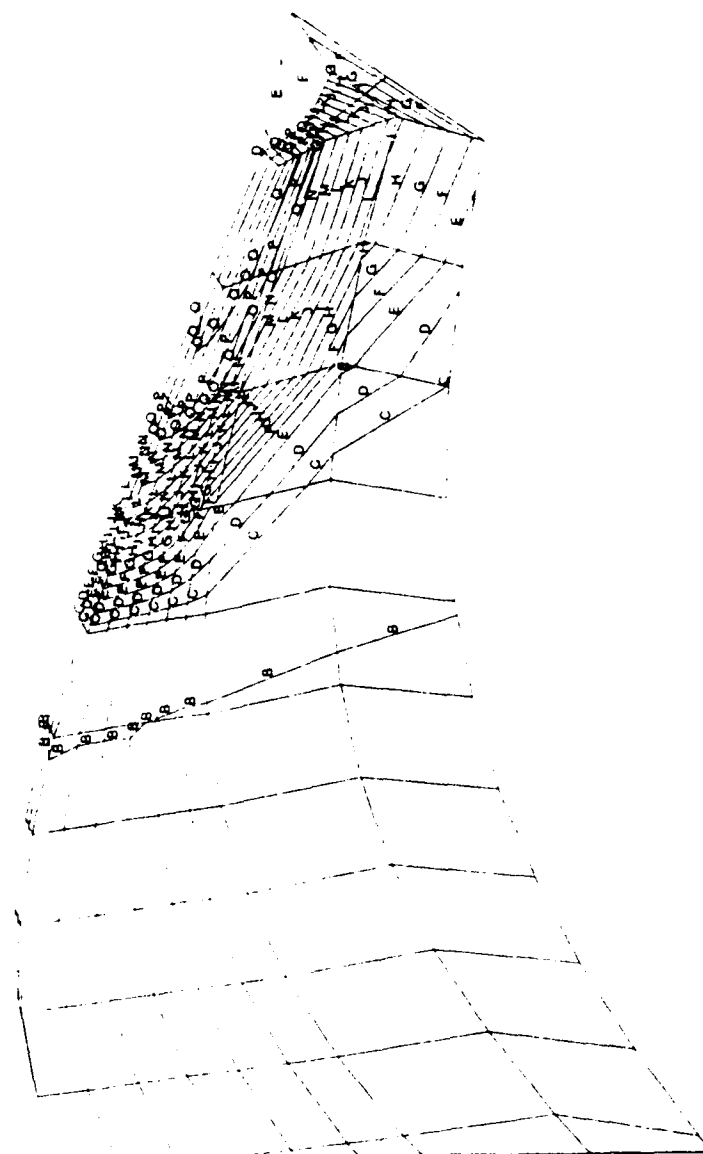


Figure 2-13. Splitter temperature distribution (in °F) at time = 0.916 second of start cycle for XD® titanium aluminides.

```

ANSYS  4.4A
APR 15 1992
9:30:48
PLOT NO. 3
POST1  STRESS
STEP=2
ITER=458
TIME=0.916
TEMP
SMX =1215

ZV =1
*DIST=0.4718
*XF =1.327
*YF =-1.297
*ZF =0.080084
ANGZ=90
PRECISE HIDDEN
A = 50
B = 70
C = 90
D = 110
E = 130
F = 150
G = 170
H = 190
I = 210
J = 230
K = 250
L = 270
M = 290
N = 310
O = 330
P = 350
Q = 370
R = 390
S = 410
T = 430

```

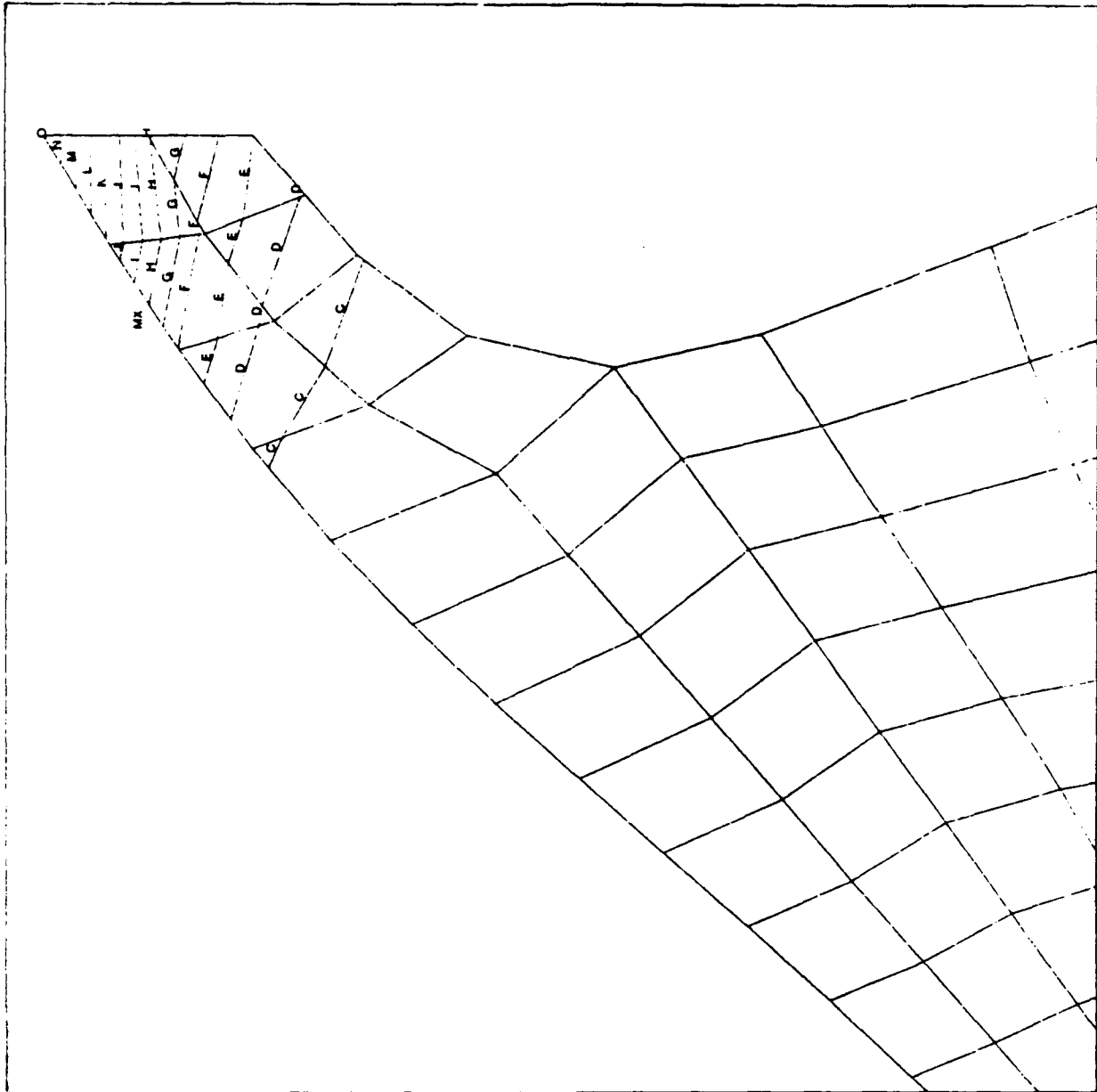


Figure 2-14. Disk temperature distribution (in °F) at time = 0.916 second of start cycle for XD® titanium aluminides.

ANSYS 4.4A  
 APR 15 1992  
 10:15:35  
 PLOT NO. 1  
 POST1 STRESS  
 STEP=3  
 ITER=1000  
 TIME=8  
 TEMP  
 SMX =1194

2V =1  
 \*DIST=0.601425  
 \*XF =1.5  
 \*YF =-1.227  
 \*ZF =0.080084  
 ANGZ=90  
 PRECISE HIDDEN  
 A = 0  
 B = 75  
 C = 150  
 D = 225  
 E = 300  
 F = 375  
 G = 450  
 H = 525  
 I = 600  
 J = 675  
 K = 750  
 L = 825  
 M = 900  
 N = 975  
 O = 1050  
 P = 1125  
 Q = 1200  
 R = 1275  
 S = 1350  
 T = 1425

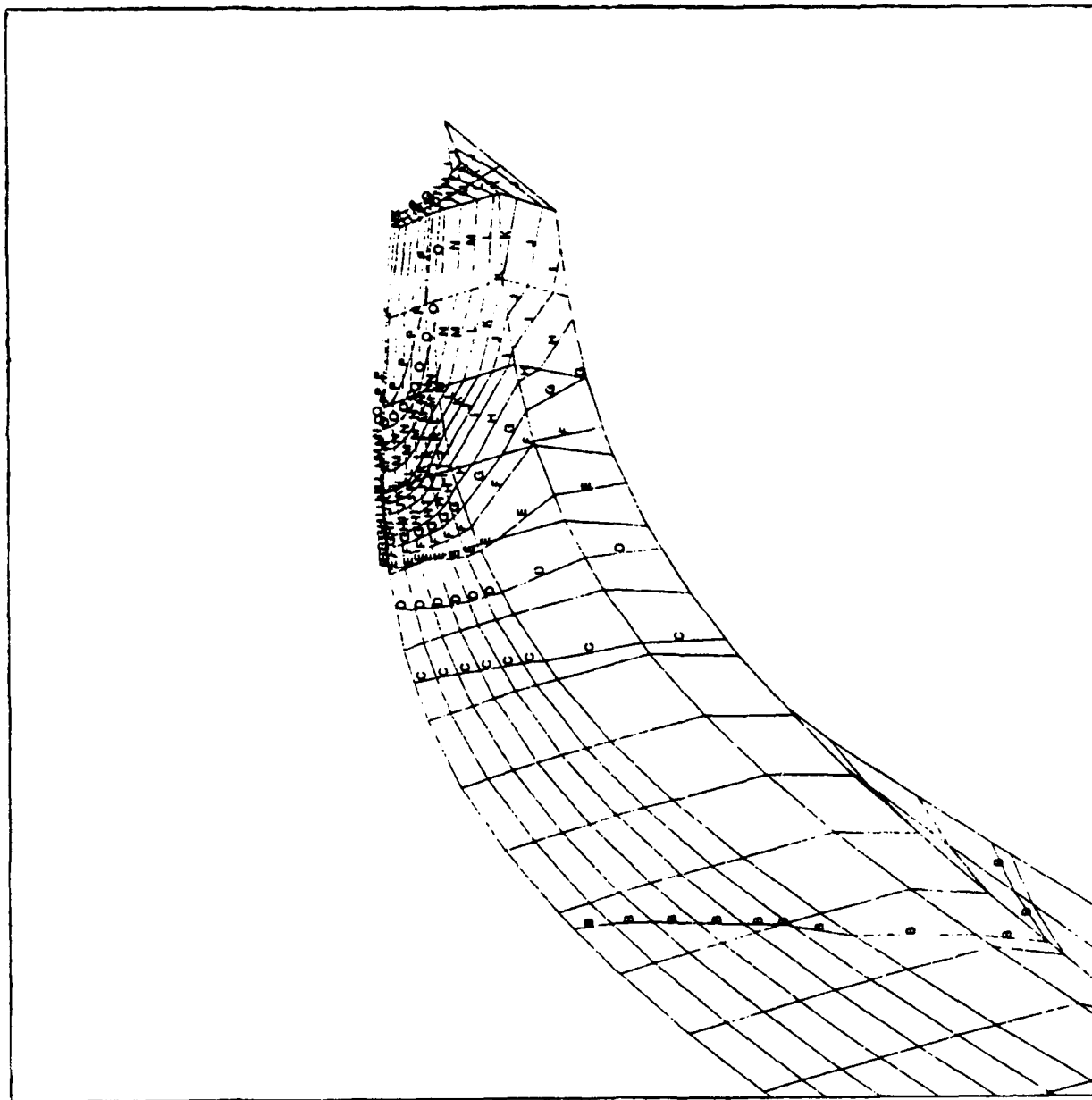


Figure 2-15. Blade temperature distribution (in °F) at time = 8 s of start cycle for XD® titanium aluminides.



```

ANSYS  4.4A
APR 15 1992
10:16:38
PLOT NO.  2
POST1  STRESS
STEP=3
ITER=1000
TIME=8
TEMP
SMX  =1194

ZV  =1
*DIST=0.520229
*XF  =1.336
*YF  =-1.305
*ZF  =0.080084
ANGZ=90
PRECISE HIDDEN
A  = 0
B  = 75
C  = 150
D  = 225
E  = 300
F  = 375
G  = 450
H  = 525
I  = 600
J  = 675
K  = 750
L  = 825
M  = 900
N  = 975
O  = 1050
P  = 1125
Q  = 1200
R  = 1275
S  = 1350
T  = 1425

```

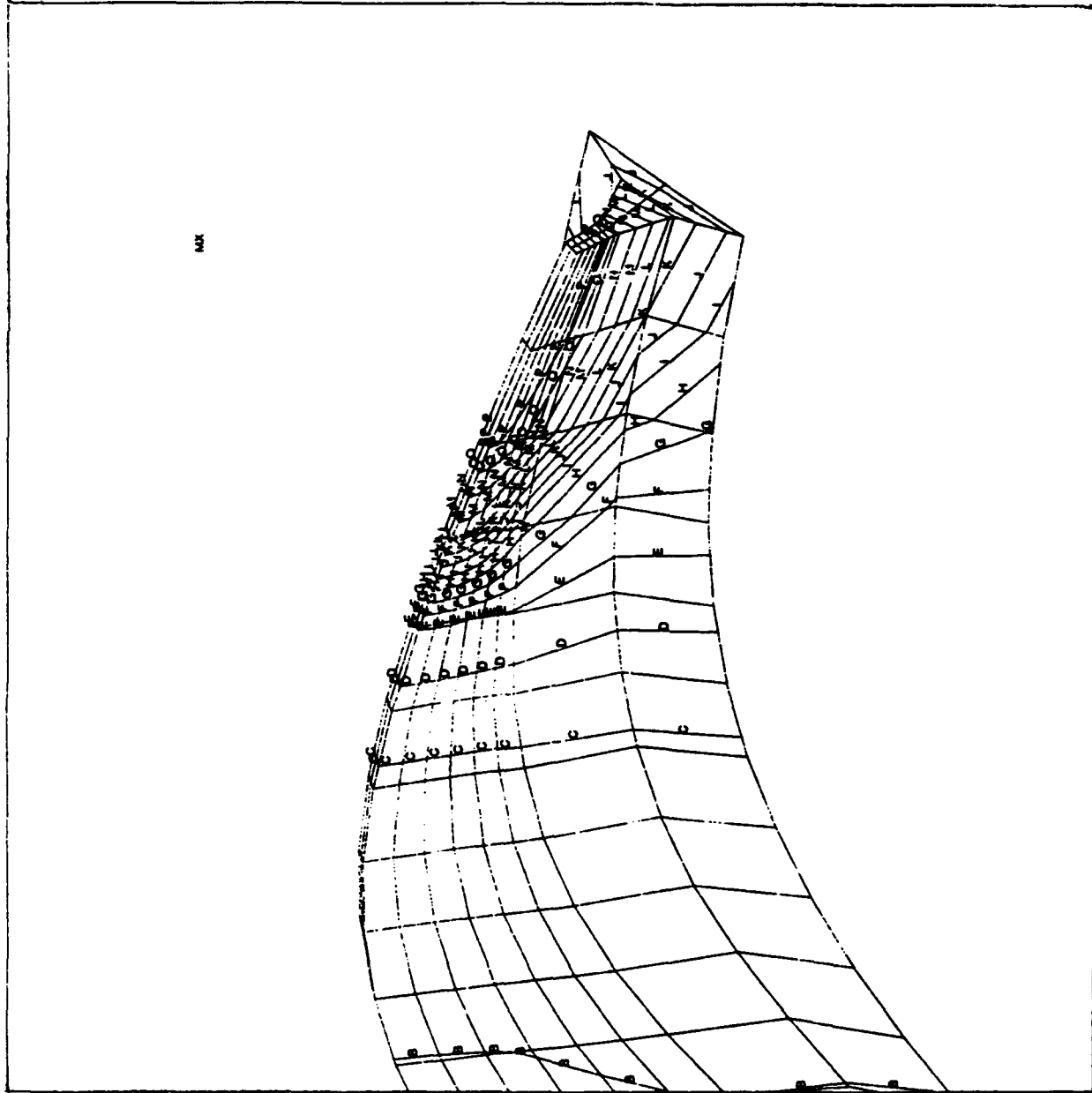


Figure 2-16. Splitter temperature distribution (in °F) at time = 8 s of start cycle for XD® titanium aluminides.

ANSYS 4.4A  
 APR 15 1992  
 10:17:33  
 PLOT NO. 3  
 POST1 STRESS  
 STEP=3  
 ITER=1000  
 TIME=8  
 TEMP  
 SMX =1194

ZV =1  
 \*DIST=0.478592  
 \*XF =1.483  
 \*YF =-1.487  
 \*ZF =0.080084  
 ANGZ=90  
 PRECISE HIDDEN  
 A = 0  
 B = 75  
 C = 150  
 D = 225  
 E = 300  
 F = 375  
 G = 450  
 H = 525  
 I = 600  
 J = 675  
 K = 750  
 L = 825  
 M = 900  
 N = 975  
 O = 1050  
 P = 1125  
 Q = 1200  
 R = 1275  
 S = 1350  
 T = 1425

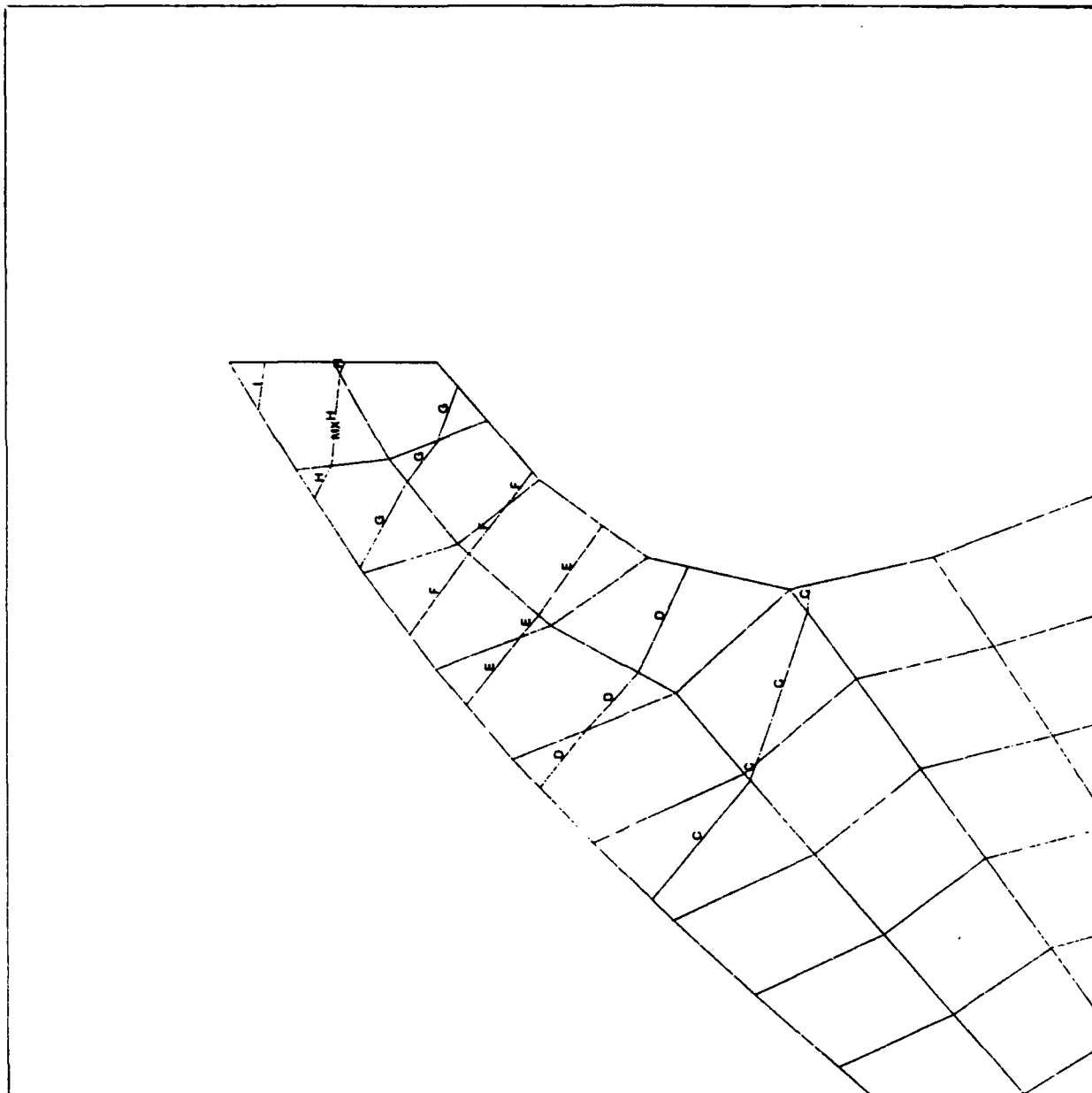


Figure 2-17. Rotor temperature distribution (in °F) at time = 8.0 s of start cycle for XD® titanium aluminides.

ANSYS 4.4A  
 APR 15 1992  
 13:16:30  
 PLOT NO. 1  
 POST26

ZV = 1  
 DIST=0.6666  
 XF = 0.5  
 YF = 0.5  
 ZF = 0.5

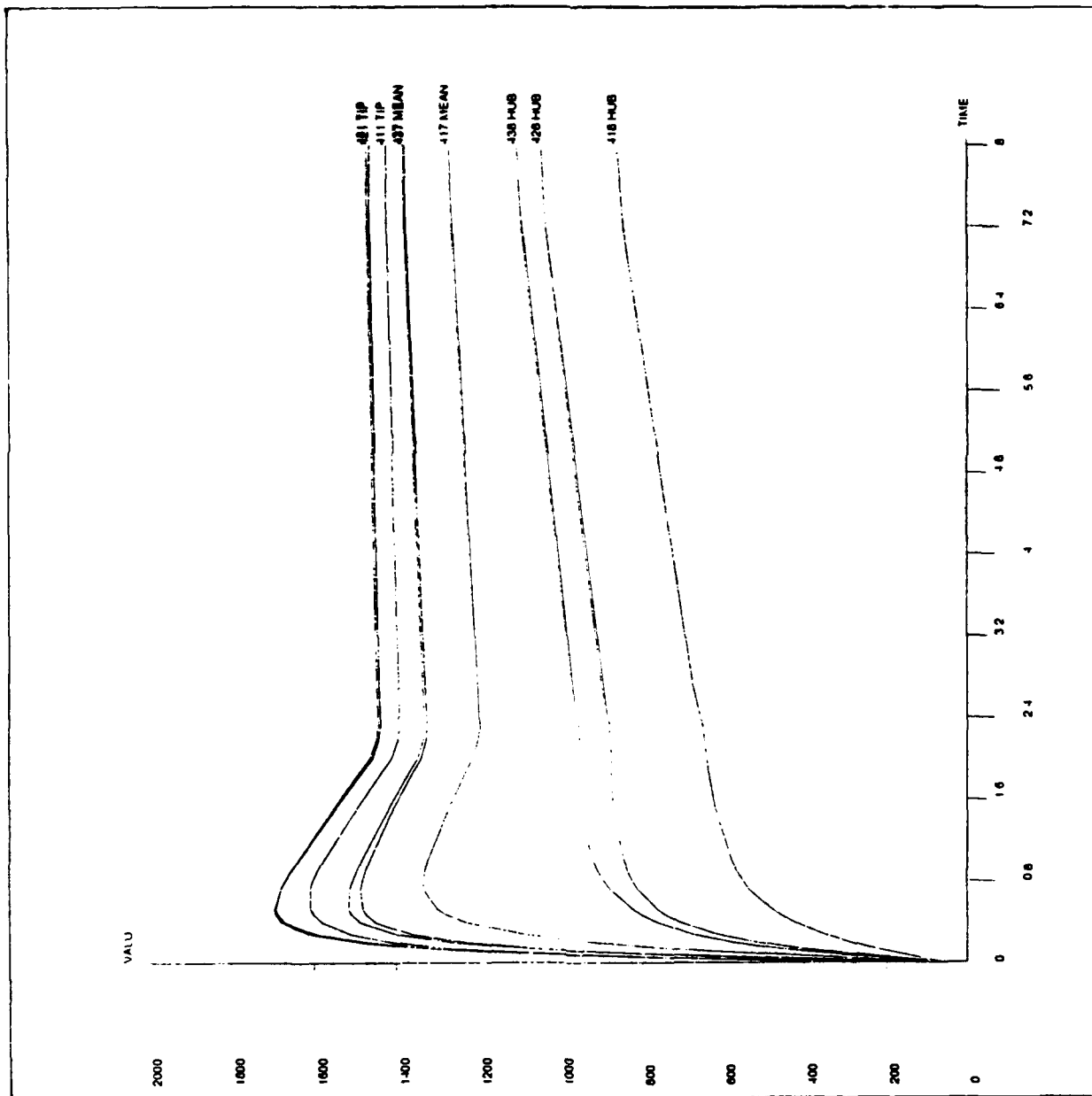


Figure 2-18. Blade estimated peak temperatures (in °F) during hot gas start cycle for XD® titanium aluminides.

ANSYS 4.4A  
 APR 15 1992  
 13:16:36  
 PLOT NO. 2  
 POST26

ZV =1  
 DIST=0.6666  
 XF =0.5  
 YF =0.5  
 ZF =0.5

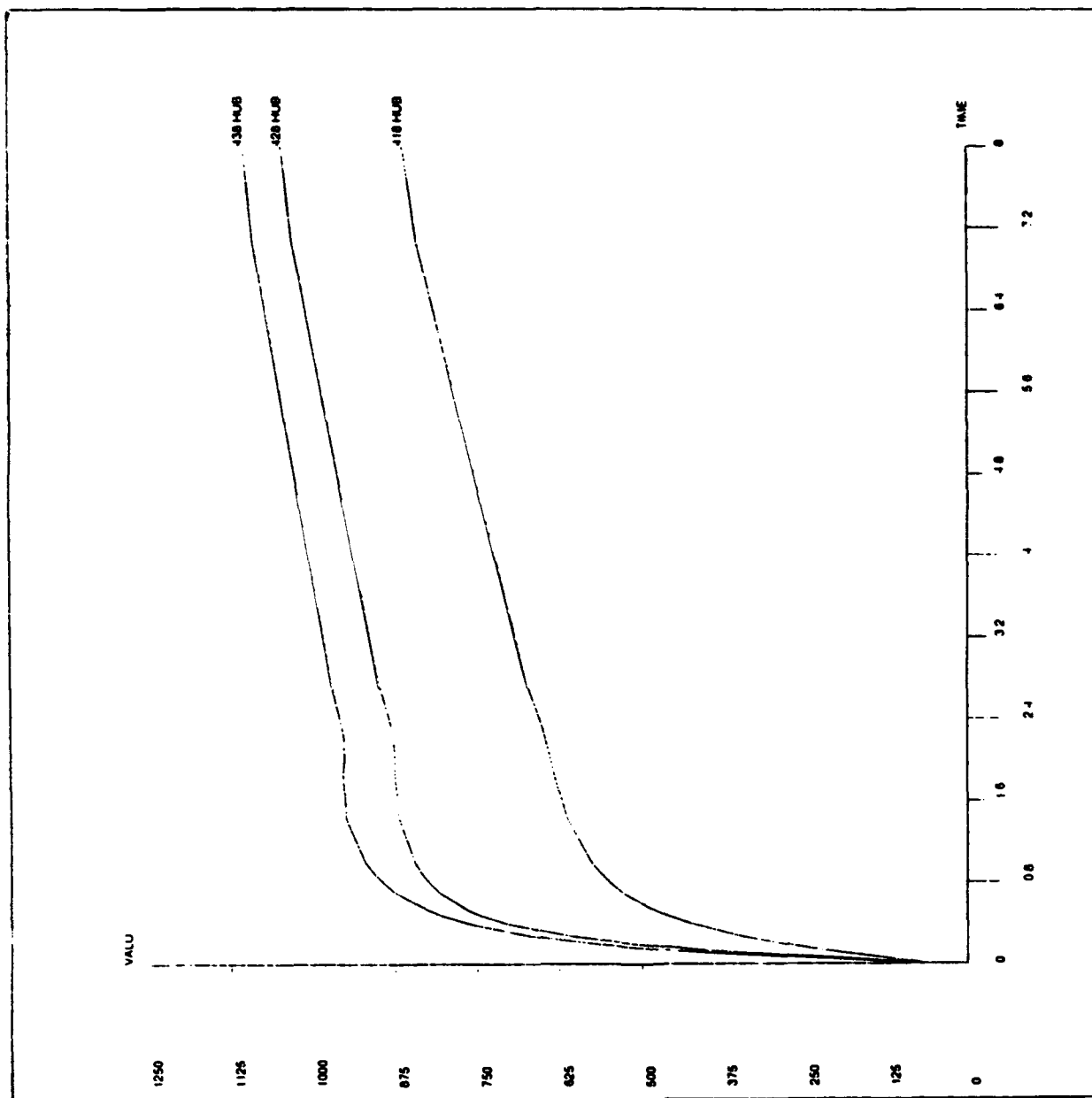


Figure 2-19. Blade hub estimated peak temperatures (in °F) during hot gas start cycle for XD® titanium aluminides.

ANSYS 4.4A  
 APR 15 1992  
 13:16:40  
 PLOT NO. 3  
 POST26

ZV =1  
 DIST=0.6666  
 XF =0.5  
 YF =0.5  
 ZF =0.5

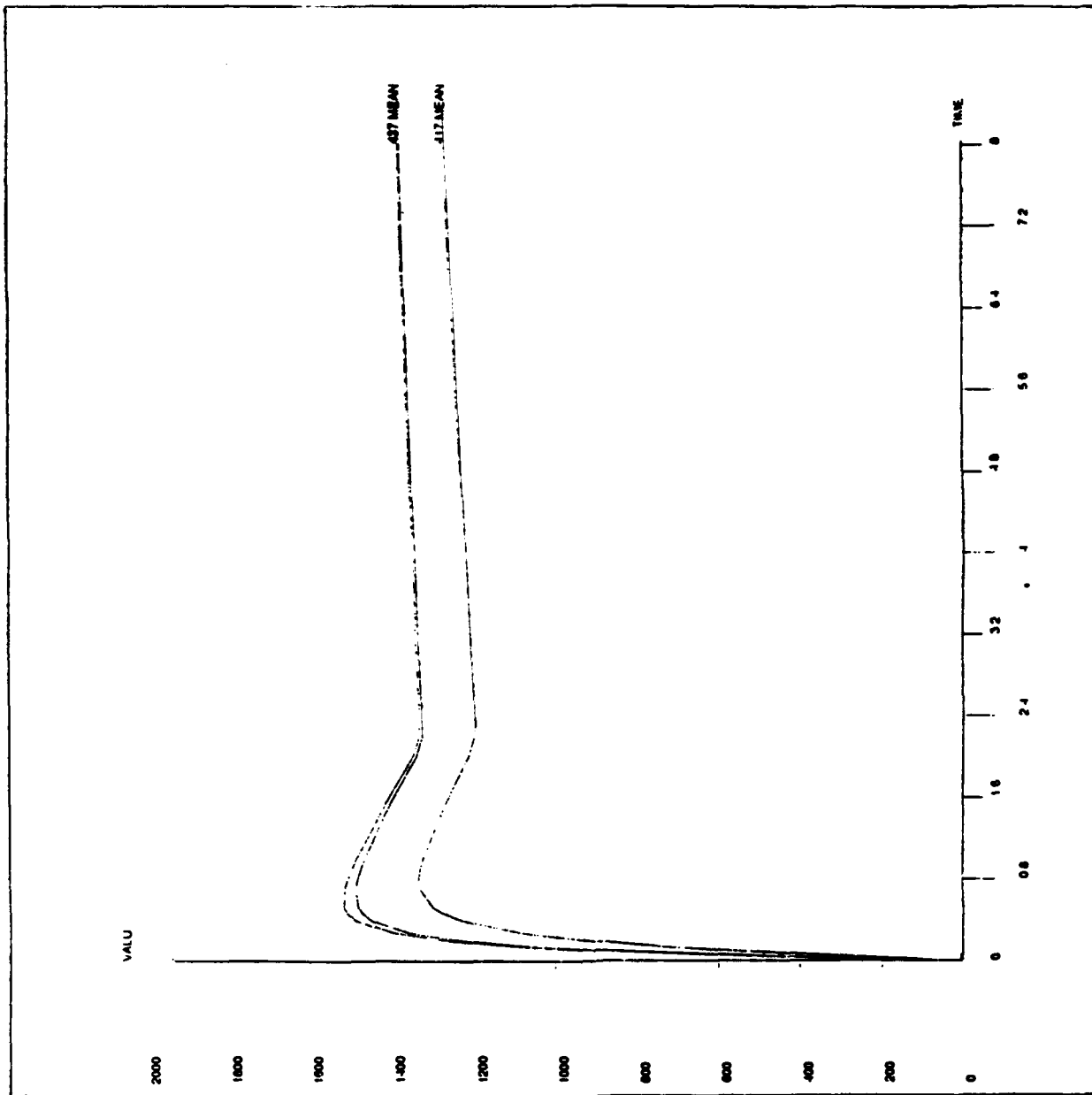


Figure 2-20. Blade mean estimated peak temperatures (in °F) during hot gas start cycle for XD® titanium aluminides.

ANSYS 4.4A  
 APR 15 1992  
 13:16:45  
 PLOT NO. 4  
 POST26  
 ZV = 1  
 DIST=0.6666  
 XF = 0.5  
 YF = 0.5  
 ZF = 0.5

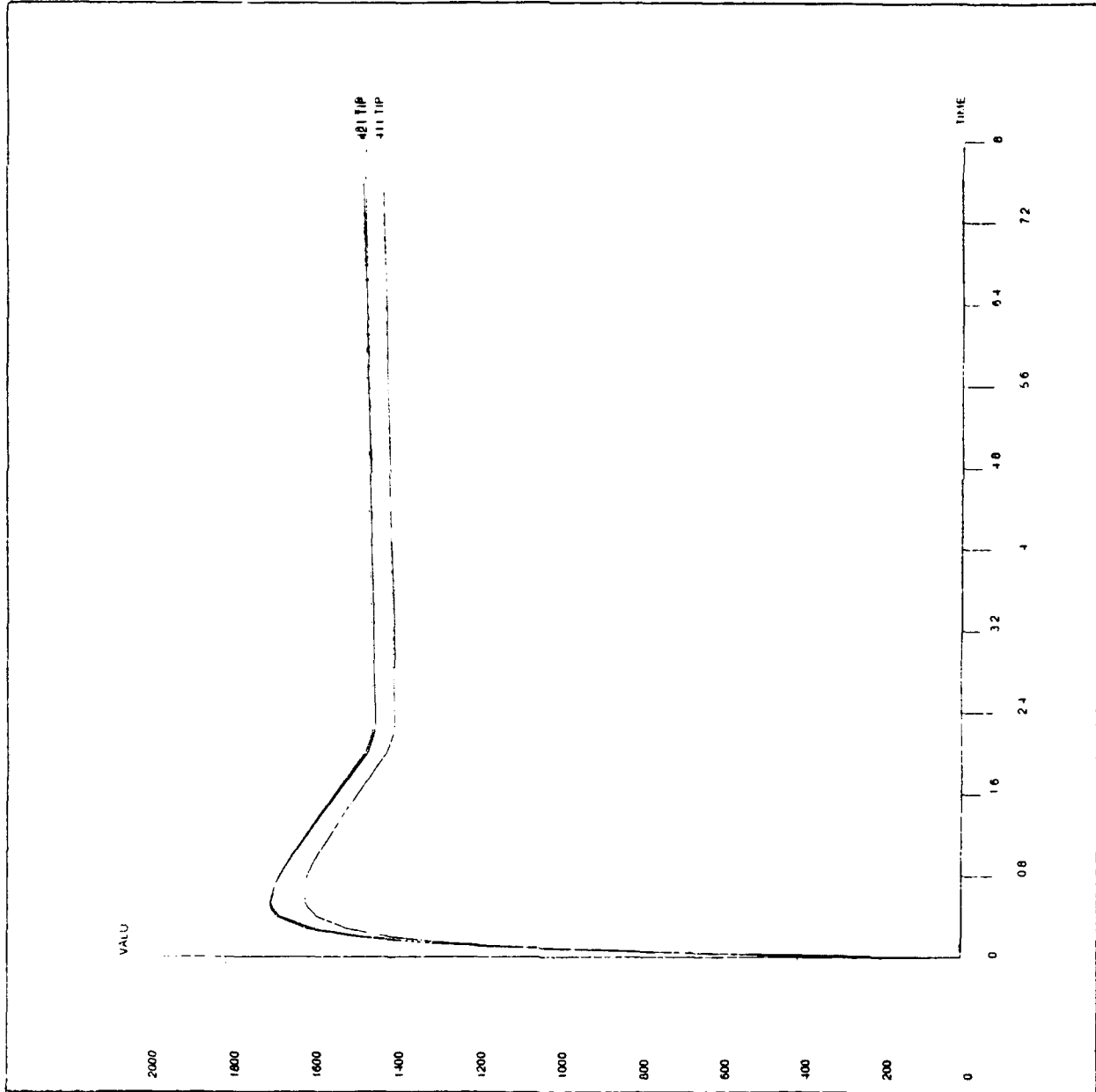


Figure 2-21. Blade tip estimated peak temperatures (in °F) during hot gas start cycle for XD® titanium aluminides.

```

ANSYS 4.4A
APR 15 1992
13:24:25
PLOT NO. 5
POST1 STRESS
STEP=2
ITER=262
TIME 0.524
TEMP
SMX -1712

2V -1
*DIST=0.375289
*XF =1.596
*YF =-1.383
*ZF =0.080084
ANGZ=90
PRECISE HIDDEN
A = 100
B = 200
C = 300
D = 400
E = 500
F = 600
G = 700
H = 800
I = 900
J = 1000
K = 1100
L = 1200
M = 1300
N = 1400
O = 1500
P = 1600
Q = 1700
R = 1800
S = 1900
T =

```

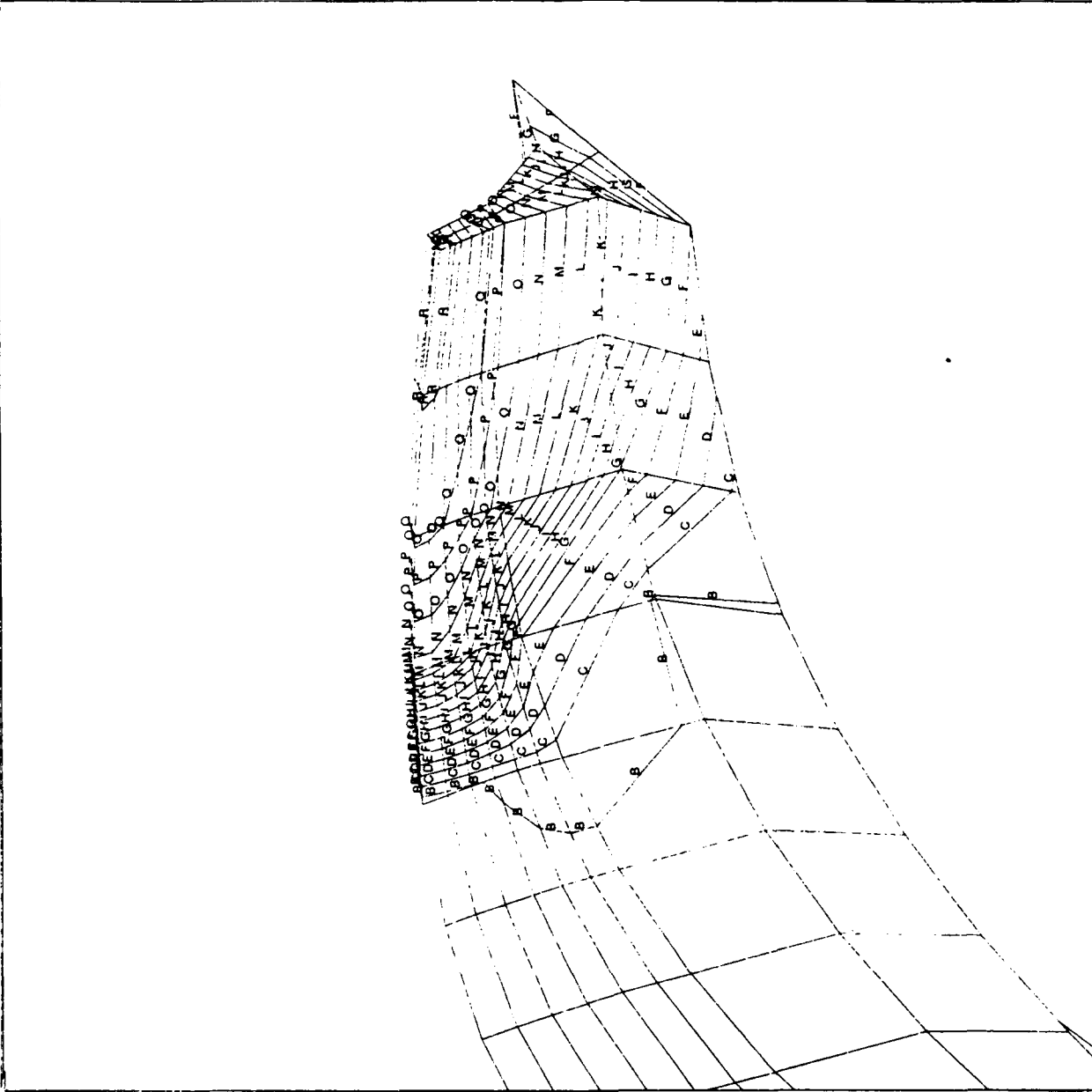


Figure 2-22. Blade estimated peak temperature distribution (in °F) at time = 0.524 s of start cycle for XD® titanium aluminides.

ANSYS 4.4A  
 APR 15 1992  
 13:25:41  
 PLOT NO. 7  
 POST1 STRESS  
 STEP=2  
 ITER=262  
 TIME=0.524  
 TEMP  
 SMX =1712

ZV =1  
 \*DIST=0.342949  
 \*XF =1.353  
 \*YF =-1.435  
 \*ZF =0.080084  
 ANGZ=90  
 PRECISE HIDDEN  
 A = 0  
 B = 100  
 C = 200  
 D = 300  
 E = 400  
 F = 500  
 G = 600  
 H = 700  
 I = 800  
 J = 900  
 K = 1000  
 L = 1100  
 M = 1200  
 N = 1300  
 O = 1400  
 P = 1500  
 Q = 1600  
 R = 1700  
 S = 1800  
 T = 1900

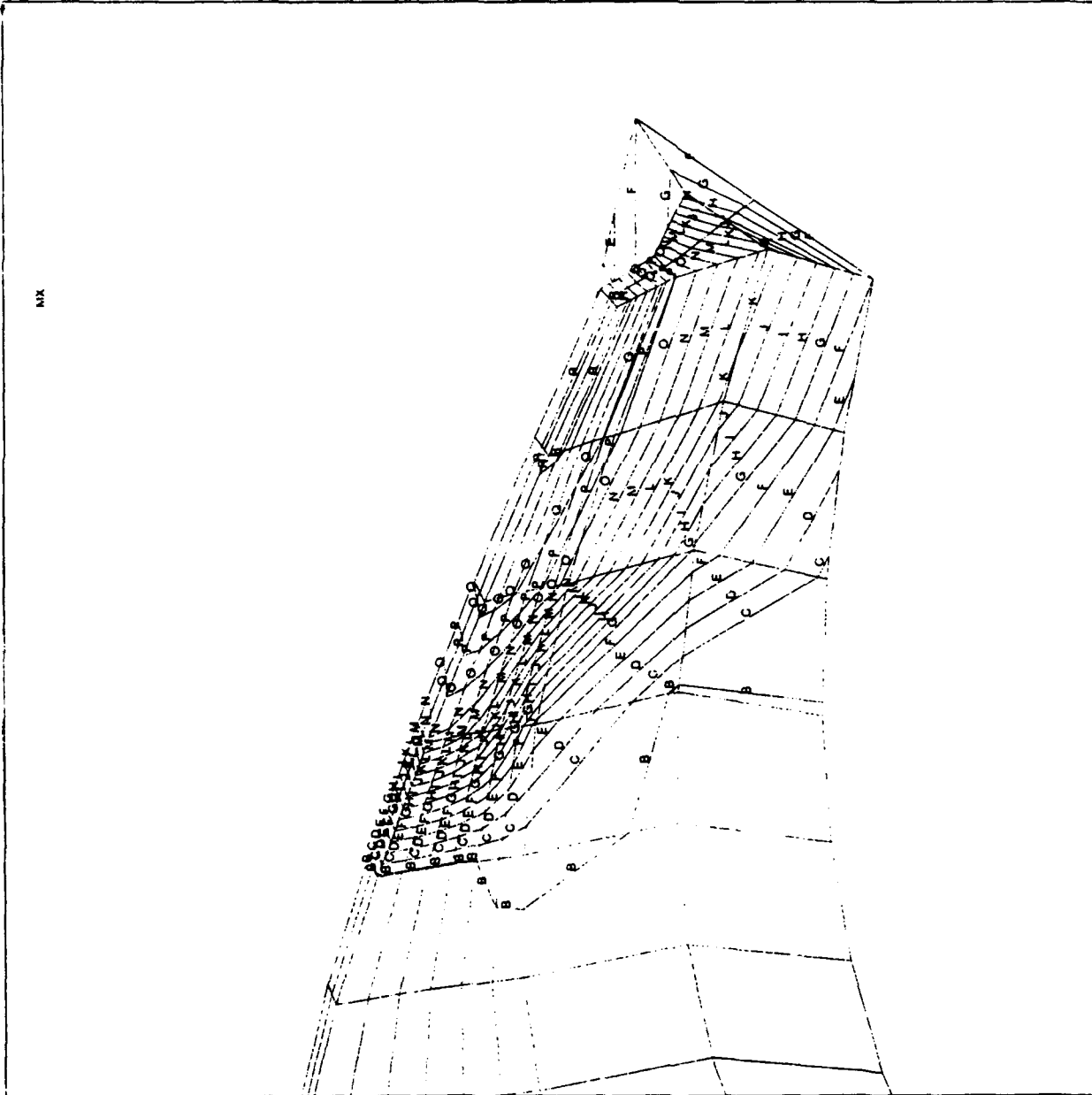


Figure 2-23. Splitter estimated peak temperature distribution (in °F) at time = 0.524 s of start cycle for XD® titanium aluminides.



```

ANSYS  4.4A
APR 15 1992
13:27:01
PLOT NO. 8
POST1  STRESS
STEP=2
ITER=262
TIME=0.524
TEMP
SMX  =1712

ZV  =1
*DIST=0.337157
*XF  =1.613
*YF  =-1.505
*ZF  =0.080084
ANG2=90
PRECISE HIDDEN
A  = 0
B  = 25
C  = 50
D  = 75
E  = 100
F  = 125
G  = 150
H  = 175
I  = 200
J  = 225
K  = 250
L  = 275
M  = 300
N  = 325
O  = 350
P  = 375
Q  = 400
R  = 425
S  = 450
T  = 475

```

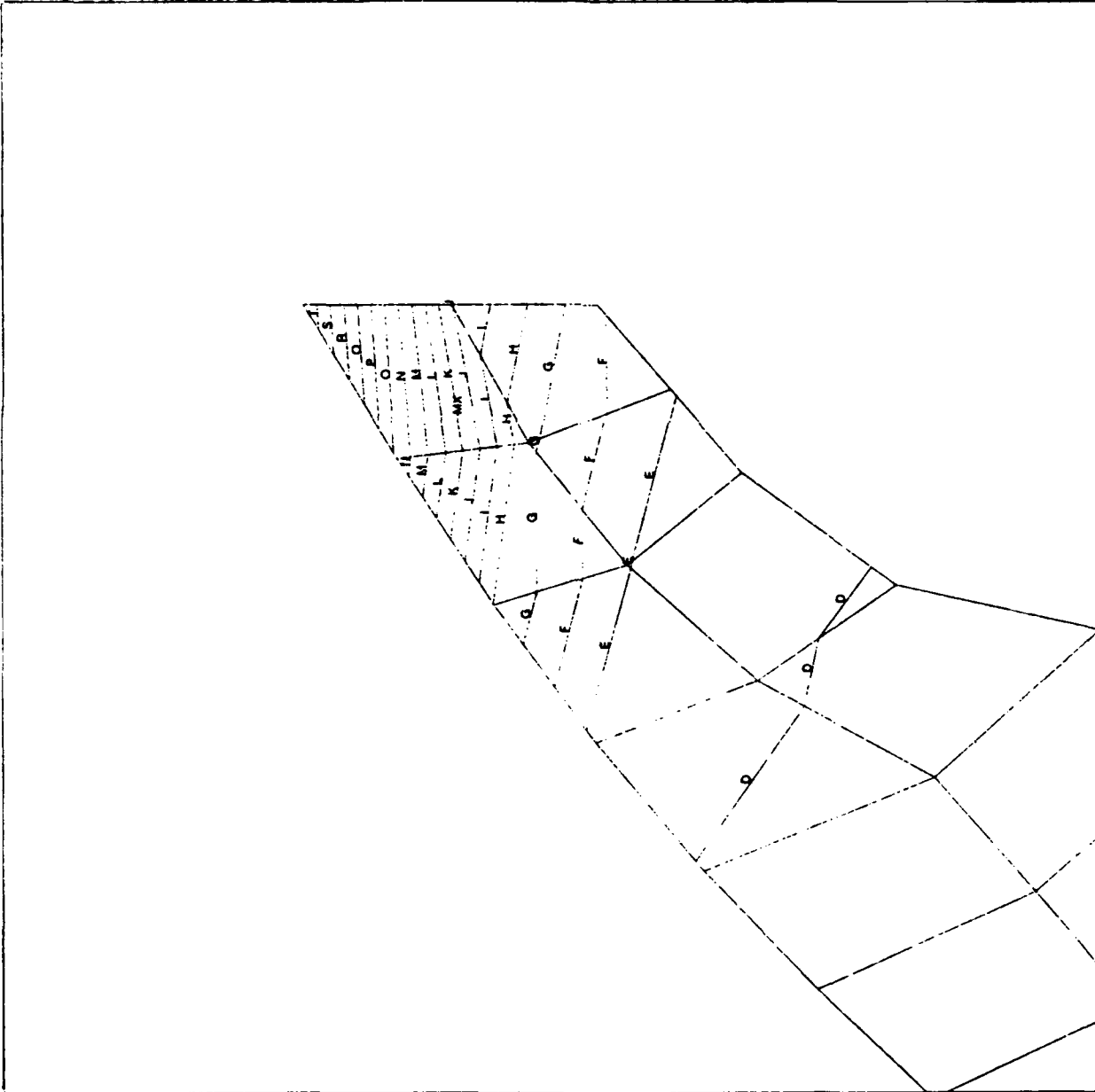


Figure 2-24. Disk estimated peak temperature distribution (in °F) at time = 0.524 s of start cycle for XD® titanium aluminides.

ANSYS 4.4A  
 APR 15 1992  
 13:31:47  
 PLOT NO. 9  
 POST1 STRESS  
 STEP=3  
 ITER=1000  
 TIME=8  
 TEMP  
 SMX =1476

ZV =1  
 \*DIST=0.65/93  
 \*XF =1.483  
 \*YF =-1.236  
 \*ZF =0.080084  
 ANG2=90  
 PRECISE HIDDEN  
 A = 0  
 B = 100  
 C = 200  
 D = 300  
 E = 400  
 F = 500  
 G = 600  
 H = 700  
 I = 800  
 J = 900  
 K = 1000  
 L = 1100  
 M = 1200  
 N = 1300  
 O = 1400  
 P = 1500  
 Q = 1600  
 R = 1700  
 S = 1800  
 T = 1900

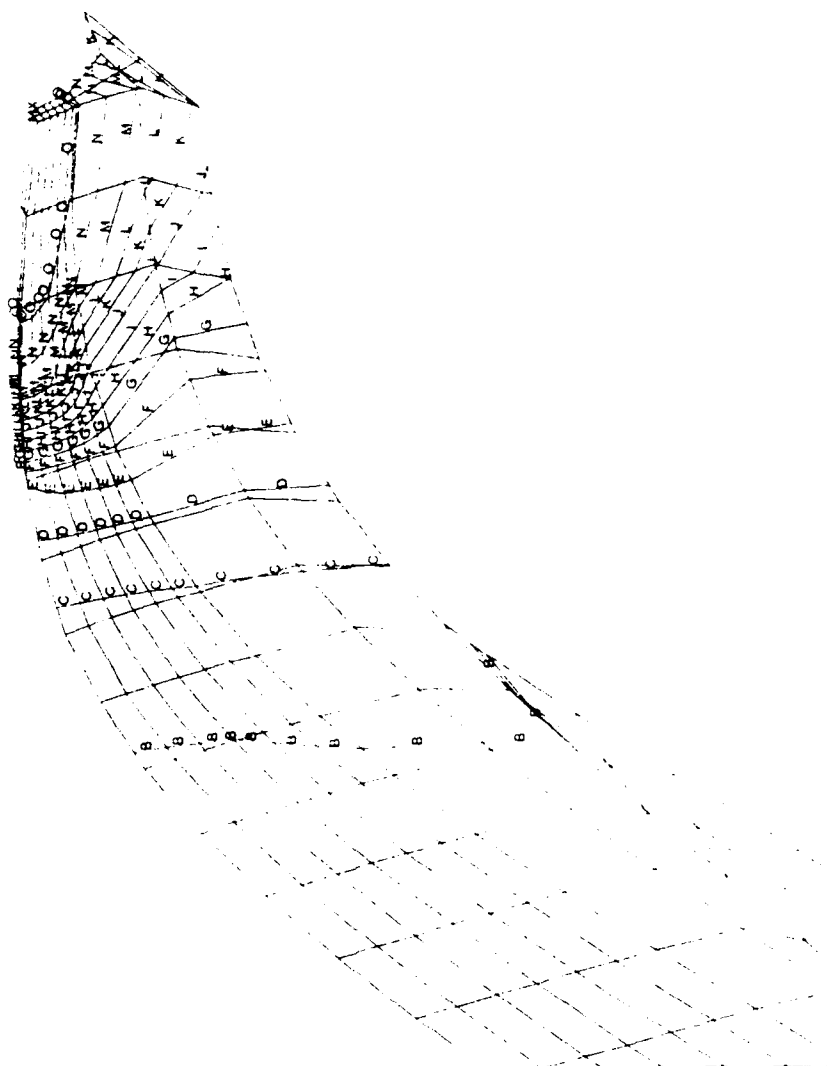


Figure 2-25. Blade estimated peak temperature distribution (in °F) at time = 8.0 s of start cycle for XD® titanium aluminides.

ANSYS 4.4A  
 APR 15 1992  
 13 32:54  
 PLT NO. 10  
 POST1: STRESS  
 STEP=3  
 ITER=1000  
 TIME=8  
 TEMP  
 SMX =1476

ZV =1  
 \*DIST=0.670362  
 \*XF =1.292  
 \*YF =-1.141  
 \*ZF =0.080084  
 ANG2=90  
 PRECISE HIDDEN  
 A = 0  
 B = 100  
 C = 200  
 D = 300  
 E = 400  
 F = 500  
 G = 600  
 H = 700  
 I = 800  
 J = 900  
 K = 1000  
 L = 1100  
 M = 1200  
 N = 1300  
 O = 1400  
 P = 1500  
 Q = 1600  
 R = 1700  
 S = 1800  
 T = 1900

MX

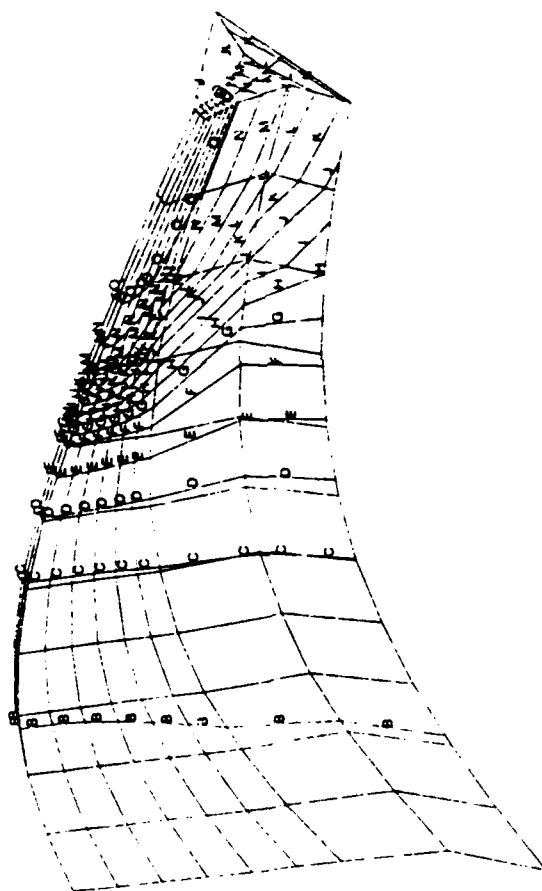


Figure 2-26. Splitter estimated peak temperature distribution (in °F) at time = 8.0 s of start cycle for XD® titanium aluminides.

ANSYS 4.4A  
 APR 15 1992  
 13:35:40  
 PLOT NO. 11  
 POST1 STRESS  
 STEP=3  
 ITER=1000  
 TIME=8  
 TEMP  
 SMX =1476

ZV =1  
 \*DIST=0.646412  
 \*XF =1.316  
 \*YF =-1.332  
 \*ZF =0.080084  
 ANGZ=90  
 PRECISE HIDDEN  
 A = 100  
 B = 150  
 C = 200  
 D = 250  
 E = 300  
 F = 350  
 G = 400  
 H = 450  
 I = 500  
 J = 550  
 K = 600  
 L = 650  
 M = 700  
 N = 750  
 O = 800  
 P = 850  
 Q = 900  
 R = 950  
 S = 1000  
 T = 1050

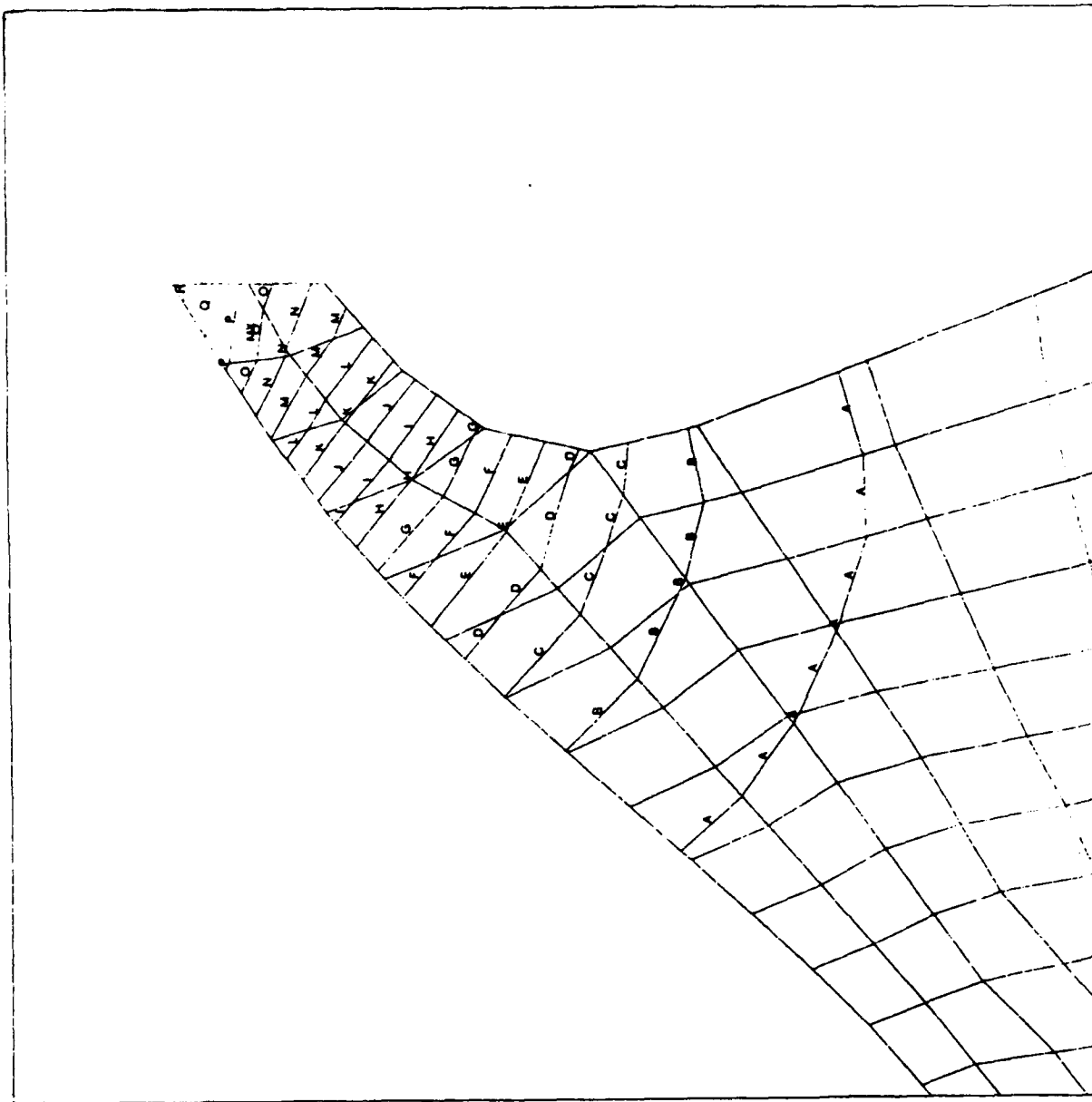


Figure 2-27. Disk estimated peak temperature distribution (in °F) at time = 8 s of start cycle for XD® titanium aluminides.

ANSYS 4.4A  
 APR 14 1992  
 10:48:47  
 PLOT NO. 1  
 PREP7 ELEMENTS  
 TYPE NUM  
 ZV =1  
 \*DIST=0.788095  
 \*XF =1.107  
 \*YF =-2.203  
 \*ZF =0.080084  
 ANGLE=90

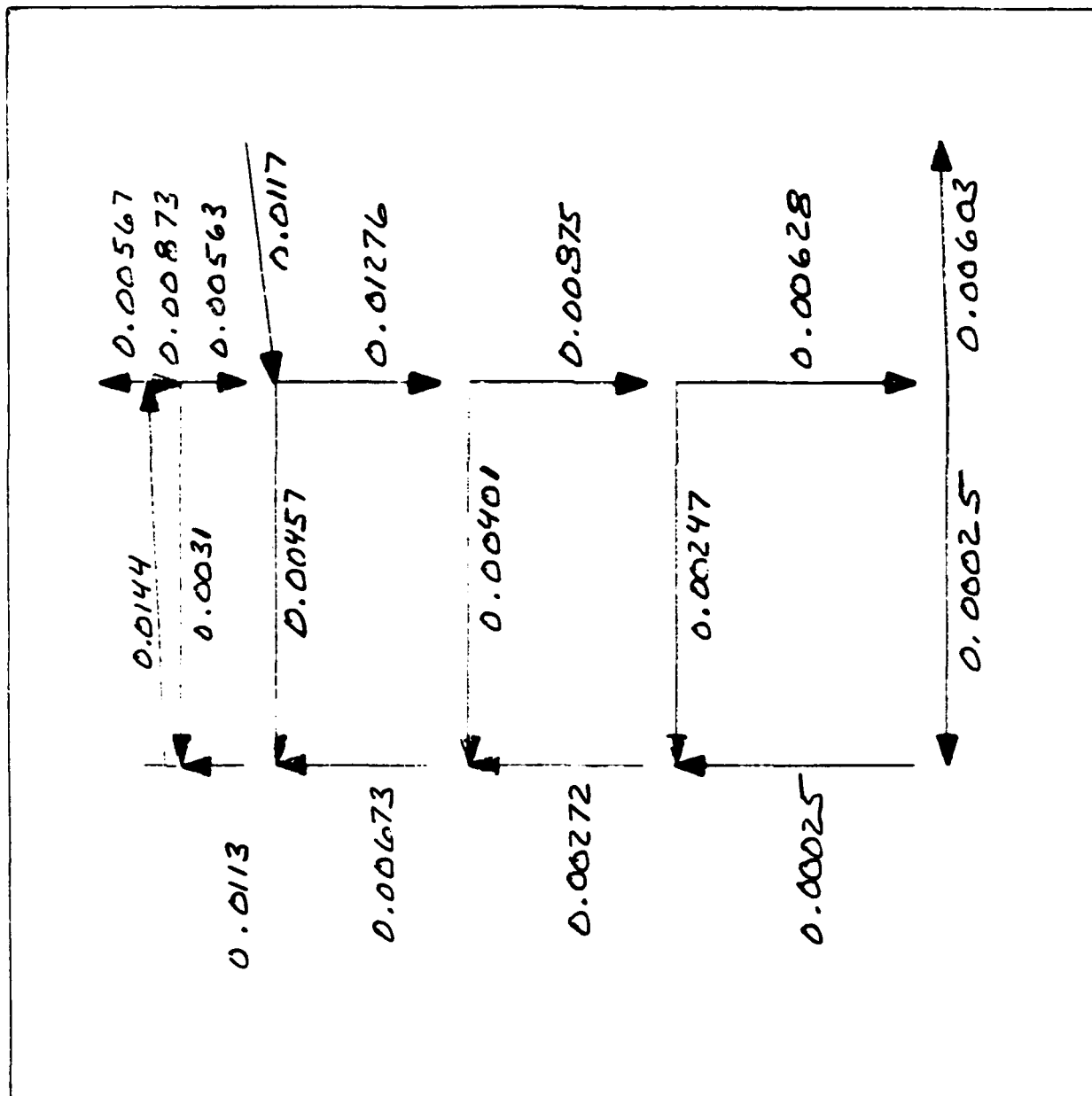


Figure 2-28. Compressor backface fluid network mass flow rates - lb<sub>m</sub>/sec.

ANSYS 4.4A  
 APR 14 1992  
 10:49:08  
 PLOT NO. 2  
 PREP7 ELEMENTS  
 TYPE NUM  
 2V = 1  
 \*DIST=0.788095  
 \*XF = 1.107  
 \*YF = -2.203  
 \*ZF = 0.080084  
 ANGLE=90

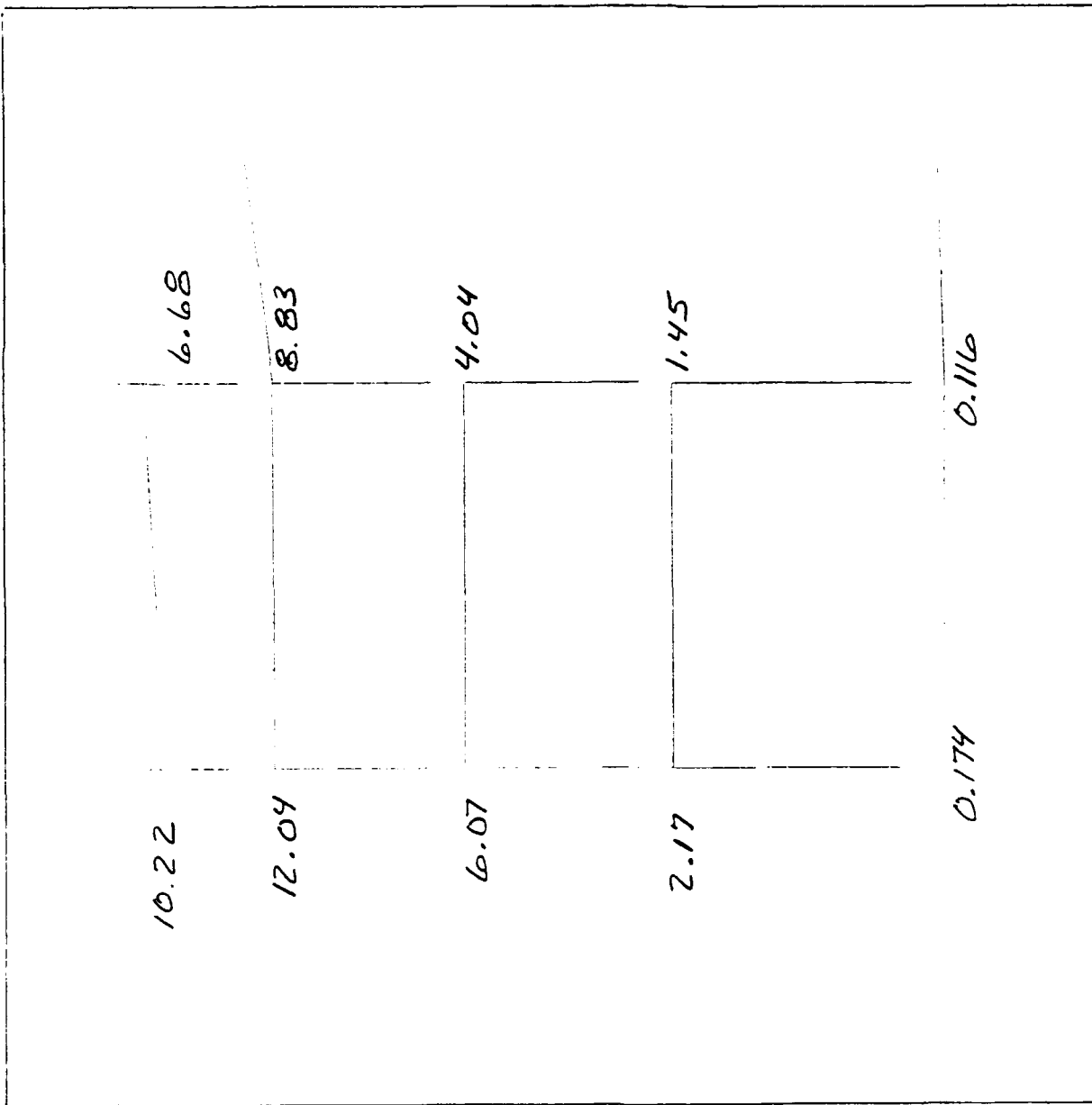


Figure 2-29. Compressor backface fluid network heat generation - btu/h.

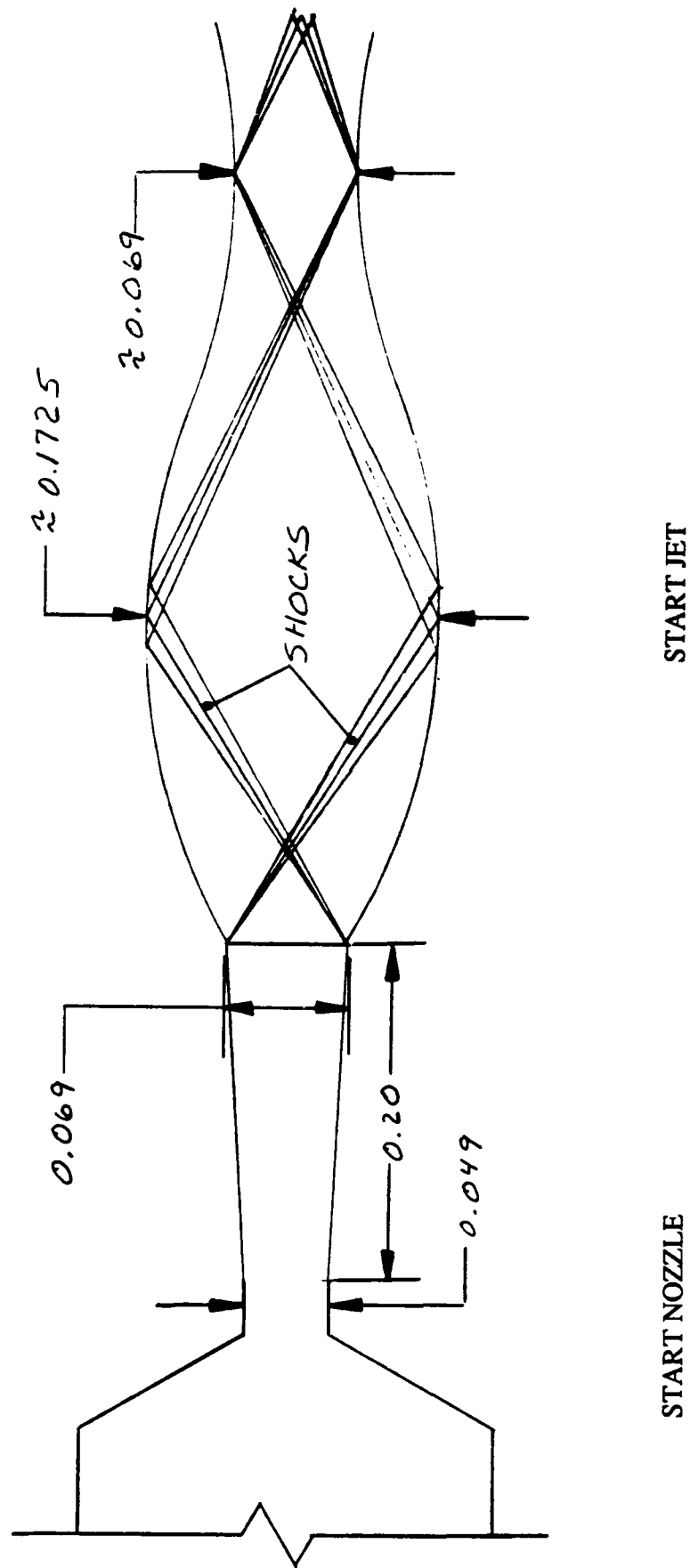


Figure 2-30. Start nozzle configuration and jet flow characteristics (dimensions are in inches).

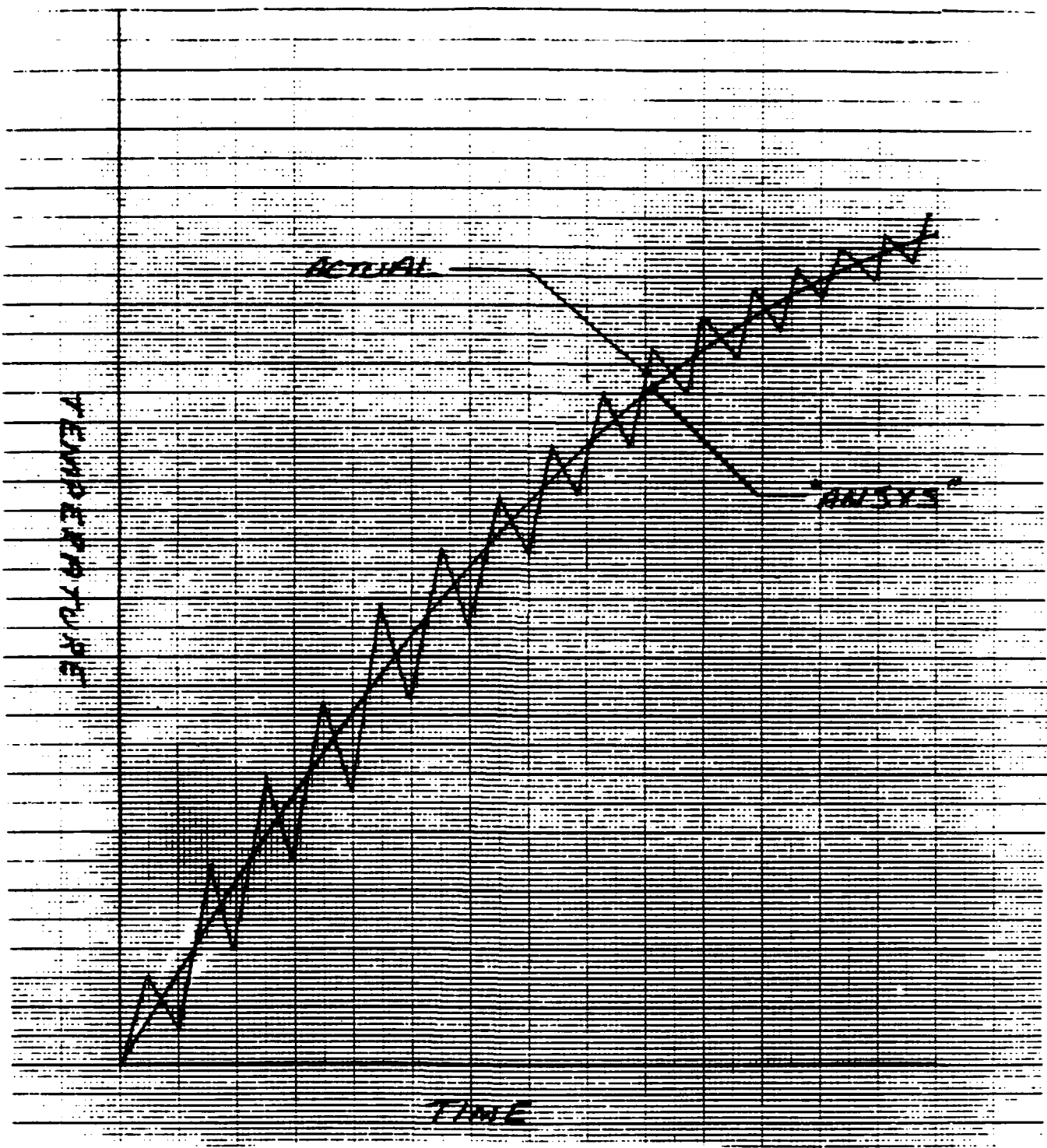


Figure 2-31. Schematic comparison between actual blade temperature and ANSYS calculated temperature.



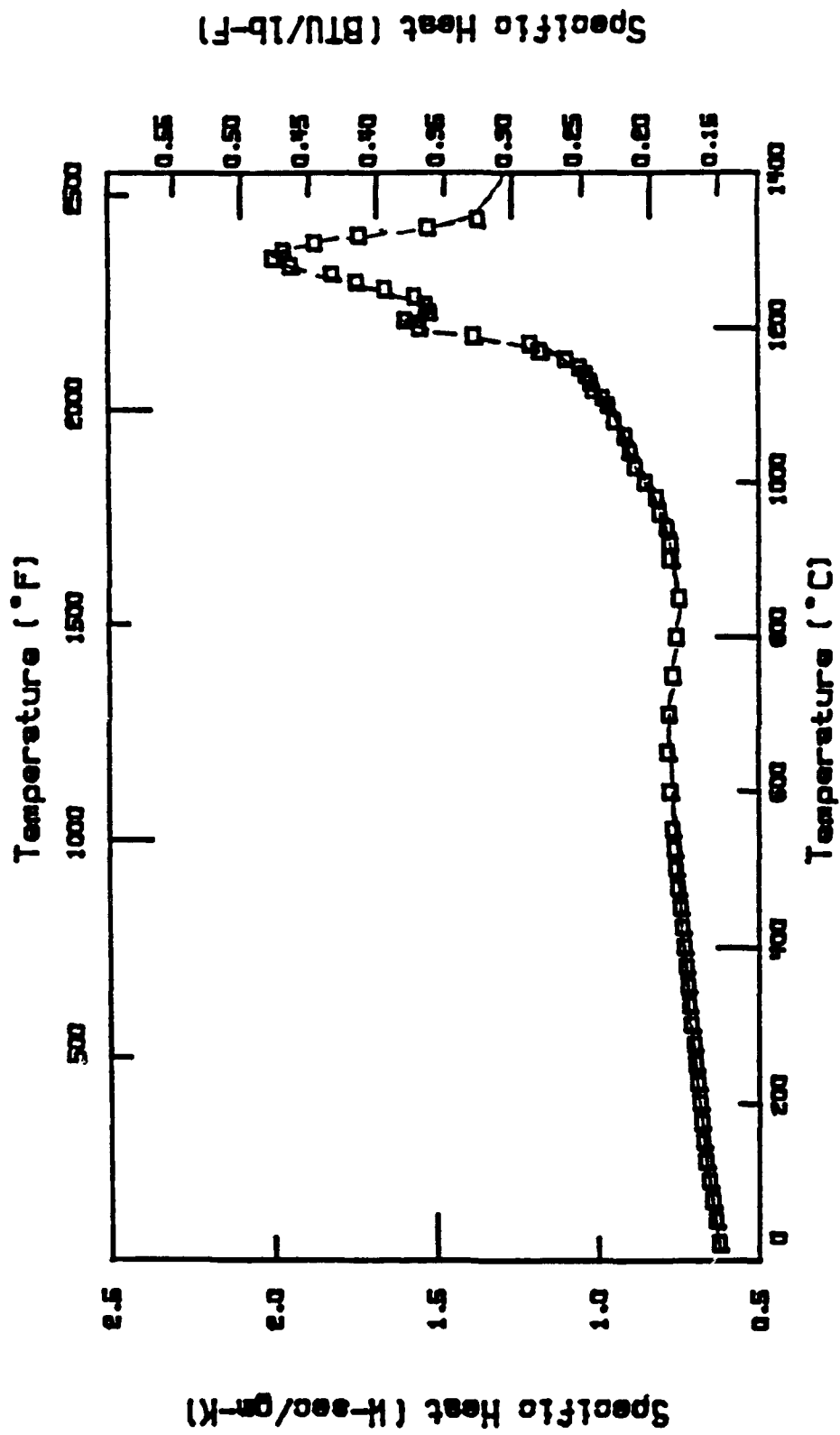


Figure 2-32. Graph depicting calculated values of specific heat vs. temperature.

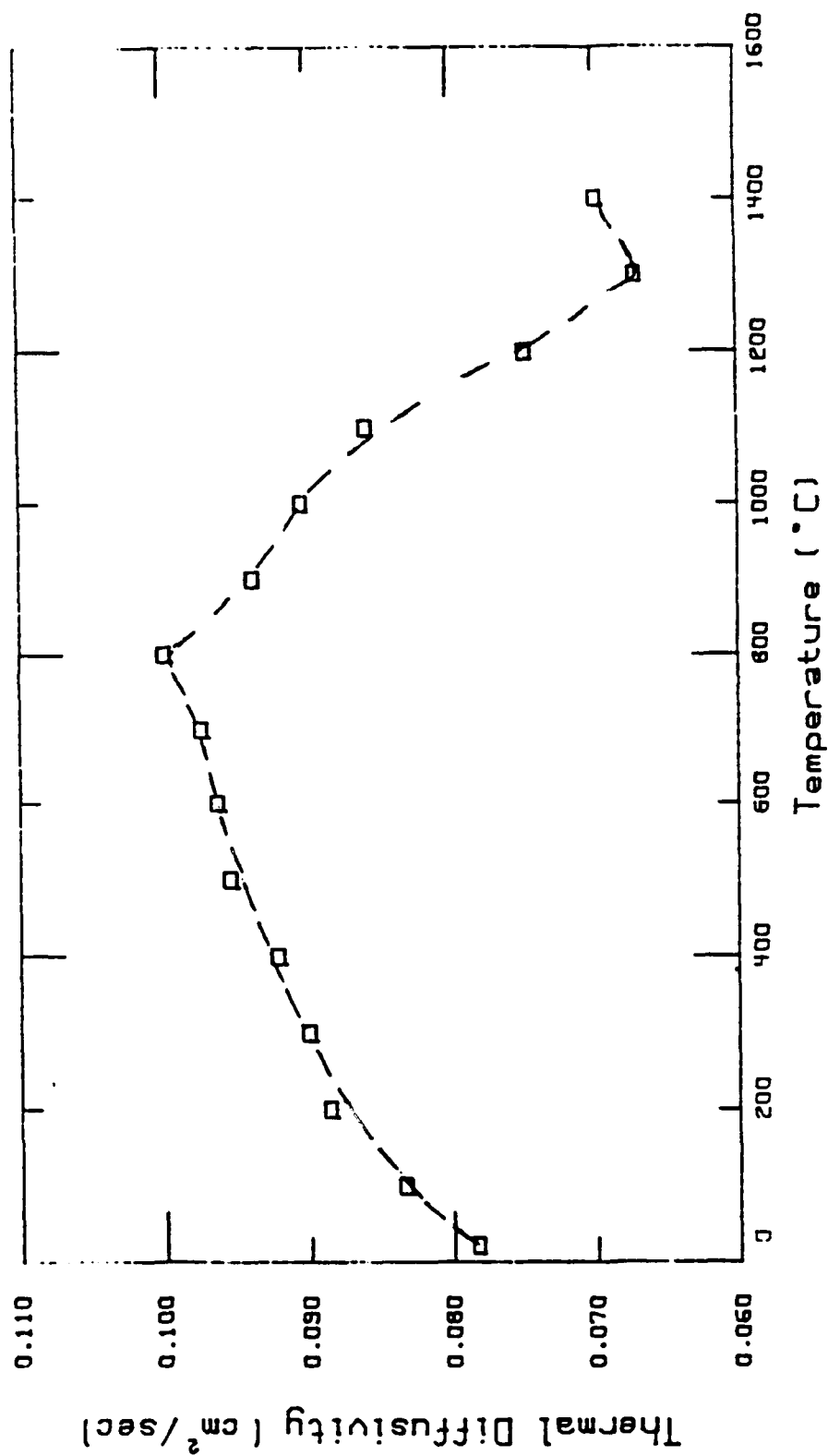


Figure 2-33. Graph depicting calculated values of thermal diffusivity vs. temperature.

□ Diffusivity      ▲ Spec/Heat

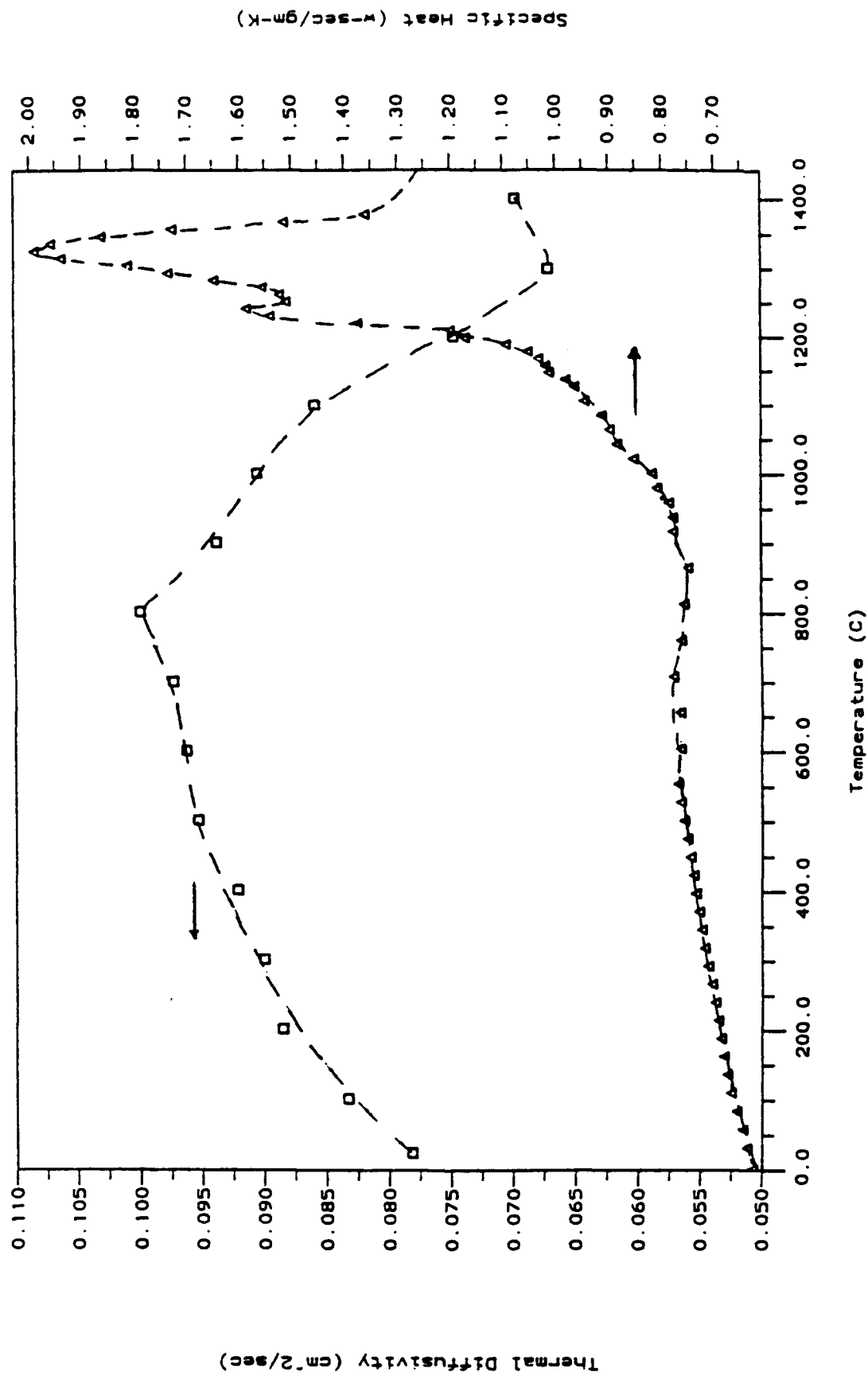


Figure 2-34. Graph comparing calculated values of specific heat and thermal diffusivity vs. temperature.

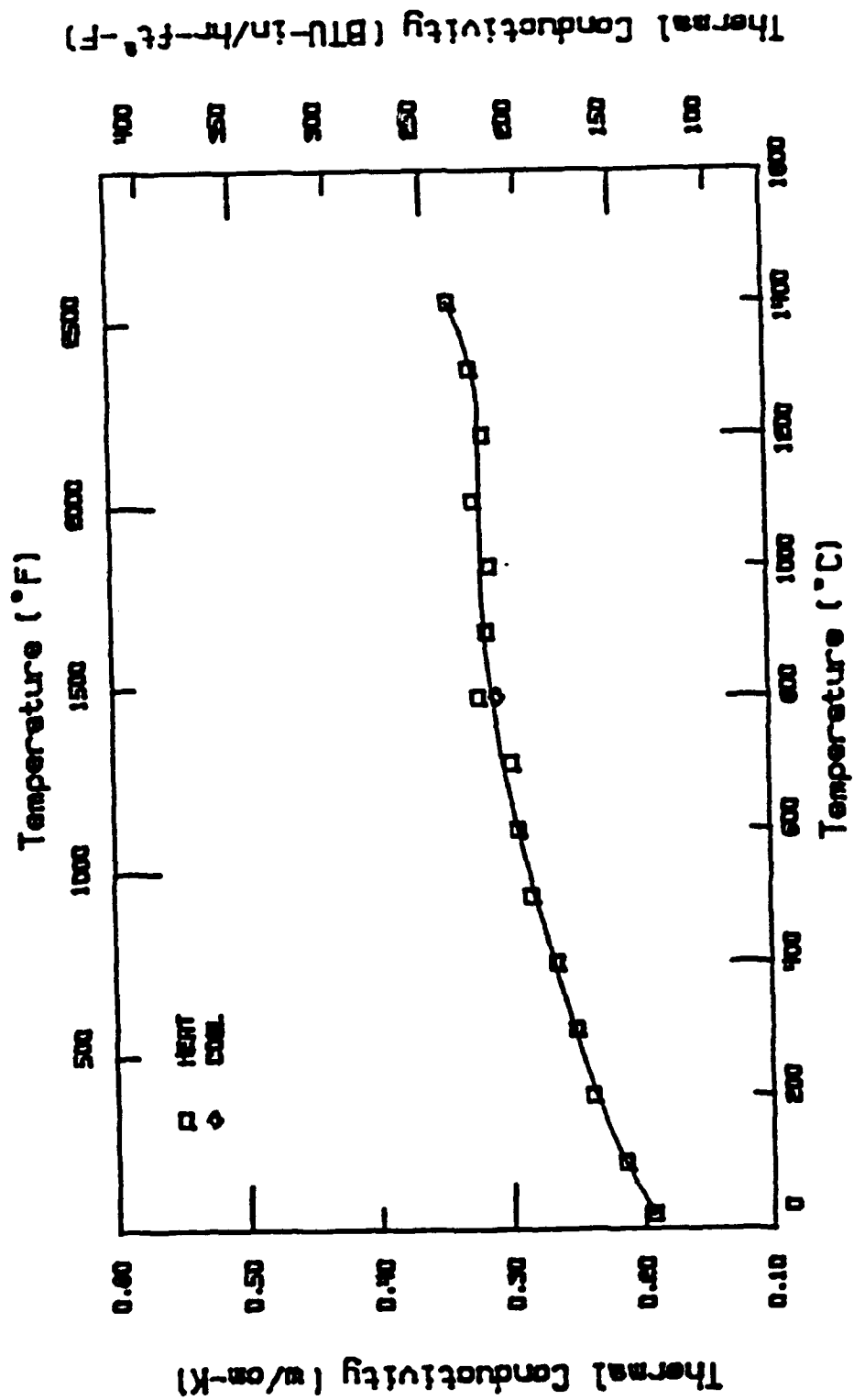


Figure 2-35. Graph depicting calculated values of thermal conductivity vs. temperature.

Table 2-1. The relative temperature and heat transfer coefficients are given at the boundary conditions of times equal to 0, 2, and 8 seconds of the start cycle.

Time (seconds)	Relative Temperature (°F)	Heat Transfer Coefficient (Btu/hr*(ft <sup>2</sup> )*(°F))
0	2000	12042
2	1650	8811
8	1650	8811

Table 2-2. Performance parameters of the engine and the XD® titanium aluminide compressor rotor for the sea level, 0.8 mach number, standard day operating condition.

Engine Parameters:

Ambient temperature (R)	519
Mach number	0.8
Turbine inlet temperature (R)	2460
Exhaust gas temperature (R)	2153
Inlet airflow (lb/s)	1.17
First shaft speed (rpm)	115000

Compressor Parameters:

Inlet pressure (psia)	22.4
Exit pressure (psia)	83.0
Inlet temperature (R)	585
Exit temperature (R)	962

Reference: "Four Inch Engine (P9005) Design Point", 100-721-022-006-214 (91/BAB) 042, by B. Beans, May 2, 1991.

### 3. Elastic stress analysis

An elastic stress analysis was conducted for steady state operation and for cartridge starting. The overspeed burst limit was determined. The elastic stress analysis was initially performed in its entirety and it was found the thermal stresses on the compressor blades during engine starting exceeded material capability. It was proposed that a high pressure hydrogen/air mixture could be used for engine start, which would reduce the impingement gas temperature, reducing blade stress. However, it was discovered shortly afterward that erroneous values for the coefficient of thermal expansion (CTE) had been used. Appropriate portions of the analysis were repeated with the proper data. The data that were used in the final analysis are shown in Table 3-1.

The analysis was carried out using an ANSYS 4.4A finite element model. An element plot of this model is shown in Figure 3-1. This model was run at both room temperature and the operating temperature; performance at the operating temperature is shown in Figure 3-2. When run at design speed, 115 krpm, this model showed that the compressor would not have 10% overspeed at either room temperature or operating temperature. The steady state bore stresses were too high, 586 MPa at 177°C (84.9 ksi at 350°F), for operating the rotor at the maximum design speed of 115 krpm. The equivalent stress plots at operating temperature and room temperature at 115 krpm are shown in Figures 3-3 and 3-4, respectively. In order to provide the required 10% burst margin, the rotor must run at engine speeds less than 108.4 krpm. Equivalent stress plots at 108.4 krpm are given in Figures 3-5 and 3-6. Since these stresses are within the limits of this material, this engine speed is acceptable. Note that, when the correct coefficients of thermal expansion were input for the operating temperature at the design speed of 115 krpm, the stresses only changed by 6.9 MPa (1 ksi). Therefore, it was deemed not necessary to repeat this portion of the analysis.

This model was also run with the average peak temperatures experienced by the blade during a cartridge start, at 0.916 s after ignition. An element plot of these temperatures is given in Figure 3-7. Engine speed at this point of the start-up was assumed to be 18,340 rpm. Equivalent stress plots for the blade and disc at these conditions are given in Figure 3-8. Note that the stresses shown are elastic stresses. Since the maximum stress of 671 MPa (97.3 ksi) shown is over the yield strength, a Neuber analysis was performed to convert this elastic stress to its plastic equivalent, shown in Figure 3-9. This Neuber stress was calculated at 583 MPa (70 ksi). Since the total plastic strain is 0.28%, and since the elongation to failure of this material at 675°C

(1245°F) is 6.8%, this is an acceptable stress level in this part. A revised stress analysis predicts that the engine can be started with start cartridge impingement on the XD® titanium aluminide compressor rotor. In order to provide an additional margin of safety, it is suggested that low start temperatures can be provided by a hydrogen/depleted air start system during development testing.

An engine simulator built-up from scrap 10.16 cm (4 in) engine hardware could be used for start cycle trials, to reduce risk to engine hardware. After the simulated impingement start cycles, the compressor rotor could be incorporated into a 10.16 cm (4 in) Demonstrator Engine. This testing could be conducted on a non-interference basis at the conclusion of the DARPA/Army 10.16 cm (4 in) Engine Test Program.

ANSYS 4.4A  
APR 22 1992  
15:05:11  
PLOT NO. 1  
PREP7 ELEMENTS  
TYPE NUM

ZV = 1  
DIST=1.238  
XF = 0.85483  
YF = -0.9659  
ZF = 0.080084  
ANG2=90  
PRECISE HIDDEN

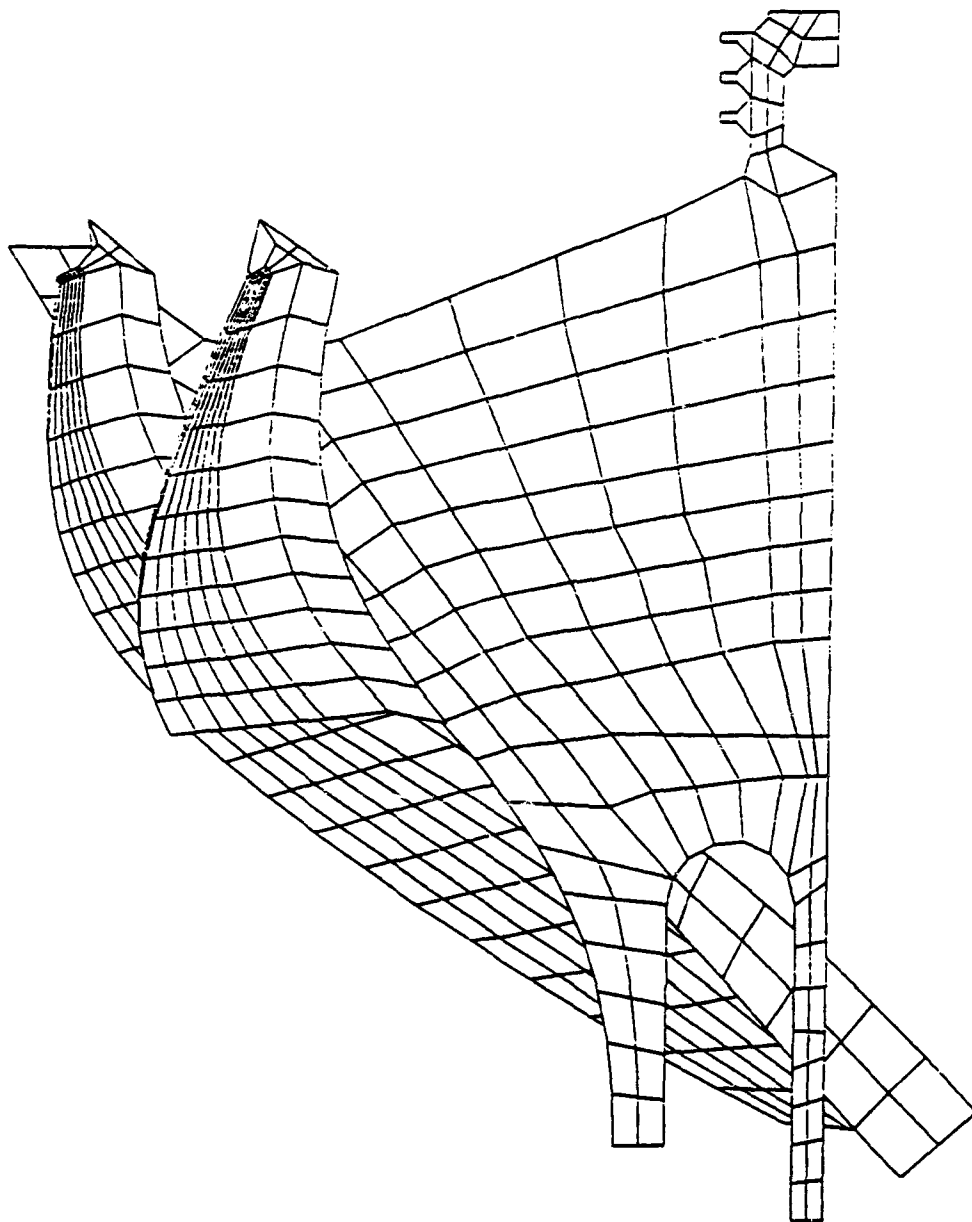


Figure 3-1. Finite element plot of the P9005, 4 inch experimental compressor engine.



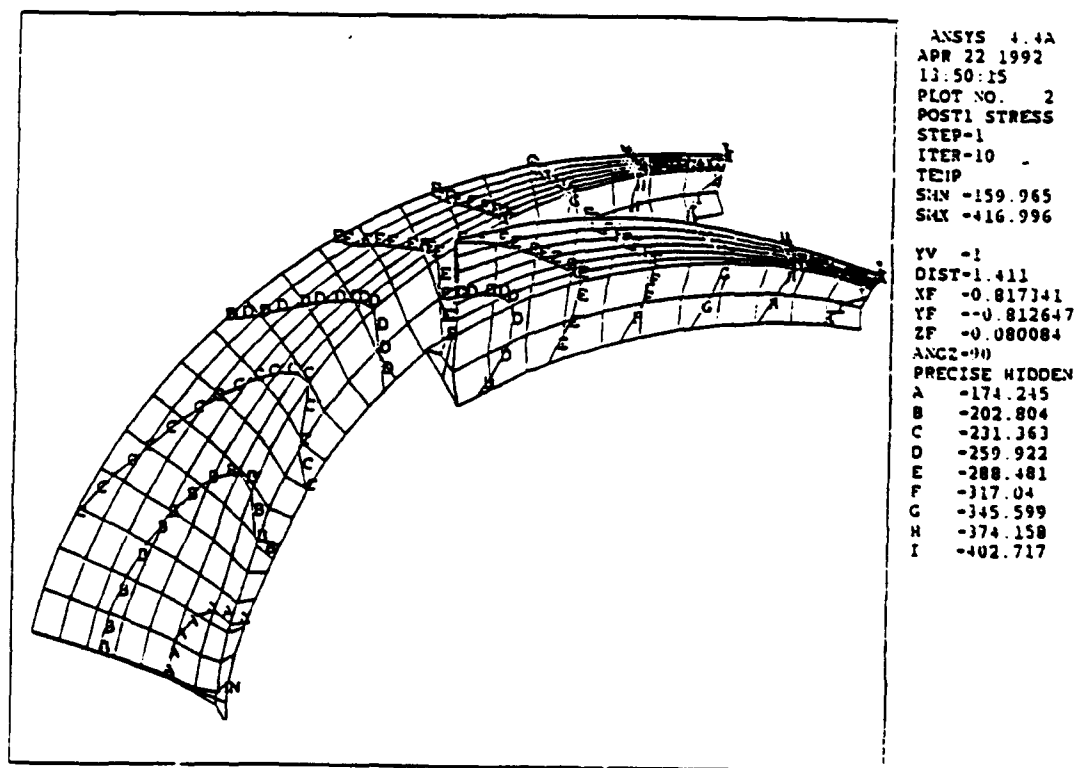
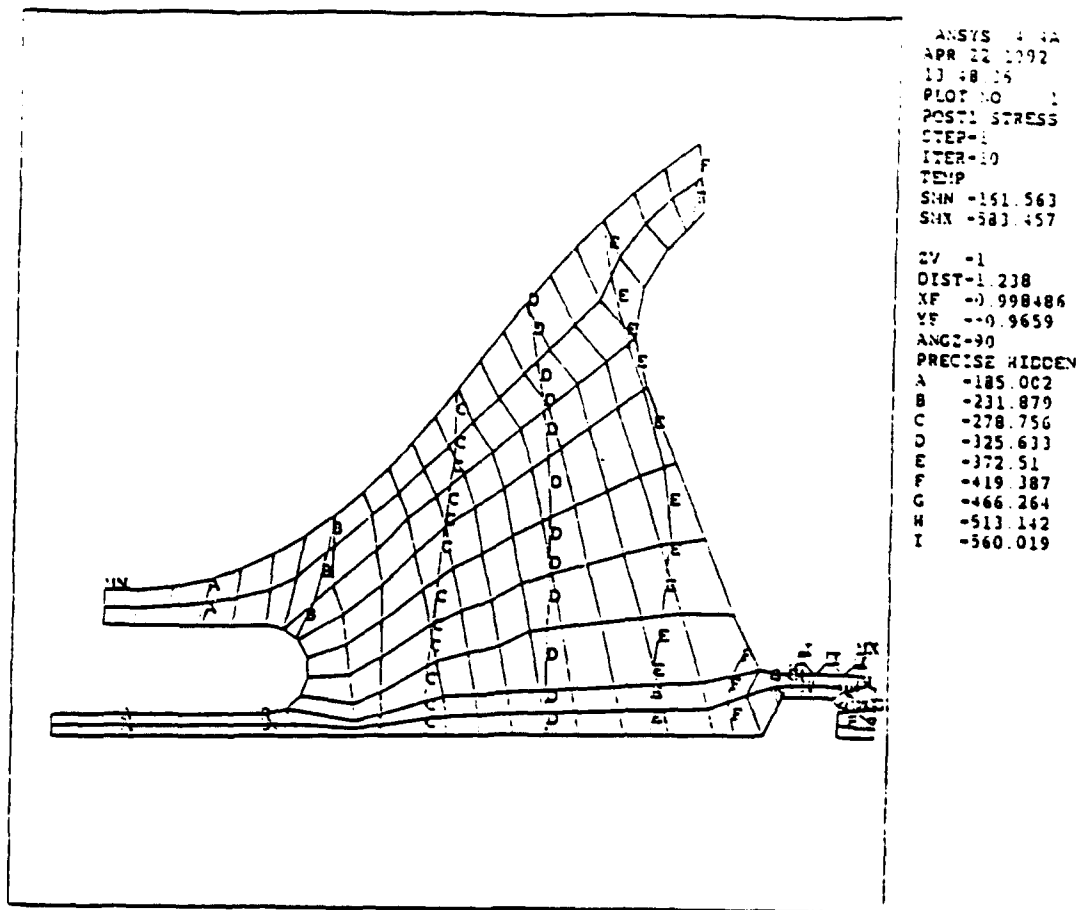


Figure 3-2. Stress analysis plots (in psi) of the disk and blade at 99.8 krpm and at the operating temperature.

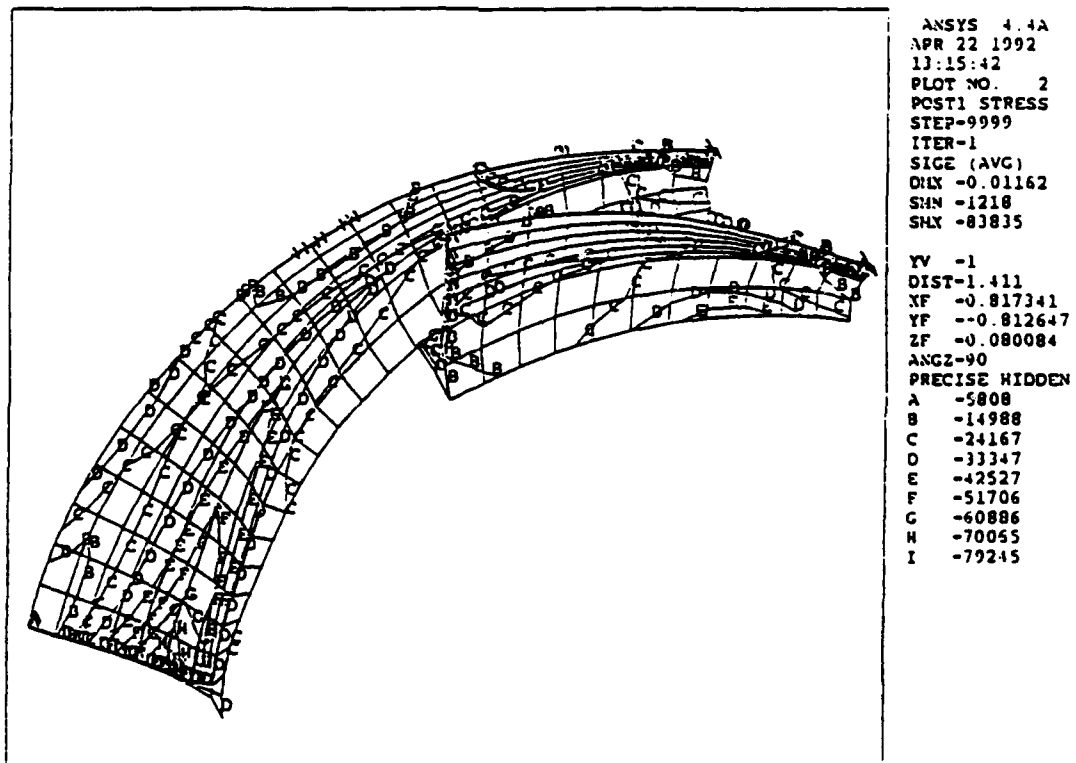
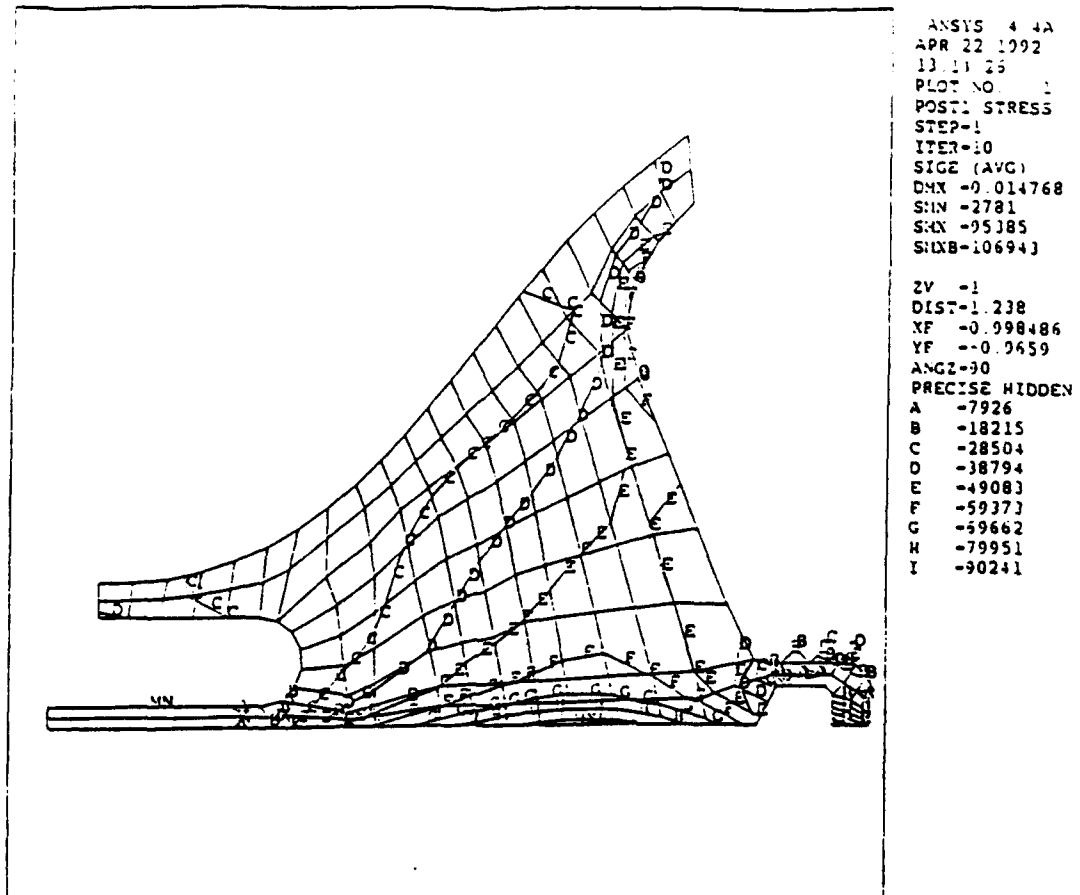
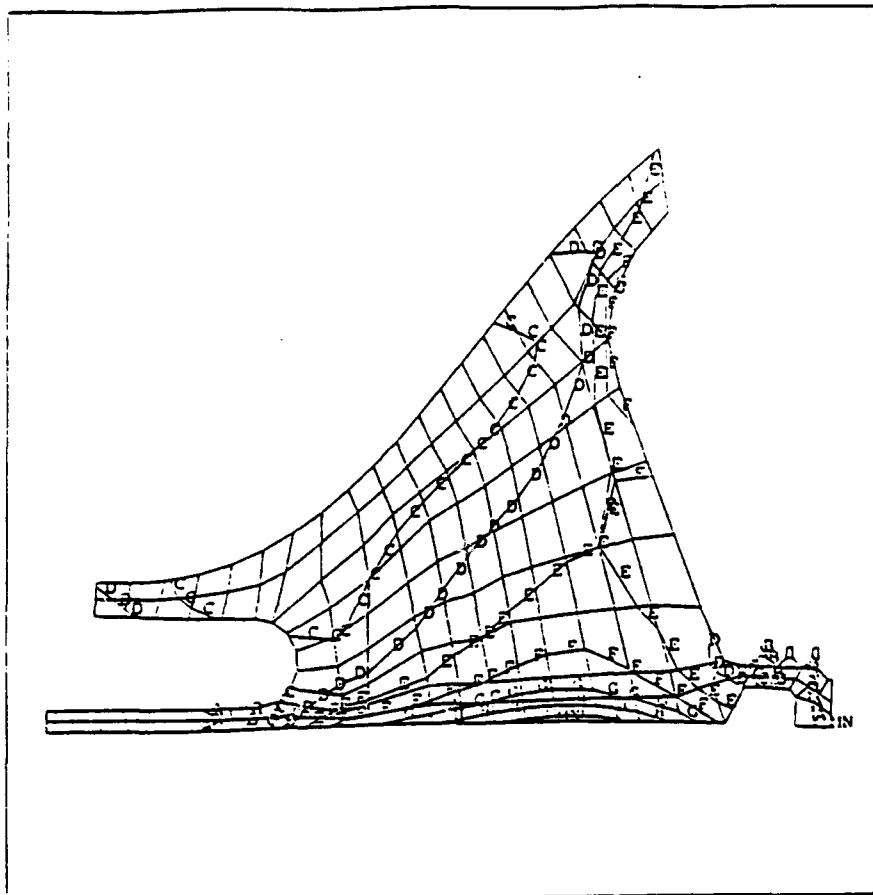


Figure 3-3. Equivalent stress analysis plots (in psi) of the disk and blade at the design speed, 115 krpm, at the operating temperature.

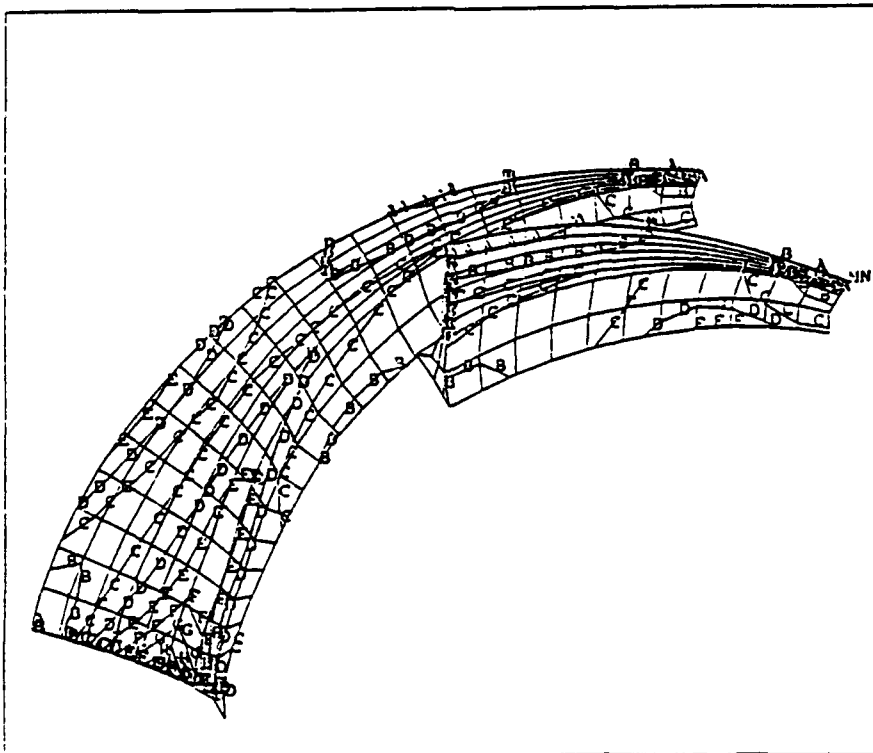


```

ANSYS 4.4A
APR 22 1992
13:35:40
PLOT NO. 1
POST1 STRESS
STEP=1
ITER=10
SICE (AVG)
DMX -0.005041
SMN -1019
SMX -93833
SMXB-105016

ZV -1
DIST=1.238
XF -0.998486
YF --0.9659
ANGZ=90
PRECISE HIDDEN
A -5176
B -16488
C -26801
D -37113
E -47426
F -57739
G -68051
H -78364
I -88676

```



```

ANSYS 4.4A
APR 22 1992
13:37:48
PLOT NO. 2
POST1 STRESS
STEP=9999
ITER=1
SICE (AVG)
DMX -0.00913
SMN -1756
SMX -82455

YV -1
DIST=1.411
XF -0.817341
YF --0.812647
ZF -0.080084
ANGZ=90
PRECISE HIDDEN
A -6240
B -15206
C -24173
D -33139
E -42106
F -51072
G -60039
H -69005
I -77972

```

Figure 3-4. Equivalent stress analysis plots (in psi) of the disk and blade at the design speed, 115 krpm, at room temperature.

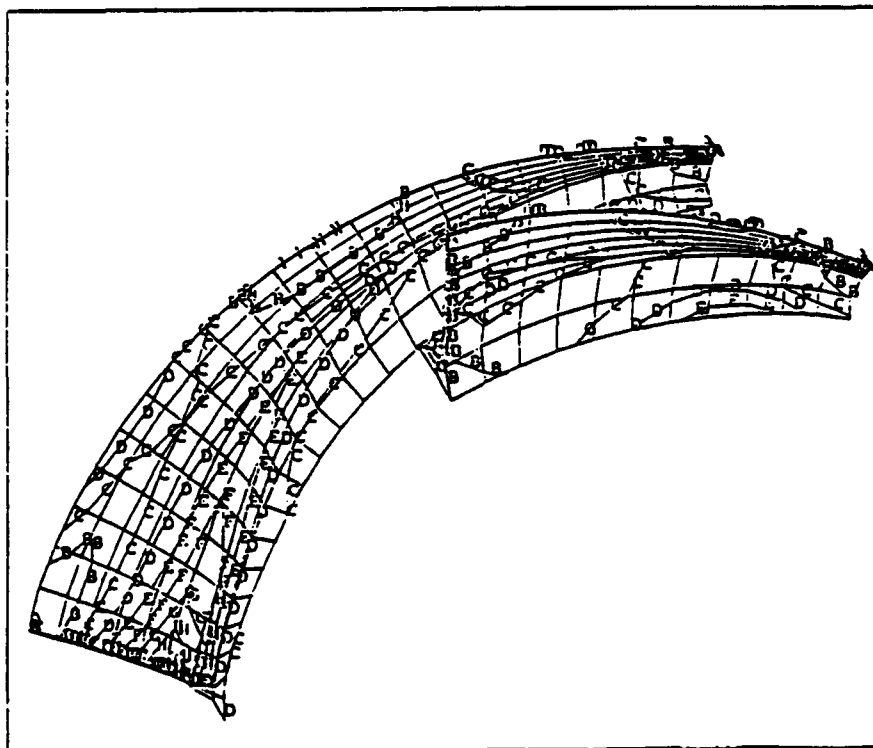
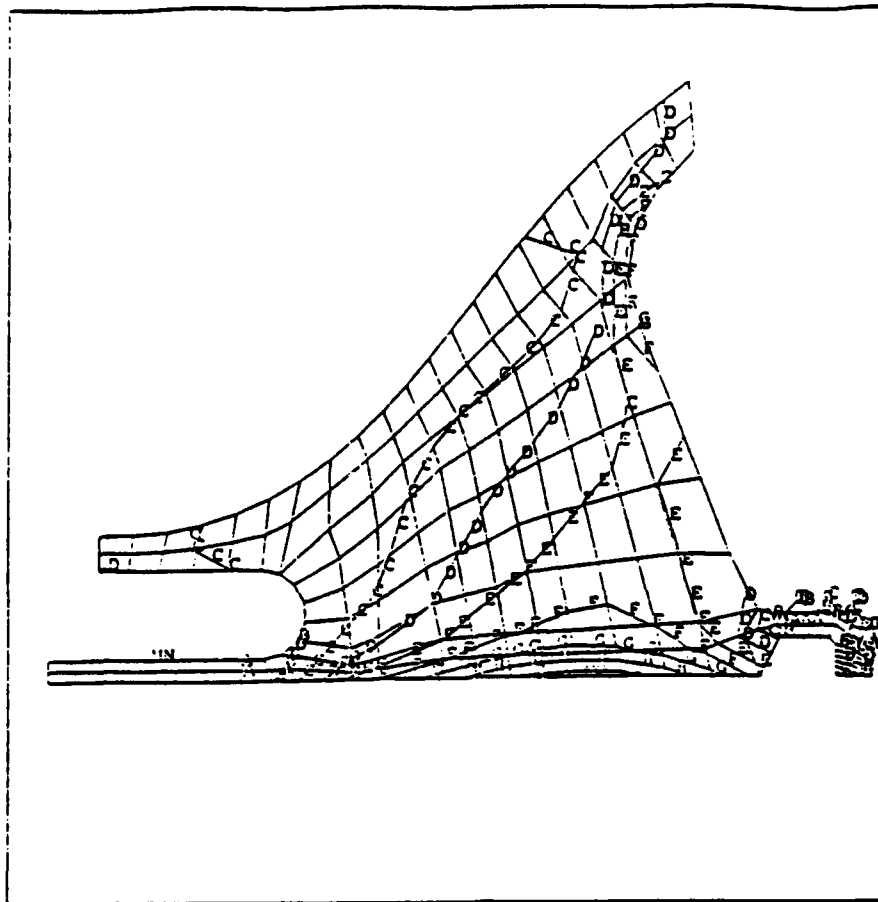
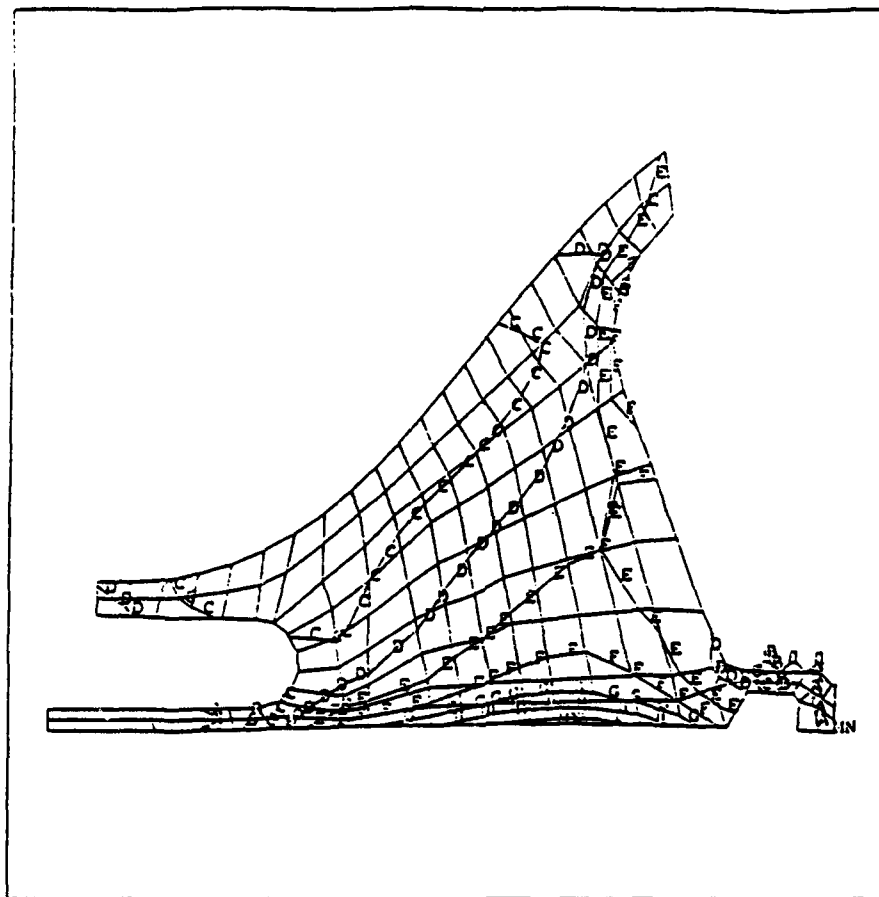
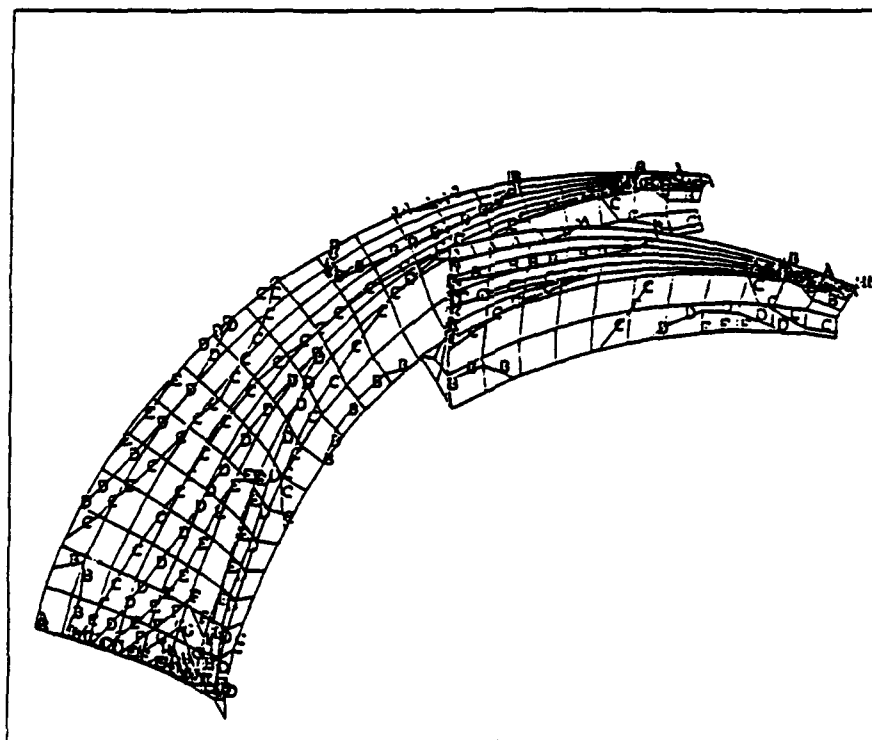


Figure 3-5. Equivalent stress analysis plots (in psi) of the disk and blade at 108.4 krpm at operating temperatures.



ANSYS 4.1A  
 APR 23 1992  
 9:37:48  
 PLOT NO. 1  
 POST1 STRESS  
 STEP-1  
 ITER-10  
 SICE (AVG)  
 DMX -0.004479  
 SMN -905.599  
 SMX -83371  
 SHXB-93308  
 ZV -1  
 DIST-1.238  
 XF -0.998486  
 YF --0.9659  
 ANG2-90  
 PRECISE HIDDEN  
 A -5487  
 B -14650  
 C -23813  
 D -32976  
 E -42138  
 F -51301  
 G -60464  
 H -69627  
 I -78790



ANSYS 4.1A  
 APR 23 1992  
 9:38:10  
 PLOT NO. 2  
 POST1 STRESS  
 STEP-9999  
 ITER-1  
 SICE (AVG)  
 DMX -0.008112  
 SMN -1561  
 SMX -73262  
 YV -1  
 DIST-1.411  
 XF -0.817341  
 YF --0.812647  
 ZF -0.080084  
 ANG2-90  
 PRECISE HIDDEN  
 A -5544  
 B -13511  
 C -21478  
 D -29445  
 E -37411  
 F -45378  
 G -53345  
 H -61312  
 I -69279

Figure 3-6. Equivalent stress analysis plots (in psi) of the disk and blade at 108.4 krpm at room temperature.

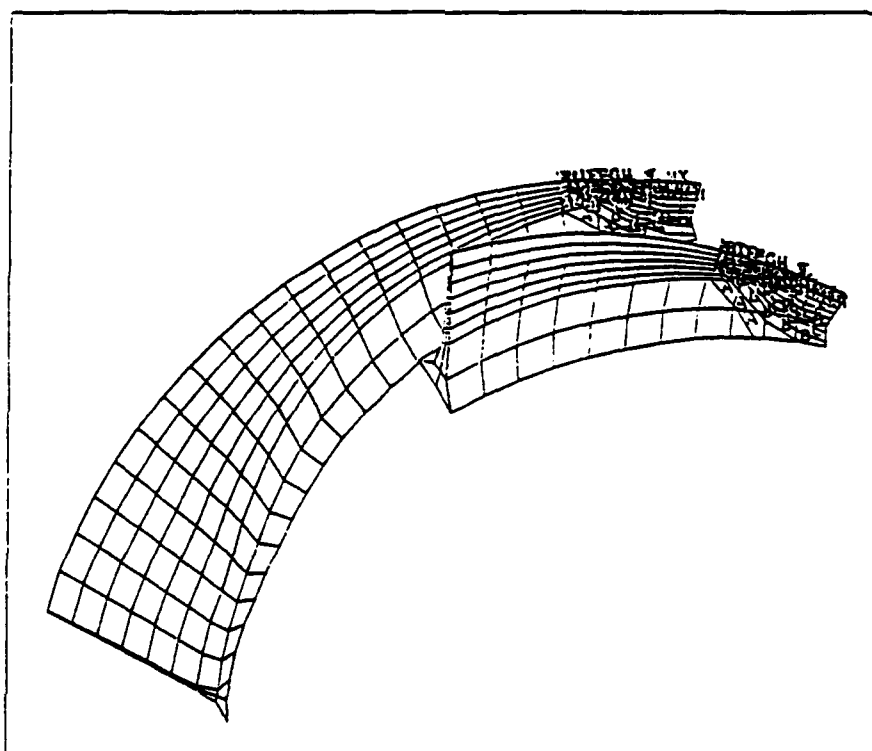
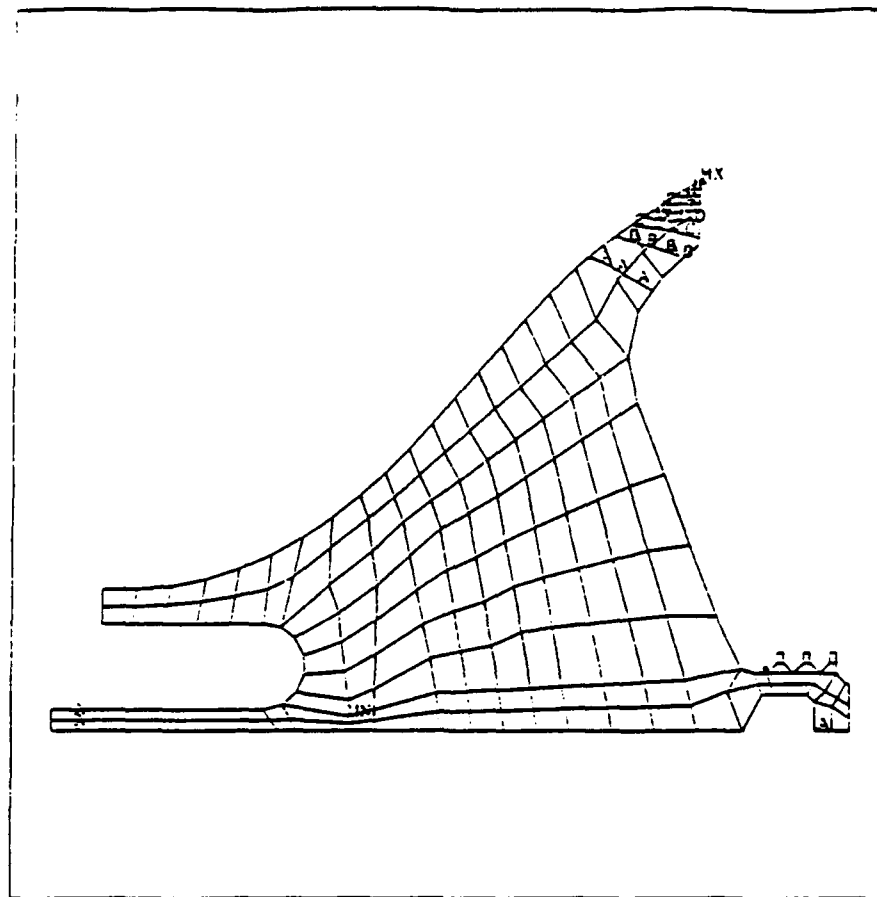
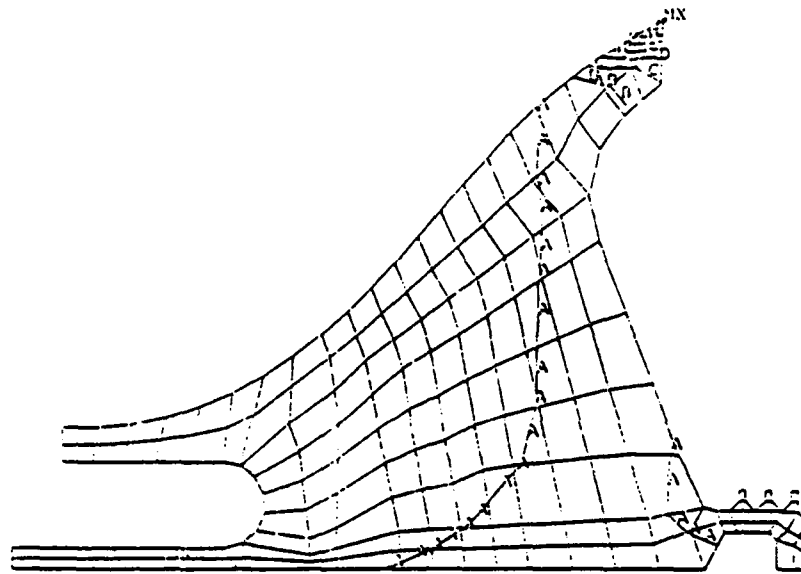
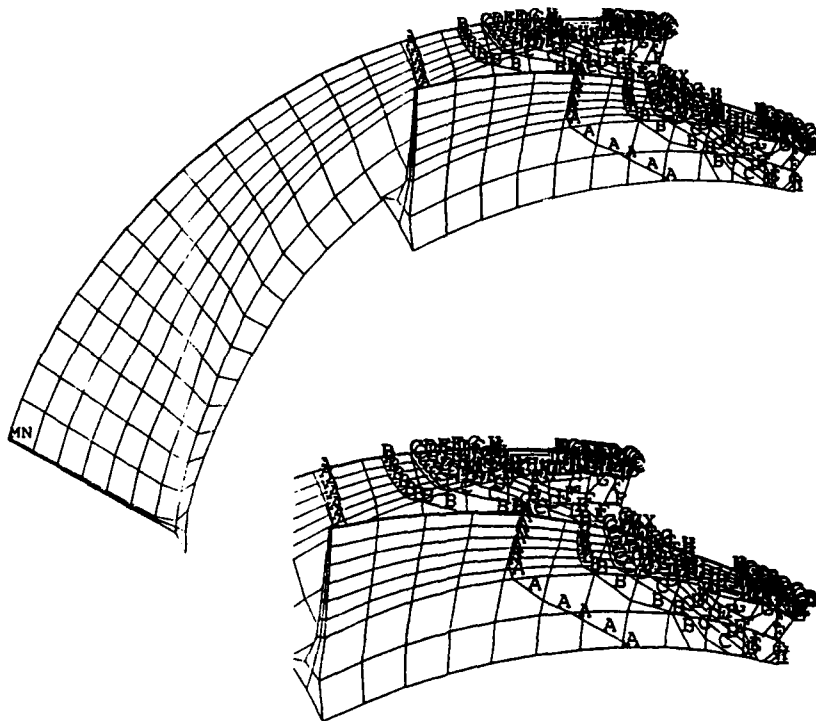


Figure 3-7. Temperature plot (in °F) of the disk and blade at 18.34 krpm at average peak temperatures experienced by the blade during a cartridge start at 0.916 second after ignition.



ANSYS 4.1A  
JUN 25 1992  
10:25:07  
PLOT NO. 1  
POST1 STRESS  
STEP=1  
ITER=10  
SIZE (AVG)  
SMN =19.100  
SMX =34045  
SHNB=40796  
  
ZV =1  
DIST=1.238  
XF =-0.998486  
YF =-0.9659  
ANGZ=90  
PRECISE HIDDEN  
A =1929  
B =5707  
C =9486  
D =13264  
E =17042  
F =20821  
G =24599  
H =28378  
I =32156



ANSYS 4.1A  
JUN 25 1992  
10:26:40  
PLOT NO. 2  
POST1 STRESS  
STEP=0999  
ITER=1  
SIZE (AVG)  
SMN =104.198  
SMX =47324  
  
YV =1  
DIST=1.411  
XF =-0.917341  
YF =-0.812647  
ZF =-0.080084  
ANGZ=90  
PRECISE HIDDEN  
A =2505  
U =16308  
C =27110  
D =37912  
E =48714  
F =59516  
G =70319  
H =81121  
I =91923

Figure 3-8. Equivalent stress analysis plots (in psi) of the disk and blade at 18.34 krpm at average peak temperatures. A53

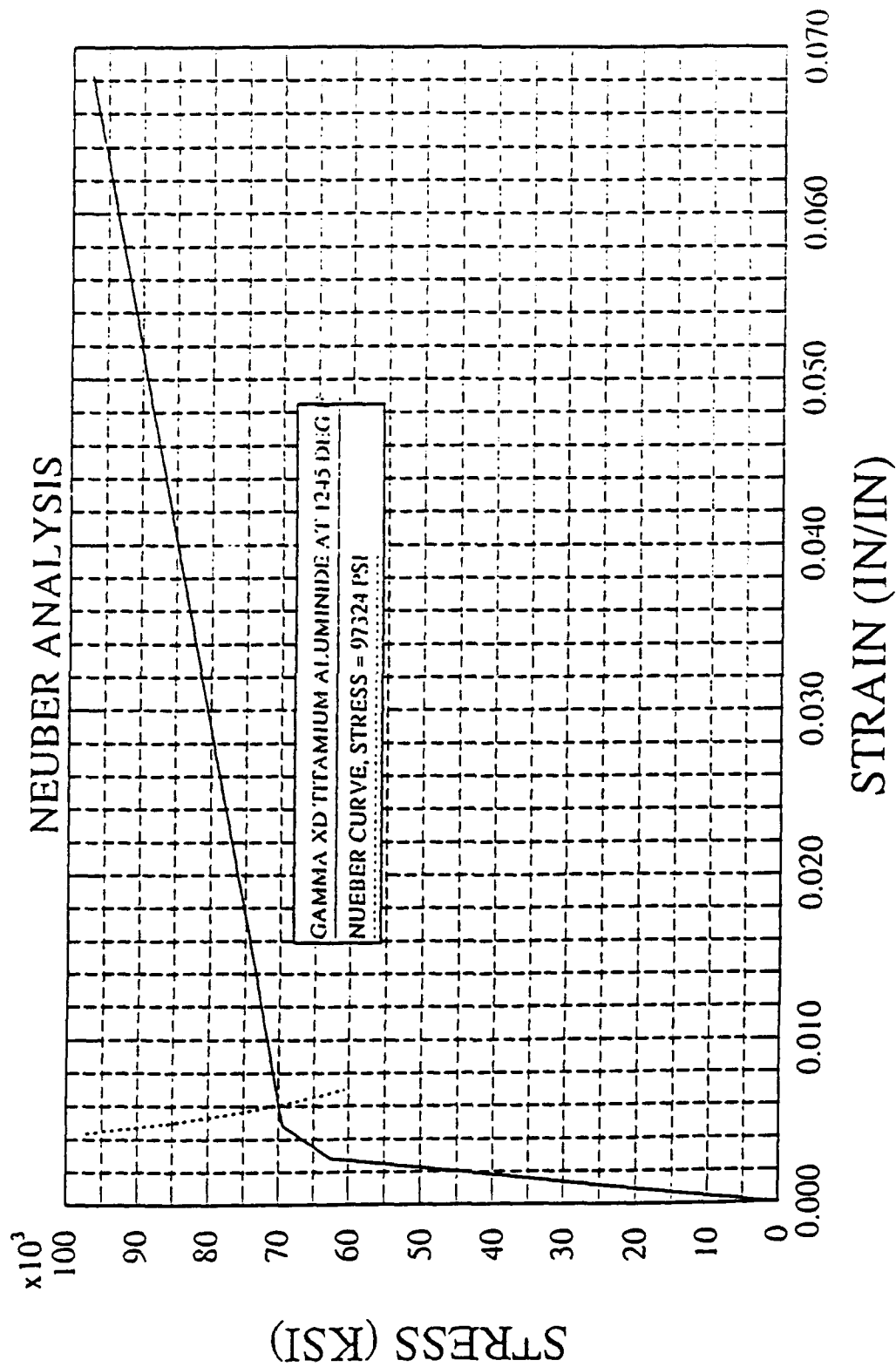


Figure 3-9. Neuber analysis for the maximum stress of 97.3 ksi at 1245°F for the XD® titanium aluminide compressor rotor.



Table 3-1. Ti-47Al-2Mn-2V + 7 volume % TiB<sub>2</sub> material properties used for the elastic stress analysis. Linear interpolation was performed to determine some data points at specific intermediate temperatures.

Temperature (°F)	Elastic Modulus (psi x 10 <sup>6</sup> )
70	25.8
500	24.7
1000	23.6
1200	23.4
1400	18.6
1600	13.5
1800	11.1
2000	6.5

Temperature (°F)	Coefficient of Thermal Expansion, x 10 <sup>-6</sup> (in/in/°F)
32	5.06
212	5.44
572	6.0
1112	6.39
1472	6.73
1652	6.89

- Poisson's ratio at 70°F = 0.3
- Density (lb<sub>f</sub>/in<sup>3</sup>) at 70°F = 0.144

#### 4. Critical flow size prediction

The critical flow size for the compressor rotor was calculated for XD<sup>®</sup> titanium aluminide. The equation used to make this prediction was:

$$K = AM_k \sigma \sqrt{\{(\pi a) / (Q^2)\}}$$

where: A = Free front surface correction factor (in this case 1.12)

M<sub>k</sub> = Free back surface correction factor (in this case 1.0)

σ = Stress normal to flaw (544 MPa or 79 ksi)

Q<sup>2</sup> = shape parameter (for a/2c = 0.33, Q = 1.7)

a = flaw depth in inches

c = 1/2 flaw surface length in inches

Note that M<sub>k</sub> varies with the ratio of crack size to back face length, and approaches 1 for large diameters. Also note that Q varies with the ratio (a/2c). It is 0 when the ratio is 0 and 2.467 when the ratio is 0.5. The stress, σ, of 544 MPa used by Williams was based on previous analysis.

The critical crack size is 0.037 cm (0.0146 in) deep and 0.11 cm (0.0442 in) long.

#### 5. Dynamic analysis

A dynamic analysis was conducted on the blades and splitters. The existing design for the compressor rotor was used to construct interference diagrams and normalized tangential displacement contour curves for the blade and the splitter. XD<sup>®</sup> titanium aluminide property data utilized in the analysis were previously shown in Table 3-1.

ANSYS version 4.4A finite element 3D models for the blade and splitter were generated from the aerodynamic definition using RATRAP. One hundred masters were used in the analysis, which included stress stiffening, spin softening and temperature effects. The disk was assumed to be rigid. The steady state temperature distributions for sea level, 0.8 mach, standard day for the blade and splitter are shown in Figures 5-1 and 5-2, respectively. The interference diagrams for the blade and splitter are shown in Figures 5-3 and 5-4, respectively. The idle and maximum operating speeds were 92,500 and 115,000 rpm, respectively.

Blade normalized tangential displacement contours are shown in Figures 5-5 to 5-18 for modes 1 to 14, respectively. All of the low modes are associated with leading edge responses. Splitter normalized tangential displacement contours are shown in Figures 5-19 to 5-21 for modes 1 to 3, respectively. The natural frequencies are listed in Table 5-1.

The blade has interferences associated with the eight starter impingement nozzles and modes 2 and 3 (12,101 and 16,165 Hz). However, at these frequencies the disturbing force is applied at the trailing edge while the response is at the leading edge. There are no significant responses, at the location of starter impingement, for frequencies less than 60,000 Hz. Also for a given disturbing force at frequencies greater than 60,000 Hz the displacement response is virtually insignificant. Therefore, the 8E interferences are not a concern for the blade. There are no 8E interferences associated with the splitter.

The main sources of dynamic excitation are the diffuser vanes (23), the impingement nozzles (8), and the inlet struts (2). The disturbances caused by the 23 diffuser vanes and the eight impingement nozzles are minimal. However, the disturbances caused by the two-inlet struts are significant. A three-inlet strut design would reduce the risk by shifting the frequency of the interference outside of the run envelope. Using a three-inlet strut would require the fabrication of a new component within the engine, but would reduce the risk on the compressor rotor.

```

ANSYS  4.4A
APR 22 1992
15:57:53
PLOT NO.  1
POST1  STRESS
STEP=1
ITER=1
TEMP
SMN  =159.965
SMX  =416.996

XV  =1
YV  =1
ZV  =1
DIST=1.657
XF  =0.817609
YF  =-0.812647
ZF  =-0.156196
VUP =X
PRECISE HIDDEN
A  =174.245
B  =202.804
C  =231.363
D  =259.922
E  =288.481
F  =317.04
G  =345.599
H  =374.158
I  =402.717

```

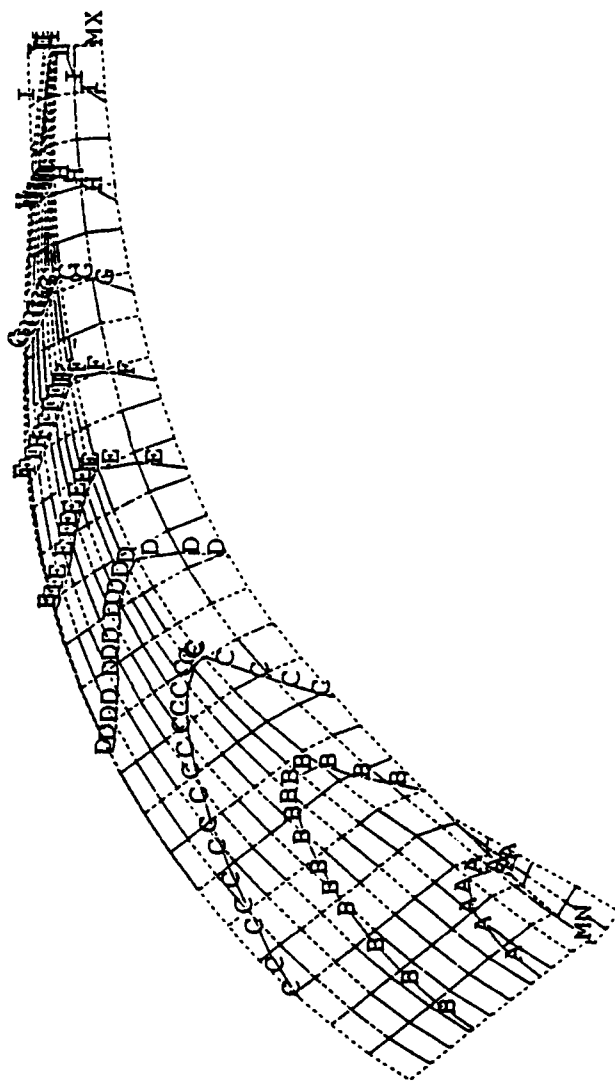


Figure 5-1. Four inch compressor blade steady state temperature distribution (in °F) for SL, 0.8 mach, standard day.

ANSYS 4.4A  
APR 23 1992  
9:28:31

PLOT NO. 1  
POST1 STRESS

STEP=1

ITER=1

TEMP

SMN =236.978

SMX =416.996

YV =1

DIST=0.76131

XF =1.232

YF =-1.227

ZF =0.671147

VUP =X

PRECISE HIDDEN

A =246.979

B =266.981

C =286.983

D =306.985

E =326.987

F =346.989

G =366.991

H =386.993

I =406.995

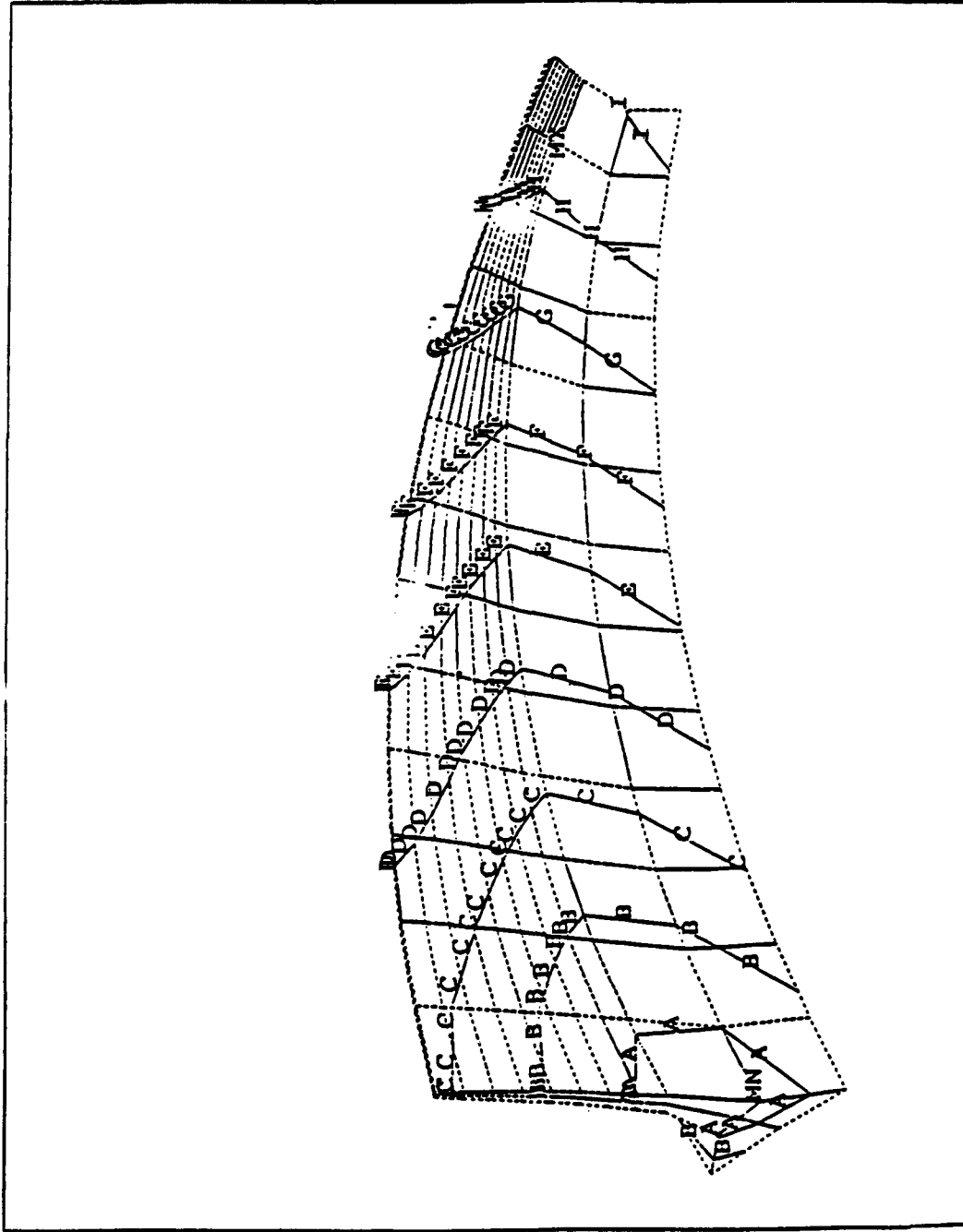


Figure 5-2. Four inch compressor splitter steady state temperature distribution (in °F) for SL 0.8 mach, standard day.

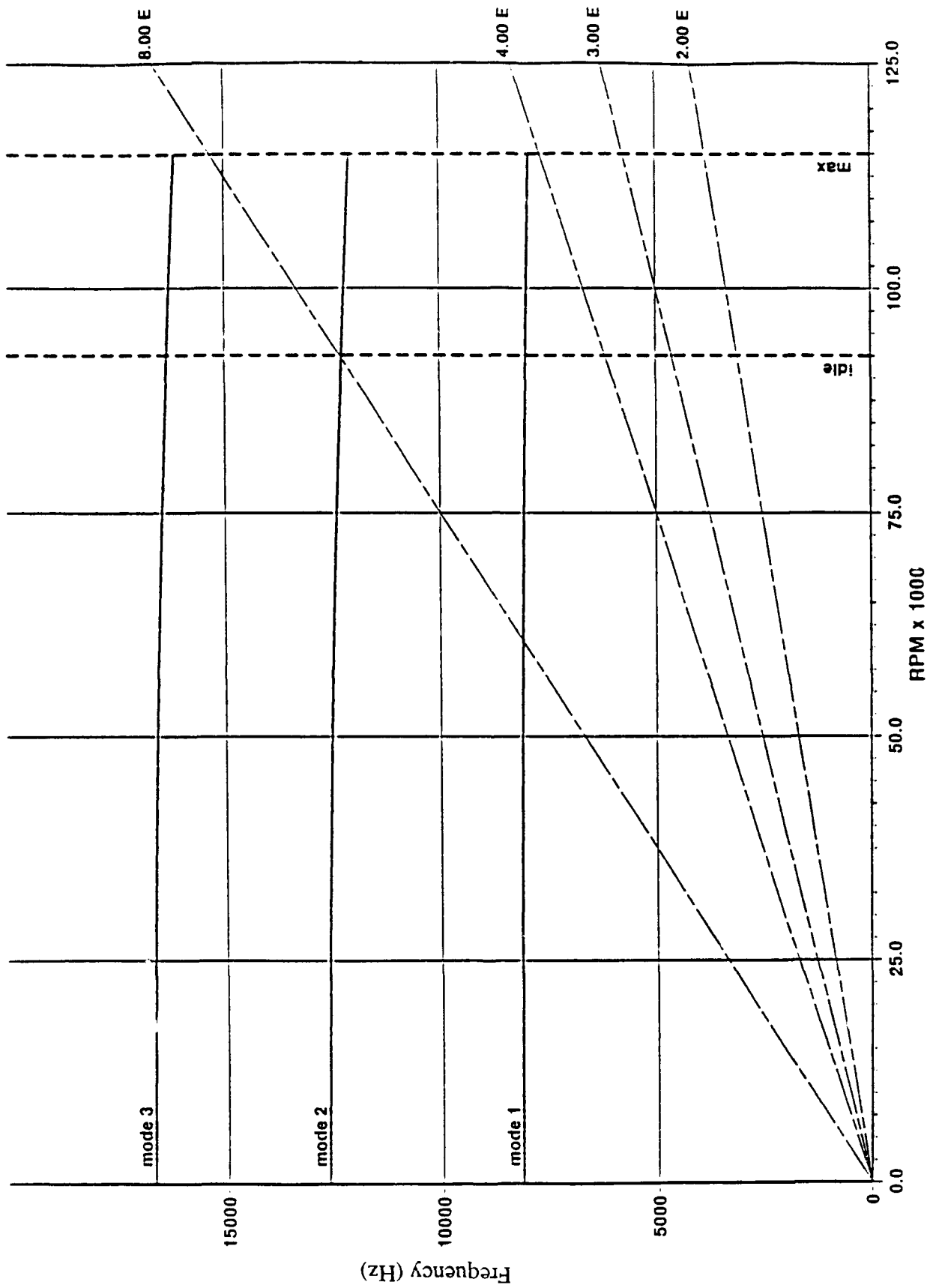


Figure 5-3. Four inch compressor blade interference diagram.

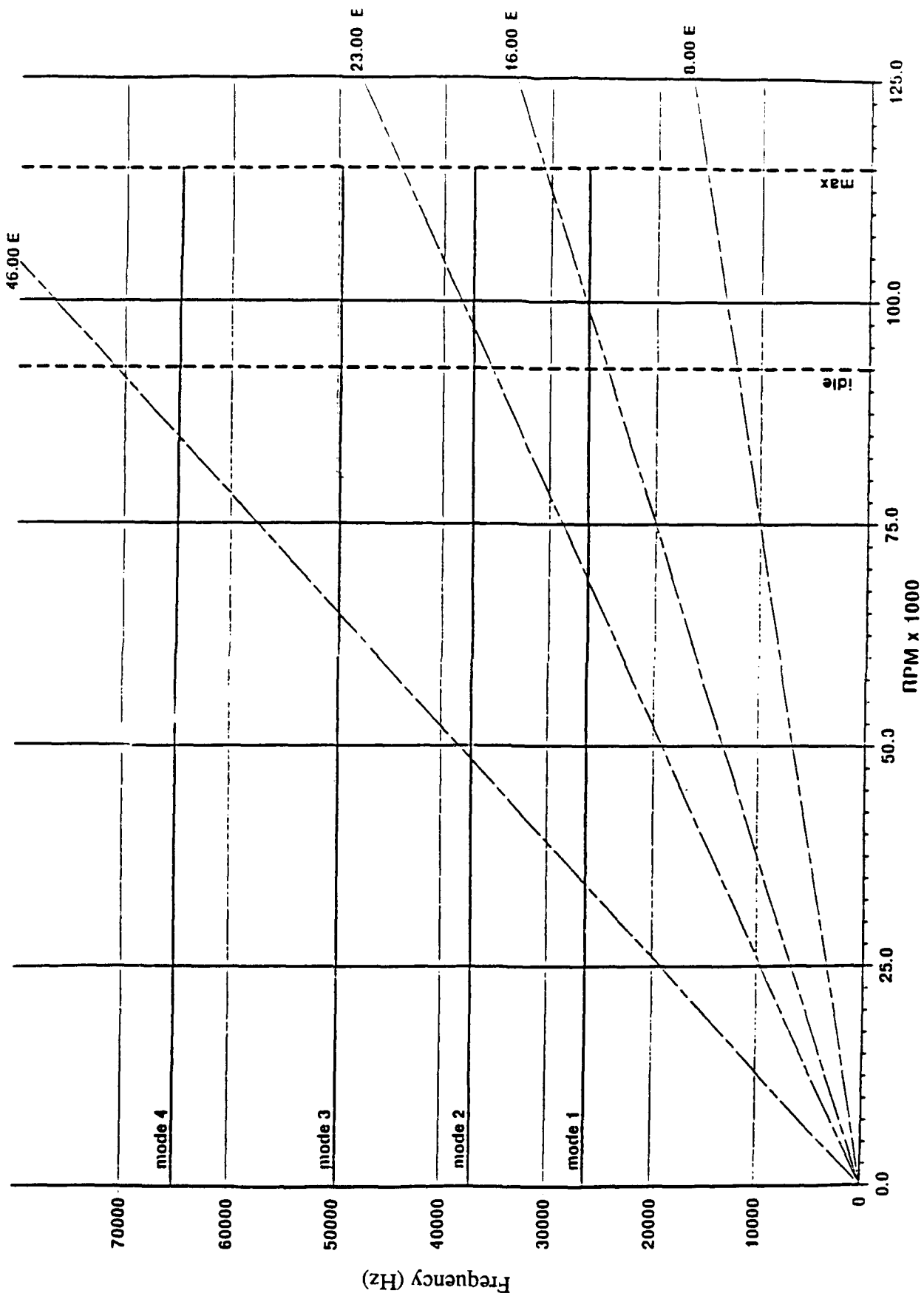


Figure 5-4. Four inch compressor splitter interference diagram.

```

ANSYS  4.4A
MAY  1 1992
15:48:45
PLOT NO.  1
POST1  STRESS
STEP=1
ITER=1
FREQ=7926
UY
CSYS=1
DMX =0.472E-04
SHN =-0.336E-07
SMX =0.420E-04

XV  =1
YV  =1
ZV  =1
DIST=1.657
XF  =0.817609
YF  =-0.812647
ZF  =-0.156196
VUP =X
PRECISE HIDDEN
A  =0.235E-05
B  =0.711E-05
C  =0.119E-04
D  =0.166E-04
E  =0.214E-04
F  =0.262E-04
G  =0.309E-04
H  =0.357E-04
I  =0.405E-04

```

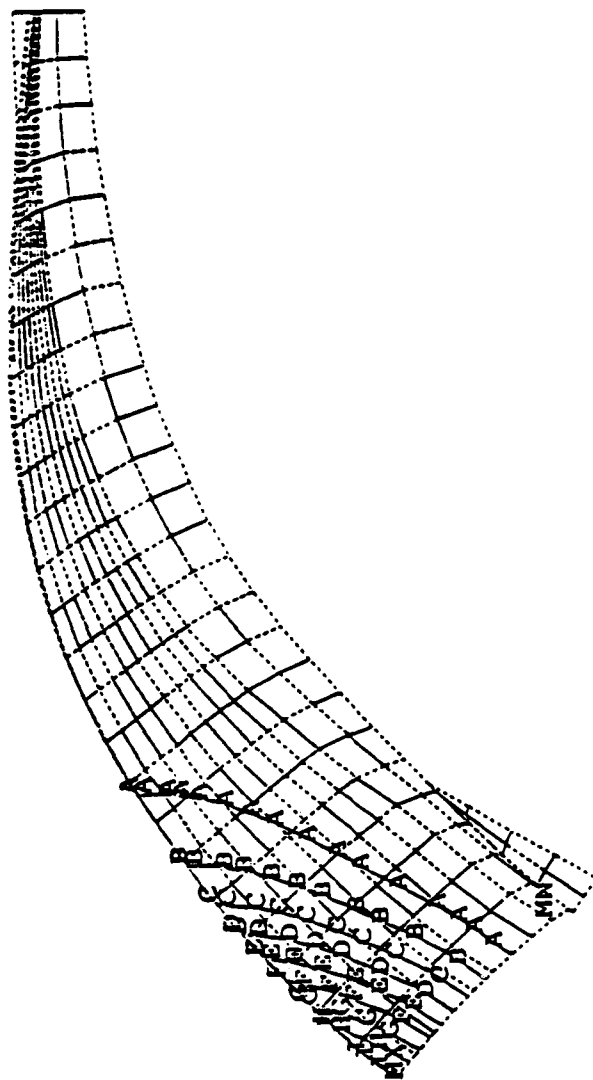


Figure 5-5. Four inch compressor blade normalized tangential displacement contours (in inches) for mode 1.



```

ANSYS  4.4A
MAY  1 1992
15:49:18
PLOT NO.  2
POST1  STRESS
STEP=1
ITER=2
FREQ=12101
UY
CSYS=1
DMX =0.162E-04
SMN =-0.124E-04
SNX =0.153E-04

XV  =1
YV  =1
ZV  =1
DIST=1.657
XF  =0.817609
YF  =-0.812647
ZF  =-0.156196
VUP =X
PRECISE HIDDEN
A  =-0.109E-04
B  =-0.777E-05
C  =-0.469E-05
D  =-0.161E-05
E  =0.147E-05
F  =0.455E-05
G  =0.763E-05
H  =0.107E-04
I  =0.138E-04

```

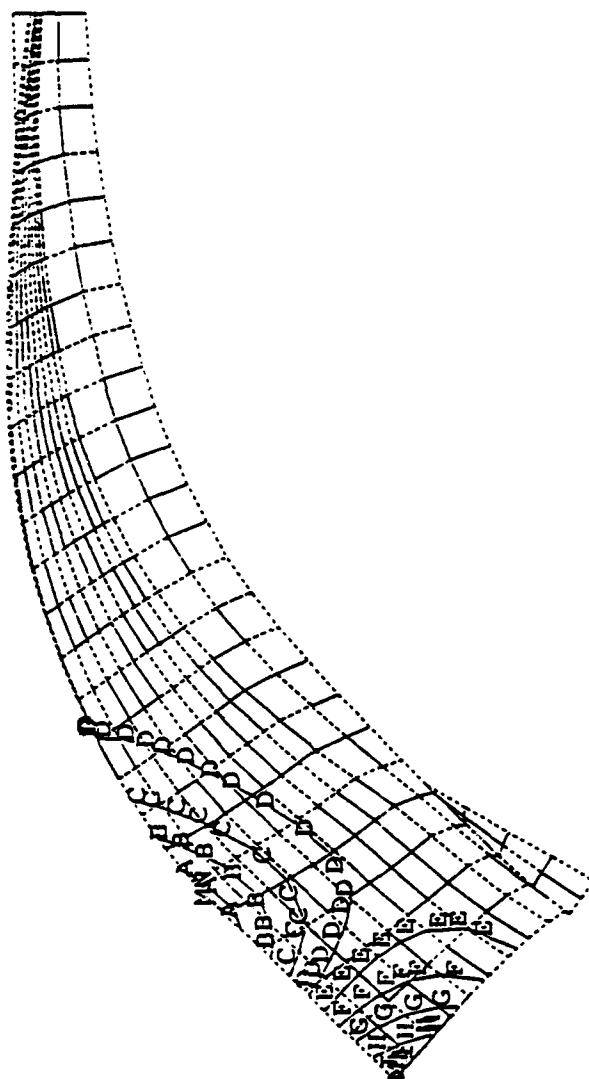


Figure 5-6. Four inch compressor blade normalized tangential displacement contours (in inches) for mode 2.

```

ANSYS  4.4A
MAY  1 1992
15:49:52
PLOT NO.    3
POST1  STRESS
STEP=1
ITER=3
FREQ=16165
UY
CSYS=1
DMX =0.136E-04
SMN =-0.120E-04
SMX =0.964E-05

XV  =1
YV  =1
ZV  =1
DIST=1.657
XF  =0.817609
YF  =-0.812647
ZF  =-0.156196
VUP =X
PRECISE HIDDEN
A  =-0.108E-04
B  =-0.840E-05
C  =-0.599E-05
D  =-0.359E-05
E  =-0.118E-05
F  =0.123E-05
G  =0.363E-05
H  =0.604E-05
I  =0.844E-05

```

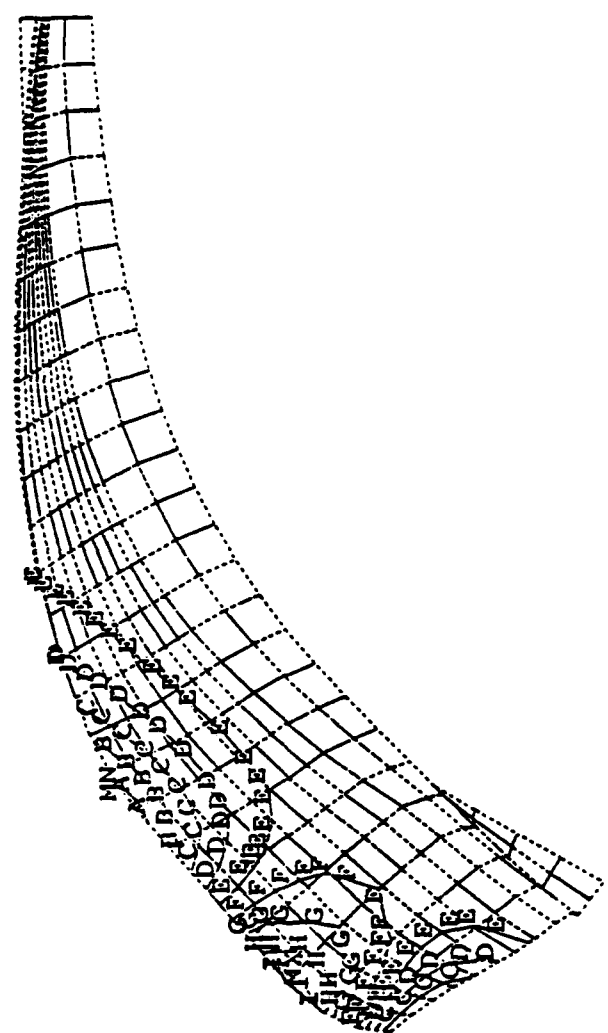


Figure 5-7. Four inch compressor blade normalized tangential displacement contours (in inches) for mode 3.

```

ANSYS  4.4A
MAY  1 1992
15:50:17
PLOT NO.  4
POST1  STRESS
STEP=1
ITER=4
FREQ=20172
UY
CSYS=1
DMX =0.526E-05
SMN =-0.435E-05
SMX =0.333E-05

XV  =1
YV  =1
ZV  =1
DIST=1.657
XF  =0.817609
YF  =-0.812647
ZF  =-0.156196
VUP =X
PRECISE HIDDEN
A  =-0.392E-05
B  =-0.307E-05
C  =-0.221E-05
D  =-0.136E-05
E  =-0.508E-06
F  =0.345E-06
G  =0.120E-05
H  =0.205E-05
I  =0.290E-05

```

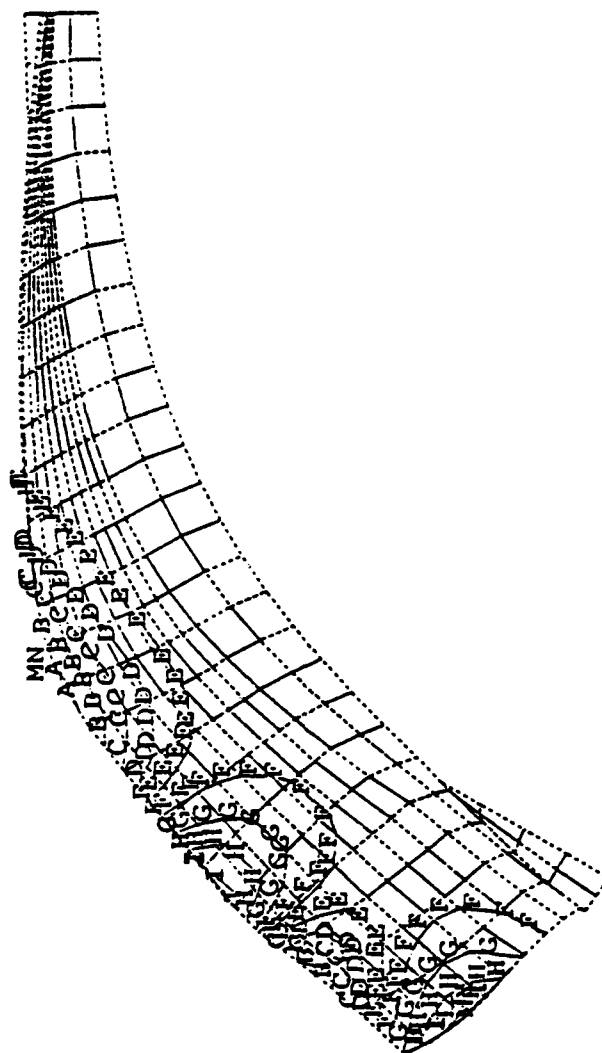


Figure 5-8. Four inch compressor blade normalized tangential displacement contours (in inches) for mode 4.

```

ANSYS  4.4A
MAY  1 1992
15:50:49
PLOT NO. 5
POST1  STRESS
STEP=1
ITER=5
FREQ=23859
UY
CSYS=1
DMX =0.975E-05
SMN =-0.724E-05
SMX =0.942E-05

XV  =1
YV  =1
ZV  =1
DIST=1.657
XF  =0.817609
YF  =-0.812647
ZF  =-0.156196
VUP =X
PRECISE  HIDDEN
A  =-0.632E-05
B  =-0.447E-05
C  =-0.261E-05
D  =-0.763E-06
E  =0.109E-05
F  =0.294E-05
G  =0.479E-05
H  =0.664E-05
I  =0.850E-05

```

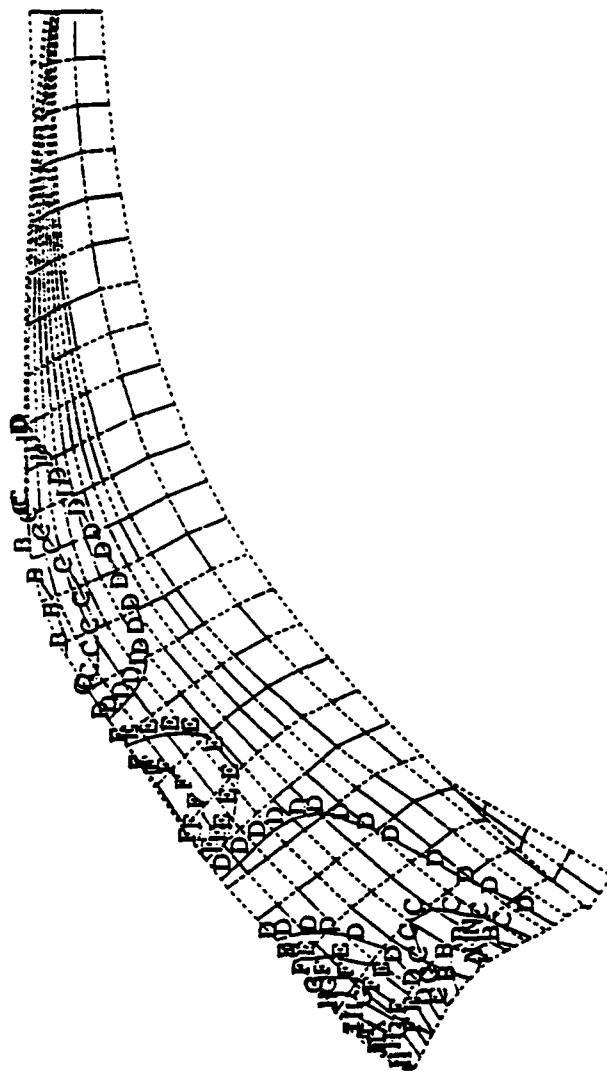


Figure 5-9. Four inch compressor blade normalized tangential displacement contours (in inches) for mode 5.

ANSYS 4.4A  
MAY 1 1992  
15:51:14  
PLOT NO. 6  
POST1 STRESS

STEP=1  
ITER=6  
FREQ=26126  
UY

CSYS=1  
DMX =0.240E-05  
SMN =-0.880E-06  
SMX =0.231E-05

XV =1  
YV =1  
ZV =1  
DIST=1.657  
XF =0.817609  
YF =-0.812647  
ZF =-0.156196  
VUP =X

PRECISE HIDDEN  
A =-0.703E-06  
B =-0.349E-06  
C =0.504E-08  
D =0.359E-06  
E =0.713E-06  
F =0.107E-05  
G =0.142E-05  
H =0.177E-05  
I =0.213E-05

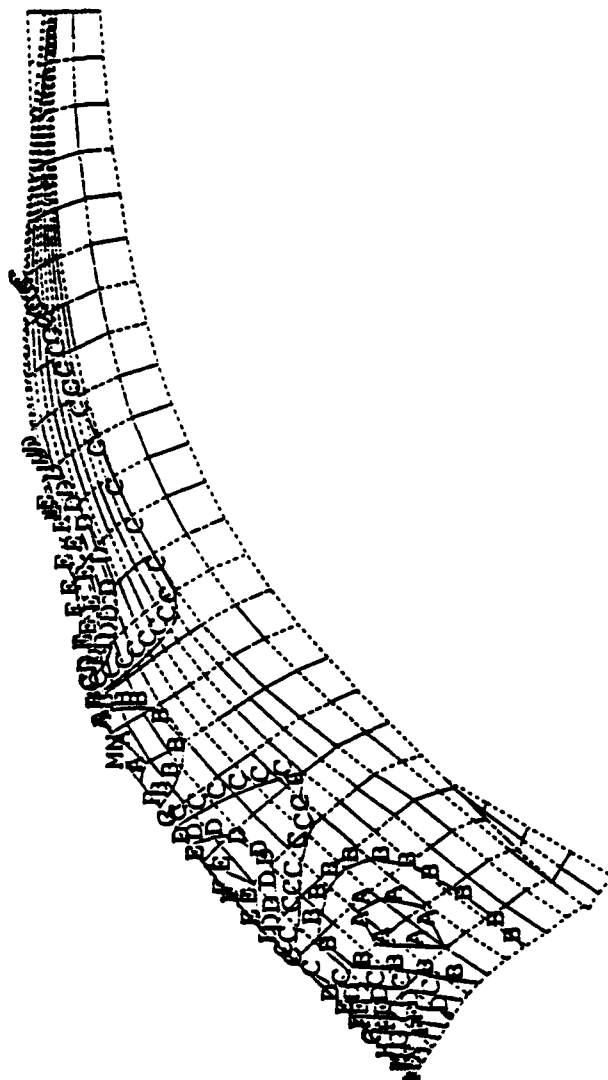


Figure 5-10. Four inch compressor blade normalized tangential displacement contours (in inches) for mode 6.



ANSYS 4.4A  
MAY 4 1992  
10:16:05

PLOT NO. 2  
POST1 STRESS

STEP=1

ITER=8

FREQ=34838

UY

CSYS=1

DMX =-0.226E-05

SMN =-0.219E-05

SMX =-0.113E-05

XV =1

YV =1

ZV =1

DIST=1.657

XF =-0.817609

YF =-0.812647

ZF =-0.156196

VUP =X

PRECISE HIDDEN

A = -.201000E-05

B = -.164000E-05

C = -.127000E-05

D = -.900000E-06

E = -.531000E-06

F = -.163000E-06

G = 0.206000E-06

H = 0.575000E-06

I = 0.943000E-06

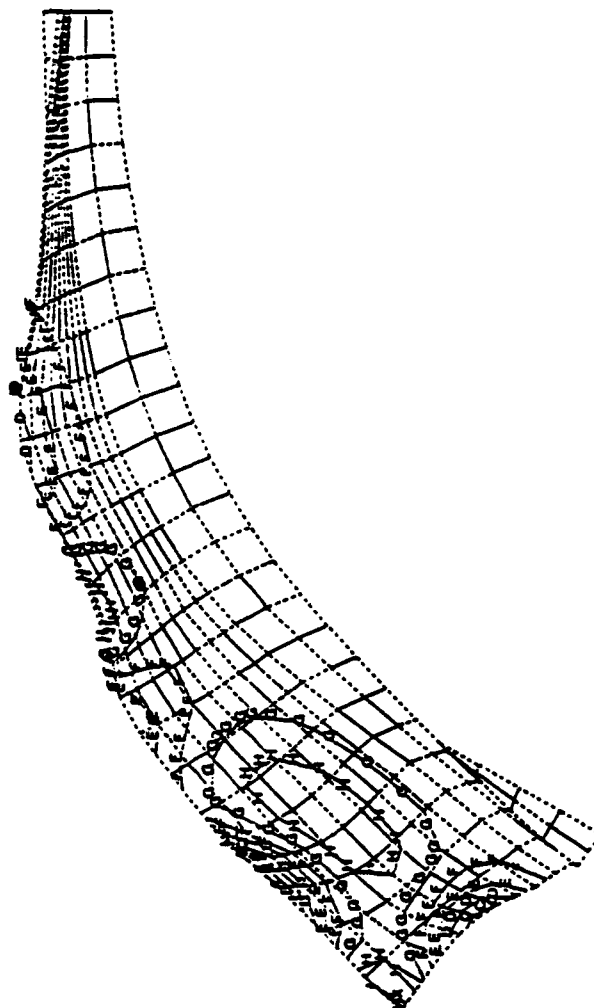


Figure 5-12. Four inch compressor blade normalized tangential displacement contours (in inches) for mode 8.

ANSYS 4.4A  
MAY 4 1992  
10:16:40  
PLOT NO. 3  
POST1 STRESS  
STEP-1  
ITER-9  
FREQ=37127  
UY

CSYS=1  
DMX =0.398E-05  
SMN =-0.378E-05  
SMX =0.242E-05

XV =1  
YV =1  
ZV =1  
DIST=1.657  
XF =0.817609  
YF =-0.812647  
ZF =-0.156196  
VUP =X

PRECISE HIDDEN  
A = -.344000E-05  
B = -.275000E-05  
C = -.206000E-05  
D = -.137000E-05  
E = -.681000E-06  
F = 0.782000E-08  
G = 0.697000E-06  
H = 0.139000E-05  
I = 0.208000E-05

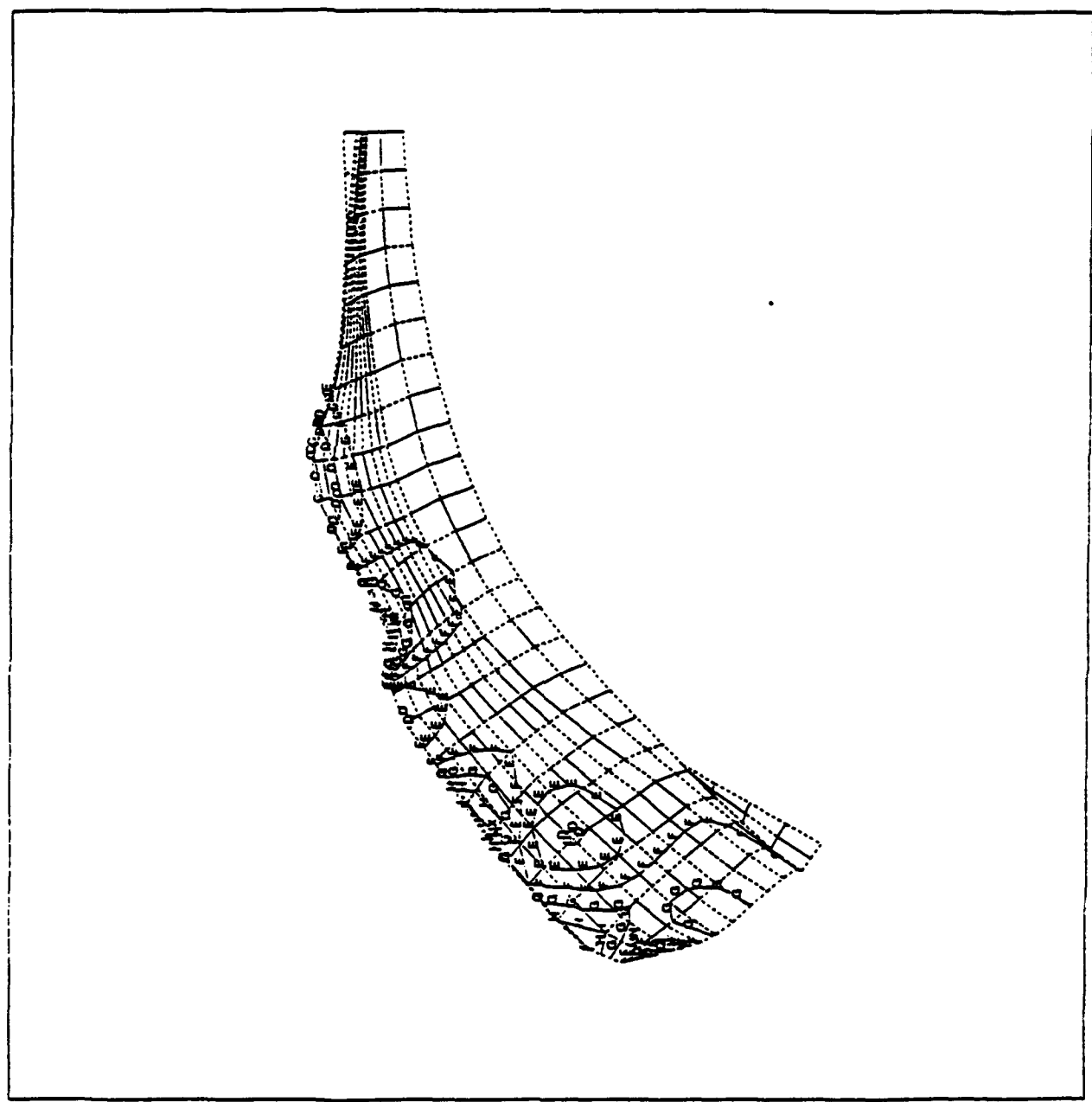


Figure 5-13. Four inch compressor blade normalized tangential displacement contours (in inches) for mode 9.



ANSYS 4.4A  
MAY 4 1992  
10:17:20

PLOT NO. 4  
POST1 STRESS  
STEP=1  
ITER=10  
FREQ=43100  
UY

CSYS=1  
DMX =0.530E-06  
SMN =-0.289E-06  
SMX =0.385E-06

XV =1  
YV =1  
ZV =1  
DIST=1.657  
XF =0.817609  
YF =-0.812647  
ZF =-0.156196  
VUP =X

PRECISE HIDDEN  
A = -.252000E-06  
B = -.177000E-06  
C = -.102000E-06  
D = -.270000E-07  
E = 0.480000E-07  
F = 0.123000E-06  
G = 0.198000E-06  
H = 0.273000E-06  
I = 0.348000E-06

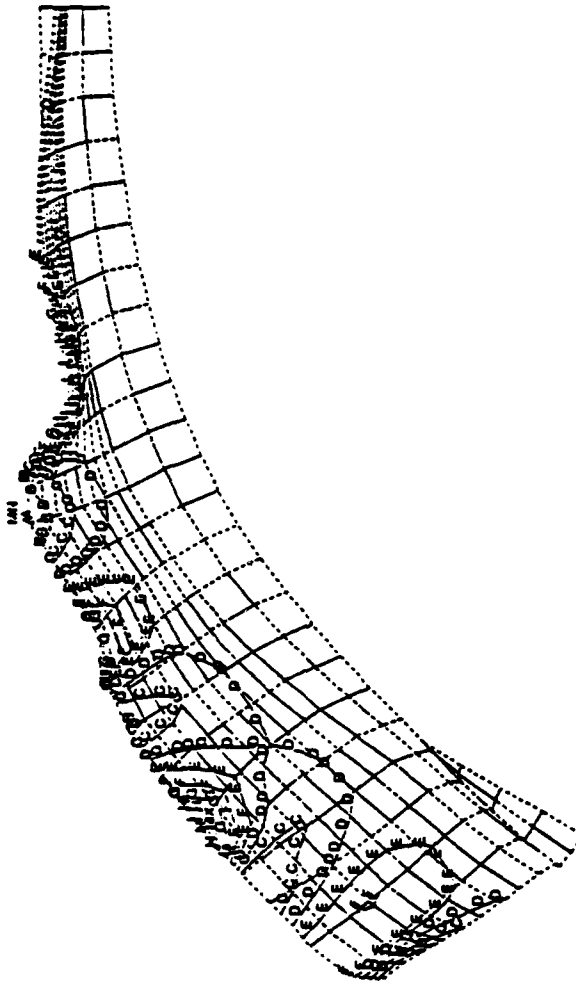


Figure 5-14. Four inch compressor blade normalized tangential displacement contours (in inches) for mode 10.

```

ANSYS  4.4A
MAY  4 1992
10:32:04
PLOT NO.    5
POST1  STRESS
STEP=1
ITER=11
FREQ=46829
UY
CSYS=1
DMX =-0.276E-05
SMN =-0.263E-05
SMX =-0.260E-05

XV  -1
YV  -1
ZV  -1
DIST=1.657
XF  -0.817609
YF  -0.812647
ZF  -0.156196
VUP  -X
PRECISE  HIDDEN
A  = -.234000E-05
B  = -.176000E-05
C  = -.118000E-05
D  = -.597000E-06
E  = -.163000E-07
F  =  0.565000E-06
G  =  0.115000E-05
H  =  0.173000E-05
I  =  0.231000E-05

```

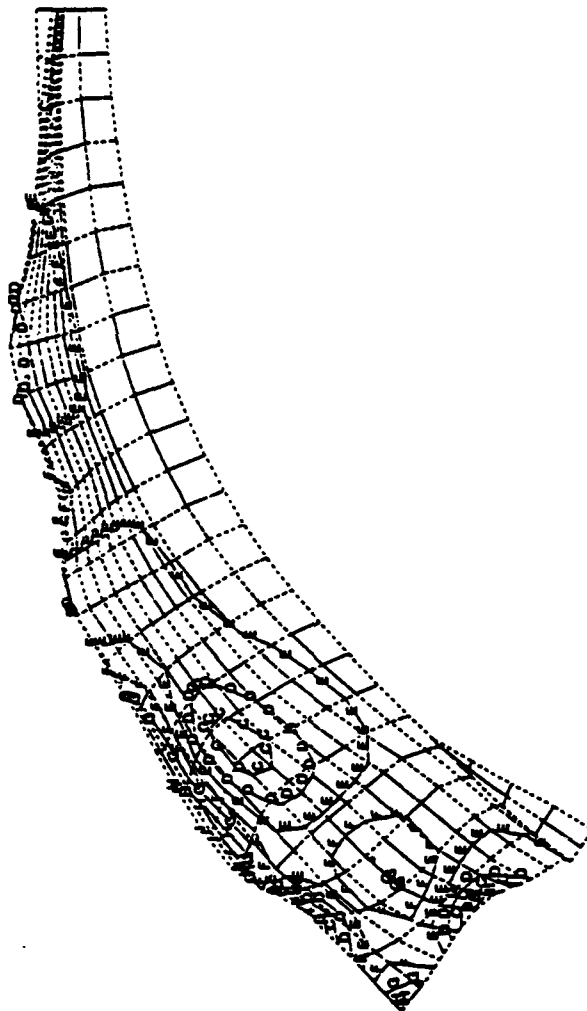


Figure 5-15. Four inch compressor blade normalized tangential displacement contours (in inches) for mode 11.

ANSYS 4.4A

MAY 4 1992

10:32:33

PLOT NO. 6

POST1 STRESS

STEP=1

ITER=12

FREQ=51300

UY

CSYS=1

DMX =-0.162E-06

SMN =-0.721E-07

SMX =-0.110E-06

XV =1

YV =1

ZV =1

DIST=1.657

XF =-0.817609

YF =-0.812647

ZF =-0.156196

VUP =X

PRECISE HIDDEN

A =-.620000E-07

B =-.418000E-07

C =-.216000E-07

D =-.139000E-08

E =0.188000E-07

F =0.390000E-07

G =0.592000E-07

H =0.794000E-07

I =0.996000E-07

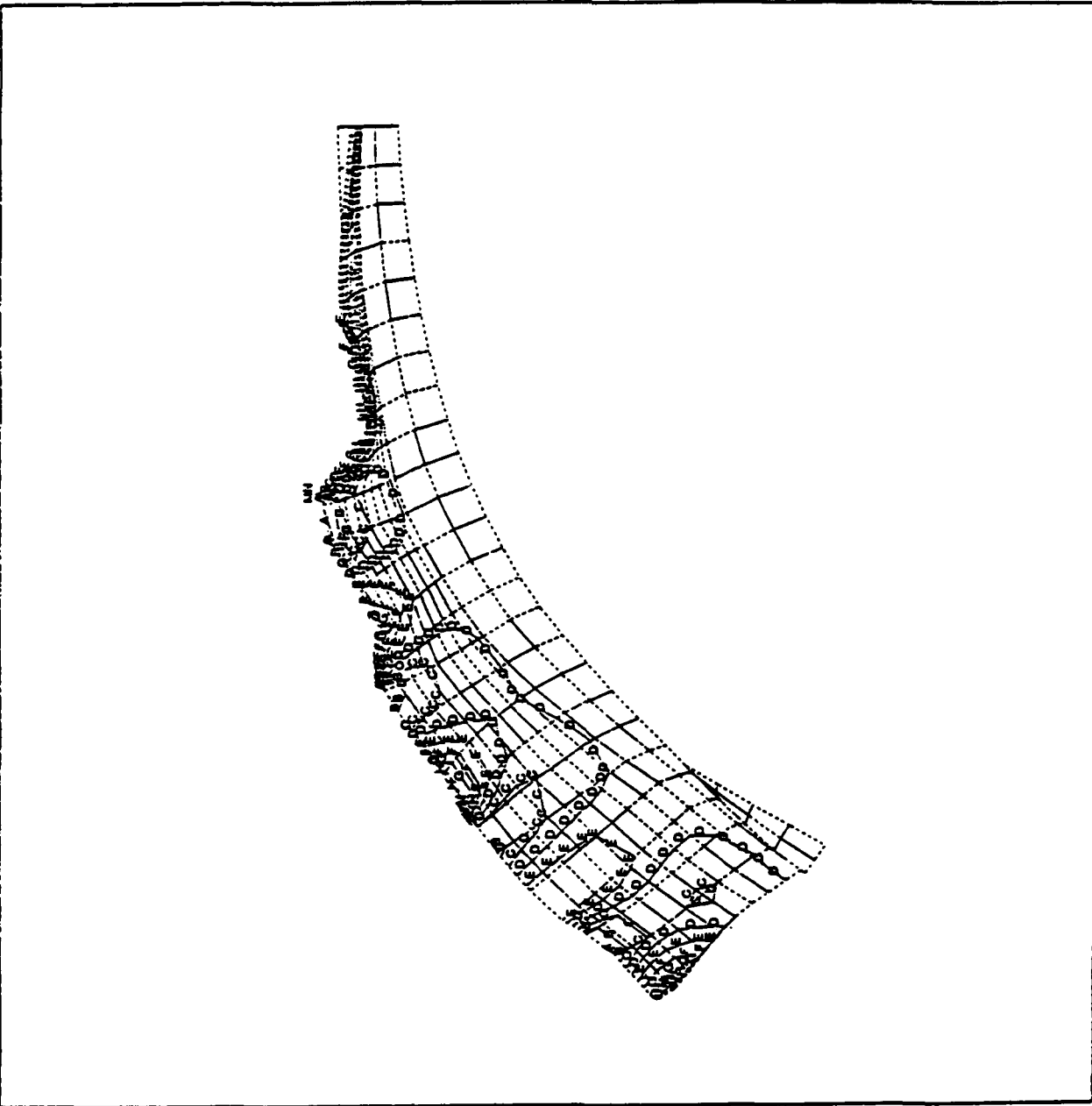


Figure 5-16. Four inch compressor blade normalized tangential displacement contours (in inches) for mode 12.

```

ANSYS  4.4A
MAY  4 1992
10:33:02
PLOT NO. 7
POST1  STRESS
STEP-1
ITER-13
FREQ=58078
UY
CSYS=1
DMX =-0.148E-05
SMN =-0.928E-06
SMX =-0.139E-05

XV  -1
YV  -1
ZV  -1
DIST=1.657
XF  -0.817609
YF  -0.812647
ZF  -0.156196
VUP -X
PRECISE  HIDDEN
A  = -.799000E-06
B  = -.542000E-06
C  = -.285000E-06
D  = -.273000E-07
E  =  0.230000E-06
F  =  0.487000E-06
G  =  0.744000E-06
H  =  0.100000E-05
I  =  0.126000E-05

```

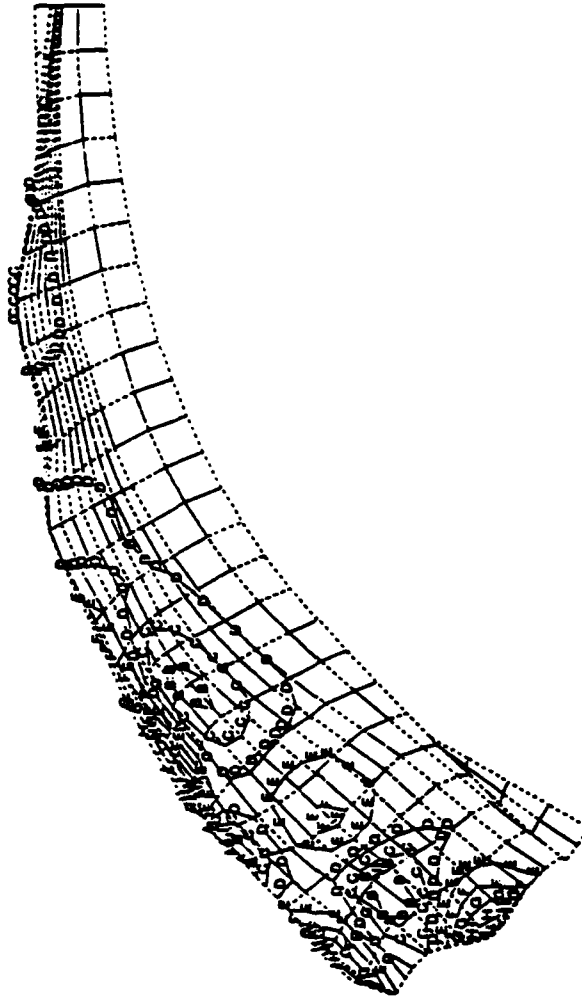


Figure 5-17. Four inch compressor blade normalized tangential displacement contours (in inches) for mode 13.

ANSYS 4.4A  
MAY 4 1992  
10:33:36

PLOT NO. 8  
POST1 STRESS

STEP=1  
ITER=14  
FREQ=59834  
UY

CSYS=1  
DMX =0.210E-05  
SMN =-0.177E-05  
SMX =0.145E-05

XV =1  
YV =1  
ZV =1  
DIST=1.657  
XF =0.817609  
YF =-0.812647  
ZF =-0.156196

VUP =X

PRECISE HIDDEN

A = -.159000E-05  
B = -.123000E-05  
C = -.876000E-06  
D = -.518000E-06  
E = -.161000E-06  
F = 0.196000E-06  
G = 0.554000E-06  
H = 0.911000E-06  
I = 0.127000E-05

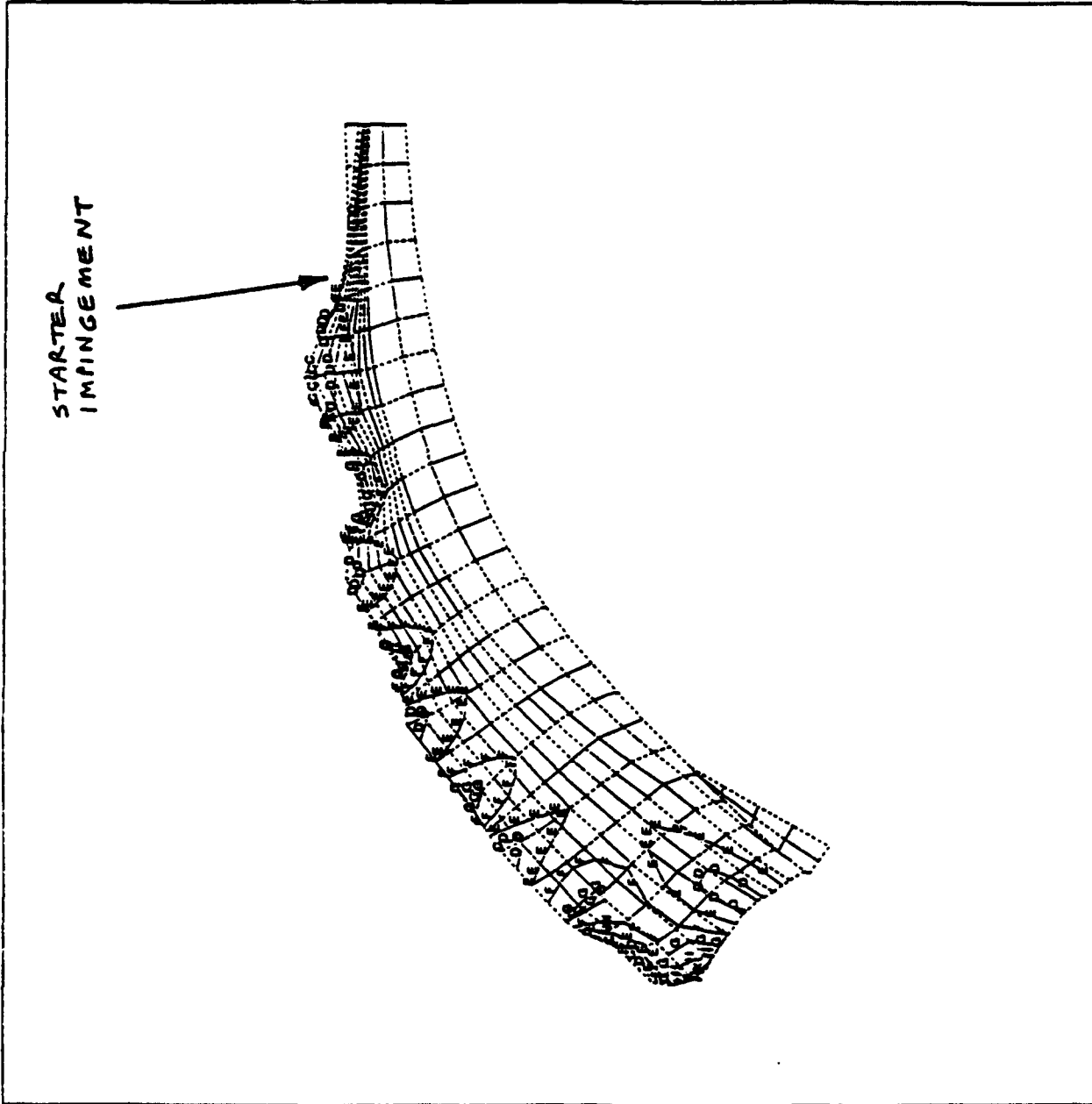


Figure 5-18. Four inch compressor blade normalized tangential displacement contours (in inches) for mode 14.

```

ANSYS  4.4A
MAY  1 1992
17:06:15
PLOT NO.  1
POST1  STRESS
STEP=1
ITER=1
FREQ=26479
UY
CSYS=1
DMX =0.941E-05
SMN =-0.271E-07
SMX =0.673E-05

YV  =1
DIST=0.76131
XF  =1.232
YF  =-1.227
ZF  =0.671147
VUP =X
PRECISE HIDDEN
A  =0.349E-06
B  =0.110E-05
C  =0.185E-05
D  =0.260E-05
E  =0.335E-05
F  =0.411E-05
G  =0.486E-05
H  =0.561E-05
I  =0.636E-05

```

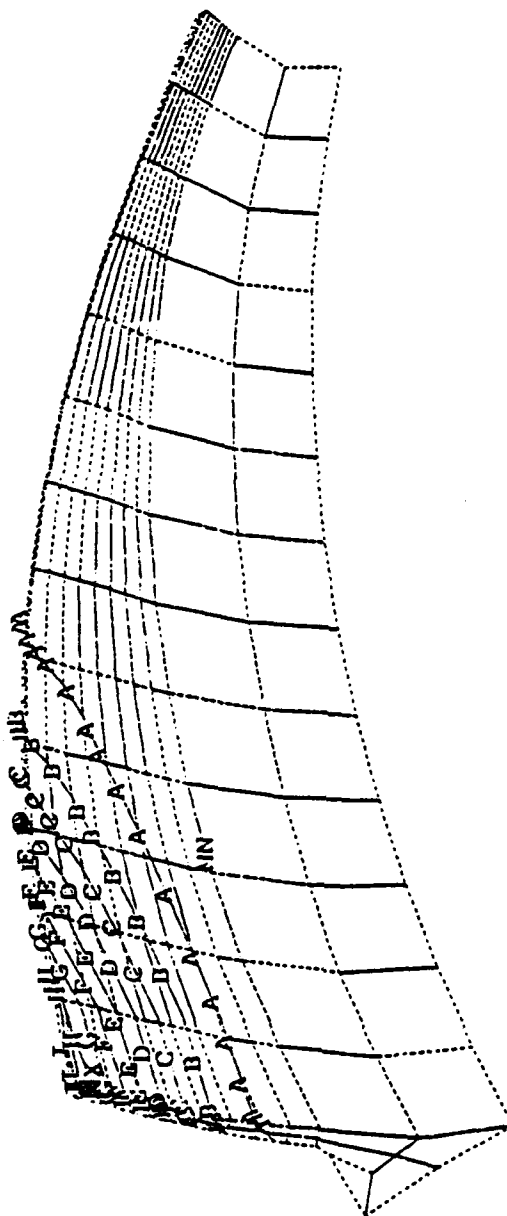


Figure 5-19. Four inch compressor splitter normalized tangential displacement contours (in inches) for mode 1.

ANSYS 4.4A

MAY 1 1992

17:06:31

PLOT NO. 2

POST1 STRESS

STEP=1

ITER=2

FREQ=37235

UY

CSYS=1

DMX =0.298E-05

SMN =-0.185E-05

SMX =0.190E-05

YV =1

DIST=0.76131

XF =1.232

YF =-1.227

ZF =0.671147

VUP =X

PRECISE HIDDEN

A =-0.164E-05

B =-0.122E-05

C =-0.806E-06

D =-0.390E-06

E =0.258E-07

F =0.442E-06

G =0.858E-06

H =0.127E-05

I =0.169E-05

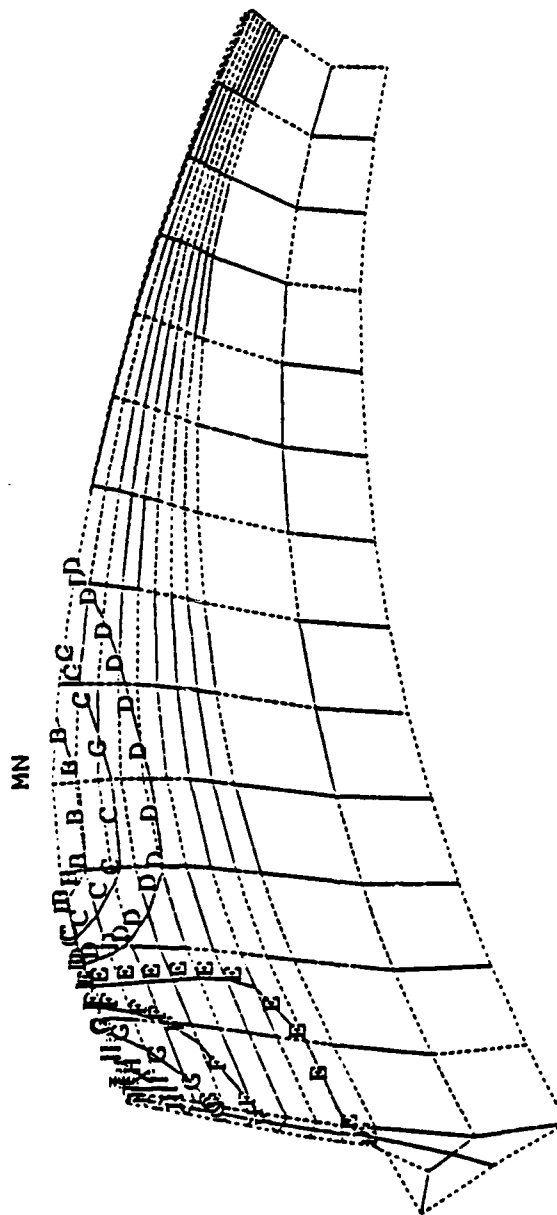


Figure 5-20. Four inch compressor splitter normalized tangential displacement contours (in inches) for mode 2.

ANSYS 4.4A

MAY 1 1992

17:07:02

PLOT NO. 3

POST1 STRESS

STEP=1

ITER=3

FREQ=49659

UY

CSYS=1

DMX =0.210E-05

SMN =-0.120E-05

SMX =0.936E-06

YV =1

DIST=0.76131

XF =1.232

YF =-1.227

ZF =0.671147

VUP =X

PRECISE HIDDEN

A =-0.108E-05

B =-0.842E-06

C =-0.605E-06

D =-0.368E-06

E =-0.131E-06

F =0.106E-06

G =0.343E-06

H =0.580E-06

I =0.817E-06

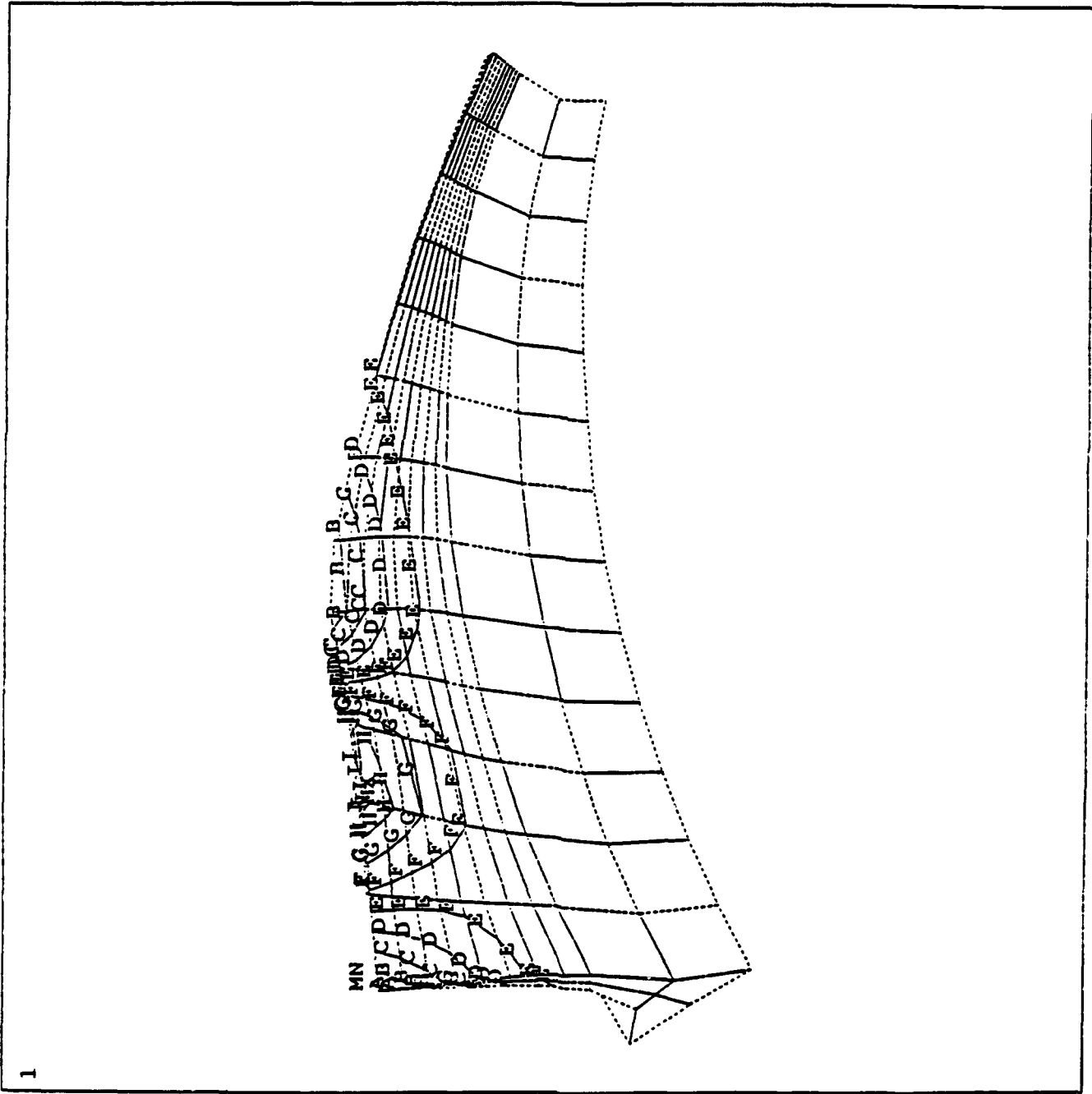


Figure 5-21. Four inch compressor splitter normalized tangential displacement contours (in inches) for mode 3.



Table 5-1. Natural frequencies of blade and splitter components of compressor rotor.

MODE	NATURAL FREQUENCY (Hz)			
	BLADE		SPLITTER	
	static	115000 rpm	static	115000 rpm
1	8164	7926	26308	26479
2	12646	12101	37123	37235
3	16686	16165	49744	49659
4	20576	20172	65129	64764
5	24150	23859	83626	82960
6	26137	26126	100250	99670
7	30627	30523		
8	35012	34838		
9	37095	37127		
10	43255	43100		
11	47109	46829		
12	51505	51300		
13	58541	58078		
14	60266	59834		
15	63370	63315		

## 6. Rotor attachment and blade tip growth analyses

Based on a previous finite element analysis, it was determined that the forward pilot of this compressor requires a minimum diametral interference fit of 0.0005 cm (0.0002 in), while the aft pilot requires a minimum diametral interference of 0.0015 cm (0.0006 in). A summary of blade growth is given in Figure 6-1. The fits and blade deflections were taken from this analysis for 115 krpm with design point steady state operating metal temperatures.

Figure 6-2 is a graphical comparison of XD<sup>®</sup> titanium aluminide and stainless steel impeller growth. The blade tip growth values are shown since they determine the tip-to-shroud running clearance under hot and rotating conditions. Since the officially-released impeller coordinate files assume stainless steel material properties, the stainless impeller growth values represent the baseline case. The baseline impeller has been configured for a uniform running clearance of 0.0127 cm (0.005 in) at design conditions. With a material change to XD<sup>®</sup> titanium aluminide, the following clearance changes occur:

The running clearance increases by 0.03 cm (0.012 in) in the leading edge region.

The running clearance increases by 0.01 cm (0.004 in) in the impeller "knee" area.

The running clearance increases by 0.015 cm (0.006 in) in the trailing edge region.

To avoid performance degradation due to these increased clearances, the XD<sup>®</sup> titanium aluminide impeller should be manufactured to the stainless steel design coordinates and shimmed 0.015 cm (0.006 in) upstream in the flow path. This will compensate for the smaller XD<sup>®</sup> titanium aluminide growth from the knee area to the trailing edge. Though the clearance in the leading edge region will not be reduced, the associated performance penalty will not be too severe for demonstration purposes.

Should the XD<sup>®</sup> titanium aluminide impeller program be continued beyond the demonstration phase, optimum performance can be achieved with a re-contoured compressor cover. In no case does it seem necessary to modify the impeller geometry as a result of a material change from stainless steel to XD<sup>®</sup> titanium aluminide.

node	original axial location	original radial location	final axial location	final radial location	axial disp	radial disp
LE TIP 221	-0.0322	1.239	-0.04523	1.247822	-0.01303	0.008822
231	-0.09607	1.239428	-0.1083	1.248122	-0.01222	0.008694
241	-0.16302	1.242837	-0.17392	1.250905	-0.0109	0.008068
251	-0.23134	1.25019	-0.24064	1.25732	-0.00929	0.00713
261	-0.30028	1.262102	-0.30787	1.268176	-0.00759	0.006073
271	-0.36953	1.278893	-0.37545	1.283934	-0.00592	0.005041
281	-0.43868	1.30068	-0.44309	1.304841	-0.00441	0.004161
291	-0.50705	1.326508	-0.51022	1.330026	-0.00317	0.003518
301	-0.5743	1.356866	-0.57653	1.359979	-0.00223	0.003113
311	-0.64022	1.391456	-0.64176	1.394357	-0.00154	0.002901
321	-0.705	1.429635	-0.706	1.432457	-0.001	0.002822
331	-0.77122	1.470961	-0.7717	1.473779	-0.00048	0.002818
341	-0.83867	1.515531	-0.83859	1.518381	0.000081	0.00285
351	-0.90706	1.561414	-0.90638	1.564343	0.000675	0.002929
361	-0.97742	1.606007	-0.97612	1.609062	0.001294	0.003055
371	-1.05063	1.650285	-1.04869	1.653522	0.001941	0.003236
381	-1.12888	1.691947	-1.12631	1.69543	0.002568	0.003483
391	-1.21228	1.732935	-1.20917	1.736741	0.003109	0.003807
401	-1.30203	1.772104	-1.29848	1.776319	0.003543	0.004215
411	-1.39619	1.811771	-1.39227	1.816487	0.003917	0.004716
421	-1.49377	1.852481	-1.48955	1.857775	0.004221	0.005293
TE TIP 431	-1.5932	1.8946	-1.58876	1.900464	0.004443	0.005864

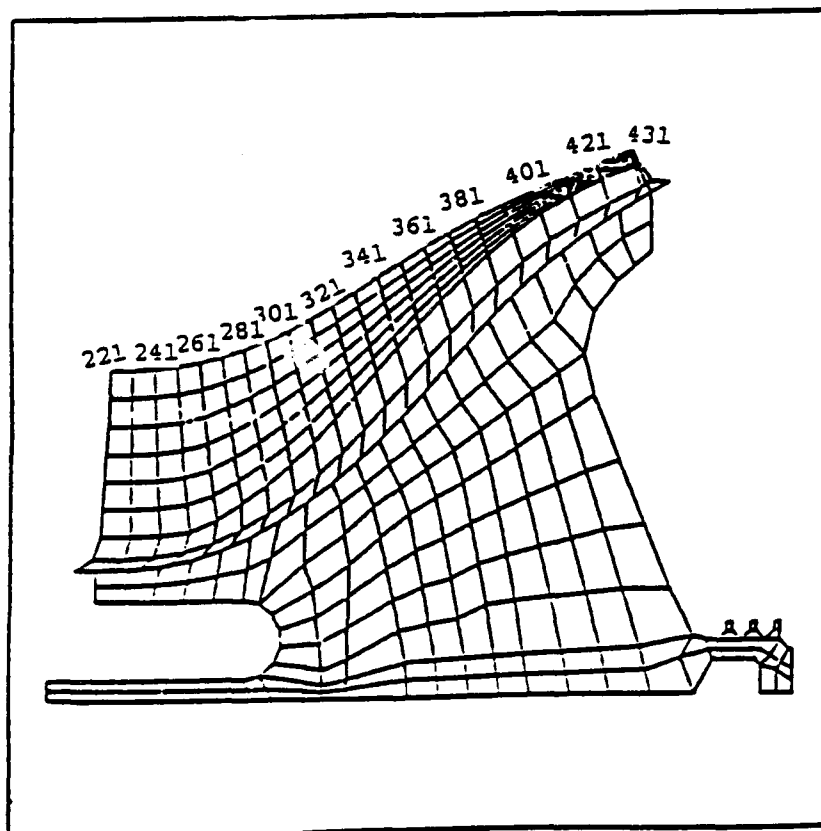


Figure 6-1. Blade tip displacements (in inches). Note, axial zero is located at blade leading edge root.

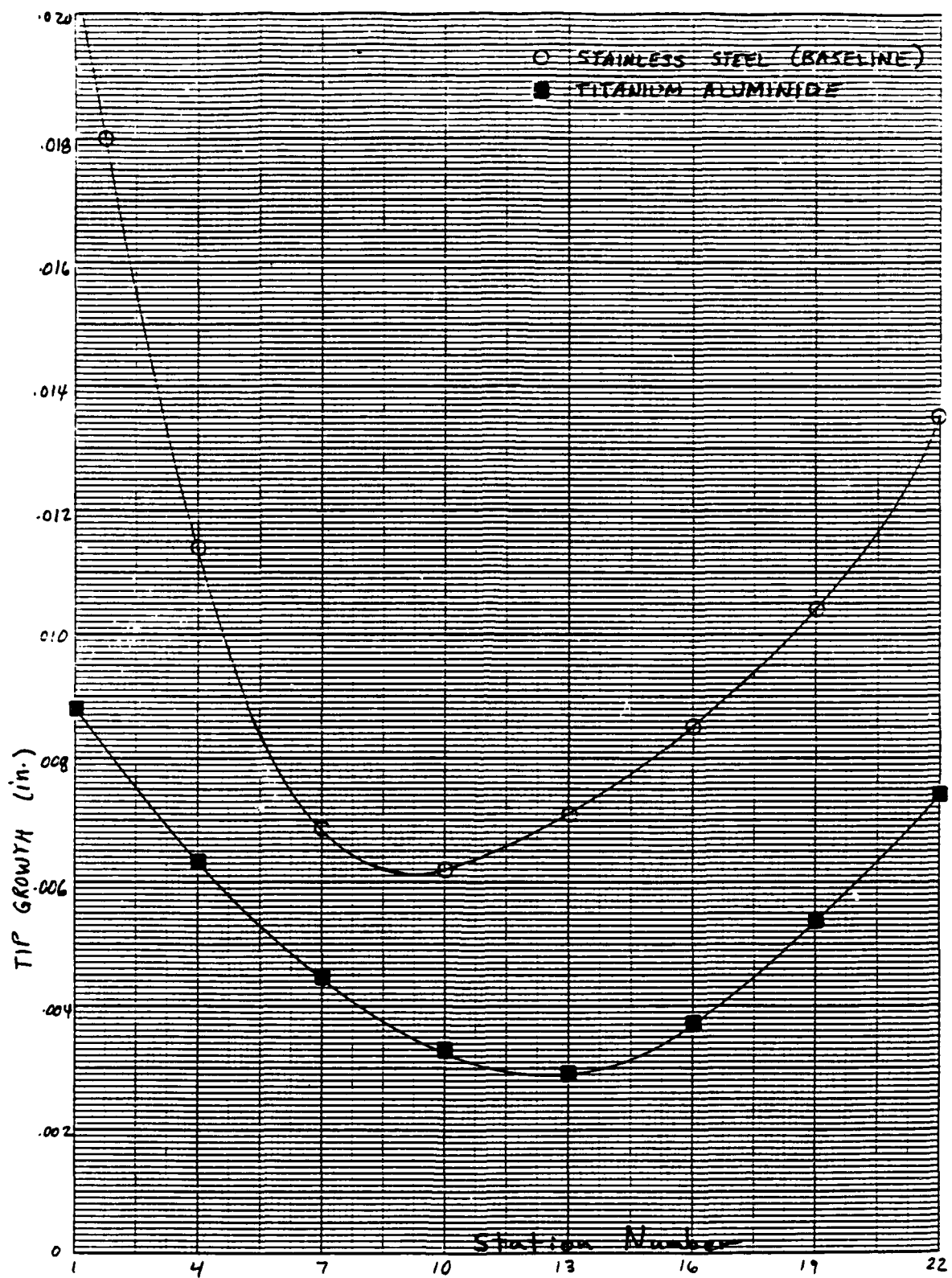


Figure 6-2. Impeller tip growths for the 4 inch mixed-flow compressor rotor. Material comparisons are shown between stainless steel and XD® titanium aluminide.

## **APPENDIX B--MECHANICAL PROPERTIES**

Table B-I. Room-temperature tensile test data for as-HIPed (fully equiaxed microstructure) and heat-treated (fully lamellar microstructure) Ti-45Al-2Mn-2V + 7 volume % TiB<sub>2</sub> alloy. All failures occurred in the gauge radius except that specimen marked with an asterisk where failure occurred within the gauge section.

Material Condition	Strain Rate	Yield Strength (MPa)	Fracture Strength (MPa)	Ductility (% elongation)
As HIPed	4 x 10 <sup>-5</sup>	554	639	0.61
As HIPed	4 x 10 <sup>-5</sup>	468	568	0.87
HIPed + 1340°C/1h*	2 x 10 <sup>-4</sup>	593	741	0.62
HIPed + 1340°C/1h	2 x 10 <sup>-4</sup>	643	787	0.64
HIPed + 1340°C/1h	2 x 10 <sup>-5</sup>	570	708	0.53

Table B-II. Tensile properties of the Ti-45Al-2Mn-2V + 7 volume % TiB<sub>2</sub> alloy performed at various temperatures for lamellar and lamellar + equiaxed microstructures.

Lamellar Microstructures:

Temperature (°C)	Strain Rate	Yield Strength (MPa)	Fracture Strength (MPa)	Ductility (% elongation)
20	6.8 x 10 <sup>-5</sup>	634	634	0.19
20	9.7 x 10 <sup>-5</sup>	593	628	0.29
200	9.7 x 10 <sup>-5</sup>	549	579	0.30
200	9.7 x 10 <sup>-5</sup>	584	640	0.36
500	6.8 x 10 <sup>-5</sup>	557	557	0.13
500	9.7 x 10 <sup>-5</sup>	569	610	0.31
700	9.7 x 10 <sup>-5</sup>	459	593	0.95
700	9.7 x 10 <sup>-5</sup>	466	590	0.98*
900	9.7 x 10 <sup>-5</sup>	234	276	> 5.00
900	9.7 x 10 <sup>-5</sup>	221	269	> 5.00

Lamellar + Equiaxed Microstructures:

Temperature (°C)	Strain Rate	Yield Strength (MPa)	Fracture Strength (MPa)	Ductility (% elongation)
20	6.8 x 10 <sup>-5</sup>	612	652	0.30
20	9.7 x 10 <sup>-5</sup>	572	655	0.47
200	9.7 x 10 <sup>-5</sup>	555	593	0.30
200	9.7 x 10 <sup>-5</sup>	538	593	0.37
500	6.8 x 10 <sup>-5</sup>	559	628	0.36
500	9.7 x 10 <sup>-5</sup>	583	699	0.58
700	9.7 x 10 <sup>-5</sup>	455	638	1.95
700	9.7 x 10 <sup>-5</sup>	421	638	2.10*
900	9.7 x 10 <sup>-5</sup>	241	283	> 5.00
900	9.7 x 10 <sup>-5</sup>	234	286	> 5.00

\* Represent samples that broke in the gauge section of the sample.

Table B-III. Short-rod fracture toughness results for testing performed at Metcut at room temperature and 200°C (392°F) in air.

Specimen Identification	Morphology	$K_{QVM}$ (MPa√m)	$K_{QV}$ (MPa√m)	Sections of Invalidity in ASTM E1304-89 <sup>22</sup>
SRL1	lamellar	24.7	22.0	9.2, 9.5.2, 9.3.3
SRL2	lamellar	23.7	21.3	8.2, 9.2, 9.5.3
SRM1	lamellar + equiaxed	21.9	20.1	8.2, 9.2,
SRM2	lamellar + equiaxed	22.6	21.9	9.2, 9.5.3
SRL3	lamellar	32.9		8.3.5.1, 9.2, 9.5.2, 9.5.3
SRL4	lamellar	33.2		8.3.5.1, 9.2, 9.5.2, 9.5.3
SRM4	lamellar + equiaxed	29.8		8.3.5.1, 9.2, 9.5.2, 9.5.3
SRM5	lamellar + equiaxed	26.6	25.8	8.2, 9.2, 9.5.2

Table B-IV Fracture toughness results performed on notched-bend specimens tested in 3-point bend at 20°C (68°F), 200°C (392°F), 300°C (572°F), and 400°C (752°F) in air. Each of the 8 test specimens had been subjected to a heat treatment to produce a lamellar microstructure.

Testing Temperature (°C)	Fracture Toughness (MPa√m)
20	15.8
20	15.8
200	17.2
200	20.0
300	20.7
300	22.5
400	20.3
400	22.5

Table B-V. High-cycle fatigue data for testing performed at room temperature and 200°C, at a frequency of 60 Hz and R ratio of -1, on Ti-45Al-2Mn-2V + 7 volume % TiB<sub>2</sub> material heat treated at 1340°C for 1 h that has a fully lamellar microstructure. Testing was stopped at 10<sup>7</sup> cycles.

Test Temp (°C)	Maximum Stress (MPa)	Cycles to Failure	Remarks
20	586	6100	FG
20	552	26500	FG
20	517	1495700	FG
20	483	1176400	RI
20	483	2120700	FG
20	462	5214900	FG
20	462	10000000	RUNOUT
20	414	10000000	RUNOUT
200	552	1300	FG
200	534	138300	FG
200	517	354100	FG
200	483	1373100	FG
200	448	6420000	FG
200	414	10000000	RUNOUT
200	276	10000000	RUNOUT
200	172	10000000	RUNOUT

FG: Failed in the gauge section.

RI: Failed in radius gauge section interface.

RUNOUT: Test terminated at 10<sup>7</sup> cycles without failure.



Table B-VI. Results of creep testing performed at 800°C (1472°F) on Ti-45Al-2Mn-2V + 7 volume % TiB<sub>2</sub> material heat treated at 1340°C (2444°F) for 1 h that has a fully lamellar microstructure.

Sample ID number	Stress (MPa)	0.5% Creep Strain (h)	1.0% Creep Strain (h)	2.0% Creep Strain (h)	Creep Strain % at 20 h	Creep Strain % at 30 h	Creep Strain % at 50 h	Steady State Creep Rate (%/h)	Final Creep (%)*	Total Hours	Elong (%)*	R. A. (%)	Remarks
T8-1	138	1.75	5.00	14.00	2.63	3.69	6.09	0.111	33.82	129.9	38.7	50.8	
T8-2	138	1.75	5.50	16.00	2.36	3.30	5.20	0.0923	32.38	135.1	33.8	54.4	OQ
T8-3	207	0.75	1.75	4.00	13.03			0.436	36.97	26.6	38.2	45.2	
T8-4	207	0.50	1.50	4.00	12.20			0.411	26.15	26.1	33.0	44.5	
T8-8	207	0.75	1.75	3.75	13.10			0.408	32.21	25.9	36.0	44.9	
T8-5	276	0.50	0.75	1.50				1.28	21.97	7.0	26.8	35.7	
T8-6	276	0.50	0.75	1.75				1.31	22.12	7.5	27.9	31.9	OQ
T8-7	345	0.25	0.25	0.50				4.93	14.15	1.9	22.9	29.4	

OQ: Test failed in the outer quarter of gauge section.

\* Final creep (%) is the last recorded value before failure; elongation (%) is directly measured after failure.

138 MPa

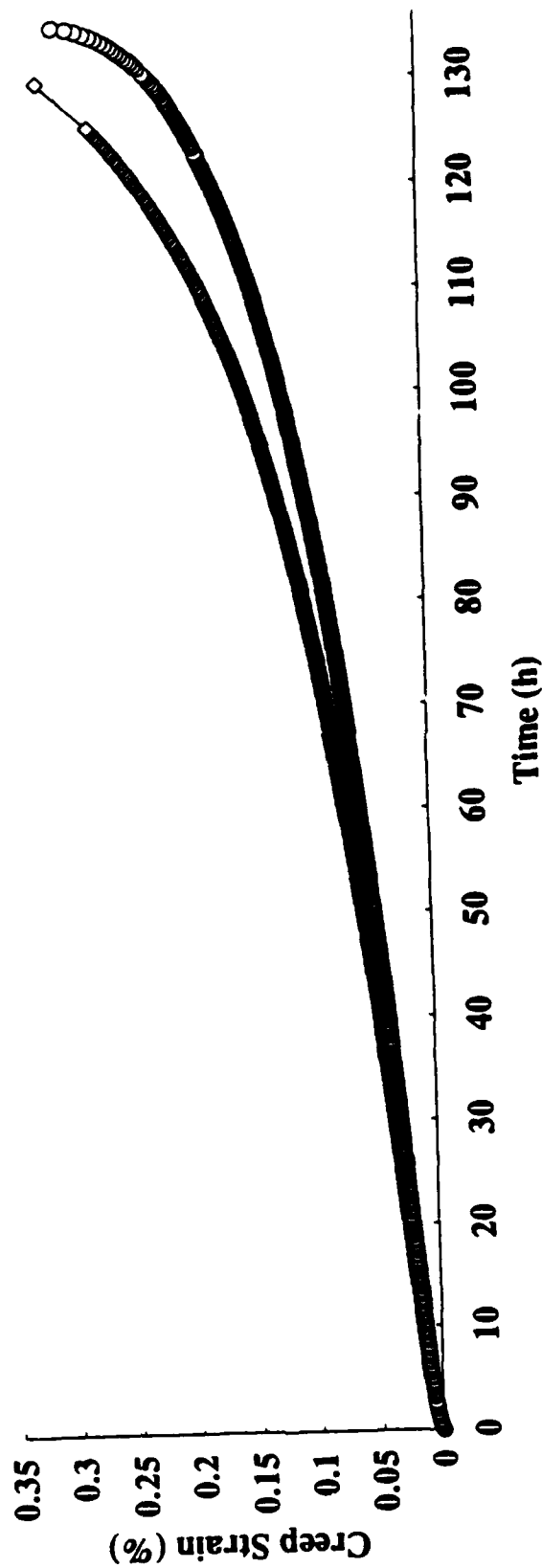


Figure B-1. Creep behavior of 2 test specimens of Ti-45Al-2Mn-2V + 7 volume % TiB<sub>2</sub> alloy, heat treated to a fully lamellar microstructure and tested at 800°C (1472°F) and 138 MPa (20 ksi).

207 MPa

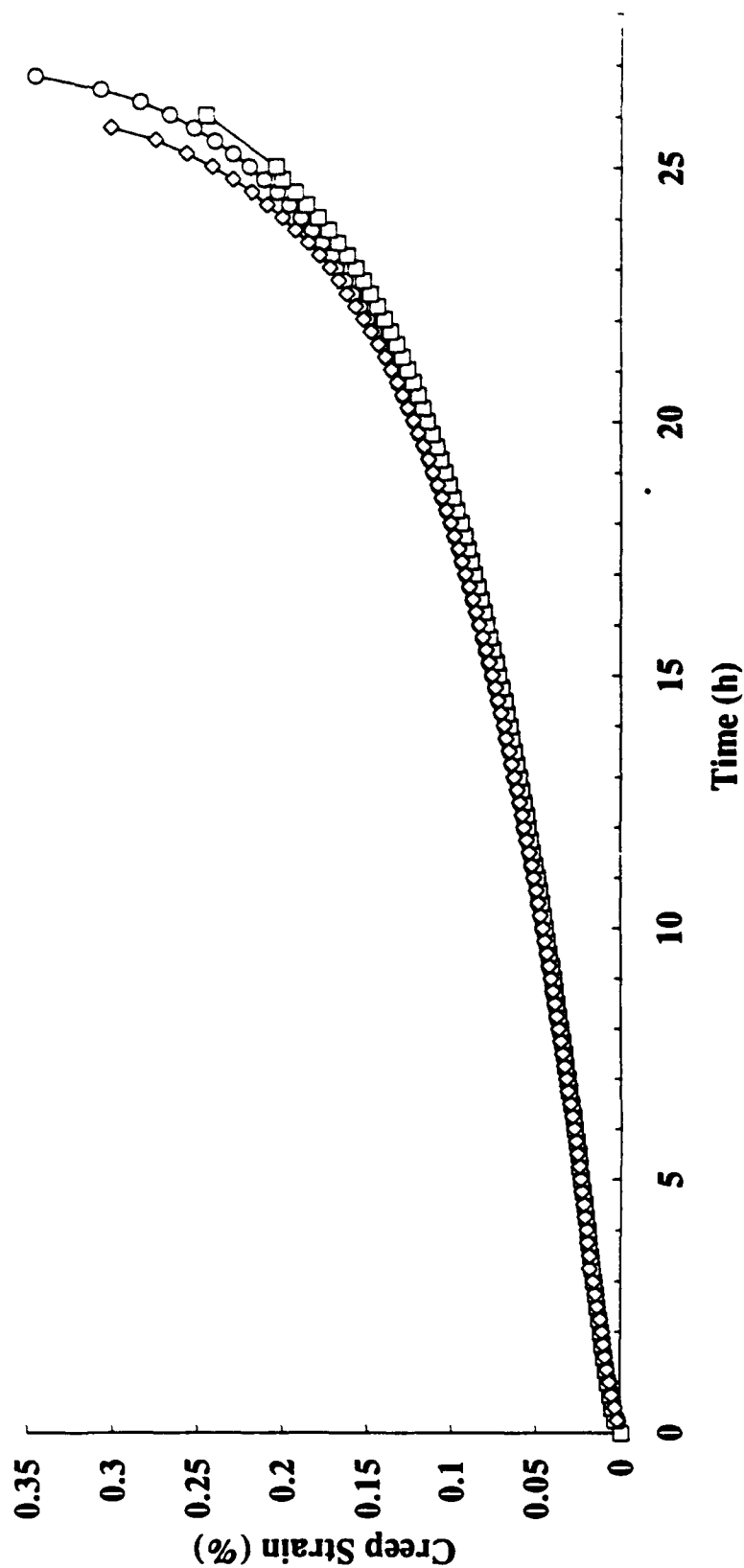
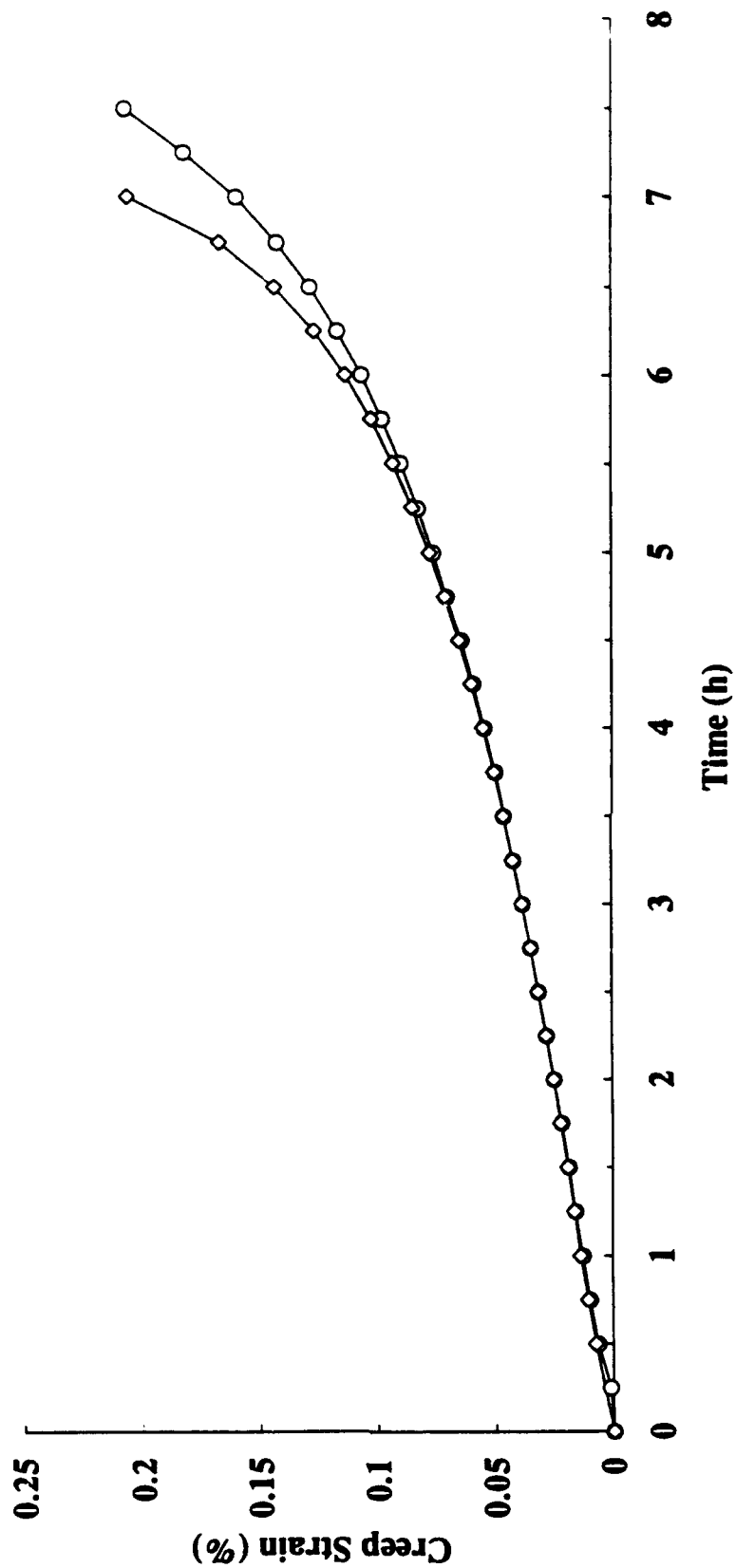


Figure B-2. Creep behavior of 3 test specimens of Ti-45Al-2Mn-2V + 7 volume % TiB<sub>2</sub> alloy, heat treated to a fully lamellar microstructure and tested at 800°C (1472°F) and 207 MPa (30 ksi).

276 MPa



B8

Figure B-3. Creep behavior of 2 test specimens of Ti-45Al-2Mn-2V + 7 volume % TiB<sub>2</sub> alloy, heat treated to a fully lamellar microstructure and tested at 800°C (1472°F) and 276 MPa (40 ksi).

345 MPa

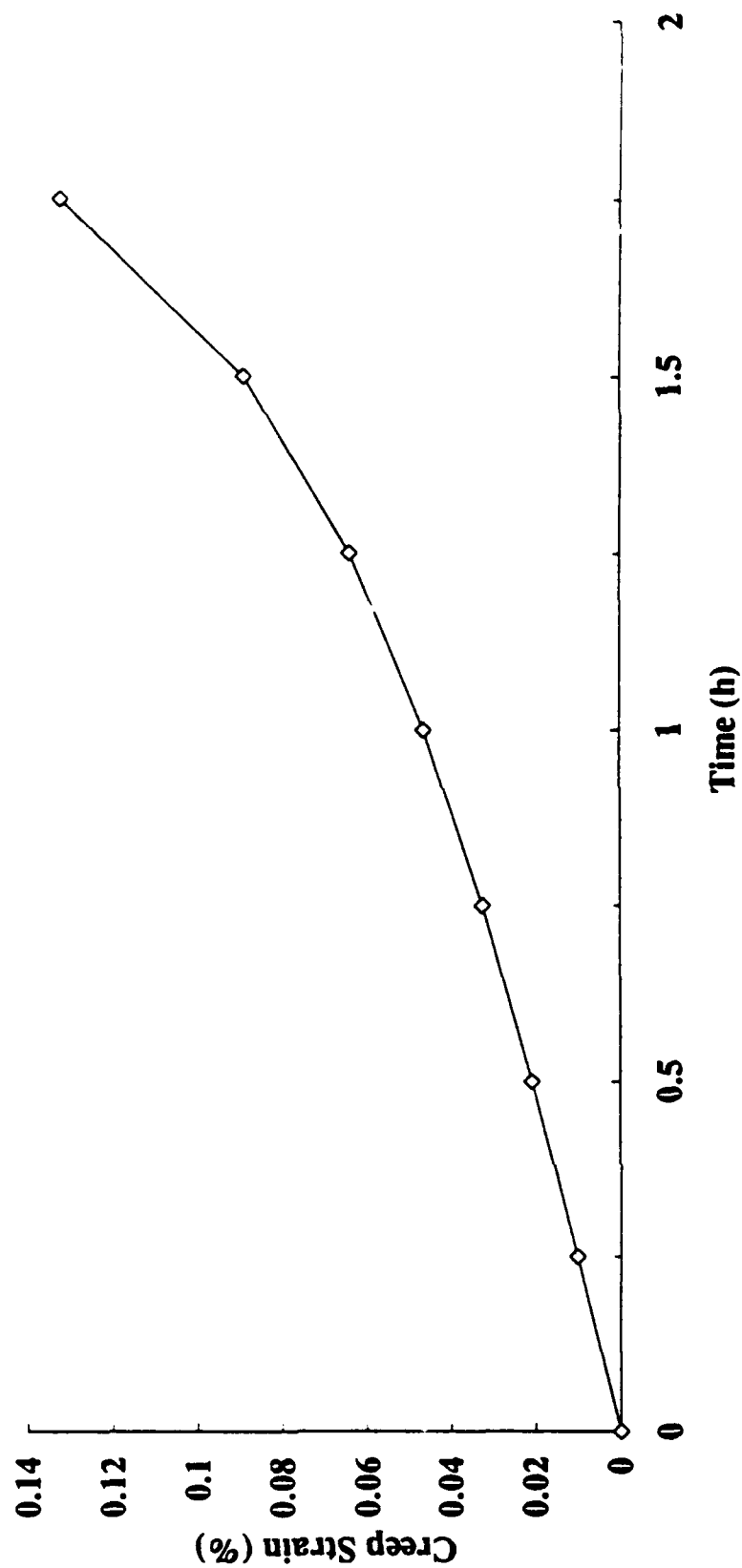


Figure B-4. Creep behavior of 1 test specimen of Ti-45Al-2Mn-2V + 7 volume % TiB<sub>2</sub> alloy, heat treated to a fully lamellar microstructure and tested at 800°C (1472°F) and 345 MPa (50 ksi).

# DISTRIBUTION LIST

No. of Copies	To
1	Office of the Under Secretary of Defense for Research and Engineering, The Pentagon, Washington, DC 20301
	Director, U.S. Army Research Laboratory, 2800 Powder Mill Road, Adelphi, MD 20783-1197
1	ATTN: AMSRL-OP-CI-AD, Technical Publishing Branch
1	AMSRL-OP-CI-AD, Records Management Administration
	Commander, Defense Technical Information Center, Cameron Station, Building 5, 5010 Duke Street, Alexandria, VA 22304-6145
2	ATTN: DTIC-FDAC
1	MIAC/CINDAS, Purdue University, 2595 Yeager Road, West Lafayette, IN 47905
	Commander, Army Research Office, P.O. Box 12211, Research Triangle Park, NC 27709-2211
1	ATTN: Information Processing Office
	Commander, U.S. Army Materiel Command, 5001 Eisenhower Avenue, Alexandria, VA 22333
1	ATTN: AMCSCI
	Commander, U.S. Army Materiel Systems Analysis Activity, Aberdeen Proving Ground, MD 21005
1	ATTN: AMXSY-MP, H. Cohen
	Commander, U.S. Army Missile Command, Redstone Scientific Information Center, Redstone Arsenal, AL 39809-5241
1	ATTN: AMSMI-RD-CS-R/Doc
	Commander, U.S. Army Armament, Munitions and Chemical Command, Dover, NJ 07801
1	ATTN: SMCAR-AET
1	Director, U.S. Army Research Laboratory, Aberdeen Proving Ground, MD 21005
	Director, Benet Weapons Laboratory, LCWSL, USA AMCCOM, Watervliet, NY 12189
1	ATTN: AMSMC-LCB-TL
	Commander, U.S. Army Foreign Science and Technology Center, 220 7th Street, N.E., Charlottesville, VA 22901-5396
1	ATTN: AIFRTC, Applied Technologies Branch, Gerald Schlesinger
	U.S. Army Aviation Training Library, Fort Rucker, AL 36360
1	ATTN: Building 5906-5907
	Commander, U.S. Air Force Wright Research & Development Center, Wright-Patterson Air Force Base, OH 45433-6523
1	ATTN: WRDC/MLLP, M. Forney, Jr.
	NASA - Marshall Space Flight Center, MSFC, AL 35812
1	ATTN: Mr. Paul Schuerer/EH01
	General Dynamics, Convair Aerospace Division, P.O. Box 748, Fort Worth, TX 76101
1	ATTN: Mfg. Engineering Technical Library

No. of  
Copies

To

- 1 Department of the Army, Aerostructures Directorate, MS-266, U.S. Army Aviation R&T Activity, AVSCOM, Langley Research Center, Hampton, VA 23665-5225
- U.S. Army Vehicle Propulsion Directorate, NASA Lewis Research Center,  
2100 Brookpark Road, Cleveland, OH 44135-3191
- 1 ATTN: AMSRL-VP
- 1 NASA - Lewis Research Center, 2100 Brookpark Road, Cleveland, OH 44135-3191
- Director, Defense Intelligence Agency, Washington, D.C. 20340-6053
- 1 ATTN: ODT-5A (Mr. Frank Jaeger)
- Atlantic Research, 5945 Wellington Road, Coainesville, VA 22312
- 1 ATTN: Ms. Michele Abraham
- Ford Motor Company, Room S-2065 Science Lab., Dearborn, MI 48124-2053
- 1 ATTN: Dr. John Allison
- Pratt and Whitney, P.O. Box 109600, MS 707-26, West Palm Beach, FL 33410-9600
- 1 ATTN: Mr. Ralph Anderson
- Rockwell International Corporation, 201 N. Douglas Street, El-Segunda, CA 90245
- 1 ATTN: Mr. Sami El-Soudani
- GE Aircraft Engineer, 1000 Western Avenue, M/S 37403, Lynn, MA 01910
- 1 ATTN: Mr. James Fleck
- ARC Amercom, 8928 Fullbright Avenue, Chatsworth, CA 91311
- 1 ATTN: Mr. Vincent Fry
- Lockheed Aeronautical Systems Co., 86 S. Cobb Dr., Bldg. C1, Marietta, GA 30063
- 1 ATTN: Mr. Timothy Ginter, D73/C3, Zone 0648
- General Dynamics, MZ 5860, P.O. Box 748, Fort Worth, TX 76101-0748
- 1 ATTN: Mr. David Gordon
- Rockwell International Science Center, 1049 Camino dos Rios, P.O. Box 1085,  
Thousand Oaks, CA 91360
- 1 ATTN: Dr. Jeffrey Graves
- Garrett Engine Division, 111 S. 34th St., P.O. Box 5217, MS 5034V, Phoenix, AZ 85010
- 1 ATTN: Dr. James Hall
- 1 Titanium Metals Corp., P.O. Box 2128, Henderson, NV 89009
- GM Corp. Advanced Engineering Staff, 30300 Mound Rd., A/MD-31, Warren,  
MI 48090-9040
- 1 ATTN: Ms. Susan Hartfield-Wunsch
- Howmet Corp./Applied Research Div. - CTL, 1500 South Warner Street,  
Whitehall, MI 49461-1895
- 1 ATTN: Mr. Blair London

No. of Copies	To
1	Crucible Materials Corporation, P.O. Box 88, Pittsburgh, PA 15230 ATTN: Mr. John Moll
1	Textron Specialty Materials, Two Industrial Avenue, Lowell, MA 01851 ATTN: Mr. Peter Nagy
1	Textron Lycoming, 550 S. Main Street, Stratford, CT 06497-2452 ATTN: Dr. Vinod Nangia
1	United Technologies Corporation, 400 Main Street, East Hartford, CT 06108 ATTN: Mr. Paul Nisson
1	GM Corp./Allison Gas Turbine, 333 W. First Street, Ste 200, Dayton, OH 45402 ATTN: Dr. John Petrusha
1	Allied-Signal Aerospace Co., 717 N. Bendix Drive, Southbend, IN 46620 ATTN: Mr. Richard Rateick, Jr.
1	MSNW Inc., P.O. Box 865, San Marcos, CA 92069-0300 ATTN: Dr. George Reynolds
1	GM Corp./Allison Gas Turbine, P.O. Box 420, Speed Code W06, Indianapolis, IN 46206-0420 ATTN: Mr. Ronald Roessier
1	GE Corp. R&D, P.O. Box 8, Bldg., K-1, MB-265, Schenectady, NY 12301 ATTN: Dr. R. Grant Rowe
1	McDonnell Douglas Corporation, P.O. Box 516, MC 1021322, St. Louis, MO 63166 ATTN: Ms. Catherine Sabinash
1	RMI Titanium Co., 1000 Warren Avenue, Niles, OH 44446 ATTN: Mr. John Schley
1	Allied Signal Aerospace, 3000 Presidential Drive, Ste 300, Fairborn, OH 45324 ATTN: Mr. David Stanforth
2	Director, U.S. Army Research Laboratory, Watertown, MA 02172-0001 ATTN: AMSRL-OP-CI-D, Technical Library
1	AMSRL-OP-CI-D, Visual Information
1	AMSRL-OP-PR-WT
15	AMSRL-MA-MA, Wego Wang (COR)